



HAL
open science

0D/1D combustion modeling for the combustion systems optimization of spark ignition engines

Sokratis Demesoukas

► **To cite this version:**

Sokratis Demesoukas. 0D/1D combustion modeling for the combustion systems optimization of spark ignition engines. Other. Université d'Orléans, 2015. English. NNT : 2015ORLE2024 . tel-02902187

HAL Id: tel-02902187

<https://theses.hal.science/tel-02902187>

Submitted on 18 Jul 2020

HAL is a multi-disciplinary open access archive for the deposit and dissemination of scientific research documents, whether they are published or not. The documents may come from teaching and research institutions in France or abroad, or from public or private research centers.

L'archive ouverte pluridisciplinaire **HAL**, est destinée au dépôt et à la diffusion de documents scientifiques de niveau recherche, publiés ou non, émanant des établissements d'enseignement et de recherche français ou étrangers, des laboratoires publics ou privés.

ÉCOLE DOCTORALE
ÉNERGIE, MATÉRIAUX, SCIENCES DE LA TERRE ET DE L'UNIVERS

LABORATOIRE PRISME

THÈSE présentée par :
Sokratis DEMESOUKAS

soutenue le : **17 juillet 2015**

pour obtenir le grade de : **Docteur de l'université d'Orléans**

Discipline: **Énergétique**

**Modélisation 0D/1D de la combustion pour
l'optimisation des systèmes de combustion des mo-
teurs à allumage commandé**

-

**0D/1D combustion modeling for the combustion
systems optimization of spark ignition engines**

THÈSE dirigée par :

Pascal HIGELIN

Professeur, Université d'Orléans

RAPPORTEURS :

Fabio BOZZA

Professore Ordinario, Università di Napoli "Federico II"

Luis LE MOYNE

Professeur, Université de Bourgogne, Président du Jury

JURY :

Xavier TAUZIA

Maître de Conférences (HDR), École Centrale Nantes

Alessio DULBECCO

Dr. Ingénieur, IFPEN

Christian CAILLOL

Maître de Conférences, Université d'Orléans

Andrei BOIARCIUC

Dr. Ingénieur, Renault SAS

Dédié à Angélique

Dedicated to Angelica

Αφιερώνεται στην Αγγελική

Remerciements

Cette thèse a été effectuée avec la collaboration du laboratoire PRISME de l'Université d'Orléans et de RENAULT SAS.

Je tiens à remercier M. Andrei Boiarciuc, qui a été le tuteur industriel de cette thèse et avec qui j'ai passé la plus grande partie de cette thèse pour la bonne coopération, ses conseils techniques, sa persistance pour obtenir les meilleurs résultats et pour le temps qui m'a consacré sachant qu'il n'en avait pas beaucoup.

Je remercie aussi M. Christian Caillol qui a encadré cette thèse surtout pour la patience qui a fait avec moi pendant ces années en m'expliquant comment il faut orienter mon discours scientifique. Il m'a rassuré pendant des moments difficiles et il m'a montré la bonne direction scientifique plusieurs fois.

Je remercie aussi Pr. Pascal Higelin, qui a dirigé cette thèse et qui m'a confié ce travail de recherche. Je souhaite aussi remercier M. Alain Floch qui a eu l'initiative de lancer cette thèse CIFRE au sein de Renault.

Je tiens aussi à remercier les professeurs Fabio Bozza et Luis Le Moyne qui ont accepté de juger mon travail de thèse et d'être rapporteurs dans le jury de la soutenance. En plus, je remercie M. Xavier Tauzia et M. Alessio Dulbecco qui ont été examinateurs dans le jury de la soutenance.

Après avoir passé une longue période de la thèse dans l'entreprise je tiens à remercier M. Cédric Servant et M. Benoit Lorenzon pour avoir fourni les calculs 3D de mécanique des fluides et leurs conseils. Je tiens aussi à remercier M. Jérôme Ponge et M. Nacer Sekfane pour leurs conseils techniques. Je remercie aussi M. Yann Videt qui m'a énormément aidé avec les dessins CAO.

Dans le laboratoire PRISME, je tiens à remercier tout d'abord mon ami Pierre Bréquigny, qui m'a beaucoup soutenu pendant des périodes difficiles. Cette bonne ambiance entre nous a donné une collaboration scientifique. Je tiens aussi à remercier Salim Sayssouk pour son bon humeur et son aide avec plusieurs problèmes quotidiens que j'ai rencontré. Tous les membres du laboratoire m'ont aidé d'une façon différente même si j'étais absent pendant la plupart du temps et je les remercie sans faire références à des noms afin de n'oublier personne.

Contents

Chapter 1 Context of contemporary SI combustion engines design.....	15
1.1 Introduction	15
1.2 Pollutant emissions and law-imposed limitations.....	16
1.3 Carbon dioxide emissions and future goals.....	16
1.4 The Spark Ignition combustion engine	18
1.5 Solutions for the emissions and consumption reduction	22
1.5.1 Downsizing by turbocharging	23
1.5.2 Compression ratio adjustment.....	24
1.5.3 Variable Valve Actuation (VVA).....	25
1.5.4 High Research Octane Number (RON) fuels.....	26
1.5.5 Mixture Dilution	26
1.6 Concise description of Spark Ignition combustion and emissions.....	26
1.6.1 Nitrogen Oxides (NO _x)	28
1.6.2 Carbon Monoxide (CO).....	29
1.6.3 Hydrocarbons (HC).....	30
1.7 Research tools for development of Spark Ignition Combustion	30
1.7.1 Computational Fluid Dynamics tools	31
1.7.2 Tools for chemical processes description.....	32
1.7.3 0D System simulation	32
1.8 Objectives and structure of this work.....	34
Chapter 2 Turbulent premixed combustion: physics and models	37
2.1 Laminar premixed flames.....	37
2.2 Flame stretch	40
2.3 Aerodynamic turbulence	41
2.4 Turbulent premixed flames.....	44
2.4.1 Flame propagation inside the combustion chamber	47
2.5 Comparison of turbulent flame models.....	48
2.5.1 Laminar flame surface.....	49
2.5.2 Laminar flame speed	50
2.5.3 Aerodynamic turbulence	51
2.5.4 Eddy Burn Up model.....	51
2.5.5 Fractal model.....	52
2.5.6 Flame Surface Density model	53
2.5.7 Results and discussion of the comparison	53
2.5.8 Conclusion for the comparison of models	61

Chapter 3 Development and validation of a SI combustion model	63
3.1 Piston kinematics	64
3.2 Numerical solver	65
3.3 Two-zone thermodynamic modeling.....	66
3.3.1 Mass and energy conservation	66
3.3.2 Composition of each zone.....	66
3.4 Heat transfer	67
3.5 Reconstructed heat release rate	68
3.6 Flame Geometry	68
3.6.1 Concise description of the flame geometry model	68
3.6.2 Validation of geometric model.....	69
3.7 Overview of the combustion model	71
3.8 Turbulence	72
3.9 Flame-wall interaction sub-model.....	72
3.9.1 Quenching of laminar flames.....	73
3.9.2 Quenching of turbulent flames	74
3.9.3 Flame-wall interaction wrinkling for the entire flame	75
3.10 Validation of flame-wall interaction sub-model.....	76
3.10.1 Experimental setup	76
3.10.2 Validation results.....	77
3.11 Conclusion for the wall-flame interaction impact.....	83
3.12 Post flame reactions sub-model	84
3.12.1 Contribution of CO to the heat release rate	84
3.12.2 Contribution of HC to the heat release rate	85
3.13 Validation of post flame reactions sub-model	88
3.13.1 Experimental setup	88
3.13.2 Impact of CO on the heat release rate	89
3.13.3 Impact of HC on the heat release rate.....	92
3.14 Conclusion for the post-flame reactions	94
3.15 Impact of flame stretch	94
3.16 Validation of flame stretch sub-model	96
3.16.1 Experimental setup for flame stretch impact.....	96
3.16.2 Validation results for flame stretch impact.....	97
3.17 Conclusion for impact of flame stretch.....	105
Chapter 4 Model validation for different engine configurations	107
4.1 Test bed engine description	107
4.2 Comparison with optimal advance angle engine test bed results.....	110
4.2.1 Typical evolutions of combustion variables in a cycle.....	114

4.2.2 Operating points of particular interest.....	126
4.2.3 Results for all operating points	129
4.3 Specific tests for sub-model validation	133
4.3.1 Fuel/air equivalence ratio variation.....	134
4.3.2 Gasoline/Ethanol fuel	136
4.3.3 Variable valve timing	141
Chapter 5 Conclusion and Perspective	147
5.1 Comparison of turbulent premixed combustion models	147
5.2 Flame-wall interaction	148
5.3 Post flame reactions.....	148
5.4 Impact of flame stretch on heat release.....	149
5.5 Model validation for different engine configurations.....	149
5.6 Perspective	149
Appendix A Thermodynamic model.....	151
A.1 System of differential equations	151
A.2 Composition of fresh gases zone.....	158
A.3 Composition of burnt gases zone.....	160
A.4 Thermodynamic properties of zones	163
Appendix B Geometric model.....	169
B.1 Burnt gas volume calculation	171
B.2 Mean flame surface calculation in function of the distance from the wall.....	180
Appendix C Flame Surface density equation	183
Appendix D Supplementary results of optimal advance configuration.....	185
Appendix E Résumé du manuscrit en français	207
E.1 Contexte de la conception contemporaine des moteur à allumage commandé... 207	
E.2 Combustion de pré-mélange turbulente: Physique et modélisation..... 209	
E.3 Développement et validation d'un modèle de combustion à allumage commandé... 211	
E.4 Validation du modèle pour des différentes configurations de moteur	213
E.5 Conclusions et perspectives	214
References.....	219

Nomenclature

Abbreviations

0D	Zero Dimensional (only function of time)
1D	One Dimensional (only one spatial variable and time)
BDC	Bottom Dead Center
CAD	Computer Aided Design
CAXX	Crank Angle when XX % of charge has been burnt
CFD	Computational Fluid Dynamics
DEM	Dilution Exponent Multiplier
DI	Direct Injection
DNS	Direct Numerical Simulation
EGR	Exhaust Gases Recirculation
EVC	Exhaust Valve Closing
EVO	Exhaust Valve Opening
EXX	Fuel with XX % volume fraction of ethanol and 1-XX % of gasoline
FSD	Flame Surface Density
HC	HydroCarbons
IMEP	Indicated Mean Effective Pressure
IVC	Inlet Valve Closing
IVO	Inlet Valve Opening
KPP	Kolmogorov Petrovskii Piskunov
LES	Large Eddy Simulation
LHS	Left Hand Side
LHV	Lower Heating Value
PFI	Port Fuel Injection
RANS	Reynolds Averaged Navier-Stokes
RBG	Residual Burnt Gases
RHS	Right Hand Side
RON	Research Octane Number
SI	Spark Ignition
TDC	Top Dead Center
TKE	Turbulent Kinetic Energy
VCR	Variable Compression Ratio
VVA	Variable Valve Actuation
VVL	Variable Valve Lift
VVT	Variable Valve Timing

Latin letters

A	Surface (m^2)
c_p, c_v	Specific heat capacity under constant pressure or volume (J/kg/K)
D	Destruction term (J/sec)
D_3	Fractal exponent (-)
Da	Damköhler number (-)
D_m	Mass or species diffusion (m^2 /sec)
D_{th}	Thermal diffusion (m^2 /sec)
h	Specific enthalpy (J/kg)
H_p	Piston Position (m)
h_r	Enthalpy of reaction (J/kg)
J	Inertial moment ($kg \cdot m^2$)
K	Mean flow kinetic energy (J)
k	Turbulent flow kinetic energy (J)
Ka	Karlovitz number (-)
k_f/b	Chemical rate forward/backward (mol/sec)
K_i	Numerical solver constant (-)
L	Markstein length (m)
Le	Lewis number (-)
L_T	Integral length scale (m)
m	Mass (kg)
M	Molar weight (kg)
Ma	Markstein number (-)
N	Engine speed (RPM)
N_{tumble}	Turbulent tumble number (-)
p	Pressure (Pa)
P	Production term (J/sec)
Pe	Peclet number (-)
Q	Heat (J)
R	Perfect gas constant for each species (J/kg/K)
Re	Reynolds number (-)
R_f	Flame radius (m)
s	Specific entropy (J/kg/K)
s_b	Absolut flame speed (m/sec)
Sc	Schmidt number (-)
s_L	Laminar flame speed (m/sec)
s_R	Propagation flame speed (m/sec)
s_T	Turbulent flame speed (m/sec)
t	Time (sec)
T	Temperature (K)
u	Flow velocity (m/sec)
U	Mean flow svelocity (m/sec)

u Specific internal energy (J/kg)
 u' Turbulent intensity (m/sec)
 V Volume (m^3)
 v Specific volume (m^3/kg)
 X Species mole fraction (-)
 x_b Burnt mass fraction (-)
 y Variable in numerical solver
 Y Species mass fraction (-)
 y_b Burnt volume fraction
 Ze Zeldovich number (-)

Greek letters

α	Exponent for temperature (-)
β	Exponent for pressure (-)
γ	Ratio of specific heats c_p/c_v (-)
Γ	Efficiency function (-)
δ	Distance of the flame from the wall (m)
δ_L	Laminar flame thickness (m)
δ_p	Thickness of preheat zone (m)
δ_r	Thickness of reaction zone (m)
ε	Geometric compression ratio (-)
η	Efficiency (-)
θ	Crank angle (deg)
κ	Flame stretch (sec^{-1})
λ	Thermal conductivity (W/m/K)
μ	Wavenumber (m^{-1})
λ_T	Taylor length (m)
ν	Kinematic viscosity (m^2/sec)
\mathcal{E}	Flame wrinkling (-)
ρ	Density (kg/m^3)
Σ	Flame Surface Density (m^2/m^3)
φ	Fuel/Air equivalence ratio (-)
ω_{eng}	Engine speed (rad/sec)

Indices/Exponents

<i>0</i>	Typical definition
<i>air</i>	Air
<i>b</i>	Burnt gases
<i>b</i>	Backwards (reaction)
<i>c</i>	Crevice
<i>d</i>	Displacement
<i>e</i>	Exhaust
<i>ent</i>	Entrainment
<i>eq</i>	Chemical equilibrium
<i>equ</i>	Wrinkling equilibrium
<i>f</i>	Forward (reaction)
<i>ff</i>	Flame front
<i>fl</i>	Full load
<i>free</i>	Free flame
<i>fuel</i>	Fuel
<i>i</i>	Inlet
<i>inf</i>	Influence
<i>L</i>	Laminar
<i>P</i>	Piston
<i>p</i>	Preheat
<i>pf</i>	Post flame
<i>Q</i>	Quenching
<i>r</i>	Reaction
<i>ST</i>	Stoichiometric
<i>T</i>	Turbulent
<i>t</i>	Turbulent
<i>u</i>	Fresh gases
<i>w</i>	Wall

Chapter 1 Context of contemporary SI combustion engines design

1.1 Introduction

One of the major challenges for spark ignition engines, as well as for any type of thermal engine, is the reduction of pollutant emissions and of the specific fuel consumption. It is believed that spark ignition engines have an important contribution to the problem of the global warming of the atmosphere as well as to air pollution, since this kind of engine is used in 90% of the vehicles, which are globally used in the transport domain. [1]

Since the 1970's, the global number of vehicles increases with a constant rate of the order of 16 million vehicles per year, although this number is low for the years after 2000. This increase has led respectively to a linear increase of global fuel consumption, in order that the needs of transportation are met. According to [2], in 2010 the limit of one billion vehicles, which circulate globally, has been passed.

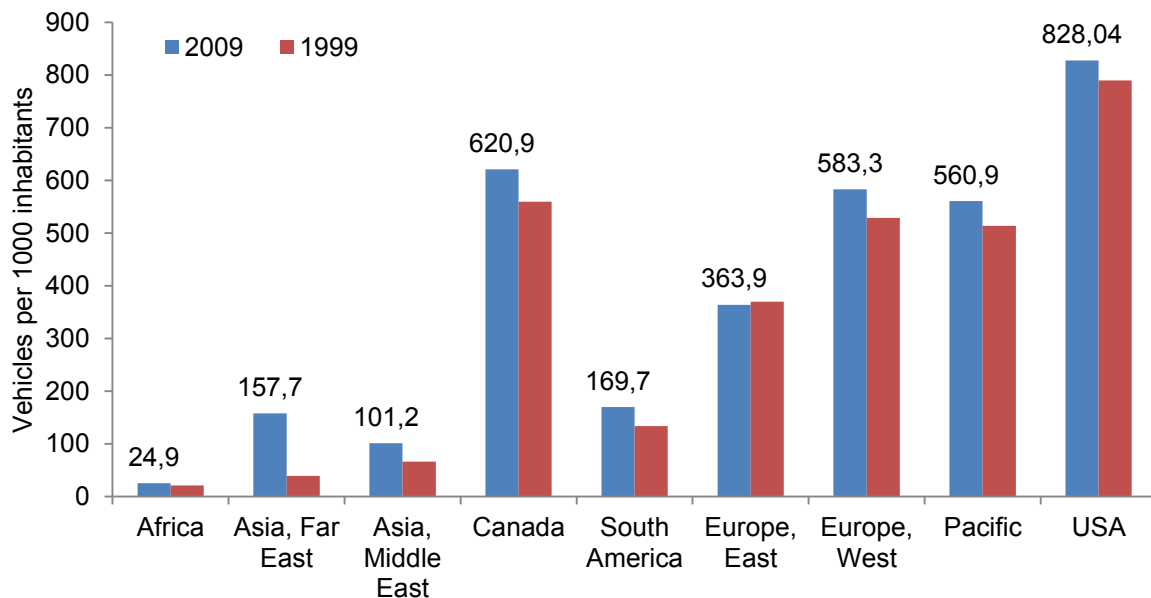


Figure 1-1: Number of vehicles per 1000 inhabitants in various regions (Years 1999 and 2009) [2]

Global fuel consumption will increase in the future, if more inhabitants of rapidly developing countries (like China and India) become owners of vehicles. As it can be observed in Figure 1-1, which shows the average number of vehicles per 1000 inhabitants in various regions of the world, vehicle possession is exceptionally high in rich countries like USA, Canada or Western Europe, while it is still low in the developing countries like in Africa and East Europe. In addition, if the very high population of the developing countries is taken into account, the number of vehicles will increase even more than expected. Consequently, the problem of high fuel consumption and emissions will become even greater in absolute numbers and its mitigation will be difficult.

1.2 Pollutant emissions and law-imposed limitations

According to specific studies [3], spark ignition engines of vehicles in the countries of Western Europe have an average contribution of 63% on the total atmospheric emissions of nitrogen oxides (NO_x), of 69% of carbon monoxide (CO) and of 47% of unburned hydrocarbons (HC). It is stated that these emissions are harmful to the human health [4]. NO_x, especially in the form of NO₂, cause respiratory problems [4]. CO is toxic in high concentrations and HC (with the volatile organic compounds included) are carcinogenic.

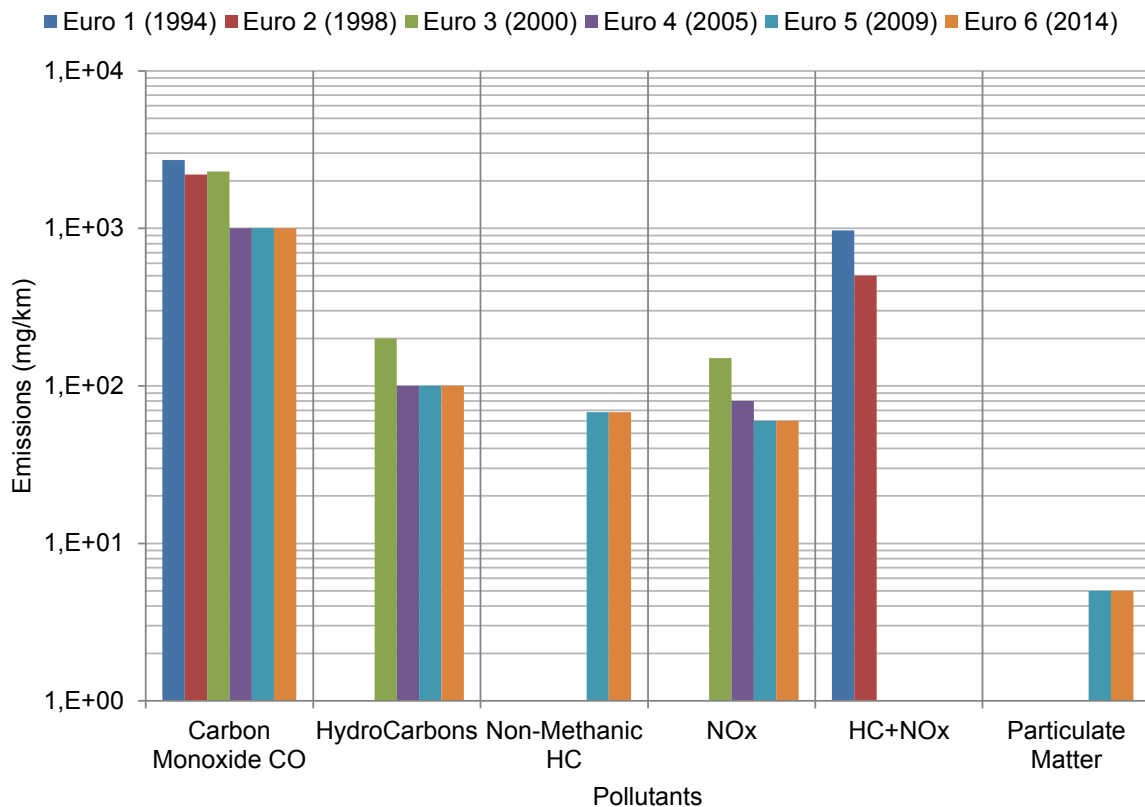


Figure 1-2: Pollutant emissions limitations passenger vehicles with Spark Ignition engines in European Union. [5]

For those reasons, specific limits of emissions from SI engines have been defined in various countries and unions such as the USA, European Union and Japan. In Figure 1-2, the emissions limitations of passenger cars for the countries of European Union throughout the years are presented. According to Euro 4 limitations, a reduction of NO_x, CO and HC emissions of 47%, 57% and 50% respectively is applied in comparison with the previous regulations (Euro 3). Moreover, Euro 5 has a goal of a further reduction of NO_x emissions. The limit shows a decrease of 60% in comparison with Euro 3 regulation. From this figure, it becomes evident that the need for the reduction of pollutants emitted by vehicles with SI engines is intensified in the late years. Legislation in European Union imposes mandatory emission reduction for new vehicles.

1.3 Carbon dioxide emissions and future goals

As it commonly accepted, the increasing concentration of carbon dioxide in the atmosphere has negative consequences on the problem of global warming of the planet. Carbon

dioxide does not constitute the sole gas emission from SI engines, since the nitrous oxide (N_2O) is 270 times more powerful as a global warming gas [3]. Nevertheless, the contribution of carbon dioxide in the global greenhouse effect is dominant versus all the other greenhouse gases, as it is shown in Figure 1-3, which depicts the percentage of the contribution of various components in the problem of the global warming of the planet.

When conventional fuels are used in SI engines, carbon dioxide emissions are in strong correlation with the specific fuel consumption and depend on the efficiency of the engine. The need to reduce of carbon dioxide emissions, namely the increase of SI engine efficiency, has its source in environmental as well as in economic reasons. In this scope, the European Automobile Manufacturers Association (Association des Constructeurs Européens d'Automobiles ACEA) defined in 2012 the goal of $120 \text{ gCO}_2/\text{km}$ [6], since the levels of carbon dioxide emissions were at $165 \text{ gCO}_2/\text{km}$ in 2002. In the scope of a similar effort, various European organization and legislative bodies have set goals and motivations for a further reduction of carbon dioxide emissions. This fact is shown in Figure 1-4, in which the desired values of carbon dioxide emissions of the present and future vehicle fleet are shown [7]. One way, which may lead to the achievement of those goals, is the improvement and optimization of the present technology of SI engines.

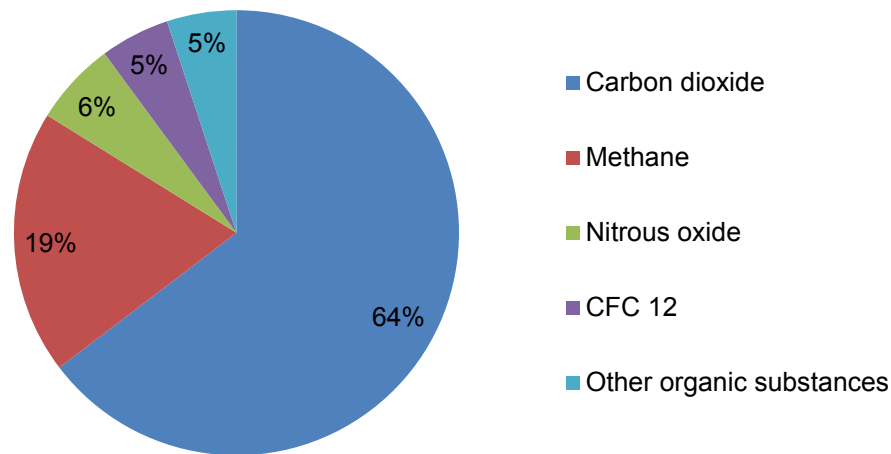


Figure 1-3: Contribution of the various greenhouse gases to the problem of global warming [3]

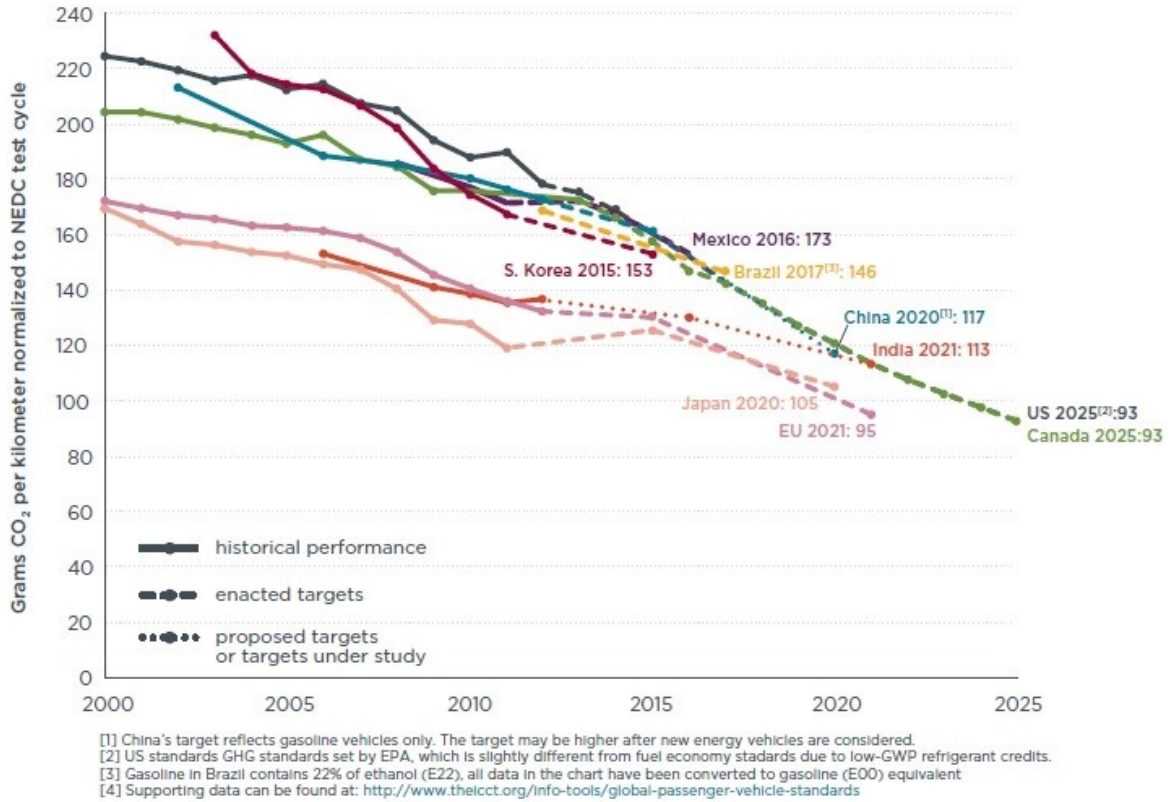


Figure 1-4: Comparison of global CO₂ regulations for passenger cars, in terms of NEDC gCO₂/km. [7]

1.4 The Spark Ignition combustion engine

The spark ignition (SI) engine is an internal combustion engine with spark ignition, designed to run on gasoline (petrol) and similar volatile fuels. It was invented in 1876 in Germany by German inventor Nikolaus August Otto. This is why sometimes a SI engine is also called an Otto engine. In most SI engines, the fuel and air are usually pre-mixed inside the intake duct before they enter the combustion chamber. This concept of mixture formation is changing: in order to improve efficiency and reduce emissions the gasoline direct injection is nowadays the state of the art in terms of SI combustion system design. The control of the power output is implemented by means of regulation of mixture mass flow, since an SI pre-mixed charge engine almost always burns a stoichiometric mixture. This means that the ratio of air mass to fuel mass is constant and equal to about 14.6 kg of air/1 kg of fuel. In the case of naturally aspirated engines (no supercharging or turbocharging) only a throttle valve controls the air quantity, which will enter the combustion chamber.

The value of fuel/air equivalence ratio ϕ is a way to express the relation between fuel and air masses (m) in the charge. When $\phi > 1$, the mixture is rich (fuel in excess) and when $\phi < 1$, the mixture is lean (air in excess).

$$\phi = \frac{m_{fuel} m_{airST}}{m_{air} m_{fuelST}} \quad (1-1)$$

Figure 1-5 and Figure 1-6 depict the strokes of a SI engine. During the intake stroke the piston moves from the Top Dead Center (TDC) to the Bottom Dead Center (BDC). The intake valves are open and permit to the fuel/air mixture to enter the cylinder. If a system of Exhaust Gas Recirculation (EGR) is installed, exhaust gases from the previous cycles also enter the cylinder. For an optimized engine, the Intake Valve Opening (IVO) occurs before

TDC (typical value 0-40 deg) and Inlet Valve Closing (IVC) after the BDC (typical value of 50 deg after BDC).

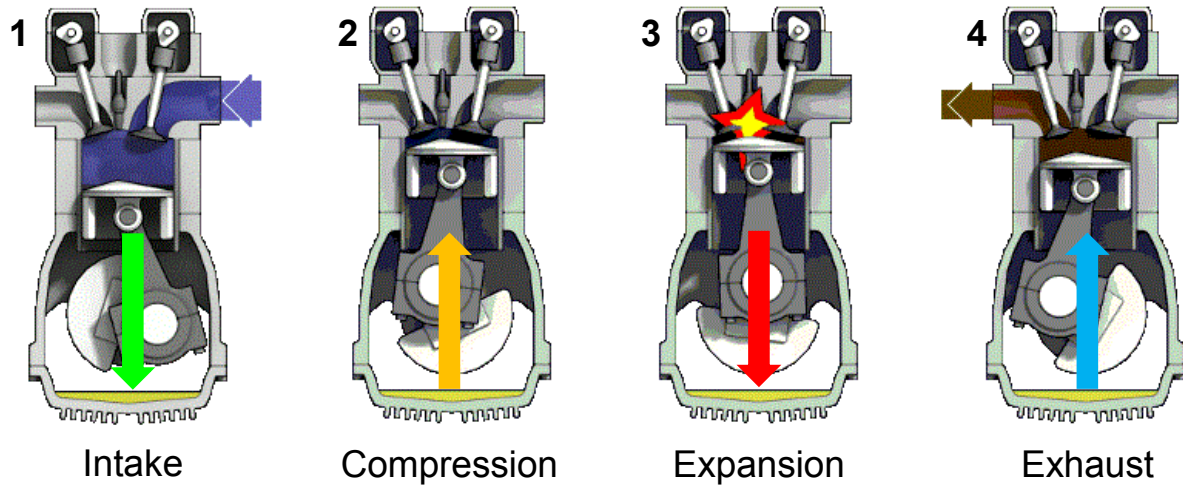


Figure 1-5: Strokes of a 4-stroke Spark Ignition engine. All four strokes make a cycle. The colored arrows show the direction of the piston displacement.

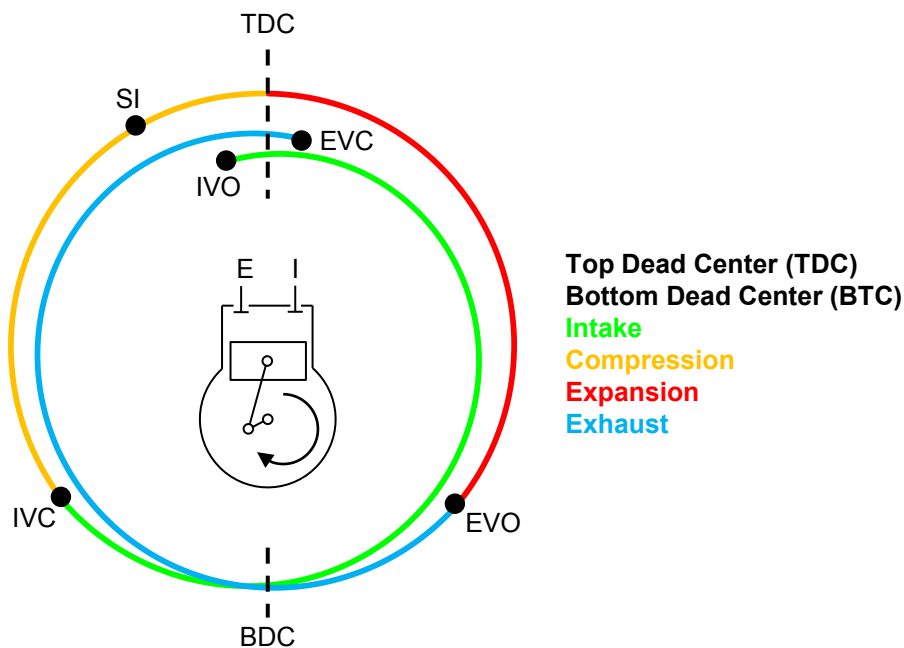


Figure 1-6: Duration of the four strokes of a SI engine. The overlap period when intake and exhaust valves are simultaneously opened is visible.

The compression stroke starts once the intake valves are closed. During this stroke, the chamber contains the premixed charge of fuel and air as well as the EGR. The piston moves from the BDC to the TDC and both cylinder pressure and temperature rise. In a typical naturally aspirated engine, ignition starts some crank angle degrees before the end of compression at TDC. The combustion process, which is deployed inside the compression and expansion strokes, takes place and the pressure and temperature rise even more.

The expansion stroke starts when the piston is at TDC. Then, it moves towards the BDC. It finishes when the Exhaust Valve Opens (EVO). This stroke is the one, which offers useful work and takes advantage of the energy released by the combustion process. The chemical energy of the fuel is transformed into mechanical work by the exerted force on the piston.

During this phase, burnt gases exist in the chamber. In this work, we will be mainly interested in the compression and expansion stroke, since it is during those two strokes that combustion takes place.

The exhaust stroke starts when the EVO. This happens before the piston reaches BDC (typical value of 50 deg before BDC). The piston moves from BDC to TDC and pushes the burnt gases to the exhaust valve. The four-stroke cycle ends when the piston reaches TDC. As it can be seen in Figure 1-6, there is an overlap period when both intake and exhaust valves remain opened. This overlap has been designed for the optimization of the engines gas exchange process. In Figure 1-9, all the important moments during the four-stroke cycle can be easily identified on a typical logP-logV diagram of an engine operating at part load.

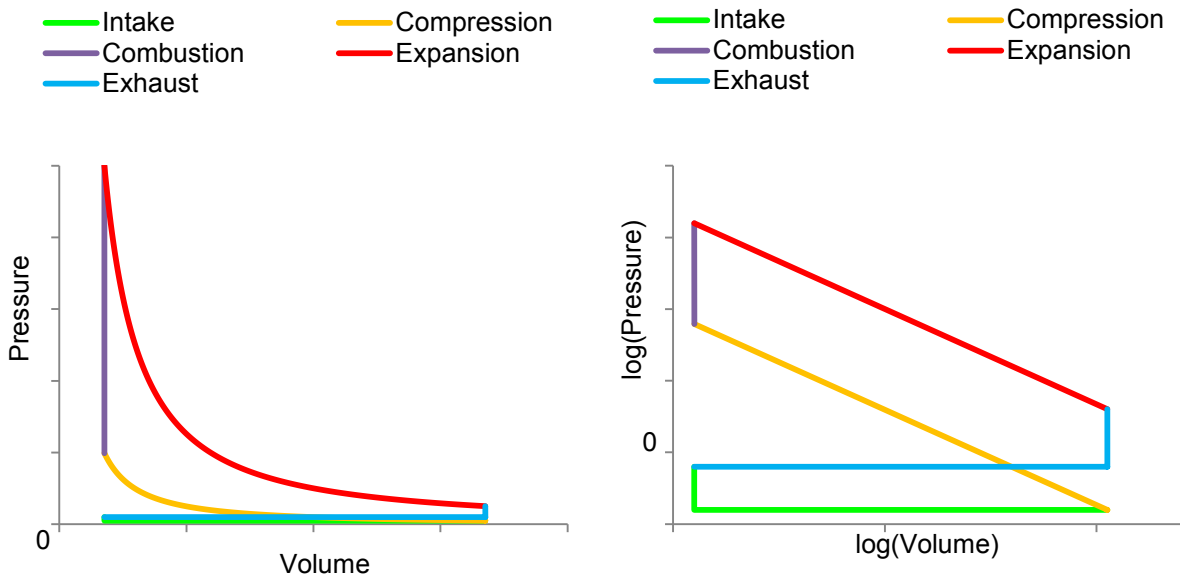


Figure 1-7: Ideal throttled constant volume cycle (Otto cycle). Combustion is ideally considered to occur instantly so as that the volume does not change.

Figure 1-8: Logarithmic (logP-logV) ideal throttled constant volume cycle (Otto cycle). (See Figure 1-7). Exhaust pressure is higher than intake pressure due to the throttling.

A theoretical tool, which is suitable for the demonstration of basic correlations through the application of basic thermodynamic equations, is the ideal cycle. The working gas is considered as ideal gas with constant thermal capacities under constant pressure (c_p) and under constant volume (c_v) throughout the cycle. In the case of a SI engine functioning at part load, the ideal constant volume cycle (Figure 1-7) represents the intake and exhaust strokes as constant pressure thermodynamic processes and the compression and expansion strokes as adiabatic processes and combustion. In Figure 1-8, a clear image of all strokes is visible. If full load of a naturally aspirated engine ($p_i = p_e$) is assumed, it can be proven by using simple thermodynamic relations that the full load indicated fuel conversion efficiency $\eta_{f,fl}$ (work/fuel energy) of this cycle is written with ε is compression ratio (maximum volume to minimum volume) and γ the ratio of heat capacities c_p and c_v :

$$\eta_{f,fl} = 1 - \varepsilon^{1-\gamma} \quad (1-2)$$

The combustion processes are often analyzed based on indicated values: the Indicated Mean Effective Pressure (IMEP) is the measure of work delivered by the engine. For the above full-throttle cycle, IMEP is defined as (m_f : fuel mass, Q_{LHV} : lower heating value of fuel,

V_d : displacement volume equal to the volume difference between the minimum and the maximum piston position):

$$IMEP_{fl} = \frac{m_f Q_{LHV} \eta_{f,fl}}{V_d} \quad (1-3)$$

In case of part load function of the engine, the new efficiency becomes:

$$\eta_f = \eta_{f,fl} \left(1 - \frac{p_e - p_i}{IMEP_{fl}} \right) \quad (1-4)$$

This relation predicts work also for a turbocharged engine and gives an increased efficiency of the thermodynamic cycle. By this simple analysis of the ideal constant volume cycle valuable conclusion on the factors, which affect fuel conversion efficiency of a SI engine, can be reached: Compression ratio ε has an effect on fuel consumption via the gross IMEP / gross efficiency, while intake and exhaust pressure have an impact on pumping MEP. Heat transfer (in a real cycle there are no adiabatic processes) issues as well as mechanical friction issues must of course be optimized in a real engine. Nevertheless, ideal cycle considerations reveal the main ways of fuel efficiency optimization for a premixed SI engine running with premixed stoichiometric charge.

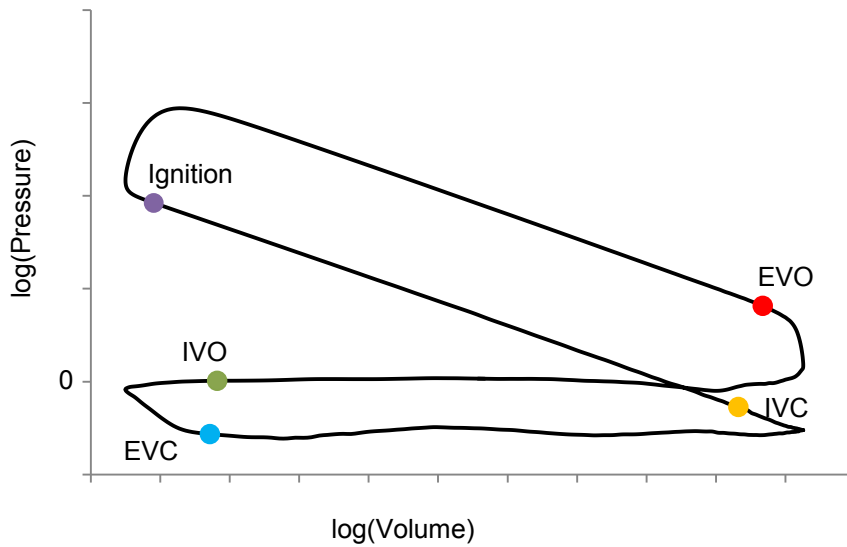


Figure 1-9: Typical LogP-LogV diagram of a SI engine functioning at part load. Applying logarithm permits a more clear view of the different strokes, the valve openings and closings, the spark ignition as well as the valve overlap period when intake and exhaust valves are open simultaneously. IVO/IVC stand for Inlet Valve Opening and Closing and EVO/EVC stands for Exhaust Valve Opening and Closing. SI stands for Spark Ignition.

1.5 Solutions for the emissions and consumption reduction

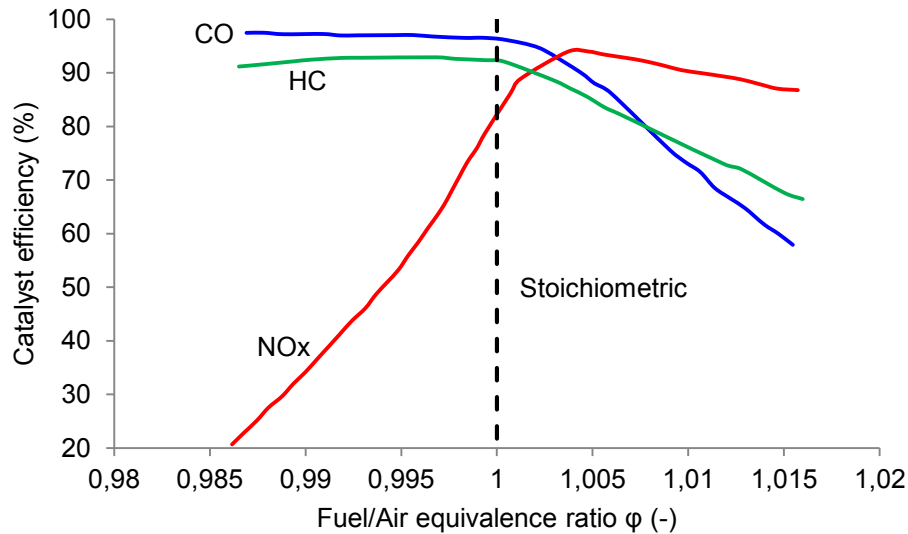


Figure 1-10: Efficiencies of a three-way catalyst for the reduction of CO, NO_x and HC emissions in function of fuel/air equivalence ratio ϕ [8]

From the era of Euro 1 regulations, the vehicle with SI engines pollutant emissions have decreased and continue to decrease substantially. This amelioration has been achieved with the development and constant improvement of catalytic converters (catalysts). Catalysts oxidize carbon monoxide and hydro-carbons to carbon dioxide and water and the NO_x to Nitrogen and Oxygen. Nowadays, the efficiency of catalytic converters may pass 99%. Nevertheless, some limitations of catalysts have to be overcome to meet the more and more stringent pollution regulations:

- The efficiency of the catalyst varies significantly with fuel-air equivalence ratio. As a result, the catalyst efficiency only permits small changes around the stoichiometric value, as it is shown in Figure 1-10.
- The prices of valuable and rare metals (Rhodium, Platinum, Palladium), which are used for the manufacturing of catalysts, rise constantly.
- The light-off temperature (temperature above which catalyst has more than 50% efficiency) is achieved after at least 40 seconds from the moment of the engine start. Consequently, during the cold-start period emissions are very high.

As it can be observed in Figure 1-10, the conversion efficiencies of CO and HC increase when the mixture becomes leaner, while the conversion efficiency of NO_x diminishes significantly. The implementation of such catalyst in vehicles with SI engines is regulated with an oscillating fuel-air ratio around the stoichiometric value so that during the lean phase HC and CO are oxidized and during the rich phase NO_x are converted.

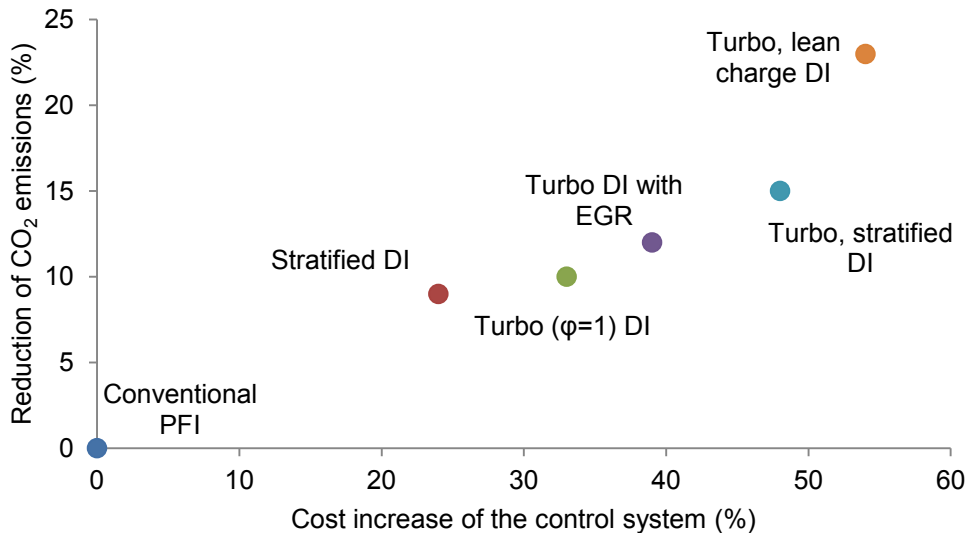


Figure 1-11: Comparative analysis in terms of cost of specific technologies for SI engines with reduced CO₂ emissions [9]

Given that it is very difficult and expensive to further reduce emissions in SI engines with the use of catalytic converters, which demand stoichiometric or quasi stoichiometric mixtures, contemporary industrial activities focus on technologies that reduce pollutant emissions inside the engine combustion chamber. Various techniques exist and can be applied to the traditional Port Fuel Injection (PFI) (fuel is injected upstream from the intake valve and fuel and air are premixed) engines or in engines equipped with direct injection (fuel is injected directly in the combustion chamber) systems. In Figure 1-11, the relative reduction of carbon dioxide emissions (increase of efficiency) for the most advanced new technologies in pure combustion systems as a function of the increase of the engine's control unit cost is shown.

The low cost of the traditional PFI SI engine maintains the interest of the industry on the development of engines of this kind. Various technological solutions applied on PFI engines aim at the optimization of the engine efficiency and at the pollutant emissions reduction. After the choice of the technological concept of a new engine, an evaluation of the contribution of the above-mentioned solutions has to be performed, whilst the industrial goal of cost reduction is always being set on foreground. This specific industrial interest on the optimization of PFI engines underlines the need for tools of evaluation of technological solutions incorporated in an engine design concept. These technical solutions will be briefly discussed in the following subsections.

1.5.1 Downsizing by turbocharging

Irrespective of displacement, spark ignition internal combustion engines convert less than 40% of the fuel energy used into mechanical energy. In low-load urban driving cycles, efficiency in many cases even falls to levels below 20% (or even 0% on idle operation). The overall engine efficiency decreases at part load engine operation because of elevated pumping losses due to the throttle mechanism. Small displacement engines provide a given output torque at a higher MEP than the one of larger displacement. Therefore, the reduction of engine size decreases the pumping losses by reducing the throttle usage. This fact leads to a

lower fuel consumption at part load operation. To attain the performance of a large engine, the charge of the small engine is compressed by the aid of a turbocharger.

Turbocharging decreases pumping losses and improves exhaust gas scavenging. Down-sized engines are characterized by higher high-pressure loops in the thermodynamic cycle leading to a better engine efficiency. The maximum pressure is increased and thus the engine efficiency is higher. Turbocharged engines have lower geometric compression rate than naturally aspirated engines due to increased knocking (auto-ignition of the fuel/air mixture under specific pressure and temperature conditions) as pressure increases.

1.5.2 Compression ratio adjustment

The most evident way to increase the engine's efficiency is to increase the geometric compression ratio (ε). The efficiency of high pressure loop increases as it can be seen in equation (1-2). Increased friction of piston mechanism as well as fuel mixture knock problems limit the practical compression ratio to 14 [8]. In general, compression ratio varies from 8-12 for SI PFI engines. One of the main solutions to prevent knock for full load engine operation is to reduce the volumetric compression ratio. However, this amendment lowers efficiency and performance of partial load operating points, in which pressure and temperature conditions do not favor knocking. As a consequence a basic idea consists in developing a system able to automatically adjust the compression ratio as function of the operating point. With Variable Compression Ratio (VCR) systems, the compression ratio is limited at high loads where the probability of having knock is high and increased at low loads. VCR technologies are still in research stage and no commercial engine has employed VCR technology up to now.

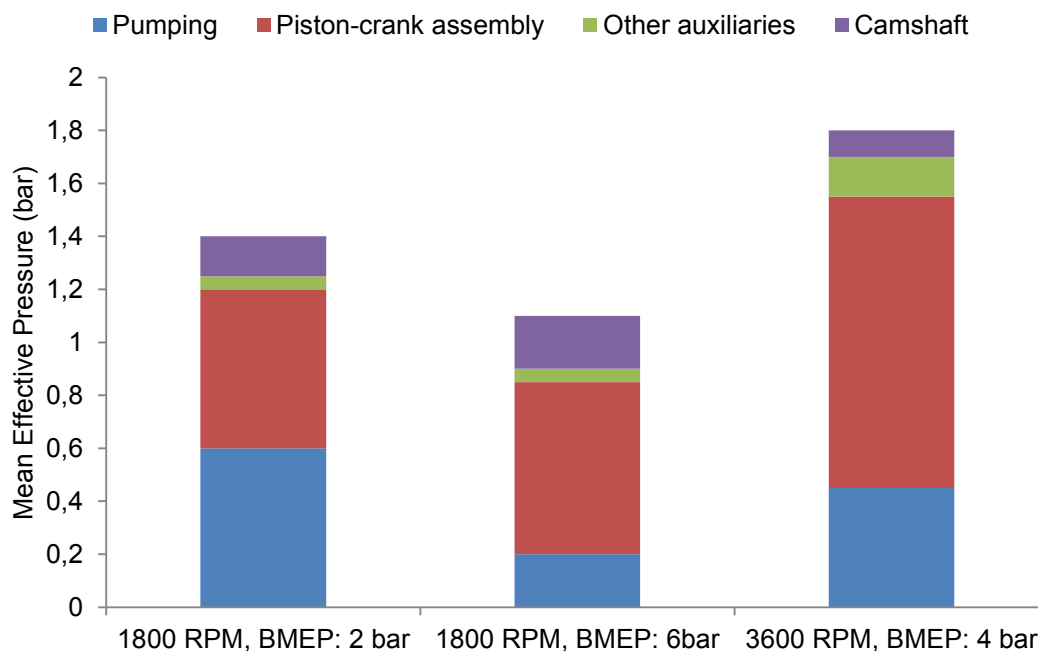


Figure 1-12: Comparison of main categories of friction losses: friction mean effective pressures at different loads and speeds for 1.6 four-cylinder overhead cam automotive SI PFI engine [10].

In Figure 1-12 the various sources of friction losses of a SI PFI engine are shown. Pumping losses decrease when load increases due to the opening of the throttle valve. Piston crank assembly losses remain almost constant when the engine's load changes, since they

depend mostly on the engine's speed. These results are useful for the understanding of the impact of technological solutions to the engine's efficiency improvement. When the compression ratio increases, the stroke of the piston may increase and the piston friction becomes more important.

1.5.3 Variable Valve Actuation (VVA)

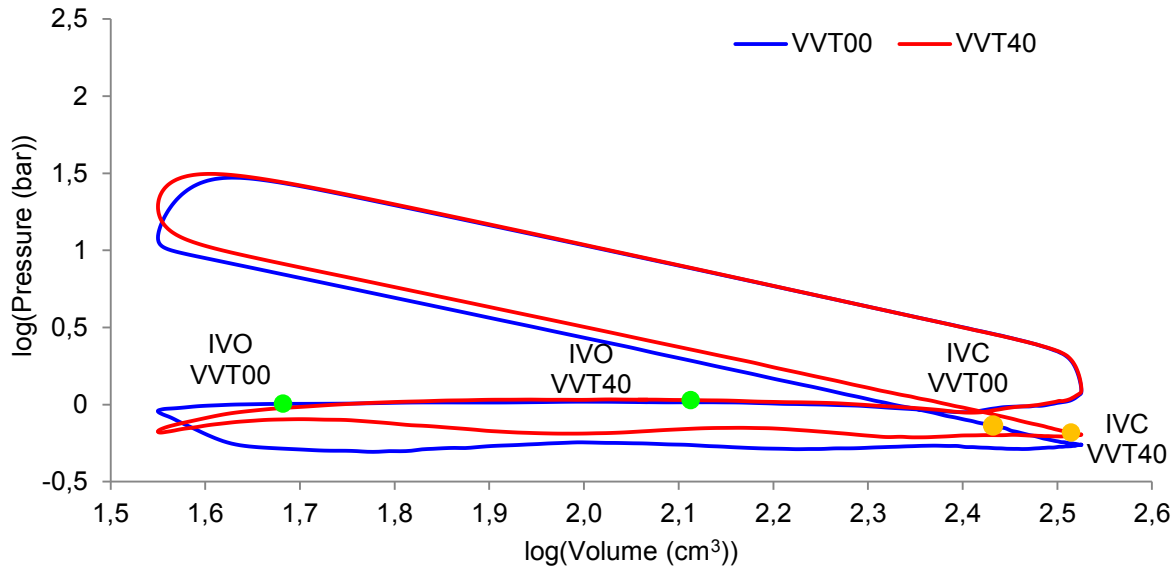


Figure 1-13: LogP-LogV diagram for two valve configurations. VVT00: standard timing, VVT40 early IVC: IMEP VVT, 2000RPM; IMEP: ~5 bar. Pumping IMEP VVT00: 0.46 bar and VVT40: 0.34 bar. Residual Burnt Gas (RBG) is increased in VVT40 configuration due to elevated overlap valve time.

A fixed valve timing is not optimal for the whole operating range of an engine. Adjustments of valve opening and closing timing can be made in order to reduce pumping losses and increase the overall efficiency. The mechanical realization of VVT is achieved by the phasing of the cam mechanism. Through combined intake and exhaust variable timing the effective compression ratio of the engine may also vary.

An example of VVT application in an engine can be observed in Figure 1-13: The engine operates at part load with an engine speed of 2000 RPM. The standard valve configuration (VVT00) has significant pumping losses (Pumping MEP: 0.46 bar). The adjusted valve timing (VVT40) opens and closes the inlet valve 40 crank angle degrees earlier than VVT00 configuration. In the case of early IVC (VVT40), the throttle valve is opened more in order to compensate the intake shortage due to the closed valve. Consequently, the pressure drop downstream the throttle becomes smaller and the pumping losses of VVT40 configuration are lower (Pumping MEP: 0.34 bar). It is interesting to note that the mass of Residual Burnt Gas (RBG) is significantly higher in the VVT40 case, since the valve overlap period is much greater in this case.

Another technique to improve the engines efficiency is to impose a retarded IVC. In such cases, the compression ratio is lower than the expansion ratio (principle of the Atkinson cycle). Nevertheless, the power output of the engine is diminished due to decreased fresh mixture mass (flow from the chamber to intake manifold due to piston motion). This loss may be compensated by an increased inlet pressure with the aid of a turbocharger (principle of the Miller cycle).

Variable Valve Lift (VVL) technologies also exist as a form of variable actuation. The lift of a valve may be mechanically controlled and the mass of intake mixture may be regulated. The use of throttle may be eliminated. The mechanical link of the crankshaft and of conventional camshafts does not favor the combined use of VVT and VVL technologies. Another system consists in dissociating both shafts and driving valves thanks to an electromagnetic system. Camless systems are commercially available, although not in production road vehicle engines.

1.5.4 High Research Octane Number (RON) fuels

Fuels with high RON values have the advantage of reduced self-ignition proclivity. The use of such fuels permits the increase of the geometric compression ratio. Generally, ethanol-gasoline blends are integrated into conventional gasoline fuels to increase the RON but alternative fuels like biofuels or natural gas are also used. Ethanol-gasoline blends containing up to 10% vol. ethanol, can be used without important modifications in regular SI PFI engines. It must be noted that generally ethanol-gasoline blends have slightly smaller heating value than the normal gasoline fuel. In addition, the ethanol-gasoline blend burns slightly faster than regular gasoline. These facts must be taken into account when designing an engine with such fuels.

1.5.5 Mixture Dilution

Exhaust Gas Recirculation (EGR) is often considered to dilute the fresh gas mixture. In SI PFI engines, exhaust gases return to inlet manifold and reenter the combustion chamber. For constant engine speed, the mass of gas, which passes through the throttle, is the same as in the case without EGR. Nevertheless, only a percentage of this mass consists of fuel air mixture. In order to intake the same quantity of fresh charge, the throttle valve must be opened more. Consequently, throttling losses in the low pressure loop are decreased. If the EGR mass is cooled, it reduces the temperature of the charge at the beginning of compression and thus helps decreasing NO_x emissions. This temperature diminution leads to less favorable conditions for knocking. On the contrary if EGR mass is not cooled, its addition favors knocking. Typically, mass fractions of recirculated exhausted gases in SI engines can range from 0 to 15%. The presence of EGR decreases the flame speed and this impact must be taken into account when using EGR strategies.

1.6 Concise description of Spark Ignition combustion and emissions

Combustion in SI engines with premixed air-fuel charge is a complex process. This complexity lies in the following facts: (i) combustion evolves in three-dimensional, unsteady and turbulent flow field, (ii) typical gasoline fuel consists in multiple simpler components, which give a very large number of chemical reactions when they burn and (iii) combustion takes place in a field, which is confined by the walls of the combustion chamber. The wall frontier constantly changes, as the piston moves. Pollutants formation strongly depends on the combustion process and relies on various physical, chemical and geometric factors. In Figure 1-14, the combustion process as well as the basic regions of pollutant formation (NO_x , CO, HC) are shown, when a typical hydrocarbon fuel is used for combustion.

Combustion process starts with the electric discharge in the sparkplug gap. At this moment, the flow field inside the combustion chamber is highly turbulent. A flame kernel is being developed between the electrodes of the sparkplug. The flame of the initial kernel is laminar and for a short period after the kernel initiation, the kernel may be convected away from its initial center by the turbulent flow field. As the kernel interacts with turbulence, it grows and the flame gradually becomes turbulent. Turbulence increases the flame speed to values much greater than the ones of a laminar flame and creates wrinkles and corrugations on the flame front. Those wrinkles and corrugations multiply the flame surface and thus, the surface where the chemical reactions take place. When the flame reaches the vicinity of the walls of the combustion chamber, its quenching begins.

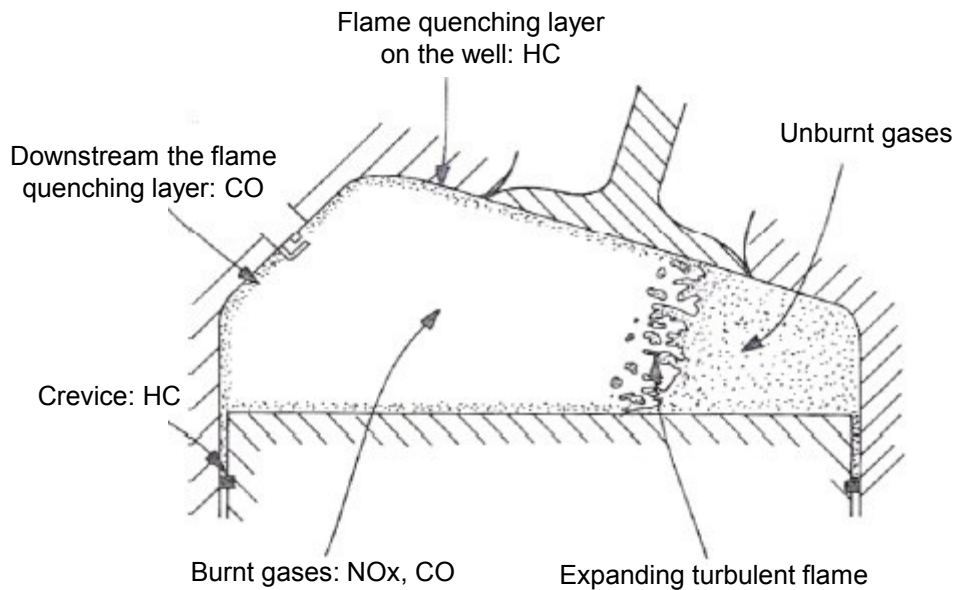


Figure 1-14: Schematic description of the combustion process in and of the regions of pollutant formation in a Spark Ignition engine with premixed charge. [11]

In the ideal case of complete combustion of a hydro-carbon with the stoichiometric air quantity, the exhaust gases would consist only of carbon dioxide, water and nitrogen, whereas in the case of lean combustion, oxygen would also be present. Nevertheless, a complete combustion never takes place for the following reasons: (i) the elementary chemical reactions never evolve only towards one direction, but they always tend to an equilibrium state between the reactants and the products. As a result, there is always a small quantity of reactants, which is not burnt. This phenomenon is called dissociation. (ii) Local conditions, like the mixture homogeneity, turbulent intensity, temperature and geometry are not ideal and often drive the flame to extinction, which is followed by the creation of unburnt or partially burnt substances (HC, CO) or to the creation of new products like NO_x. In Figure 1-16 the typical composition of exhaust gases of SI premixed charge engine is presented [9].

These values are measured without having treated the exhaust gases in any way. It is observed that the pollutants emissions are only a small percentage (of the order of 1%) of the entire exhaust gas quantity. In Figure 1-17 the distribution of species inside the pollutant gases is shown: Carbon monoxide is the dominant substance, while nitrogen oxides and unburnt hydro-carbons exist in small but non-negligible quantities. In full contrast with Diesel engines, the levels of particulate matter emissions remain very low (in terms of mass) for SI engines with premixed charge.

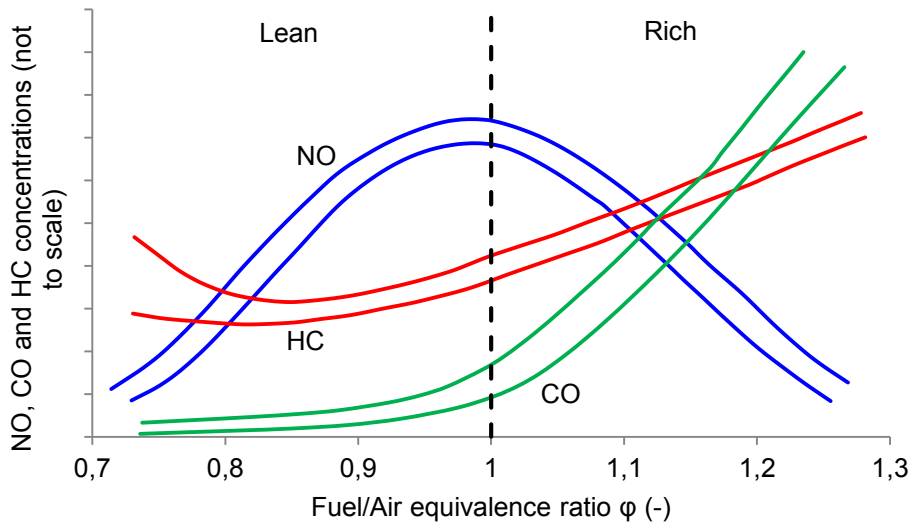


Figure 1-15 : Qualitative variation of NO, CO and HC compositions in the exhaust gas of a SI premixed charge engine in function of Fuel/Air ratio ϕ . [8]

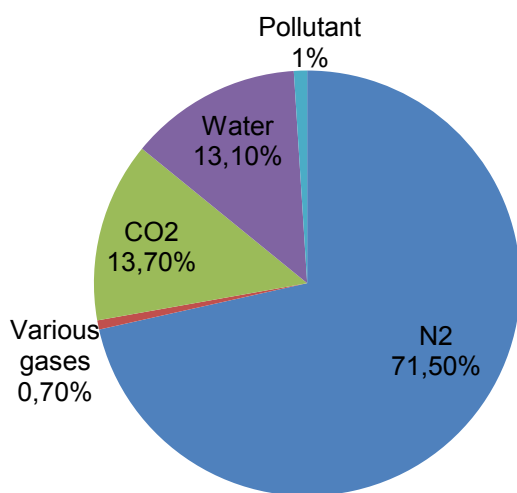


Figure 1-16: Typical (volume fraction) exhaust gas composition of a stoichiometric SI engine with premixed charge. [9]

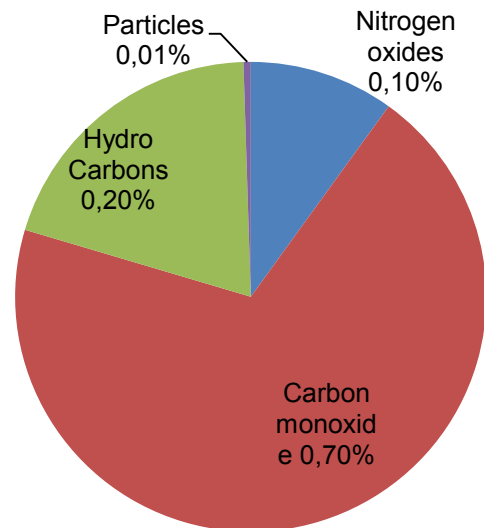


Figure 1-17: Typical (volume fraction) pollutant composition of a stoichiometric SI engine with premixed charge. [9]

1.6.1 Nitrogen Oxides (NO_x)

As it has already been mentioned, NO_x contain nitrogen oxide (NO), nitrogen dioxide (NO₂) and presumably nitrous oxide (N₂O). Nevertheless, the main pollutant within the NO_x emissions of a SI engine is NO [8], [12]. Calculations with equilibrium chemistry suggest that the concentration ratio of NO₂ to NO is negligible. These calculations have been experimentally validated. It has been shown that, in premixed charge SI engines, NO₂ constitute approximately 1-2% of the total NO_x quantity [12].

Three main mechanisms lead to the formation of NO in premixed charge SI engines: the thermal mechanism, the prompt mechanism and the nitrous oxide mechanism. According to

the thermal mechanism [8], [9], [12], [13], NO is formed from the air nitrogen inside the high temperature burnt gases, which exist behind the flame front (see Figure 1-14). This process takes place through chemical reactions, which do not reach chemical equilibrium. As temperature in the burnt gases rises, the rate of NO formation increases. Since these reactions need sufficient oxygen quantity, NO formation is favored in slightly lean mixtures, in which temperature is high enough and oxygen quantity is sufficient (see Figure 1-15). When the burnt gas temperature during the expansion stroke diminishes the NO reactions 'freeze' (cease). NO quantity remains in much higher levels than those of the equilibrium state at the exhaust temperature conditions. An important conclusion is that, NO formation is controlled by chemical kinetics rather than chemical equilibrium.

Measurements of NO concentration have shown that NO is also formed in the vicinity of the flame front [12]. The prompt mechanism explains this phenomenon. In general, this mechanism is important at low temperatures and high equivalence ratios. During combustion, the fuel molecules, which lie in the unburnt gases, (low temperature region) break into other molecules before they enter the flame front. Afterwards, a series of chemical reactions lead to the formation of NO. In contrast with the thermal mechanism, the prompt mechanism shows weak dependence with temperature. In typical engine conditions, about 5-10% of formed NO is due to the prompt mechanism and 90-95% due to the thermal mechanism [13]. Finally, NO can be formed inside the combustion chamber by the air nitrogen through the nitrous oxide mechanism [12]–[14]. This mechanism becomes important during combustion of ultra-lean mixtures and is favored at low temperatures and high pressures.

1.6.2 Carbon Monoxide (CO)

CO formation constitutes one of the basic steps of the mechanism of hydrocarbon combustion [8]. CO concentration increases abruptly in the vicinity of the flame of spark ignition engines with premixed charge. Afterwards, the formed CO oxidizes to carbon dioxide inside the burnt gases with a lower rate than the one in the flame front, due to lower temperature. Right near the flame, CO concentration is very close to the equilibrium values due to high pressure and temperature conditions. Nevertheless, as the expansion stroke evolves, burnt gas temperature decreases and the CO reactions diverge from their equilibrium rates. It has been proven [8], that the CO concentration in SI engines is lower than the maximum value inside the chamber during combustion but higher than the equilibrium value at the exhaust conditions. Thus, a valid conclusion is that the CO concentration is controlled more by chemical kinetics and less than by chemical equilibrium.

In the cases of rich mixture combustion, a shortage of oxygen prevents the complete combustion of fuel to carbon dioxide. Consequently, the concentration of CO in the burnt gases is very high (see Figure 1-15). In addition, even in the case of lean mixtures, dissociation reactions always enhance the CO formation. Globally, the CO levels inside the cylinder depend mostly on the fuel/air equivalence ratio.

Formation of CO can also happen on the basis of two secondary mechanisms. According to the first mechanism, CO is formed when the flame front reaches the cold walls of the chamber. The combustion reactions cease and intermediate combustion products are formed [13]. Among those substances, CO is also found. According to the second mechanism, a small part of fuel, which escaped from the main combustion reaction at the flame front, either is trapped in the crevice volumes or it is absorbed in the oil film on the cylinder

liner. This part of fuel reenters the combustion chamber during the expansion and exhaust strokes and is partially oxidized (due to low temperatures). This partial oxidation leads to CO formation [15].

1.6.3 Hydrocarbons (HC)

The formation and emission of hydrocarbons from SI premixed charge engines is a very complicated process. HC are formed by the contribution of multiple causes, which take place in an engine cycle. According to relevant references [8], [12], four potential mechanisms of HC formation have been identified:

- Flame quenching immediately after flame arrival at the wall.
- The mixture, which is trapped in crevice volumes escapes from combustion.
- Absorption of fuel vapor from the thin oil layer as well as from the carbon deposits, which exist on the chamber walls, during the intake and compression strokes. A desorption takes place during the expansion and exhaust strokes.
- Bad quality combustion of a certain number of cycles of an engine operating point. Incomplete combustion may occur when the combustion speed is very low. Misfire or very late ignition may also lead to the generation of HC.

It is difficult to assess quantitatively the contribution of these mechanisms to the total HC emission. The above mechanisms (apart from the one of incomplete combustion) lead to increase of HC concentration near the walls of the combustion chamber. These HC finally exit the chamber, after they have been mixed with the burnt gases during the exhaust stroke. The upward movement of the piston scavenges the cylinder walls and pushes the HC layer back into the burnt gases. During the expansion phase these HC may be oxidized depending on the temperature history and on the oxygen concentration.

1.7 Research tools for development of Spark Ignition Combustion

The traditional method of evaluation of technological solutions within the industry is the manufacturing of a prototype test engine. This engine, which contains the various technological improvements, which need to be tested, is put on a test bed. Measurements of in cylinder pressure, specific fuel consumption, air/fuel ratio as well as of other magnitudes are taken. The post-processing of these measured values allows the evaluation of the tested technological solutions by the design engineer. These test beds become more and more complex and expensive and the cost of their set up and use has significantly increased over the years. Moreover, a limited number of physical magnitudes can be measured. Under those circumstances, tools of numerical simulation become more and more popular among the industrial research teams.

Notwithstanding the above mentioned drawbacks of test beds, they remain in use in the industry essentially for evaluating new engine control strategies, validating numerical engine simulations and optimizing the full engine design. Apart from the classic engine test bed, used by the industry, a variety of special experimental devices exists and helps the research engineer to comprehend the nature of the various physical phenomena in combustion. An example of this kind of set-ups is the optical engine: Single cylinder optical engines allow the study of in-cylinder turbulent flow, combustion and emissions by permitting the implementation of several diagnostic techniques. Other tools focus on the understanding of specific

phenomena, which interact during the combustion process. Examples of this kind of tools are the spherical bomb helping to define the laminar flame speed and turbulence-flame interaction or the rapid compression machine for the understanding of the unwanted auto-ignition of the mixture under specific pressure and temperature conditions (knocking).

In the following sections the numerical tools, which are the disposal of research engineers, will be briefly described. This description will cover exclusively the tools, which are used by the industry for the development of new engines.

1.7.1 Computational Fluid Dynamics tools

Navier-Stokes equations are implemented for the description of the turbulent flow fields inside internal combustion engines. These equations are based on the conservation of mass, momentum and energy. Several resolution methods exist and are used by the various simulation applications. These approaches are the following:

- Direct Numerical Simulation (DNS): This approach is the most detailed one. It resolves the complete equations locally and without additional modeling (for non reactive flows). Such approaches require therefore a very high number of grid points. For a usual engine calculation, such an approach would require about $\sim 10^{12}$ grid points for the combustion chamber [16]. In addition, the schemes of numerical discretization must be very accurate. The cost for such a calculation is very high due to its overwhelming needs in terms of computer power. Consequently, the use of DNS in the industrial practice is rare. DNS is used in the field of academic research for the understanding of fundamental phenomena, for which experimental research is difficult or impossible.
- Reynolds Averaged Navier-Stokes (RANS): This technique employs the assumption that the flow field velocity or temperature can be expressed as a sum of two values: The mean value of and the fluctuation value. The usual Navier-Stokes equations are written for the mass, momentum and energy equations for their mean values and for their fluctuation values. Numerous additional terms containing the fluctuation values appear and need to be modeled. This modeling covers all turbulent scales. As a consequence, this technique offers a realistic image of the mean flow field. Thanks to the modeling of multiple terms, the computational needs of this approach are relatively modest. As a result of its correct description of mean values and of its low computational time demand, RANS is widely used in industrial practice for engine component design.
- Large Eddy Simulation (LES): A compromise of the computational demand and of the detailed description of physics is given by the LES technique. For the large eddies (turbulent scales) the Navier-Stokes equations are solved. On the other hand, for the small eddies modeling is implemented. This separation of the scales resolution can be justified by the nature of large scales, which are highly anisotropic (change significantly among the different directions) and thus, very hard to model. On the contrary, the small scales enhance the dissipation (turbulence destruction by diffusion) and may be modeled similarly to the RANS approach. This approach is assumed to give a physical description of the flow field, which is close to the DNS response, and to be rather close to RANS approach in terms of computational time [17]. Since it is a fairly new tool, it remains expensive for industrial

use. An example of LES calculation of a multi-cylinder engine can be found in [18], [19].

1.7.2 Tools for chemical processes description

- Complex chemistry: Complex reactive phenomena, which take place at a flame front, impose more obstacles to the fast solution of the flow field equations. Performing flow calculation after having integrated a direct approach for chemical reactions is a heavy undertaking. Complex chemistry mechanisms contain hundreds of species and thousands of reaction between these species. Each species requires a conservation equation. The addition of several hundred equations increases significantly the computational time. In addition, the reaction rates, the thermal and species diffusion coefficients depend on functions of species mass fractions and temperature. A dissuading consequence of these facts is that computational time increases exponentially. Another drawback of complex chemistry is that the interaction between the fluid flow and chemistry are not, in most cases, correctly described and thus chemistry calculations do not have the appropriate input data.
- Global chemistry: In order to mitigate the previously mentioned issues, it is common practice to reduce the complex chemical schemes into much smaller ones, called global schemes. The most influential reactions and species are traced and a new reduced group of reactions is created. This tracing can be performed manually or by the use of special algorithms. This procedure requires deep knowledge of the combustion chemistry. Nevertheless, the research engineer may use the already reduced schemes, as they are proposed by other specialists. This kind of schemes is widely implemented in CFD codes, in spite of their lack of precision. This use is justified by the much smaller computational weight they require.
- Tabulated chemistry: A very promising trend in chemical calculations for combustion is the method of tabulating results of complex chemistry. To begin with, a table containing all the influential parameters (e.g. pressure, temperature, air/fuel ratio) is created. Then, calculations of complex chemistry on academic configurations are performed and finally the results are tabulated and are ready to be used in flow field models. In this manner, the complex chemistry calculations are performed in advance and the flow field calculation is much faster without the loss of precision of the chemistry description.

1.7.3 0D System simulation

System simulation or zero-dimensional (0D) simulation regroups a large spectrum of models, which are generally conceived from empirical or semi-empirical approaches. The quality of this type of models should not diverge from the industrial know-how. The results of system simulation must be in accordance with the ones from more complex simulations (CFD for example) or from the experimental results. Both CFD results and experimental results are used for the validation of 0D models. The complexity of 0D models depends on the modeled system as well as on the desired outputs. Their complexity varies from simple mathematical models to phenomenological models including the physics of the phenomena through state or reduced transport equations.

In the automobile industry the application of system simulation varies significantly in function of the system, which is to be modeled. For example, in the case of powertrain modeling the needed responses will be the engine's consumption, the pollutant emissions or even the noise and the thermal fluxes. OD modeling offers numerous advantages, but the most important one is their computational speed. Their computational time is very low and is comparable with the time of real time applications. Another important advantage is that these models are extended on multiple disciplines allowing the modeling of all types of systems (mechanical, electrical, thermal, etc.).

The principle of system simulation lies in the decomposition of a complex system into the several sub-systems. A modeling representation is made for each elementary sub-system. The model's fidelity to the real process is always a tradeoff between the required precision and the short computational time. Afterwards, the sub-models are assembled together and all the interactions among them are taken into account. The second phase is the identification and the calibration of the model's parameters. The database of numerical results and experimental measurements is used during the calibration phase. The final model calibration is performed either by validating separately each sub-model or by a global model validation. Ideally, both global and partial validations are desired.

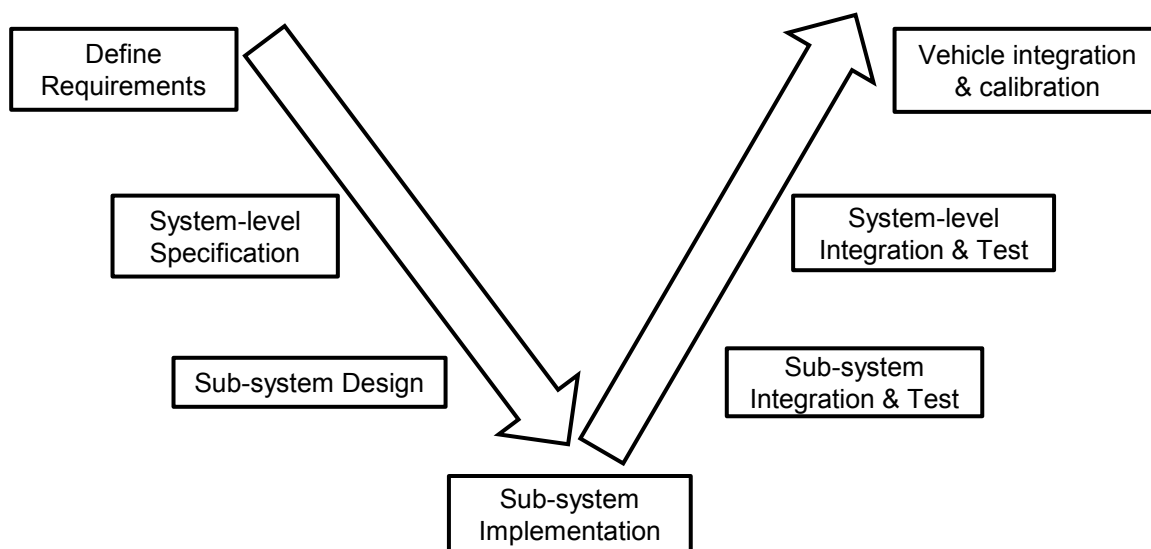


Figure 1-18: Model based Design in the form of a “V” diagram

In the automobile industry the projects are systematically organized with the aid of a “V” process. This process is based on the decomposition of the global complex system (vehicle) into less complex sub-systems. This decomposition is usually made in terms of functionality. Each sub-system is evaluated by its performance while it always retains its links with the main system. The gain of this kind of modeling is visible since each sub-system can be modeled separately and may be integrated in the simulator of the global system. This tool permits the rapid verification of the system response and shows if modifications are needed. Any potential modifications may be applied with minor delays from the beginning of the development phase.

The creation of high quality system models has, as a prerequisite, the deep comprehension of the physical phenomena, which occur in the various sub-systems. Knowledge of several scientific domains is also needed, in order to bind together all the processes, which are

implicated in the complex system. After the mathematical formulation of the model, its equations must be written in a form of computational algorithm.

Numerical simulation (and system modeling in particular) is used in various levels and phases of an engineering project. For a given sub-system, several system models can be used depending on the conceived engineering application. For example, a detailed phenomenological model is used for the prediction of combustion in a SI engine and another model is used for the control of the engine, which is more mathematical but quicker than the physical model.

System simulation is very attractive to the automobile industry thanks to its modest needs of computational time, its possibility to analyze various systems and to the facility of construction of a global model from the basic sub-models. Zero dimensional and one dimensional models are used for internal combustion engine modeling either for the control of the engine or for the optimization of the engine's performance, consumption and emissions. The use of such models improves the delays and diminishes the cost of production of new engines.

For all those reasons, the development of 0D-1D models may respond to the engine conception demands. The challenge for the new models lies in the compromise of the computational time and of the precision of the models, while focusing in the efficiency or the research and development model.

1.8 Objectives and structure of this work

Contemporary engineering in the automobile industry focuses on increasing the efficiency and on the reduction of pollutant emissions of internal combustion engines. The technological concepts, which allow attending these goals, need to be evaluated in terms of their contribution to the global engine system's amelioration. The imposed temporal and cost constraints, which always exist on new engine's development projects, favor the use of 0D-1D modeling in the scope of various stages of the project, in which techniques of short loop must be applied.

This work is dedicated to the zero-dimensional modeling of combustion in a Spark Ignition premixed charge engine. The physical modeling of the combustion process is of crucial importance for a proper 0D model. An analysis of the combustion process reveals its elementary physical phenomena. Then, suitable sub-models for each phenomenon may be developed. Afterwards, the entire combustion model may be used in a one-dimensional code, which resolves the gas exchange process of the engine.

The predictive capabilities of the resulting model must be assessed through the exploitation of experimental data of case studies with different applied technological concepts. Several models must be tuned by the use of experimental data, in order that they become precise and quick enough. This tuning process introduces elevated costs and delays and constitutes an undesirable situation.

Even if the resulting model describes SI combustion of premixed charge, it can be also used for the simulation of direct injection engines after the addition of suitable modeling, which will describe the atomization and evaporation of spray. Dedicated stratified charge modeling approaches must be introduced as well, and coupled to combustion modeling. An example of such modeling is found in [20].

Thesis outline

This introductory chapter has presented the contemporary context of SI engines design. A brief introduction on the global goals of improvement of performance and pollutant emissions decrease has been given. The levers of efficiency improvement as well as a description of SI combustion and pollutant emissions have been presented. The basic elements of the research tools, which aid the engineer to model physical phenomena, have been discussed. The advantages as well as the uses of system modeling in the industrial context set the goals of this work.

In the second chapter, the fundamental aspects of turbulent premixed combustion are presented. The various phenomena, which constitute the combustion process, are analyzed. The basic theory for laminar flame speed and flame stretch is treated. Details about the nature and calculation manners of aerodynamic turbulence are given inside this chapter. The existing models of turbulent combustion are identified and a comparison of them is performed, whose results allow choosing the most appropriate model for 0D SI combustion modeling.

In the third chapter, the global combustion model for SI engines is presented. Details about the accompanying thermodynamic and heat transfer model are given. The proposed combustion model is analyzed. Near wall processes such as flame-wall interaction, flame extinction and post flame reactions will be discussed and appropriate models will be proposed. The impact of flame stretch at the starting stage of SI combustion is discussed. These results constitute the scientific core of this thesis and mark its contribution to SI combustion modeling.

In the fourth chapter, the proposed model is validated against experimental data. A special care has been given to the choice of test bed engine configurations. The goal is to underline the quality of responses of each sub-model and to reveal the potential limitations of the proposed modeling approach in the scope of industrial use.

Chapter 2 Turbulent premixed combustion: physics and models

In this chapter, basic theoretical aspects of the premixed turbulent combustion are exposed. These theoretical fundamentals are indispensable for a correct modeling of the combustion process in a SI engine. The discussion focuses on the phenomena, which affect the fuel consumption speed in the turbulent flame front: the laminar flame and its characteristics, the flame stretch and the turbulence and its impact on the flame. They will offer the basis for the discussion of turbulent premixed combustion. The main types SI combustion are presented and a comparison of three typical models, which have been coded into GT-POWER™ commercial 1D simulation software, is performed in order to find out which model is more physically pertinent for the description of combustion.

2.1 Laminar premixed flames

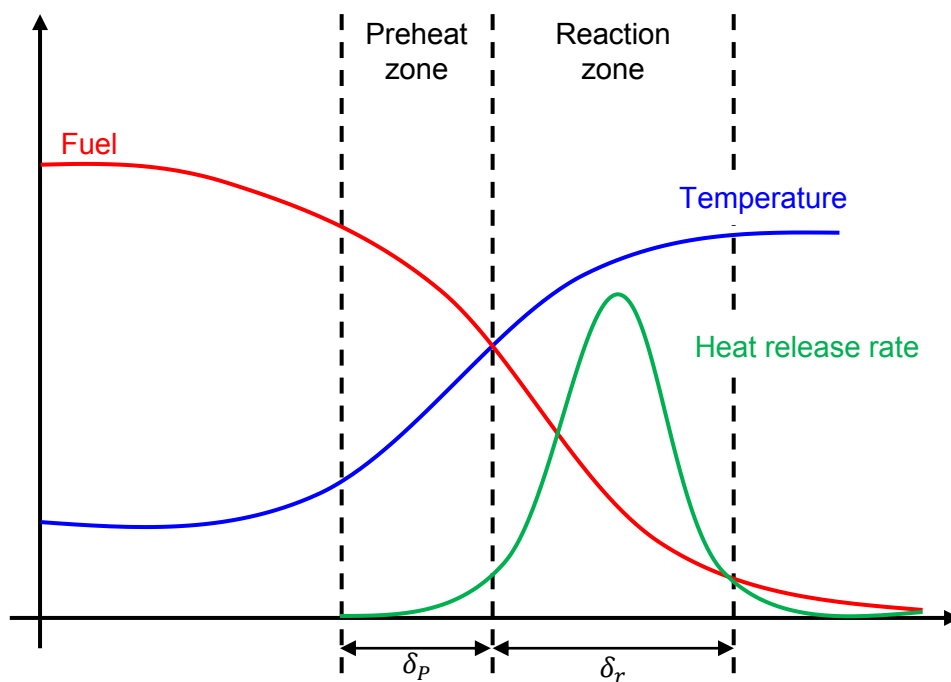
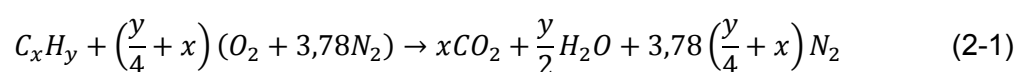


Figure 2-1: Laminar premixed flame front

When the temperature of a fuel/air mixture becomes higher than the ignition temperature, an exothermic reaction starts and produces locally reactive species. Heat and species diffuse towards the fresh gases and the flame propagation begins. The flame consumes the reactants and leaves behind the products of combustion. The global chemical reaction for the combustion process of a Hydro Carbon with the stoichiometric air quantity is the following:



According to the theory of Mallard and Le Châtelier (1883), the region between the burnt and the fresh gases can be divided into two zones: the reaction zone and the preheat zone as shown in Figure 2-1. In the reaction zone, the chemical reaction and diffusions phenome-

na are dominant and generate heat flux towards the fresh gases. The top of the heat release in this zone is due to the chemical reactions. In the preheat zone, temperature increases till it reaches ignition level and thus chemical reactions are activated.

The flame speed can be defined in several ways. In this work the definitions by Poinso et Veynante [17] are retained:

- The laminar flame (consumption) speed s_L is a global magnitude and, in the case of a planar flame, is associated with the speed of consumption of the fresh gases.
- The absolute velocity s_b or flame propagation velocity is defined locally and corresponds to the normal velocity of the flame front.

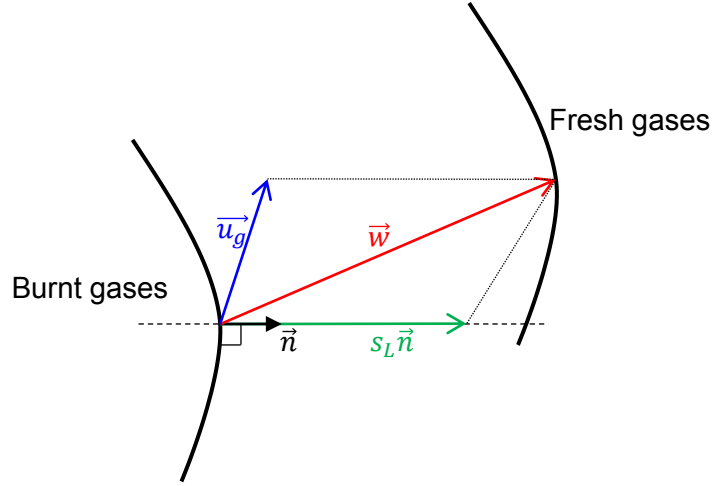


Figure 2-2: Flame and gas velocities

In Figure 2-2, the velocity \vec{w} is the displacement velocity of the flame front from the point of view of an exterior coordinate system. The fresh gases in front of the flame front have a velocity \vec{u}_g . The laminar flame speed is normal to the flame front (\vec{n}). The following relation may be written:

$$\vec{w} = s_L \vec{n} + \vec{u}_g \quad (2-2)$$

In a planar or spherical flame \vec{u}_g and \vec{w} share the same direction with the vector \vec{n} . In such cases, the propagation flame speed $s_b = \vec{w} \cdot \vec{n}$ is directly the sum of the laminar flame speed (consumption of fresh gases speed) and the gas speed u_g of the fresh gases:

Another important magnitude of the laminar flame is the laminar flame thickness δ_L^0 . The laminar flame thickness (δ_L^0) can be defined as the ratio between the thermal diffusivity (D_{th}), and of the unstretched laminar flame speed (s_L^0) (the term of flame stretch will be defined and discussed later in this section). It is also called “diffusive thickness”. The thermal diffusivity is a function of the thermal conductivity of fresh gases (λ_u), the heat capacity of fresh gases ($c_{p,u}$) and of the density of fresh gases (ρ_u).

$$\delta_L^0 = \frac{\lambda_u}{c_{p,u} \rho_u s_L^0} = \frac{D_{th}}{s_L^0} \quad (2-3)$$

As it is explained in [17], in practice this flame thickness is very small. An alternative correlation, proposed by Blint in [21], takes into account the ratio of the burnt gas and fresh gas temperature and is used in this work.

$$\delta_L = 2\delta_L^0 \left(\frac{T_b}{T_u}\right)^{0.7} \quad (2-4)$$

This definition lies on the assumption of equilibrium of thermal and molecular diffusion. The laminar flame thickness can be considered as equal to the sum of the thickness of the reaction zone δ_r and of the thickness of the preheat zone δ_p (see Figure 2-1).

During the propagation of a laminar flame front, various instabilities (gravitational, hydrodynamic or thermodiffusive) may appear and influence flame dynamics. These instabilities may induce heterogeneities of species concentration or temperature. Those heterogeneities will cause local equilibrium perturbations of thermal or species diffusion. These perturbations are responsible for the deformation or the displacement of the flame front. As it is explained in [17], in most cases and especially in turbulent flames, those instabilities are often neglected. However, research on turbulent combustion [22]–[25] suggest that thermodiffusive mechanisms could be the source of additional flame wrinkling in turbulent flames.

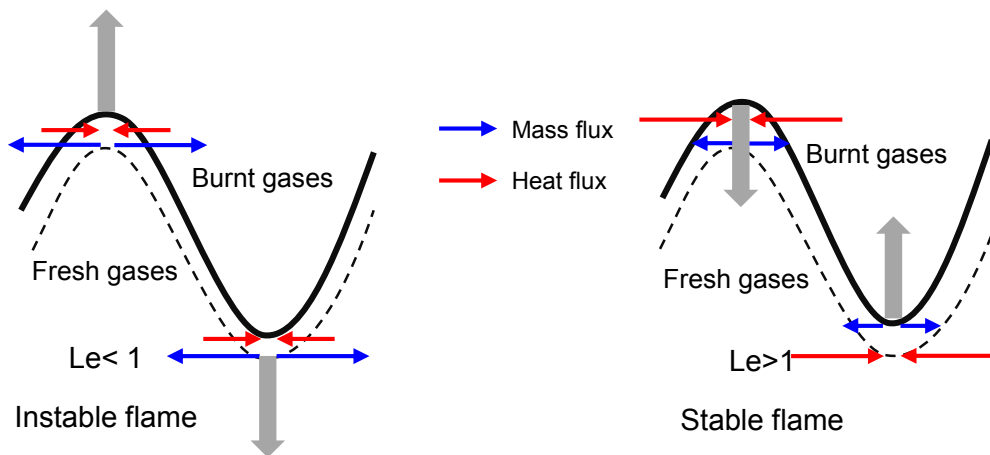


Figure 2-3: Sketch of thermodiffusive instabilities: For $Le < 1$, molecular diffusion (blue arrows) is larger than heat diffusion (red arrows) and the wrinkling of the flame front is enhanced by the differential of flame speeds (left figure). For $Le > 1$ (right figure), a stable planar flame is obtained.

Thermodiffusive instabilities are controlled by the relative impact of species and thermal diffusion of fresh gases. The Lewis number is defined as the ratio of thermal and species diffusivity of the deficient reactant (fuel in lean and oxygen in rich combustion):

$$Le = \frac{D_{th}}{D_m} \quad (2-5)$$

As it is described in [17]:

- If the molecular diffusion of reactants is higher than the thermal diffusivity ($Le < 1$), when the flame front is convex towards the fresh gases, reactants diffuse towards burnt gases faster than heat diffuse towards cold fresh gases. These reactants are heated and then burn faster, increasing the local flame speed s_L which is higher than the speed s_L^0 of a planar flame front. On the other hand, for fronts convex towards the burnt gases, reactants diffuse in a large zone and the flame velocity is decreased compared to s_L^0 . This situation is unstable: the flame front wrinkling (as well as the flame surface) increases.
- When the species molecular diffusivity is lower than the heat diffusivity ($Le > 1$), a similar analysis shows that the flame is stable: the flame surface decreases.

The Lewis number can be altered by changing the fuel (hydrogen/air mixtures have low values of Lewis number for example). The fuel/air equivalence ratio φ is and also a parameter, which influences the Lewis number.

2.2 Flame stretch

Flame stretch represents the rate of increase of the flame surface in function of time. For an infinitesimally small flame surface, flame stretch has been defined by Williams [26] as:

$$\kappa = \frac{1}{A} \frac{dA}{dt} \quad (2-6)$$

It can be proven (see in [17] for a mathematical proof), that the flame front stretch is the sum of two contributions: one due to flow-non uniformity (flame strain term) and one due to the curvature of the flame front (flame curvature term). For simple flame configurations (planar or spherical flames) the above terms may be null. For example a spherically expanding flame in a stationary gas has zero strain and its stretch is only due to curvature. The flame stretch is written in function of the flame radius. R_f is the flame radius and s_b is the propagation speed defined as the flame radius change rate. Under the assumption of constant pressure combustion the flame stretch of this spherical flame can be expressed also with the aid of the laminar flame speed s_L . Flame stretch is inversely proportional to the flame radius.

$$K = \frac{1}{A} \frac{dA}{dt} = \frac{2}{R_f} \frac{dR_f}{dt} = \frac{2s_b}{R_f} = \frac{2}{R_f} \frac{\rho_u}{\rho_b} s_L \quad (2-7)$$

Flame stretch has an impact on the laminar flame speed. An unstretched (s_L^0) and a stretched (s_L) laminar flame speed can be defined. The first works (such as [27]) that treated this subjects assumed a linear relation between the unstretched and stretched laminar flame speeds:

$$s_L = s_L^0 - L_u \kappa \quad (2-8)$$

L_u is the Markstein length from the fresh gases side. The Markstein number for the fresh gases (Ma_u) can be defined as the ratio of the Markstein length to the flame thickness:

$$Ma_u = \frac{L_u}{\delta_L^0} \quad (2-9)$$

L_b is the Markstein length from the burnt gases side. This magnitude is much easier to measure in an experimental configuration. The Markstein number for the burnt gases (Ma_b) can be defined as the ratio of the Markstein length to the flame thickness:

$$Ma_b = \frac{L_b}{\delta_L^0} \quad (2-10)$$

The Markstein length L_b [28] can be calculated by the following relation (Ze is the Zeldovich number)

$$L_b \simeq \frac{Ze}{2} \left(1 - \frac{1}{Le}\right) \delta_L^0 \quad (2-11)$$

The Zeldovich number is a function of an activation energy of the fuel/air mixture E , the perfect gas constant R and the fresh (T_u) and burnt (T_b) gas temperatures:

$$Ze = \frac{E}{RT_b^2} (T_b - T_u) \quad (2-12)$$

The Markstein length and thus the flame stretch sensitivity to stretch is linked with thermodiffusive instabilities (Matalon and Matkovsky [27]) and the Lewis number.

It becomes evident by this discussion, that the flame stretch depends on the composition of the mixture as well as on its Lewis number (through the Markstein lengths) and that it is high for small flame radii (flame radius is small during the beginning of combustion). Usually, the unstretched laminar flame speed is given by correlations for each fuel. In those correlations, the laminar flame speed is a function of the fuel/air equivalence ratio (φ), the cylinder pressure (p), the fresh gas temperature (T_u) and the RBG fraction. Flame stretch can have a major impact on the laminar flame speed. A sub-model of flame stretch impact on the laminar flame speed, is developed in the next chapter.

2.3 Aerodynamic turbulence

Turbulence is a complex phenomenon in fluid mechanics and is very difficult to model even for non-reactive flows. Turbulent flow is three dimensional, rotational, unsteady and highly diffusive. The flow has a large spectrum of dynamically active scales [29]. A continuous energy cascade is observed, which spans along a large bandwidth (see Figure 2-4).

The spectrum of the turbulent kinetic energy k cascade has regions of specific physical processes. Each of them has an associated characteristic length scale. The integral of the spectrum E for all scales gives the turbulent kinetic energy k . The description of the characteristic length scales is the same for reactive and non-reactive flows.

$$k = \int_0^{\infty} E(\mu) d\mu \quad (2-13)$$

The modeling approaches of turbulent flows use the composition of a mean velocity field (\bar{u}) and a turbulent velocity field (u'). The resultant velocity is written:

$$u = \bar{u} + u' \quad (2-14)$$

It will be shown in a following section that 0D combustion models need the estimation of a “global” turbulent intensity (u'). This global property exists only for a turbulent flow, which is homogeneous (invariant when spatially translated) and isotropic (without preferred direction). In SI engines turbulence can be characterized as homogeneous and isotropic during the phase of combustion [8]. For an homogeneous and isotropic turbulence, the characteristic length scales are [30]:

Integral length scale: The eddies of the integral length scale are the largest and they contain the greatest part of the turbulent kinetic energy. They have low frequency and large fluctuations. In an engine their size, which is called integral length scale (L_T), is limited by the cylinder head - intake valve geometry and piston position.

Taylor microscale: Those eddies dissipate the kinetic energy through the Joule effect. Their scale length is the Taylor microscale (λ_T). The eddies of Taylor microscale maintain the greatest part of the flow enstrophy (integral of the square of the vorticity). An approximation for the Taylor length scale is found in the equation (2-15) (ν is the kinematic viscosity):

$$\lambda_T = 15 \sqrt{\frac{L_T \nu}{u'}} \quad (2-15)$$

Kolmogorov length scale: This length scale indicates the length of the smallest eddies, which dissipate the turbulent kinetic energy. Those are eddies of small length and of high frequency. This is why the assumption of homogeneous and isotropic flow is valid for this region of turbulent kinetic energy. The characteristic length scale of these structures is the Kolmogorov length scale (η_k). An approximation for the Kolmogorov scale is found in equation (2-16):

$$\eta_k = L_T \left(\frac{u' L_T}{\nu} \right)^{0.75} \quad (2-16)$$

In general, combustion models need an estimation of the turbulent intensity (u') and of the integral length scale (L_T). In order to obtain a simplified yet representative model of turbulence in the combustion chamber, the main flow pattern of the charge must be known.

In the combustion chambers of PFI engines, three main aerodynamic motions are identified: The “swirl”, “the squish” and “the tumble” [31]. The charge motion and direction for those patterns is described in Figure 2-5. A well-known feature, which is inherent in the swirl and tumble flows, is that they require energy to generate the vortex during suction stroke. This energy comes primarily from the kinetic energy of the gases entering the cylinder through the inlet valve. So to increase the swirl intensity, the gas velocities must be high at the inlet valve, thereby, requiring a smaller cross-sectional area of the inlet valve. This is one of the major compromises of the swirl flows, that is, the requirement of large inlet valve for larger suction of air flow during high engine rpm and the requirement of smaller inlet valve for better swirl intensity generation. The technologies which increase turbulence in the combustion chamber by amplifying the tumble motion are the most usual, because they permit the conservation of a high volumetric efficiency [31]. Therefore, tumble motion is predominant for the creation of turbulence in SI internal combustion engines.

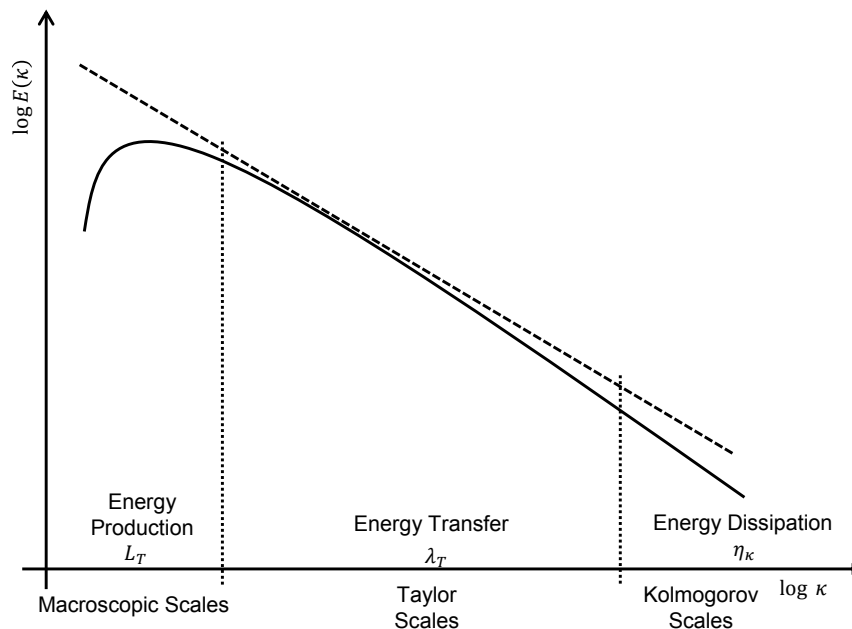


Figure 2-4: Turbulent energy cascade. Three regions of the turbulent frequency spectrum are identified: The energy production region with the high energy eddies of integral length scale, the region of energy transfer from high length to low length structures with the characteristic Taylor microscale and the energy dissipation region of highly viscous Kolmogorov structures.

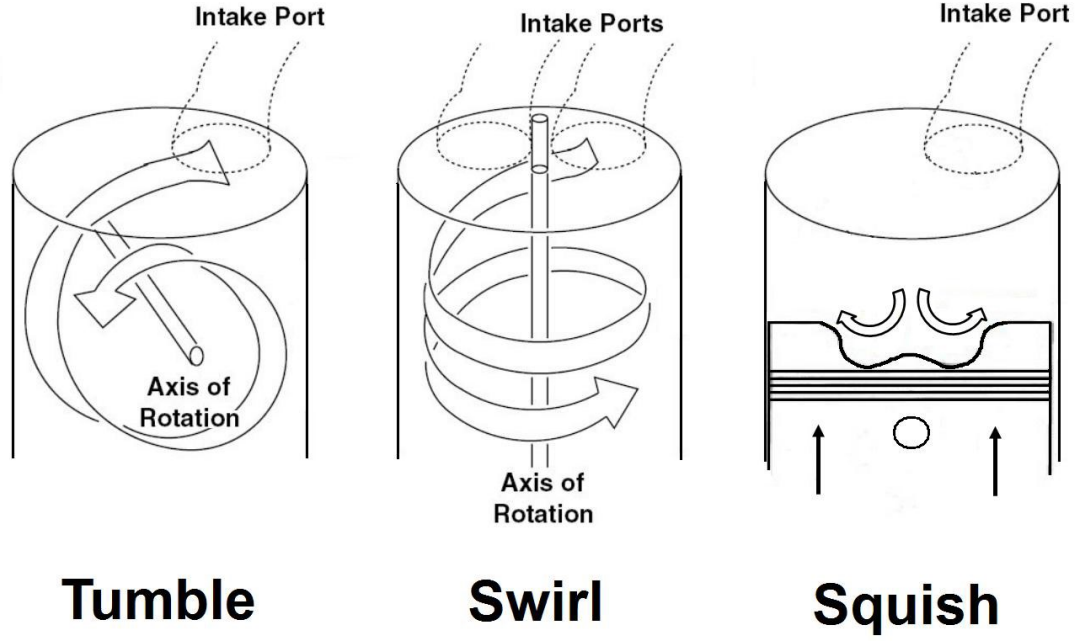


Figure 2-5: The three main charge motions in the combustion chamber.

Since the principal motions are identified, the phenomenology of turbulence permits to write two conservation equations: One for the mean kinetic energy (K) and one of the turbulent kinetic energy (k) [32]–[34]. This kind of modeling of the mean and turbulent energy is called K - k modeling. These two equations describe the rate of change of the kinetic energy of the mean flow field and of the kinetic energy of the turbulent field. The mean kinetic energy, which enters in the chamber, is transformed into turbulent kinetic energy (production term P) and changes also due to the mass flow into the exhaust and due to the density variation.

The turbulent kinetic energy is produced by the transfer of the kinetic energy of the mean flow field, is destroyed by viscous dissipation and changes due to the density variation and of the flow at the exhaust valve. The production and the dissipation terms are modeled with the aid of characteristic times (t_p, t_D) and coefficients (c_p, c_D). Mean flow velocity (U_f) is used for the calculation of the production term.

$$\begin{aligned} \frac{dK}{dt} &= c_{in} \frac{1}{2} \dot{m}_{in} u_{in}^2 + c_{out} \frac{1}{2} \dot{m}_{out} u_{out}^2 - P + K \frac{\dot{m}_{ex}}{m} + K \frac{\dot{\rho}}{\rho} \\ \frac{dk}{dt} &= P - D + k \frac{\dot{m}_{ex}}{m} + k \frac{\dot{\rho}}{\rho} \\ P &= c_p \frac{K}{t_p}, D = c_D \frac{k}{t_D}, t_p = \frac{U_f}{L_T}, t_D = \frac{u'}{L_T}, L_T = c_L V^{1/3} \end{aligned} \quad (2-17)$$

The assumption of homogeneous and isotropic turbulence leads to the relation:

$$u' = \sqrt{\frac{2}{3} k} \quad (2-18)$$

The K - k model was chosen in this work, since it is reported [33] to calculate values near the 3D results with a single set of coefficients for various engine operating points.

2.4 Turbulent premixed flames

The way of the interaction of a premixed flame with the turbulent flow field, in which the flame is developed, can be described by the comparison of characteristic turbulent and chemical scales length and time scales. With such an analysis, various turbulent premixed combustion regimes are revealed. In each of these regions, different physical and chemical phenomena control the interaction between the flame and the turbulent flow and the phenomenology of combustion. This results in a better understanding of the flame structure and leads to a more physical combustion modeling.

Several researchers have proposed the use of premixed turbulent combustion regime diagrams. The most widely used diagram is the one of Borghi [35], as it was later modified by Peters [36]. For the construction of this diagram, three non-dimensional numbers are used:

- The (turbulent) Reynolds number $Re = (u' L_T)/\nu$, which can be also written as $Re = (u' L_T)/(s_L \delta_L)$, under the assumption that the Schmidt $Sc = \nu/(s_L \delta_L)$ number is equal to unity.
- The Damköhler number $Da = (L_T/u')/(\delta_L/s_L) = \tau_T/\tau_{ch}$, which is the ratio of the turbulent time to the chemical time.
- The Karlovitz number $Ka = \tau_{ch}/\tau_K$, which is the ratio of the chemical time scale to the Kolmogorov time scale. Under the assumption of homogeneous and isotropic turbulence the Karlovitz number is written: $Ka = \left(\frac{L_T}{\delta_L}\right)^{-1/2} \left(\frac{u'}{s_L}\right)^{3/2}$

Concerning the choice of the appropriate thickness of a premixed flame for the tracing of the region of heat release, a second Karlovitz number can be defined based on the reaction thickness: $Ka_r = \left(\frac{\delta_r}{\eta_k}\right)^2 = \frac{1}{100} Ka$.

The turbulent Reynolds number describes the competition between the destabilizing effects of inertial forces and the stabilizing effect of the viscous forces. Reactive flows with high Reynolds numbers are characterized by large fluctuations. The Damköhler number correlates the time for turbulent mixing with the time for the completion of chemical reactions. High Damköhler numbers describe flames, in which reactions happen quickly and the limiting factor of combustion is the mixing processes. Those flames show distinct flame fronts. On the contrary, flames with low Damköhler numbers are controlled by chemical kinetics of the reactions, are characterized by high mixing rates and are known as "well-stirred reactors". Finally, the Karlovitz number compares the thickness of the region, in which the chemical reactions take place, (laminar flame thickness), with the smallest turbulent scale (Kolmogorov length scale). The Karlovitz number can also be considered as an order of magnitude of the flame stretch.

From the definitions of the non-dimensional numbers, it is evident that the ratios u'/s_L and L_T/δ_L can be written as a function of those numbers:

$$\frac{u'}{s_L} = Re \left(\frac{L_T}{\delta_L}\right)^{-1} \quad (2-19)$$

$$\frac{u'}{s_L} = Da^{-1} \frac{L_T}{\delta_L} \quad (2-20)$$

$$\frac{u'}{s_L} = Ka^{2/3} \left(\frac{L_T}{\delta_L} \right)^{2/3} \quad (2-21)$$

With the aid of these equations, the so called "Borghi-Peters diagram" is constructed (see Figure 2-6), which categorizes the turbulent premixed combustion in several regions.

The X axis of Figure 2-6 shows the ratio of the integral length scale to the laminar flame thickness, while the Y axis shows the ratio of the turbulent intensity to the laminar flame speed. In Table 2-1, the various regimes of turbulent premixed combustion, as they are identified by the Borghi-Peters diagram, are summarized and their characteristics are described schematically. The figures in the last column represent the flame front (thick black line), which propagates from the burnt gases (white region) to the fresh gases (grey region). Those figures describe the particular flame morphology of the flame in each combustion regime.

In the regime of wrinkled flamelets, the turbulent intensity is smaller than the laminar flame speed. Therefore, the mechanism of laminar propagation is stronger than the mechanism of corrugations of the flame front. The flame front is only wrinkled, while its thickness is not altered since the smaller turbulent eddies (Kolmogorov scales) cannot enter the flame front structure because they are greater than its thickness ($Ka < 1$). The reaction zone as well as the chemical kinetics are not sensitive at the presence of the turbulent flow field.

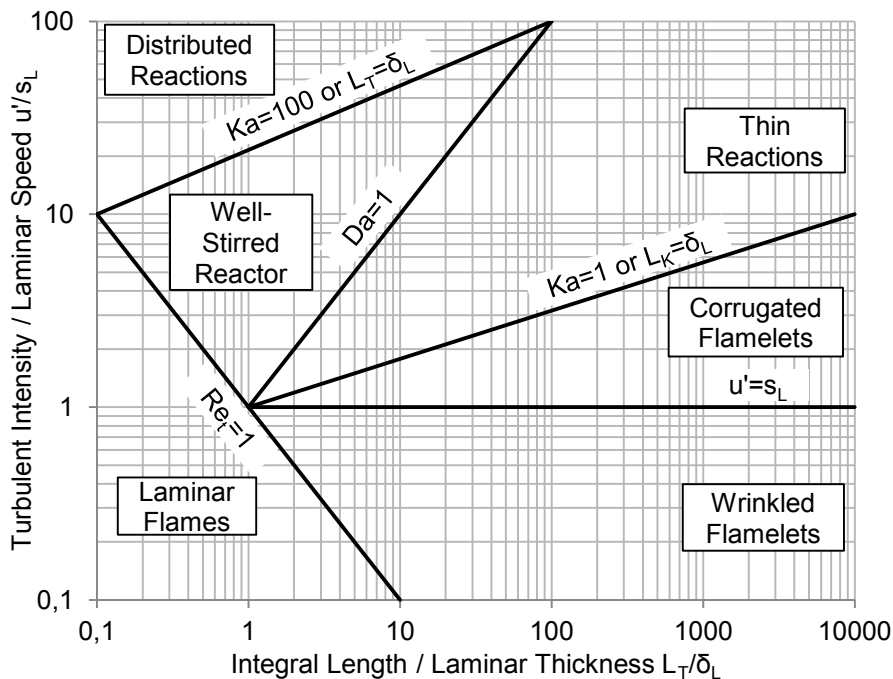


Figure 2-6: Borghi-Peters diagram of turbulent premixed combustion.

In the regime of corrugated flames, the turbulent intensity is larger than the laminar flame speed. The corrugation mechanism is the strongest. In addition, due to the strong folding of the flame front, pockets of fresh gases may be detached from the continuous flame front and appear in the burnt gases zone. Likewise, pockets of burnt gases may appear in the zone of fresh gases. Nevertheless, the flame structure is not affected by the turbulent fluctuations and remains quasi-steady, since $Ka < 1$.

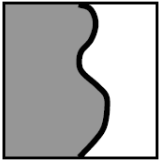


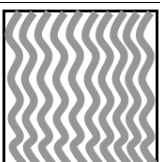
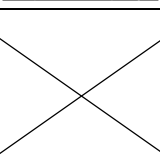
The previous region expands till the borderline on which $Ka = 1$. This limit is known as the Klimov-Williams criterion. This line defines the two flamelet regimes (wrinkled and corru-

gated), in which chemical kinetics can be described by the properties of the laminar flame (s_L, δ_L). Based on this remark, the premixed turbulent combustion in these regimes can be modeled by the principles of laminar flamelets, considering that the interaction between the flame front and turbulence is exclusively of kinematic nature.

For Karlovitz numbers greater than unity, the flame enters the regime of thin reaction zones. In this regime, the smallest turbulent eddies may enter into the preheat zone of the flame, but not into the reaction zone. This happens because they are greater than the thickness of the reaction zone ($Ka_r < 1$). In this manner, the mechanisms of heat and mass transfer are accelerated in the preheat zone due to turbulent convection. The flame has a greater thickness (thickened flame or thin reaction zone), whilst the flame structure remains unaffected by the turbulent movement though it may present wrinkles.

The next regime of the Borghi-Peters diagram is the one of the well-stirred reactor. In this regime, the Damköhler number is smaller than unity, namely the time scale of turbulent mixing is smaller than the chemical time scale. Therefore, this combustion process is controlled by chemical kinetics. The main characteristic of this regime is that the intense turbulent mixing causes a perfect stirring between the reactants and the products of combustion. As a result, no flame front can be distinguished. In other words, the notion of thin reaction zone, in which the chemical reactions take place, does not exist.

Table 2-1: Turbulent premixed combustion regimes

Combustion regime	Re	Da	Ka	Ka_δ	u'/s_L	Flame depiction
Wrinkled flamelets	> 1	> 1	< 1	< 1	< 1	
Corrugated flamelets	> 1	> 1	< 1	< 1	> 1	
Thin reactions zone	> 1	> 1	> 1	< 1	> 1	
Well-stirred reactor	> 1	< 1	> 1	< 1	> 1	
Broken reaction zones	> 1	< 1	> 1	> 1	> 1	

Finally, in the broken reaction zones regime, where $Ka_r > 1$ or $Ka > 100$, the smallest turbulent eddies enter into the reaction zone, since they are smaller than its thickness. High heat loss is observed, due to the turbulent convection, from the reaction zone to the preheat

zone. The temperature of the reaction zone decreases abruptly. The fuel/air mixture diffuses into areas of low temperature, where flame quenching is observed, and the combustion ceases. In general, in this regime a premixed flame cannot exist and this is why there is no flame depiction in the last column of Table 2-1.

2.4.1 Flame propagation inside the combustion chamber

As it explained by Heywood [11], the spark discharge generates a high temperature kernel of the order of 1 mm in diameter between the electrodes of the sparkplug. The growth of this initial flame kernel is quasi-laminar and highly stretched. A gradual transition to a turbulent flame occurs as the local flow increasingly distorts the flame front. In addition the flame kernel is convected away from the spark plug electrodes [37]–[39] by the mean and the turbulent flow field. The flame front is wrinkled by both the mean flow and turbulence and its shape may change from spherical to elliptical [37]. In the end of this transition stage, the flame kernel can no longer be convected by the flow, because the enflamed mass is too important to be convected by the flow field. During this stage, the heat release rate due to combustion is very low (compared to the fuel energy content). Therefore, the increase of cylinder pressure is very low. When the flame is fully-developed, turbulence wrinkles considerably the flame front and the flame propagates throughout the combustion chamber. During this stage the greatest part of the energy content is released.

If the globally wrinkled and turbulent flame is examined microscopically, it is observed that its structure remains laminar and its thickness is always thin. The flame, as it will be shown in the next chapters, is placed in the combustion regime of corrugated flames (since usually $u' > s_L$) or less probably in the regime of wrinkled flamelets.

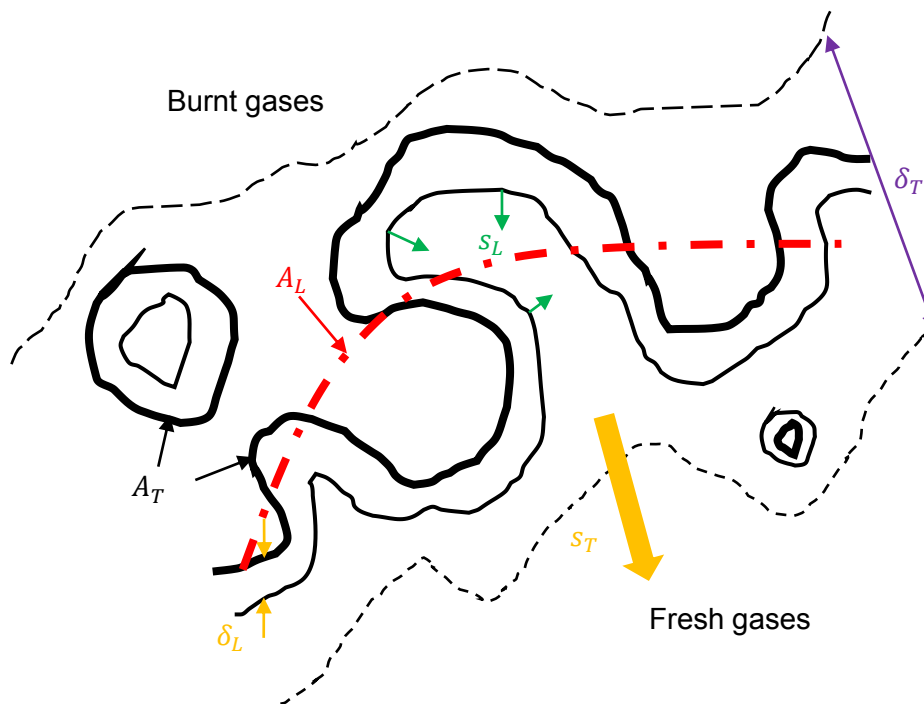


Figure 2-7: Wrinkled turbulent flame with corrugations.

In Figure 2-7 a depiction of the turbulent flame front is presented. The contour of the turbulent flame front is depicted as a reaction sheet of small thickness. This sheet shows intense wrinkles and corrugations at various length scales. The total surface of this contour is

called turbulent flame surface (A_T) A contour of a fictitious mean flame surface (A_L) can be defined. In 0D modeling, this mean flame surface is considered spherical. The entire turbulent flame is defined by the contours of its rear and forward fronts. Those two contours define the turbulent flame thickness (δ_T). The turbulent flame speed (s_T) is the speed of flame propagation in the fresh gases. Locally, every flame element (every small part of the reaction zone) has a laminar flame thickness (δ_L) and propagates toward the fresh gases with the laminar flame speed (s_L). The laminar flame speed is a function of the fuel, the fuel/air equivalence ratio (φ), the cylinder pressure (p), the fresh gases temperature (T_u) and the presence of RBG. If the flame stretch, which is particularly high at the beginning of combustion, is also taken into account, then the Lewis and Markstein number as well as the strain and curvature effects have an impact on the laminar flame speed. The wrinkling factor (\mathcal{E}) is defined as the ratio of the turbulent to laminar flame speed or as the ratio of the turbulent to the mean flame surface. The assumption that these two ratios are equal, was proposed initially by Damköhler and it is generally accepted.

$$\mathcal{E} = \frac{s_T}{s_L} = \frac{A_T}{A_L} \quad (2-22)$$

Finally, the turbulent flame propagation is observed till the moment it comes in contact with the chamber walls. After this point, extinction mechanisms take place till the flame is totally extinguished. During this phase the wrinkling of the flame front diminishes under the impact of the flow boundary layer, the increased heat losses towards the cold wall and the confinement of the flame by the wall.

In a zero-dimensional context, the burning mass rate can be written as follows (with the aid of equation (2-22)):

$$\frac{dm_b}{dt} = \rho_u A_T s_L = \rho_u A_L s_T = \rho_u A_L s_L \mathcal{E} \quad (2-23)$$

Various models have been proposed for the calculation of the turbulent flame speed (s_T) or equivalently the wrinkling ratio (\mathcal{E}). Three combustion models, which represent the three main trends of zero-dimensional spark ignition combustion modeling have been chosen and are compared in the next section. This comparative study permits identifying the most adapted model, in order to take into account the flame-wall interaction.

2.5 Comparison of turbulent flame models

The contemporary design of Spark Ignition (SI) internal combustion engines dictates high combustion efficiency while conserving performance. In order to achieve this goal, different technical definitions, such as variable valve timing and lift (intake / exhaust), variable compression ratio, Exhaust Gas Recirculation (EGR) or variable aerodynamics, are proposed within the framework of industrial practice. Those technical definitions have to be evaluated by some kind of testing, experimental or numerical. Experimental evaluations are often of high cost and under some circumstances impossible to conduct. These reasons promote the use of numerical solutions for the above mentioned evaluation.

One Dimensional (1D) engine modeling is a well-established practice in the industry. Its response for the gas exchange process in an internal combustion engine is neither as exact as three dimensional solutions of Computational Fluid Dynamics (CFD), nor it gives a good description of the physics of the flow in an internal combustion engine. However, it is suffi-

ciently accurate for industrial purposes and significantly quicker than the CFD solutions. Nevertheless, in 1D approaches, implemented in commercial software, combustion is simulated by Wiebe functions (in most of the cases) through which little or no prediction can be made. Consequently, the evaluation of various technical definitions remains restricted. This gap is filled by 0D phenomenological, physical models, which take into account the various aspects of spark ignition combustion such as laminar flame speed and thickness and turbulence.

Various 0D combustion models are proposed in the literature, which aim to predictively describe the heat release rate. Each one of them takes into account the geometry of the combustion chamber, the turbulent intensity, and the Residual Burnt Gas (RBG) effects. Each model has different calibrating constants. Those coefficients play a key role in the predictive capacity of the model.

A comparison of different approaches for 0D Spark Ignition modeling with experimental data is proposed. Versions of Eddy Burn Up, Fractal and Flame Surface Density (FSD) models have been coded into GT-POWER™ platform as “user models”. GT-POWER™ offers the connection among the gas-exchange process, the thermodynamics of the cylinder and the combustion models. The comparison focuses on the impact of the turbulence on the flame front and on the simulation of heat release and shows the predictive capabilities of each approach. The sufficient description of SI combustion and the behavior of the calibrating coefficients are discussed.

0D modeling solutions in SI combustion have been developed over the last decades, with aim to numerically optimize the design of the internal combustion engines. Every approach incorporates several sub-models: Laminar flame surface, laminar flame speed, aerodynamic turbulence, turbulent flame propagation or turbulent wrinkling of the flame and possibly auto-ignition calculations and pollutant formation predictions.

The essential difference among various models lies on the description of physics of turbulent combustion. Every model is based on the hypothesis that aerodynamic turbulence enhances heat release rate by increasing the surface of the flame front and does not alter significantly the inner flame structure. Consequently, in all models a global turbulent flame speed or a wrinkling factor is calculated. All length scales of aerodynamic turbulence are assumed to be larger than the flame front thickness (flame is in the so called “flamelet” regime).

Another theory that describes the combustion mechanism in SI engines is the entrainment of turbulent eddies in the flame front. These eddies burn inwards from peripheral ignition sites to be consumed in a characteristic time with the laminar burning speed. The entrainment velocity is given by an algebraic equation from the flamelet modeling relations. The entrainment theory is rather a mathematical modeling that agrees with the S-shaped burned mass fraction, which is observed in experiments [40], [41]. Entrainment combustion mechanisms have not been experimentally observed in real premixed flames. Nevertheless, the mathematical efficiency of this theory makes it a popular choice in 0D modeling.

2.5.1 Laminar flame surface

Combustion starts by imposing a spherical flame kernel with a radius of 0.5 mm, between the electrodes of the spark plug. Up to this moment, no model for initial kernel formation has

been introduced. The combustion chamber was drawn with Computer Aided Design (CAD) software. In order to calculate the laminar flame surface, the laminar flame was considered as part of a sphere, which is centered in the middle of the spark plug. This sphere was drawn for various combinations of flame radii and piston heights. After the subtraction of the surface in contact with the chamber, the free surface of the “flame” and its volume are calculated by the software. Those values are tabulated and used as an input by the combustion model. Thus, in every approach the laminar flame surface is calculated as:

$$A_L = f(R_f, H_p) \quad (2-24)$$

A_L is the laminar (spherical) flame surface, R_f is the laminar flame radius and H_p the piston height. It is worth mentioning that this CAD model is fully parametrical. Consequently, a new tabulation can be quickly calculated if geometrical dimensions of the combustion chamber are altered. An example of such a design is given in Figure 2-8.

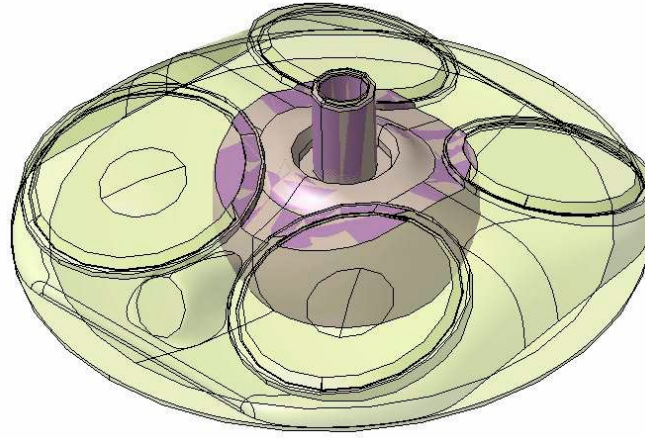


Figure 2-8: Combustion chamber in CAD software

2.5.2 Laminar flame speed

Laminar speed is one of the inputs for modeling flame propagation. Empirical correlations proposed by Metghalchi and Keck [42], [43] are used in our study. Those relations are based on experiments in pressure vessels. Notwithstanding that those results were acquired for pressures significantly lower than those that appear in SI engines, those correlations are widely used in combustion modeling. The correlation (see equation (2-25)) for isooctane, which is the fuel used in this study, is a function of fuel-air ratio (φ), fuel, cylinder pressure (p), fresh gases temperature (T_u) and RBG mole fraction (X_{RBG}).

$$s_L = s_L^0(\varphi) \left(\frac{T_u}{T_0} \right)^\alpha \left(\frac{p}{p_0} \right)^\beta (1 - 2.06X_{RBG}^b) \quad (2-25)$$

$$s_L^0 = B_m + B_\varphi(\varphi - \varphi_0)^2 = 0.263 - 0.847(\varphi - 1.13)^2$$

$$\alpha = 2.18 - 0.847(\varphi - 1)$$

$$\beta = -0.16 + 0.22(\varphi - 1)$$

Laminar flame speed (s_L) is given as a function of laminar speed for standard conditions ($p_0 = 1 \text{ atm}, T_0 = 298 \text{ K}$) and of corrections by the fresh gases temperature (T_u), cylinder pressure (p) and RBG fraction (X_{RBG}). The exponents α and β are calculated as a function of the fuel/air equivalence ratio φ and of predefined constants for isooctane, which are also

valid for gasoline, *i.e.* the fuel in this study. Dilution Exponent Multiplier ($b = 0.733$) is a parameter of the RBG fraction influence on laminar flame speed. The RBG fraction in this study is calculated by simulating the gas exchange process with GT-POWER™.

2.5.3 Aerodynamic turbulence

In spite of the existence of 0D turbulence models for combustion chambers, 3D CFD results were used in order to calculate the turbulent intensity and an algebraic relation was used for the integral length scale (L_T). Various 0D turbulence models were tested but their responses were not satisfactory in comparison with 3D CFD data. Thus, it was decided to use 3D CFD data for the turbulent intensity (u').

The original 3D results gave a spatially averaged and temporally evolving turbulent kinetic energy (TKE) (k) for each operating point of the engine. The solution of flow equations was acquired through STARCD™ software, with a Reynolds Averaged Navier Stokes (RANS) method. Under the assumption of homogeneous and isotropic turbulence, TKE was converted in turbulent intensity (u') by the equation (2-18), as explained in [44]:

The integral length scale (L_T) of aerodynamic turbulence is essential for combustion modeling, since it is implicated in every approach tested in this study. It represents the largest turbulent eddies and is considered to be proportional to the distance between the cylinder head and the shroud of the intake valve. This parameter of the flow is therefore imposed by the geometry of the combustion chamber and it is modeled as a function of the chamber volume, as in [32], [45], [46].

$$L_T = C_{L_T} V^{1/3} \quad (2-26)$$

2.5.4 Eddy Burn Up model

$$\frac{dm_{ent}}{dt} = \rho_u A_L (s_L + s_T) \quad (2-27)$$

$$\frac{dm_b}{dt} = \frac{m_{ent} - m_b}{\tau_b} \quad (2-28)$$

Combustion is modeled in two steps: Firstly, the fresh gases, which have a density ρ_u , are entrained (m_e) in the flame front at a speed, assumed to be equal to the sum of a laminar and a turbulent component (s_T). Secondly, the entrained mass is burned (m_b) in a characteristic time (τ_b). The end of combustion, which involves flame-wall interaction, is not described by a physical model in this approach. However, a simple solution to take into account the end of combustion is to introduce an exponential term [8]. The time from the beginning of combustion (t) and the time when the flame reaches the wall (t_{wall}) are used:

$$\frac{dm_b}{dt} = \frac{m_{ent} - m_b}{\tau_b} \exp\left(C_{tw} \frac{t_{wall} - t}{\tau_b}\right) \quad (2-29)$$

The coefficient C_{tw} was kept constant and equal to unity in this study. The characteristic burn time is defined as the ratio of the integral length scale and the laminar flame speed. In other works such as [44], the characteristic burn time depends on the Taylor microscale. The presence of an adjusting coefficient (C_{τ_b}) allows adapting the model to each operating point of the modeled engine.

$$\tau_b = C_{\tau b} \frac{L_T}{S_L} \quad (2-30)$$

The turbulent flame speed was modeled as reported in [47]. This expression is a result of the work of Zimont [48]. It is reported to well describe the freely propagating flame as well as the early flame kernel development through its exponential term.

$$s_T = Da^{0.25} u' A_{sT} \sqrt{1 + \frac{\tau_t}{t} \left[\exp\left(-\frac{t}{\tau_t}\right) - 1 \right]} \quad (2-31)$$

This relation contains a calibrating coefficient (A_{sT}) and the Damköhler number (Da). The characteristic eddy turnover time is calculated as the ratio of the integral length scale and turbulence intensity, multiplied by a coefficient ($C_{\tau t}$).

$$\tau_t = C_{\tau t} \frac{L_T}{u'} \quad (2-32)$$

2.5.5 Fractal model

In this flamelet approach, the flame front is wrinkled by aerodynamic turbulence. The wrinkling factor (\mathcal{E}) is defined as the ratio of the total surface of the flame, namely the turbulent surface (A_T), and of the laminar flame surface (which corresponds to the spherical flame surface). This ratio can be also defined as a ratio of a turbulent flame speed and of the laminar flame speed [17], [49]:

$$\mathcal{E} = \frac{A_T}{A_L} = \frac{s_T}{S_L} \quad (2-33)$$

The burning mass rate is proportional to the density of fresh gases, to the laminar flame speed and the turbulent flame surface.

$$\frac{dm_b}{dt} = \rho_u A_L S_L \mathcal{E} \quad (2-34)$$

Fractal geometry principles have been assumed to describe flame front wrinkling accurately enough. In this version of fractal modeling, which is used in [32], [34], [46], a fractal dimension (D_3) is assumed to dominate flame wrinkling between two length scales (L_{min} , L_{max}).

$$\mathcal{E} = \left(\frac{L_{max}}{L_{min}} \right)^{D_3 - 2} \quad (2-35)$$

The maximum length scale is linked to the flame radius through a calibrating coefficient. The minimum scale is equal to the Kolmogorov length scale (L_K). For isotropic and homogeneous turbulence, η_K is given by a simple relation containing the integral length scale, the turbulent intensity and the kinematic viscosity of fresh gases (ν) [33]. The fractal dimension depends on the laminar flame speed and on the turbulent intensity.

$$L_{max} = C_R R_f \quad (2-36)$$

$$L_{min} = \eta_K = L_T \left(\frac{u' L_T}{\nu} \right)^{-0.75} \quad (2-37)$$

$$D_3 = \frac{2.35u' + 2.05S_L}{u' + S_L} \quad (2-38)$$

2.5.6 Flame Surface Density model

In the Flame Surface Density (FSD) model, the wrinkling factor is calculated by a 0D differential equation [50]:

$$\frac{1}{\Xi} \frac{d\Xi}{dt} = \Gamma \left(\frac{u'}{s_L}, \frac{L_T}{\delta_L} \right) \frac{u'}{L_T} \left(\frac{\Xi_{equ} - \Xi}{\Xi_{equ} - 1} \right) - \frac{2}{R_f} \frac{\rho_u}{\rho_b} (\Xi - 1) s_L \quad (2-39)$$

This equation can be obtained by the reduction of a 3D CFD equation of the flame surface density [51]. This reduction is described in detail in [52]. Its first Right Hand Side (RHS) term represents the wrinkling of the flame by all turbulent scales, while its second term represents the thermal expansion of the spherical flame which diminishes the turbulent wrinkling of the flame front [53]. The turbulent term contains the efficiency function of the turbulent flow (Γ) and the equilibrium wrinkling factor (Ξ_{equ}).

$$\Xi_{equ} = 1 + 2 \frac{u'}{s_L} \sqrt{\frac{C \cdot \Gamma}{Sc}} \quad (2-40)$$

The presence of the efficiency function in this model takes into account the laminar flame speed (s_L) and the laminar flame thickness (δ_L) as well as the impact of all turbulent scales. Meneveau and Poinot [16] originally calculated the efficiency function numerically with Direct Numerical Simulation (DNS) by combining flame/vortex interaction with multi-fractal theories, as in [54], [55]. The strain rate of the flame front, caused by a pair of counter-rotating vortices, is integrated for all turbulent scales, assuming that each scale wrinkles independently the flame front. A fitting is performed in order to find the final expression of Γ . In this study, the adopted expression can be found in [16], [17]. The presence of the efficiency function in this model is based on the following assumptions [17]:

- No unique turbulent scale controls flame wrinkling. A wide range of turbulent scales, from Kolmogorov to integral scales, is involved in the flame wrinkling.
- The characteristics (thickness (δ_L) and speed (s_L)) of laminar flame must be taken into account, in order to model the flame wrinkling.

$$\log_{10}(\Gamma) = -\frac{1}{s + 0.4} \exp(-s - 0.4) +$$

$$[1 - \exp(-s + 0.4)] \left[\sigma_1 \left(\frac{u'}{s_L} \right)^s - 0.11 \right] \quad (2-41)$$

$$\text{with } s = \log_{10} \left(\frac{L_T}{\delta_L} \right) \text{ and } \sigma_1 = \frac{2}{3} \left\{ 1 - \frac{1}{2} \exp \left[- \left(\frac{u'}{s_L} \right)^{1/3} \right] \right\}$$

The equilibrium wrinkling factor (Ξ_{equ}) is the result of the analytical solution of the steady one-dimensional flame density equation [56]. It contains the calibrating coefficient (C) of the combustion model and it is fuel dependent through the Schmidt number (Sc).

2.5.7 Results and discussion of the comparison

A description of the engine test bed, which has been used in this comparison, is shown in section 4.1. In Figure 2-9 and Figure 2-10 the heat release rate and burnt mass fraction of

an operating point with average load at 1200 RPM is shown. The Eddy Burn Up model correctly simulates the beginning of combustion (CA0-CA10). The main combustion period (CA10-CA50) is well predicted. A sharp peak value is observed at CA50, due to the presence of the exponential term in equation (2-29), which intervenes beyond CA50 and is assumed to simulate the end of combustion. The end of combustion is simulated inaccurately by this exponential term. The other two models describe rather inaccurately the beginning of combustion. Besides, the ignition process is not modeled. The simulated heat release rate is significantly lower than the measured one. An inflexion point is observed at -1 deg BTDC. A similar trend is also reported in [46] for the fractal model. This behavior cannot be explained on physical ground. The wrinkling factors of each modeling approach can be compared thanks to equation (2-33). We introduce a wrinkling factor for Eddy Burn Up model only for the comparison of the models. The Eddy Burn Up approach does not contain the notion of wrinkling. It has to be noted, that the equivalent wrinkling factor of the Eddy Burn Up model controls the entrained mass and not the burnt mass. The order of magnitude for the flame wrinkling is far from the observed values, which are of the order of 5 [11].

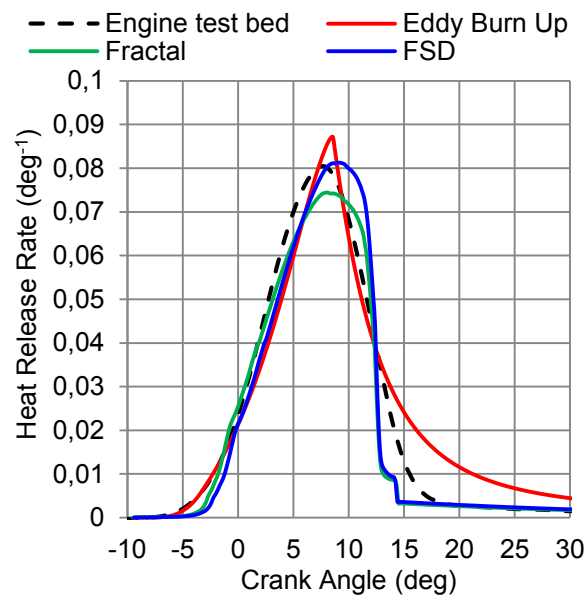


Figure 2-9: Heat release rate. Engine speed: 1200RPM, IMEP: 8 bar

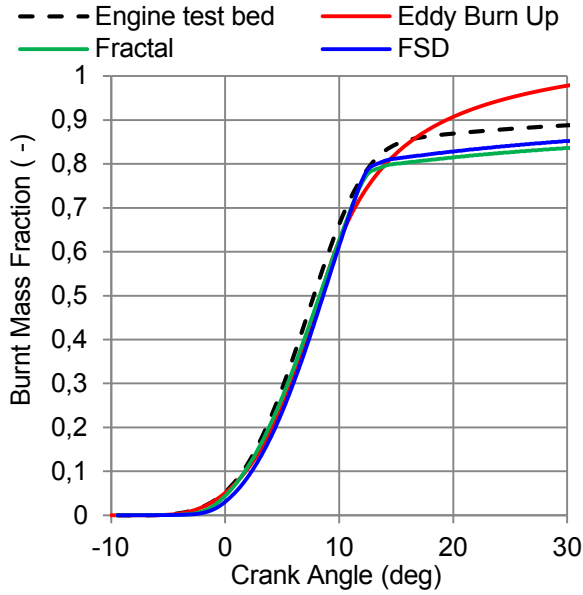


Figure 2-10: Burnt mass fraction. Engine speed: 1200RPM, IMEP: 8 bar

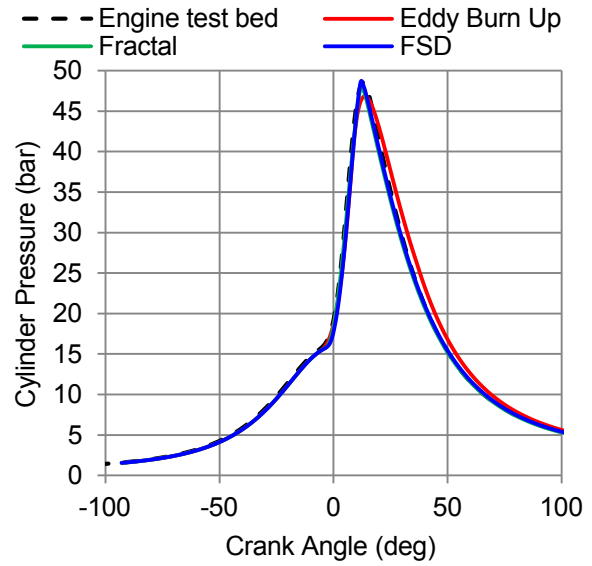


Figure 2-11: Cylinder pressure. Engine speed: 1200RPM, IMEP: 8 bar

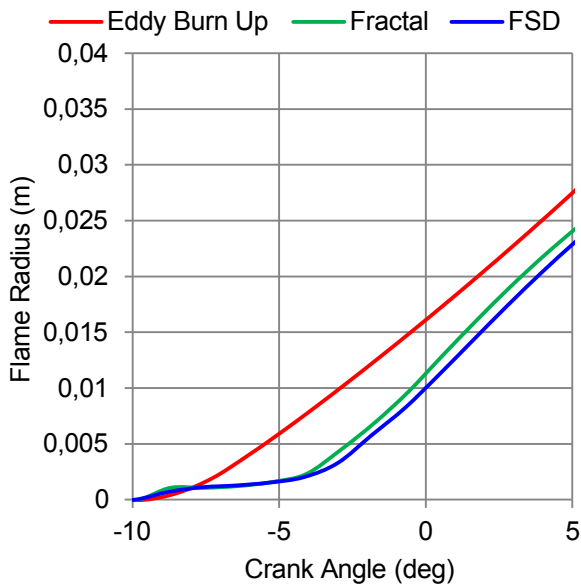


Figure 2-12: Flame radius. Engine speed: 1200 RPM, IMEP: 8 bar

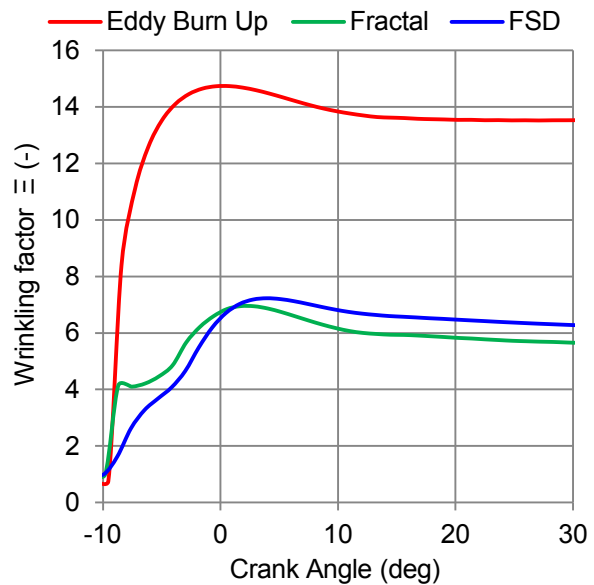


Figure 2-13: Wrinkling factor (Ξ). Engine speed: 1200 RPM, IMEP: 8 bar

The wrinkling factor comparison is presented in Figure 2-13. With the aid of those figures the inflexion point and the low heat release rate can be explained. The evolution of the flame radius is rather similar for FSD and Fractal models but different in the case of the Eddy Burn Up model (Figure 2-12). In particular, in the beginning of combustion, the flame radius is lower for FSD and fractal models due to different wrinkling of each model. The presence of the inflexion point can be explained by the wrinkling factor in Figure 2-13, which has discrepancies for the FSD and and by the mean flame surface calculated by the flame radius of Figure 2-12.

Eddy Burn Up and Fractal models start with an high wrinkling, which is not physical, as flame initiation is dominated by laminar flame speed [57]. In order to cope with this deficiency of the fractal model, the authors of [32] propose a novel formulation of the fractal dimen-

sion, which permits simulating the gradual increase of the wrinkling factor by starting from an initial value, which corresponds to laminar flame propagation. In this work, the model's capability to simulate physically the process of combustion for various operating points of the engine was evaluated. Thus, it was chosen not to integrate this purely mathematical sub-model, which adds another coefficient of adjustment. On the other side, FSD model starts with a wrinkling equal to unity thanks to the initial condition of equation (2-39). The inflexion point is the result of the change of curvature which is observed at -2 deg. If the error in the flame radius is corrected, it is highly possible that the inflexion point will be no longer observed.

Another deficiency of all three models is shown in Figure 2-13: Flame wrinkling remains quasi constant after CA50. The wall-flame interaction, which diminishes the flame wrinkling through various physical mechanisms, as discussed in [16], is not taken into account by the models. The authors of [32] propose a model for flame-wall interaction for the fractal model, by a term of exponential decay applied in the burn rate formulation. This sub-model is not based in a physical formulation and imposes the calibration of a characteristic time. For these reasons, it was not used in this work. In fact, the FSD model and fractal model are based on a physical description of the evolution of the wrinkling factor. Consequently, a pertinent modeling of flame-wall interaction would describe the modification of the wrinkling rate in function of the distance of the flame from the wall. No sharp peak is observed for those two models, since the end of combustion is not imposed, like in Eddy Burn Up model. On the contrary, the modeled flame continues to expand beyond the bore of the cylinder and laminar flame surface diminishes gradually to zero and so does the heat release rate. Cylinder pressure simulation is accurately simulated and the error on the maximum pressure is small (Figure 2-11). The pressure simulation is always more accurate than the heat release error simulation.

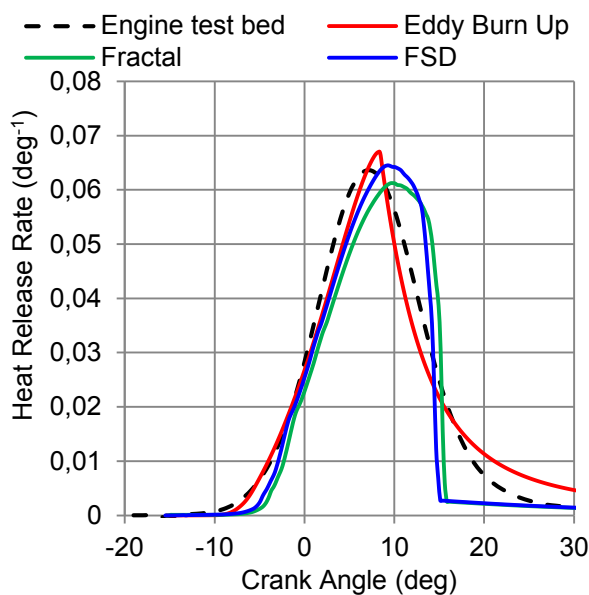


Figure 2-14: Heat release rate. Engine speed: 2000 RPM, IMEP: 3 bar

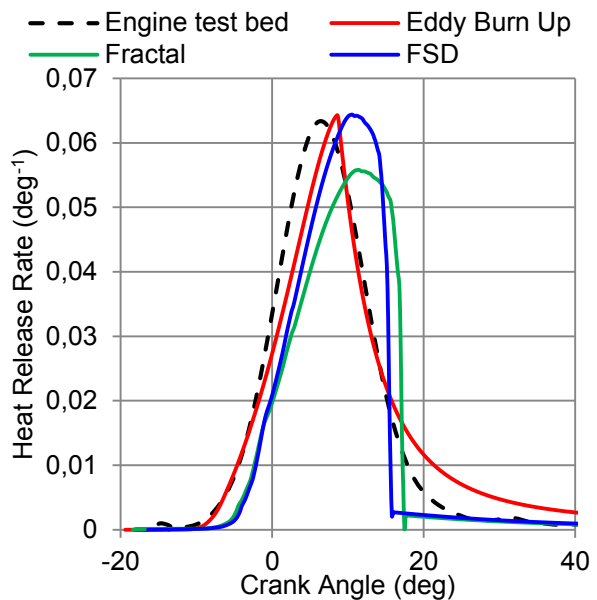


Figure 2-15: Heat release rate. Engine speed: 3000 RPM, IMEP: 3 bar

In Figure 2-14, Figure 2-16 and Figure 2-17 simulation results of an operating point with low load are shown. Heat release rate is rather well predicted. This was not always true, as it is shown in Figure 2-15. The level of RBG is high and the cycle by cycle variations are fa-

vored. In addition, the premixed combustion regime for low load points is positioned on the limit line of Karlovitz number equal to unity, as it is shown in combustion diagram in [53]. This fact implies that the flame is considerably thickened and the flamelet approach may not be appropriate [58]. Consequently, it is difficult to calculate the average heat release rate under low load conditions. Calibrating model constants was found to be difficult. In low load conditions, the presence of RBG puts into question the validity of laminar flame speed correlations (equation (2-25)). The convection of flame kernel is strong and puts into question the assumption of imposing the flame kernel in the middle of the electrodes of the spark plug. All those conditions make the modeling response less credible for low load conditions.

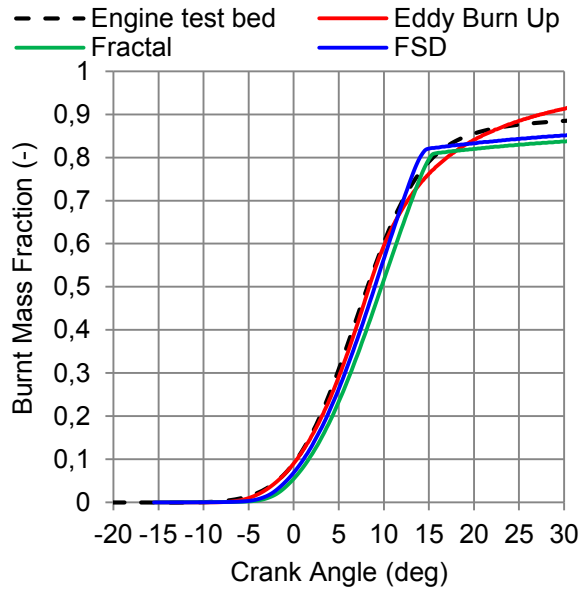


Figure 2-16: Burnt mass fraction. Engine speed: 2000 RPM, IMEP: 3 bar

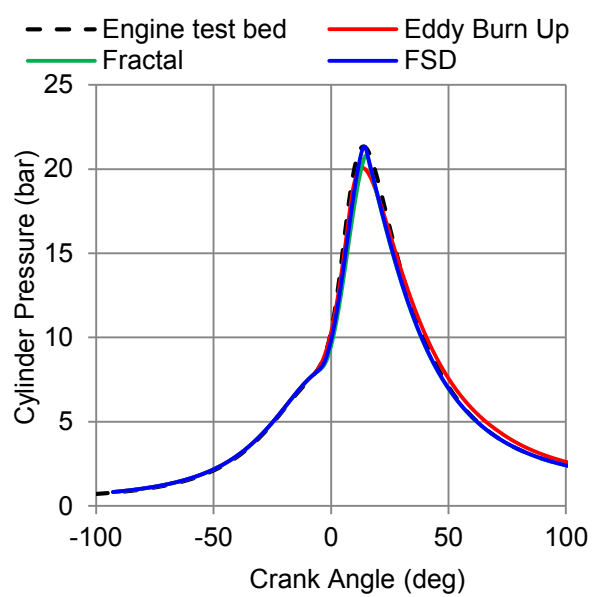


Figure 2-17: Cylinder pressure. Engine speed: 2000RPM, IMEP: 3 bar

In the following sets of figures (Figure 2-18, Figure 2-20, Figure 2-21), results of high load at 2000 RPM are shown. Before discussing the results, it must be noted that no auto-ignition model is implemented in our code and consequently the advance angle for all models equal to the test bed advance angle. Eddy Burn Up model shows the same behavior as in the average loads, with a good description of the beginning of combustion. The peak value is more elevated in the high load case. The inflexion point of the other two models is still present. An abrupt reduction of the heat release rate is observed for FSD and Fractal models. In addition, the crank angle is different between the simulated maximum heat release rate and the experimental one. This behavior is common in FSD and Fractal models. Fractal model gives a very important wrinkling in the beginning as it was shown in Figure 2-13. This results in a very rapid propagation in the beginning and the error is evident in Figure 2-20. Cylinder pressure is correctly simulated by the FSD model.

Additional results are shown for 3000 RPM high load in Figure 2-19, Figure 2-22 and Figure 2-23. In these cases, the calibration of the Fractal and FSD models was difficult. At high loads, the need for modeling the diminution of the wrinkling factor, caused by the flame-wall interaction, becomes essential.

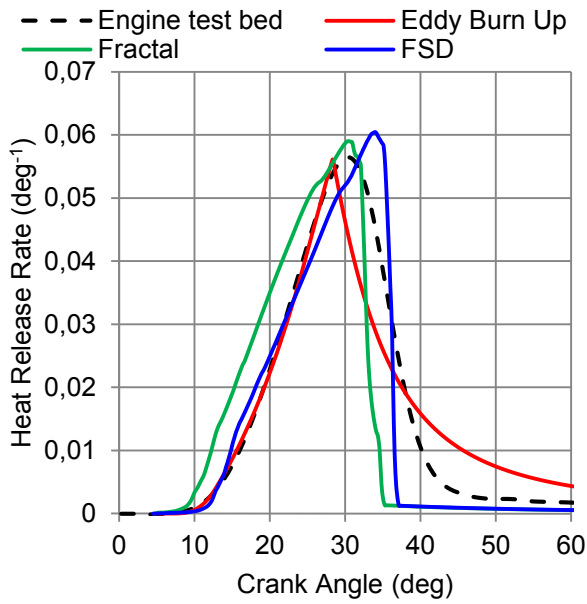


Figure 2-18: Heat release rate. Engine speed: 2000 RPM, IMEP: 18 bar

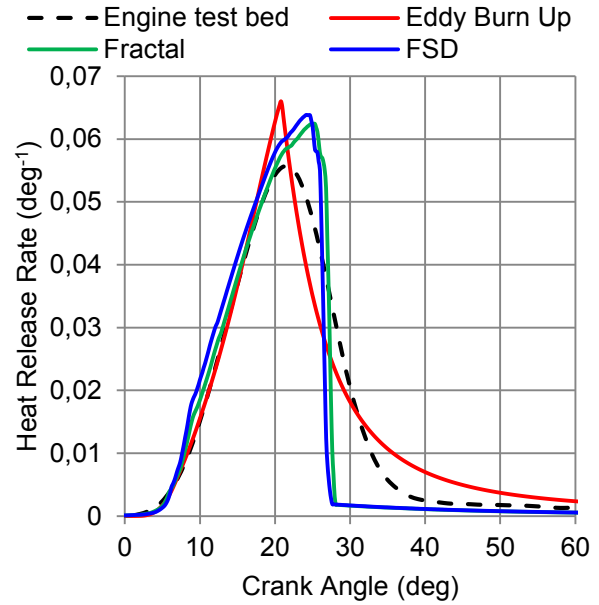


Figure 2-19: Heat release rate. Engine speed: 3000 RPM, IMEP: 16 bar

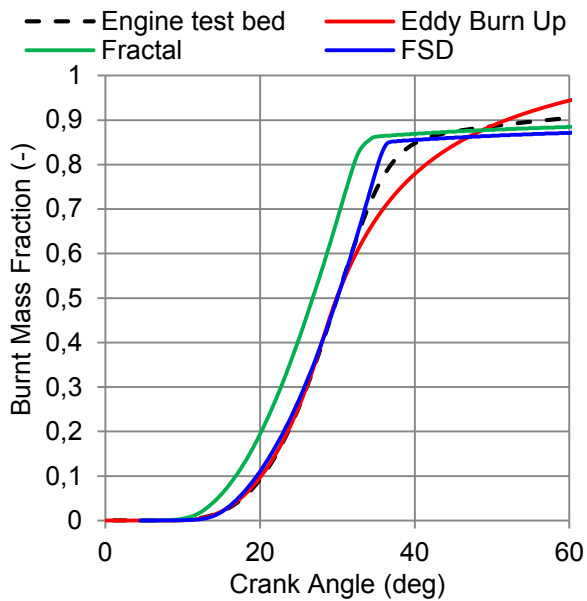


Figure 2-20: Burnt mass fraction. Engine speed: 2000 RPM, IMEP: 18 bar

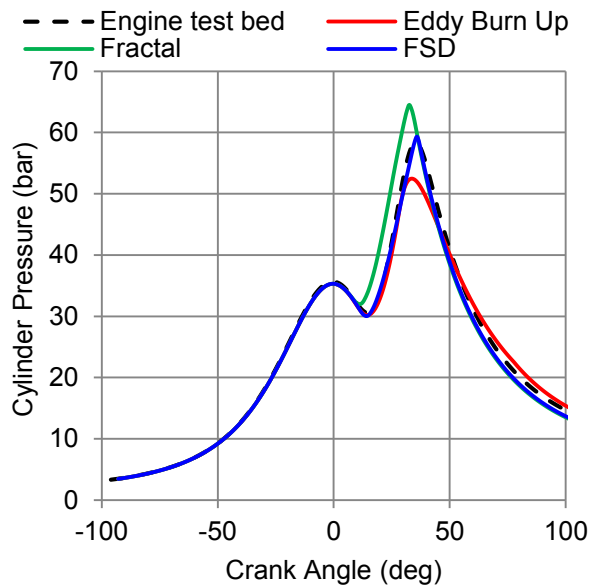


Figure 2-21: Cylinder pressure. Engine speed: 2000 RPM, IMEP: 18 bar

It has to be noted, that in Figure 2-10 the burnt mass fraction lines are not traced till EVO (151 deg corresponding to 29 crank angle degrees before BDC) but are limited till 30 deg for the sake of clarity. This is why the burned mass fraction in the experimental data line reaches a value of 0.88 at 30 deg, which seems to be small. Combustion reactions continue till EVO and the experimental burnt mass fraction reaches its maximum value of 0.97 (not shown here). The Eddy Burn Up model reaches unity before the others because the exponential term of equation (2-29) burns faster than the actual heat release rate. Fractal and FSD models do not have a modification for the end of combustion. This fact explains the observation of the abrupt diminution of the heat release rate of Fractal and FSD models, which is due to the diminution of the laminar flame surface as the flame front reaches the

wall. The same comments can be made for the burned mass fractions figures (Figure 2-16, Figure 2-20, Figure 2-22).

The relative errors of IMEP for all the presented simulations are given in Table 2-2. The average error is of the order of 5%.

Table 2-2: Test bed IMEP and relative errors of models

Engine Speed: IMEP:	1200 RPM 8 bars	2000 RPM 3 bar	2000 RPM 18 bar	3000 RPM 16 bar
Test bed	8.06	3.03	18	16
Eddy Burn Up	11%	6%	2%	1%
Fractal	1%	6%	1%	5%
FSD	1%	5%	5%	5%

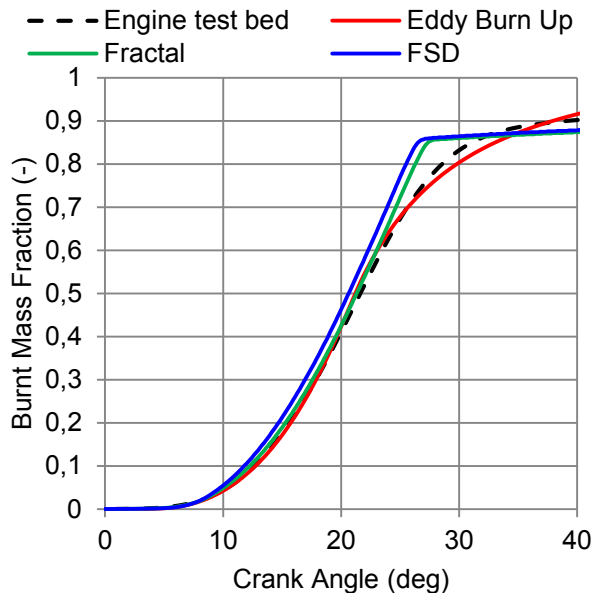


Figure 2-22: Burnt mass fraction 3000 RPM, IMEP: 16 bar

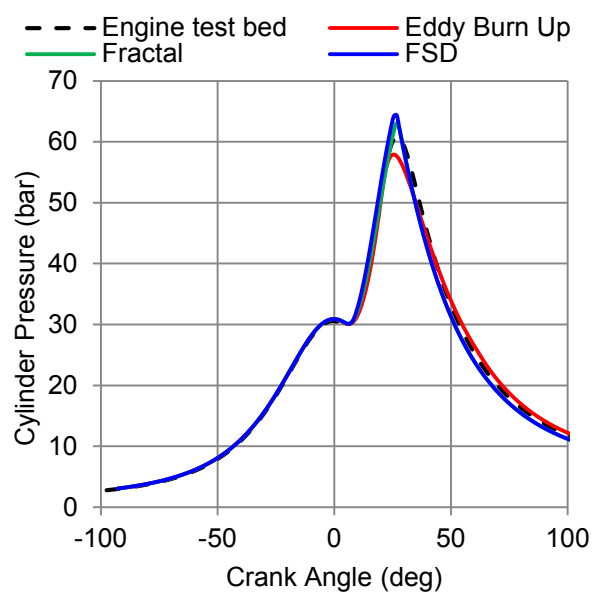


Figure 2-23: Cylinder pressure 3000 RPM, IMEP: 16 bar

The discussion of the behavior of the calibrating coefficients is of great interest. This discussion is restrained for the coefficients, which affect the turbulent combustion simulation. For every model the integral length scale is a parameter, modeled by the same relation (equation (2-26)). For Eddy Burn Up model, C_{LT} was equal to 0.04, as suggested in [45], [47]. For Fractal and FSD models, C_{LT} was equal to 0.1 for all operating points. The Eddy Burn Up contains A_{ST} and $C_{\tau\tau}$, which calibrate the turbulent flame speed. They were kept constant and equal to 2.5 and 0.55 respectively. $C_{\tau b}$ changes with the engine speed and is invariant to load changes. Its values are shown in Figure 2-26. For the Fractal model, the coefficients of the fractal dimension remain constant. C_R , which controls the maximum fractal length, is shown in Figure 2-24. The FSD calibration coefficient was extremely sensitive in variations, owing to its presence under a square root (equation (2-40)). Its behavior is shown in Figure 2-24. A summary of the coefficients of all model is given in Table 2-3.

For the coefficient of the FSD model, no clear trends can be traced. If we exclude the low loads, the coefficient shows a decrease with load and engine speed. There is no evolution

between 2000 RPM and 3000 RPM for high loads. A better calibration methodology for FSD, would include calibration on the integral length scale, as suggested in [50]. Fractal model coefficient evolution shows trends of reduction with engine load and increase with engine speed. Eddy Burn Up coefficients with the approach of integral length scale is constant with load and varies with engine speed (Figure 2-26). A general comment for the heat release rates of Fractal and FSD models is that they show similar behavior for each operating point. This observation lies in the fact that the two models share common assumptions for the flame wrinkling, as presented in the modeling section and they use the same approach for the flame propagation.

Table 2-3: Coefficients for Eddy Burn Up, Fractal and FSD combustion models.

	Eddy Burn Up	Fractal	FSD
Integral length scale L_T	$C_{LT} = 0.04$	$C_{LT} = 0.1$	$C_{LT} = 0.1$
Turbulent flame speed or wrinkling	$A_{ST} = 2.5, C_{\tau\tau} = 0.55$	$C_R, D_3(s_L, u')$	C
Burning of entrained mass	$C_{\tau b}$	-	-

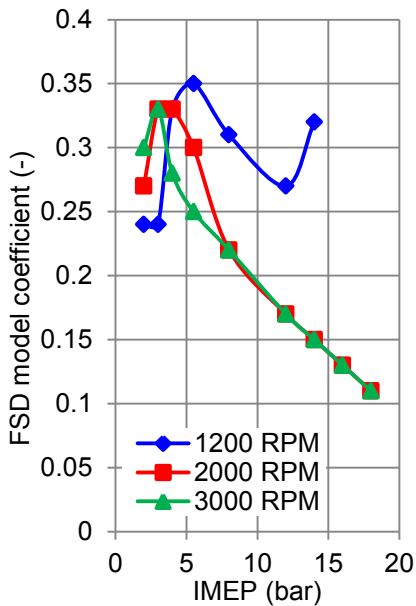


Figure 2-24: Variation of C of FSD model

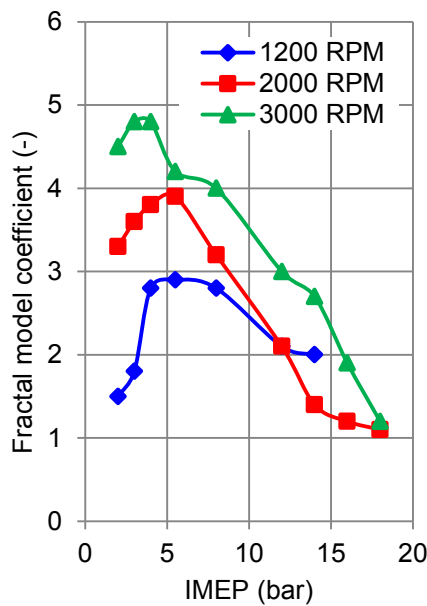


Figure 2-25: Variation of C_R of fractal model

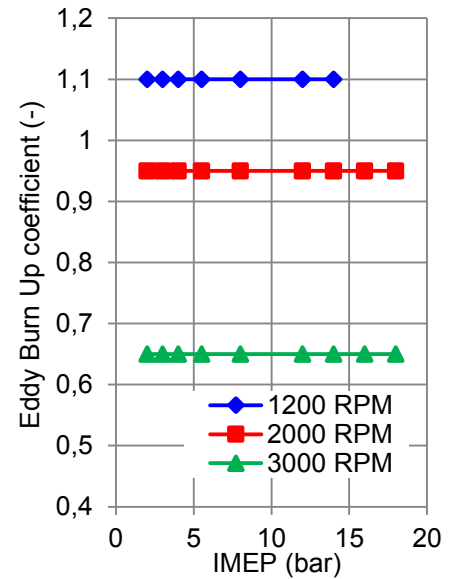


Figure 2-26: Variation of $C_{\tau b}$ of Eddy Burn Up model

The variation of coefficients shows an absence of precision on the description of turbulence-flame interaction by the models. While the engine speed is constant, the variation of engine load is represented by the influence of pressure variations on combustion. Pressure has a major influence on laminar flame thickness. This impact is expressed by the existence of the density of fresh gases in the definition of the flame thickness. When pressure increases, laminar flame speed slightly diminishes but the density of fresh gases increases and the laminar flame thickness diminishes. This diminution of flame thickness causes an increase of the flame wrinkling, which can be explained by two phenomena:

1. The diminution of the flame thickness causes hydrodynamic instabilities (Darrieus-Landau) [59].

2. More turbulent scales can wrinkle the flame, when flame thickness is reduced [60].

The models must be able to take into account the increase of flame wrinkling, when pressure increases. In Eddy Burn Up model, flame thickness is taken into account by the Da number, which exists in the turbulent flame speed (equation (2-31)). This is why the coefficient $C_{\tau b}$ remains constant for a given engine speed (Figure 2-26). In the Fractal model, the influence of pressure increase is taken into account only in the kinematic viscosity, which diminishes when pressure increases. As a consequence, the Kolmogorov (η_K) diminishes and the wrinkling factor increases. The impact of flame thickness must be considered explicitly in the Fractal model formulation. With the actual formulation flame wrinkling increases with pressure but needs an adjusted coefficient.

Fractal and FSD models integrate explicitly in their formulation an increase of the flame wrinkling, while the flame radius increases. This amplification of flame wrinkling is the effect of the increased number of turbulent structures that affect the flame front when flame radius increases. In Fractal model, this fact is taken into account by the presence of flame radius in L_{max} formulation. In FSD model, the second RHS term is negative and inversely proportional with the flame radius (equation (2-39)). Thus, the description of burnt mass rate during the combustion process is more physical with FSD and Fractal models.

The observation of the behavior of the coefficients is useful because it helps identifying the characteristic operating points of the engine, on which the models must be calibrated for a given technical concept. In addition, the predictivity of the models can be assessed on the results of the non-calibrated operating points or on the results of another technical definition.

2.5.8 Conclusion for the comparison of models

Three 0D SI combustion models (Eddy Burn Up, Fractal, FSD) were coded as user models in a GT-POWER™ single cylinder engine and simulations were performed. The comparison of the models with experimental data focuses on the impact of turbulence on the flame front and shows the predictive capabilities of each approach. After imposing of an initial flame kernel, the flame front propagation is modeled by a spherical surface. Flame surface is tabulated as a function of piston position and flame radius. The equations used for laminar flame speed and thickness were common in all models. Turbulence was acquired by 3D CFD data.

Eddy Burn up model gave a satisfactory simulation for the beginning of combustion but it does not describe correctly the end of combustion as the exponential term, which is used for describing the end of combustion, is not an adequate solution. Eddy Burn Up model contains three coefficients for the description of the turbulent flame front ($C_{\tau b}$, A_{ST} , $C_{\tau T}$). $C_{\tau b}$ varies with the engine speed and is constant with engine load, while the other two coefficients are constant. The fractal model has one coefficient (C_R), which varies with engine speed and the engine load. The coefficients that define the fractal dimension are constant. The FSD model has one coefficient that varies with the engine speed and load. Unlike turbulent intensity, which was taken from 3D CFD results, integral scale was modeled as a function of the cylinder volume. It may be viewed as another calibrating coefficient which varies with engine load or speed.

Cylinder pressure results were very satisfactory, even if the heat release rate was not accurately predicted. Calibration under low load conditions was difficult for all models. If we

exclude those points FSD and fractal coefficients show clearer trends. Both fractal and FSD models describe inaccurately the beginning of combustion and present an inflexion point in the heat release rate. This behavior relies on their common flame propagation approach and the common tabulation for flame radius. The Eddy Burn Up approach for flame propagation may be more suitable for the beginning of combustion. Fractal and FSD models show similarities in the heat release rate, which lie also in the fractal concept for modeling turbulence-flame interaction. Only the FSD model gives a physical flame wrinkling for the beginning and describes a flame with a gradually augmenting wrinkling and takes into account the impact of all turbulent scales in a physical way through its efficiency function. Flame-wall interaction reduces the flame wrinkling and heat release rate of the flame front. No diminution of flame wrinkling was observed as the flame approached the wall. This deficiency shows that wall-flame interaction modeling must be introduced.

Chapter 3 Development and validation of a SI combustion model

In the previous chapter, the presented comparison of three typical combustion models revealed which model takes into account the physics of turbulent premixed fully developed flame and it gives a rather fair image of the initial stage of combustion. It was also shown that the model must be adapted in order to describe properly the end of combustion.

Most of the models focus almost exclusively on the laminar flame characteristics and on the wrinkling phenomena of a freely propagating flame, but they lack a suitable approximation of wrinkling phenomena when the flame approaches and reaches the cylinder walls. The cylinder wall acts as a geometrical barrier, which limits the expansion of the flame front. In addition, wall temperature is much lower than the burnt gas temperature. Heat transfer from the flame front towards the cold walls reduces the flame front temperature and causes flame quenching. Last but not least, the flow in the vicinity of the walls is highly viscous (turbulent boundary layer). Therefore, flame wrinkling decreases as the flame approaches the wall. These phenomena significantly reduce the burning rate. This decrease can depend on the engine intake geometry, the combustion chamber geometry and the operating conditions [61]. As shown in [62], the suitable modeling of flame-wall interaction is an essential step towards physical modeling of the combustion process.

Another important aspect of spark ignition combustion is the presence of post-flame oxidation reactions of carbon monoxide (CO) and hydrocarbons (HC) when the flame front arrives near the chamber wall. CO concentration levels are controlled by chemical kinetics and are higher than their equilibrium values at the exhaust pressure and temperature conditions. This is due to the decrease in burnt gas temperature during expansion and exhaust strokes, which causes CO oxidation reactions to 'freeze' [63]. The impact of CO kinetics on the heat release rate is important mostly for fuel-rich mixtures. The HC formation process in SI engines is extremely complex and is a combination of multiple phenomena. However, HC formation mechanisms are strongly connected with flame quenching at the cylinder walls. The unburnt HC/air mixture, which has not reacted within the flame front, will sustain mixing with the bulk burnt gas. After the mixing processes, their temperature will increase and oxidation reactions will take place.

In addition to the near wall phenomena, of various fuels in a SI engine might be responsible for a different combustion behavior and could therefore impact the engine efficiency. For SI engines, the heat release rate is linked to flame propagation speed. In addition, while aiming to the improvement of the efficiency, oil companies looked for developing fuels that burn faster than the typical gasoline. Nevertheless, in a SI engine, the flame speed does not only depend on the fuel but also on several additional phenomena such as: turbulence, flame wrinkling, and flame stretch. As a first step to evaluate potential substitutes to gasoline, the fundamental laminar burning speed is mainly investigated [64]–[67]. Moreover, it is a key parameter for combustion modeling [45], [68]. This burning speed corresponds to the speed of a one-dimensional planar adiabatic flame in laminar conditions without any instability and it is a function of pressure, temperature, fuel, dilution and fuel/air equivalence ratio. Nevertheless, the fundamental laminar burning speed cannot be considered as the consumption speed of an expanding flame since this type of flame is submitted to strain rate and flame

curvature which are the two contributions of the flame stretch [69], which can be defined as the relative growing rate of the flame surface. The flame stretching phenomena are connected with the thermo-diffusive characteristics of the fuel [25], [28], [70].

Therefore depending on the fuel used, the different responses to the flame stretch will impact differently the flame propagation. If this effect has been fully investigated in laminar conditions [71]–[73], only a few recent studies presented flame stretch effect in Spark-Ignition engine [74]–[76]. Besides, only a few Computational Fluid Dynamics (CFD) models for spark ignition consider the laminar burning speed dependence to the flame stretch [36], [77], [78] and numerous models are mainly based on the unstretched laminar burning speed. Nevertheless, the way of taking into account flame stretch phenomena is still an open question.

The proposed models for these three phenomena (flame-wall interaction, post flame reactions and impact of flame stretch) are covered in the following sections. In addition the complements of the combustion model (Piston kinematics, numerical solver, two-zone thermodynamics, heat transfer and flame geometry) are presented.

3.1 Piston kinematics

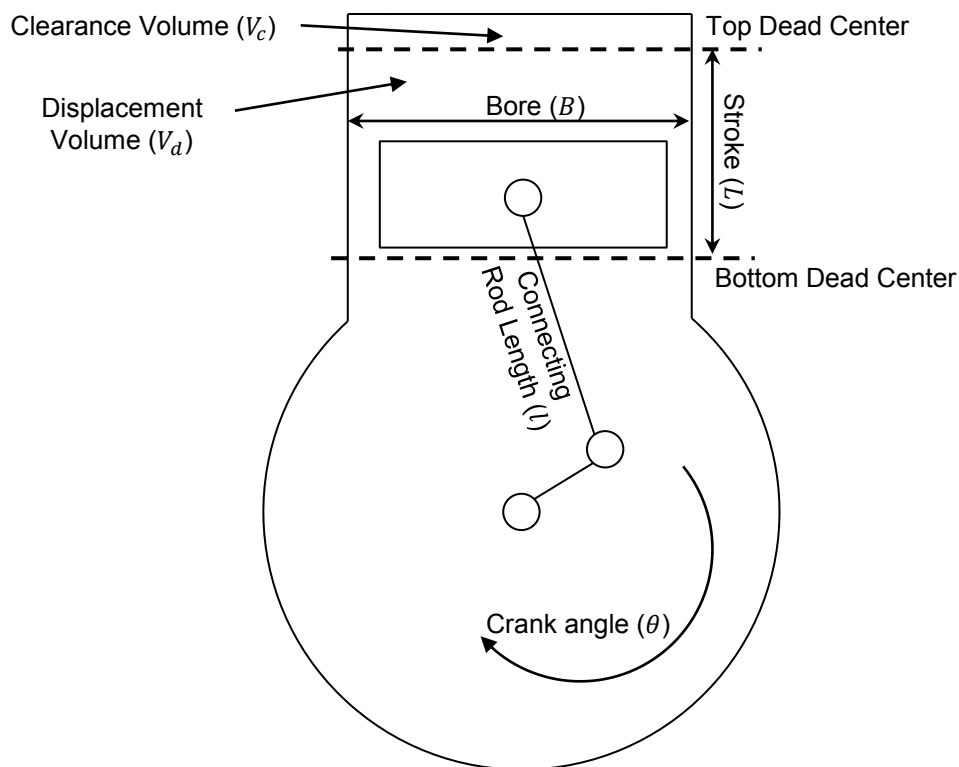


Figure 3-1: Geometry of cylinder, piston, connecting rod and crankshaft.

In Figure 3-1, a simplified representation of the combustion chamber and of the piston-rod mechanism is presented. The geometric compression ratio (ε) is the ratio of the maximum to the minimum chamber volume. The displacement volume (V_d) is the swept volume by the piston from the TDC (crank angle $\theta = 0$ deg) to the BTC (crank angle $\theta = \pm 180$ deg). The cylinder bore (B) and piston stroke (L) are defined in Figure 3-1.

$$V_d = \frac{\pi}{4} B^2 L \quad (3-1)$$

The clearance volume (V_c) is the volume of the chamber, when the piston is at TDC.

$$V_c = \frac{V_d}{\varepsilon - 1} \quad (3-2)$$

The ratio R is a function of the connecting rod length (l) and of the piston stroke (L):

$$R_L = \frac{2 \cdot l}{L} \quad (3-3)$$

The instantaneous chamber volume (V) is given by the equation (3-4):

$$V = V_c + 0.5V_d \left(R_L + 1 - \cos \theta - \sqrt{R_L^2 - \sin^2 \theta} \right) \quad (3-4)$$

The derivative of the chamber volume ($\frac{dV}{d\theta}$) is given by the equation (3-5) in rad^{-1} :

$$\frac{dV}{d\theta} = 0.5V_d \sin \theta \left(1 + \frac{\cos \theta}{\sqrt{R_L^2 - \sin^2 \theta}} \right) \quad (3-5)$$

3.2 Numerical solver

In order to obtain the evolution of various thermodynamic variables during an engine cycle, the ordinary differential equations pressure, fresh and burnt gas temperature, work and heat release, wrinkling factor, post flame reactions must be solved. In this combustion model, the Dormand Prince explicit method [79] has been used for the resolution all the differential equations. This method is a member of the Runge-Kutta family of ordinary differential equations (ODE) solvers. More specifically, it uses six function evaluations to calculate fourth-order and fifth-order accurate solutions. Its error estimation is very convenient for adaptive step size integration algorithms. In addition, the Dormand-Prince method has seven stages, but it uses only six function evaluations per step because seventh approximation is a linear combination of the previous six evaluations: the last stage is evaluated at the same point as the first stage of the next step. The main equation, which has been used in this work is:

$$y_{i+1} = y_i + \frac{35}{384}K_1h + 0 \cdot K_2h + \frac{500}{1113}K_3h + \frac{125}{192}K_4h - \frac{2187}{6784}K_5h + \frac{11}{84}K_6h \quad (3-6)$$

With

$$\begin{aligned} K_1 &= f(t, y) \\ K_2 &= f\left(t + \frac{1}{5}h, y + \frac{1}{5}K_1h\right) \\ K_3 &= f\left(t + \frac{3}{10}h, y + \frac{3}{40}h(K_1 + 3K_2)\right) \\ K_4 &= f\left(t + \frac{4}{5}h, y + \frac{44}{45}hK_1 - \frac{56}{15}K_2h + \frac{32}{9}K_3h\right) \\ K_5 &= f\left(t + \frac{8}{9}h, y + \frac{19372}{6561}hK_1 - \frac{25360}{2187}K_2h + \frac{64448}{6561}K_3h - \frac{212}{729}K_4h\right) \\ K_6 &= f\left(t + h, y + \frac{9017}{3168}K_1h + \frac{355}{33}K_2h + \frac{46732}{5247}K_3h + \frac{49}{176}K_4h + \frac{5103}{18656}K_5h\right) \end{aligned} \quad (3-7)$$

t : Independent variable, h : step of independent variable and $\dot{y} = f(t, y)$

3.3 Two-zone thermodynamic modeling

3.3.1 Mass and energy conservation

The two-zone thermodynamic model expresses the conservation of mass and energy inside the combustion chamber. In order to write these equations, from inlet valve closing angle to exhaust valve opening angle, some simplifying assumptions must be made. To begin with, the total mass is conserved, since zero blow-by losses are assumed.

$$\dot{m} = \dot{m}_u + \dot{m}_b = 0 \quad (3-8)$$

In this equation, \dot{m}_b represents the combustion rate in terms of mass and is written $\dot{m}_b = \dot{m}_{b,ff} + \dot{m}_{b,pf}$ where $\dot{m}_{b,ff}$ is determined by the flame propagation model and $\dot{m}_{b,pf}$ corresponds to the mass of gases consumed by the post-flame reactions of CO and HC, which are described in this work.

The instantaneous cylinder volume is equal to the sum of the volumes of the burnt and unburnt zones. The derivatives of the volumes of the two zones are equal to the derivative of the chamber volume (as given by the piston-rod kinematics):

$$\dot{V} = \dot{V}_u + \dot{V}_b \quad (3-9)$$

Moreover, during compression and expansion strokes, pressure is considered to propagate in an infinitely fast manner throughout the cylinder. Hence, pressure (p) is considered as spatially uniform and changes only with crank angle evolution. The fresh and burnt gas regions are considered to be in chemical equilibrium. During flame propagation, it is assumed that fresh and burnt zones are separated by the infinitely thin flame front, with no heat exchange between them. The assumption of a thin flame front is justified by the combustion regime in an SI engine [11]. The energy (3-10) and fresh gas entropy conservation (3-11) equations along with the volume conservation equation (3-9) complete the system of equations of the thermodynamic model (h is the specific enthalpy, u is the specific internal energy, and \dot{Q} is the heat exchanged by the gases with the external environment, which is determined using a wall heat transfer model):

$$\dot{Q} = m\dot{u} + p\dot{V} \quad (3-10)$$

$$\dot{S}_u = -\dot{m}_u s_u - \frac{\dot{Q}_u}{T_u} \quad (3-11)$$

All gases are considered ideal gases. the perfect gas equation is applied for each zone. The difference of specific heats under constant pressure (c_p) and constant volume (c_v) appear for each zone ($R = c_p - c_v$):

$$p = \rho_u R_u T_u = \rho_b R_b T_b \quad (3-12)$$

The detailed derivation as well as the final form of the thermodynamic equations for the pressure (p) and the fresh/burnt gas equation (T_u, T_b) is given in Appendix A.

3.3.2 Composition of each zone

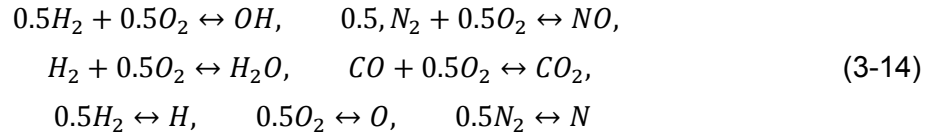
The fresh gas region is composed of seven species: Fuel, CO₂, H₂O, O₂, N₂, H₂ and CO. It contains the perfectly premixed fuel-air mixture (Fuel, O₂, N₂) and the Residual Burnt Gas (RBG), which is composed of CO₂, H₂O, O₂, N₂, H₂ and CO, which are the dominant species in cold exhaust gases. For a given RBG mass fraction, the mass fractions of each species

can be calculated by the equations of C, H, N, O atoms conservation. In the case of lean or stoichiometric mixtures, CO and H₂ mass fractions are zero. For rich mixtures, the O₂ mass fraction is zero and an additional reaction is inserted in order to close the system of equations:



The equilibrium constant of this reaction is given as a function of temperature with coefficients provided in JANAF tables [80]. This additional reaction allows the estimation of the CO mass fraction and permits the application of atom conservation, in order to calculate the rest of the species. The total RBG mass fraction at inlet valve closing is estimated by the semi-empirical relation proposed in [81]. Its estimation is crucial, as it has an important effect on engine power output and pollutant emissions. It lowers the laminar flame speed and reduces the cylinder pressure and temperature, thereby having an impact on burnt gas composition.

The burnt gas zone contains the dissociation and recombination combustion products H, O, OH, NO and N, as well as the predominant exhaust gases (CO₂, H₂O, O₂, N₂, H₂ and CO). The thermodynamic properties of each species are calculated by polynomial fitting functions shown in [82]. Atom conservation provides four equations for the calculation of species mass fractions. Seven additional reactions at equilibrium are considered:



The values of the chemical equilibrium constants of these reactions are given in [83] as a function of burnt gas temperature (T_b) and pressure (p). The various thermodynamic properties (specific enthalpy, specific internal energy, density, specific heat capacities at constant pressure and constant volume) are calculated by combining the properties of each species with a mixing law. For the calculation of the properties of each species, polynomial functions of temperature are used. Their coefficients can be found in JANAF tables [80].

The details about the calculation of the equilibrium composition as well as of species thermodynamic properties is given Appendix A.

3.4 Heat transfer

The thermodynamic model requires as input the initial pressure and composition, the volume of the combustion chamber and its rate of change as a function of crank angle, and a model for the heat transfer rate during the cycle. A classical Woschni model was used in this work. The complete description of this model can be found in [84]. The wall temperature (T_w) is considered constant for the cylinder head, piston crown and cylinder liner and equal to 453K. The heat transfer rates (\dot{Q}_u and \dot{Q}_b with $\dot{Q} = \dot{Q}_u + \dot{Q}_b$), which are used in equations (3-10) and (3-11), are modeled:

$$\dot{Q}_u = A_{u,w} h_{c,u} (T_u - T_w) \quad (3-15)$$

$$\dot{Q}_b = A_{b,w} h_{c,b} (T_b - T_w) \quad (3-16)$$

The wetted areas from each zone ($A_{u,w}$ and $A_{b,w}$) are modeled as a function of burnt mass fraction, bore and cylinder height. The convective heat transfer coefficient is modeled

as a function of pressure, temperature, cylinder bore and mean gas velocity. The coefficients of the model [84] are calibrated so that the cylinder pressure before ignition is equal to the respective measured value and the sum of net heat release and the heat transfer is equal to the burnt fuel energy.

More details for the heat transfer coefficients and for the wetted surfaces can be found in Appendix A.

3.5 Reconstructed heat release rate

Cylinder pressure data allow the reconstruction of an energy balance inside the combustion chamber while the valves are closed. The total heat release during combustion Q_{comb} consists of the work term, the internal energy term and the heat transfer term, as it can be observed in equation (3-17). The ratio of heat capacities γ can be calculated through the mean gas temperature in the chamber. No mass loss into crevice volumes is considered so any change in the internal energy is made by temperature variation. The ‘‘Woschni’’ model is used for the calculation of heat transfer. For each operating point a wall temperature is set for the cylinder liner, piston crown and cylinder head. The models constants are calibrated in order that the total heat release during combustion is the same with the converted fuel energy ($\eta_{comb}m_{fuel}LHV_{fuel}$).

$$\frac{dQ_{comb}}{d\theta} = \frac{\gamma}{\gamma - 1} p \frac{dV}{d\theta} + \frac{1}{\gamma - 1} V \frac{dp}{d\theta} + \frac{dQ}{d\theta} \quad (3-17)$$

3.6 Flame Geometry

3.6.1 Concise description of the flame geometry model

A basic assumption of 0D SI combustion modeling is that the flame starts as a sphere between the electrodes of the sparkplug. When the flame propagates inside the cylinder, its mean surface (A_L) as well as its volume (V_L) remain spherical. A numerical tool of a simplified but realistic chamber geometry was developed. It takes into account the chamber geometry through its bore, stroke, and sparkplug position and it represents the complex geometry of the cylinder head with reasonable accuracy. It gives as an output the mean surface and the volume as a function of the piston height and of the flame radius (R_f). At each crank angle step, the flame radius is calculated so that the geometrical volume (V_L) of burnt gases is equal to the burnt gas volume (V_b) from the thermodynamic model. This calculation ensures consistency of the flame propagation. The temporal evolution of the flame radius allows calculating a propagation flame speed (s_R):

$$s_R = \frac{dR_f}{dt} \quad (3-18)$$

The distribution of the mean flame surface $A_{fr}(\delta)$ is also calculated by the geometrical tool. In Figure 3-3 the principle of distance distribution is presented. The chamber geometry is shown in Figure 3-2. Several points with degrees of freedom were introduced, so as to permit the adaptation of the model geometry to that of a real engine. The validation of this geometrical tool is presented in the ‘Results and discussion’ section, and compared with the results of calculations made with a Computer Aided Design (CAD) tool.

The complete presentation of the geometric model is found in Appendix B.

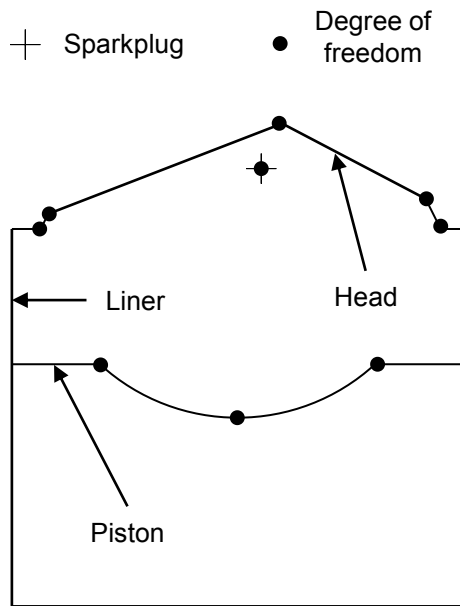


Figure 3-2: Cross section of the simplified combustion chamber. The dots (●) show the points which have degrees of freedom and can be displaced. This displacement allows the creation of the special geometries proposed in modern SI chamber concepts.

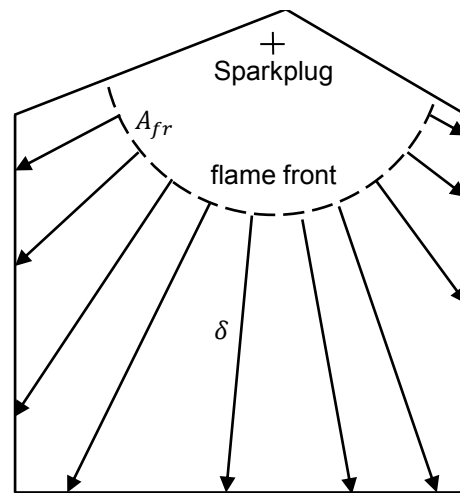


Figure 3-3: Mean flame surface distribution with respect to the chamber walls (cross-section of chamber). This figure shows the principle of the geometrical tool, which calculates the surface, the volume and the distribution of the surface as a function of the distance from the wall.

3.6.2 Validation of geometric model

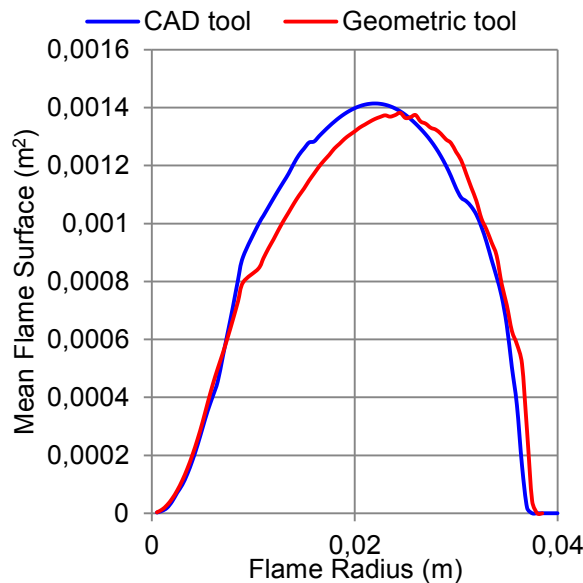


Figure 3-4: Comparison of mean spherical flame surface calculated by the CAD software and the geometrical tool used in this work. Flame radius goes from zero to half of cylinder bore. Piston position remains fixed at TDC for this example.

The quality of the simplified geometric tool was evaluated with calculations performed by a CAD tool. The exact three-dimensional geometry of the combustion chamber was available and a spherical surface, centered between the electrodes of the sparkplug, was im-

posed. This tool provides an accurate calculation of the flame surface and the enclosed volume. An offset of 1.5 mm of the chamber walls was imposed on the geometry of the CAD software. The difference between the new offset flame surface and the previous surface contains the surface fraction, which has a distance of at least 1.5 mm from the wall. The CAD tool cannot calculate the distribution of flame surface as a function of the distance from the wall directly. In Figure 3-4, a very good agreement between the two tools is observed for all flame radii during the calculation of the total mean flame surface. The evolution of the surface fraction within 1.5 mm when the mean flame surface radius varies, is shown in Figure 3-5. For low radius values, there is a discrepancy between the two calculations. This is due to the simplified pent-roof geometry of the geometric tool, whereas the exact geometry does not significantly confine the development of the initial flame kernel. The important point is that the agreement is good when the flame approaches the chamber walls. The volume of the mean flame during a combustion cycle is shown in Figure 3-6. The two volume curves almost coincide. During the final part of combustion, the burnt gas volume is almost equal to the chamber volume. This satisfactory agreement means that the geometrical tool can be used in the combustion model.

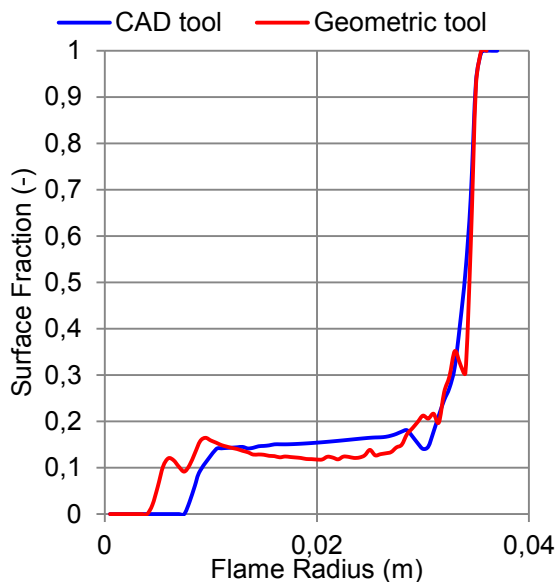


Figure 3-5: Comparison of surface fraction, which has a distance of 1.5 mm or less from the wall and is calculated by the CAD software and the geometric tool used in this work. Flame radius starts at zero. Piston position remains fixed at TDC.

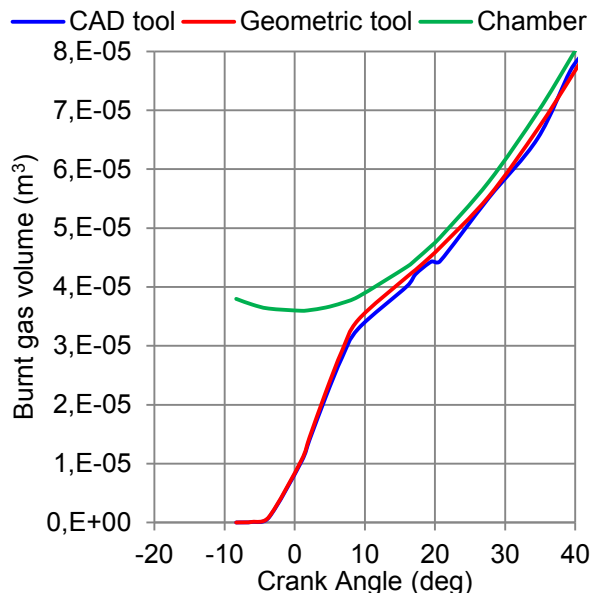


Figure 3-6: Comparison of volume of burnt gases calculated by the CAD tool and the geometric tool used in this work during a combustion cycle.

3.7 Overview of the combustion model

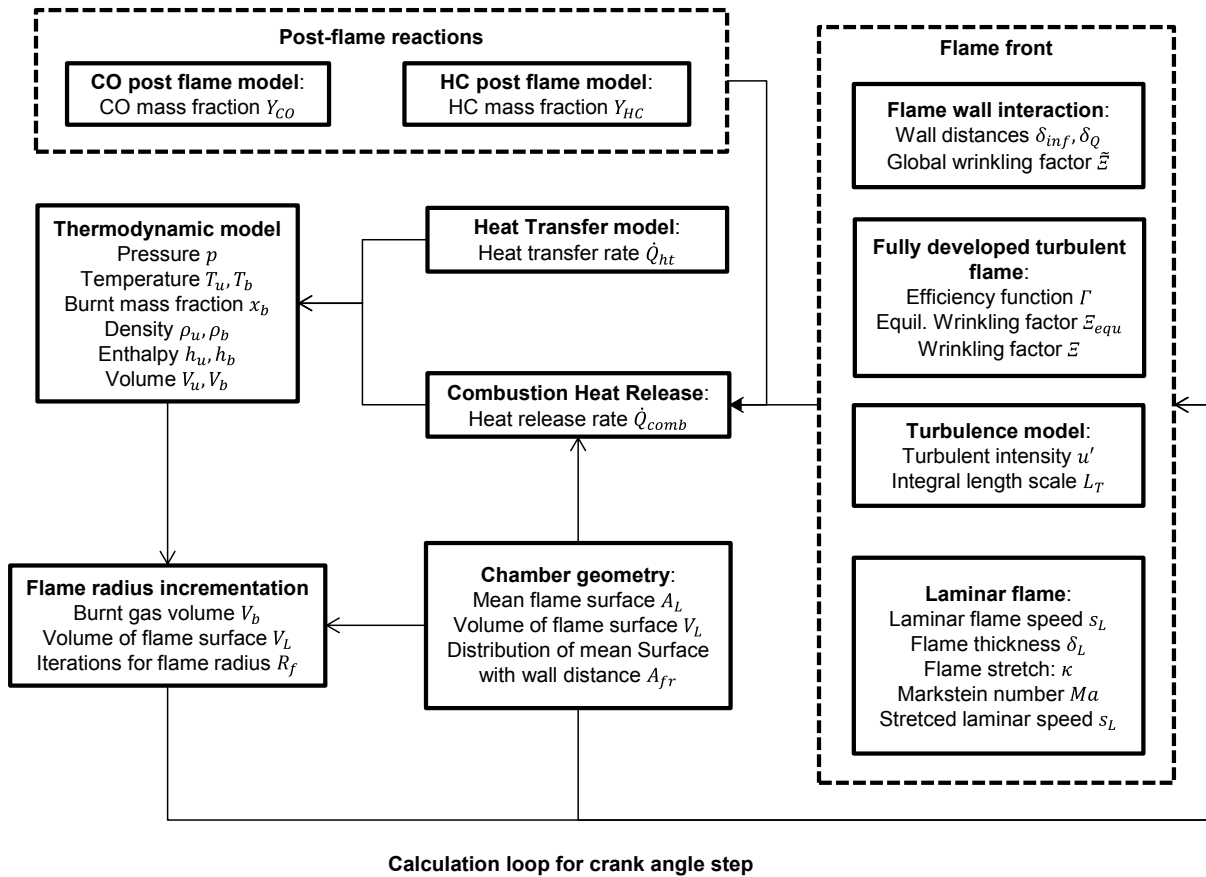


Figure 3-7: Schematic representation of the combustion model and its connections with flame geometry and thermodynamic model.

This section presents the entire combustion model. A schematic representation of the combustion model is shown in Figure 3-7. Some sub-models already described in previous work are briefly covered. The new sub-model of flame-wall interaction is described in detail. To introduce the general principles of the model, the global 0D equation of burnt mass is presented and its terms are analyzed:

The new sub-models of flame-wall interaction, post flame reactions and flame stretch are described extensively. To introduce the general principles of the model, the global 0D equation of burnt mass is presented and its terms are analyzed:

$$\dot{Q}_{comb} = \dot{Q}_{ff} + \dot{Q}_{pf}$$

$$\dot{Q}_{ff} = \dot{m}_{fuel,ff} \Delta h_{r,fuel} \quad (3-19)$$

$$\dot{Q}_{pf} = \dot{m}_{CO} \Delta h_{r,CO} + \dot{m}_{HC} \Delta h_{r,fuel}$$

This equation divides the combustion heat release rate in two terms. The first term is the fast heat release from the flame front (\dot{Q}_{ff}) and is equal to the fuel mass rate ($\dot{m}_{fuel,ff}$) multiplied by the specific reaction enthalpies (Δh_r) of the fuel. The heat release rate due to post-flame reactions is contained in the second term. It represents the energy released by post-flame reactions of CO and unburnt HCs and contains their mass change (\dot{m}) rates as well as their specific reaction enthalpies (Δh_r) with the oxygen contained in the intake air. The first

Right Hand Side (RHS) term of \dot{Q}_{ff} is then written in terms of burnt mass rate ($\dot{m}_{b,ff}$), assuming that the fuel mass ($\dot{m}_{fuel,ff}$) reacts with the stoichiometric air mass (the relative composition of the fresh gases is not altered) with AFR being the stoichiometric air mass:

$$\dot{m}_{b,ff} = \dot{m}_{fuel,ff}(1 + AFR) \quad (3-20)$$

Under the flamelet assumption, the combustion reaction is assumed to be fast enough so that the dominant effect of turbulence on the flame is to wrinkle the flame surface, while the inner flame structure is not significantly altered by the turbulent flow field. The flame front burnt mass rate $\dot{m}_{b,ff}$ is modeled using a flame propagation combustion model under the flamelet assumption:

$$\dot{m}_{b,ff} = \rho_u s_L A_L \mathcal{E} \quad (3-21)$$

It contains the fresh gas density (ρ_u), the laminar flame speed (s_L), the mean flame surface (A_L) and the wrinkling factor (\mathcal{E}). The flame starts as a kernel of burnt gases in the vicinity of the sparkplug and then propagates towards the walls, while being wrinkled by turbulence. As soon as the flame approaches the wall various phenomena take place.

3.8 Turbulence

As is well known, aerodynamic turbulence wrinkles the flame (increases its surface) by changing its stretch and strain characteristics. The calculation of the wrinkling factor (\mathcal{E}) involves estimating the integral length (L_T) and turbulence intensity (u'). In this work a 0D turbulence model was used (see section 2.3, equation (2-17)). It contains one equation for the global kinetic energy (K) and one for the turbulent kinetic energy (k). The crucial assumption is that turbulence is homogenous and isotropic throughout the combustion chamber. An experimental assessment [85] of the turbulent intensity of the engine used in this work was performed and the results were used to calibrate the 0D turbulent model. The experimental velocities are decomposed through filtering in a low frequency component (mean velocity field) and a high frequency component (fluctuation velocity field). The fluctuation field is used for the turbulent intensity. These results have been used for the calibration of the 0D turbulent model. A thorough explanation of this model can be found in [32], [33].

3.9 Flame-wall interaction sub-model

Combustion is strongly influenced by the presence of walls, which may affect the flame in many ways, one of which is quenching. In addition, the flame significantly impacts the flow in the vicinity of the wall as well as the heat transfer from the cylinder to the wall. Flame-wall interaction physics becomes even more complicated when combustion takes place in the chamber of an internal combustion engine. When the flame reaches the cold wall, viscous dissipation effects limit the ability of turbulence to wrinkle the flame and the heat release diminishes. High heat losses from the flame towards the cold wall also decrease the reaction rate of the flame front. Finally, the flame is quenched because of the cooling of reactants or sudden extinction at the walls. Despite the complexity of the flame-wall interaction, a thorough understanding of the phenomenon as well as a modeling approach is needed in the case of SI combustion, as the heat release rate is reduced by the flame front when the flame approaches the wall and flame quenching has an impact on HC emissions.

Research investigations into flame-wall interaction and quenching focus mainly on laminar flames, and may be experimental and/or numerical [86]–[90]. However, numerical research has also been conducted on turbulent flame-wall interaction [91], [92]. Most of the efforts of flame-wall interaction modeling in 0D applications are covered by an overall modeling approach of the ‘end of combustion’ period. The final mass burning rate is well approximated by an exponential decay [68]. This empirical modeling approach does not take into account the numerous phenomena which evolve as the flame approaches the wall. In addition, the description of the heat release rate is not always close to experimental results.

In order to develop a 0D flame-wall interaction model, some assumptions were made due to the limitations that 0D modeling imposes on spatial considerations. In the present study, flame-wall interaction is modeled as a new local wrinkling factor for the parts of the flame surface near the cylinder wall. The model considers the combustion chamber shape, including the sparkplug position and the flame surface that expands inside the combustion chamber.

3.9.1 Quenching of laminar flames

The analysis of quenching phenomena is much simpler for laminar than for turbulent flames. 0D laminar quenching results can nevertheless provide valuable information for the analysis of turbulent flames in SI engines. The most important quantity for flame quenching is the quenching distance (δ_Q), defined as the minimum distance between the flame and the wall. The characteristic dimensionless quenching number is the Péclet number ($Pe = \delta_Q/\delta_L$). When performing experimental measurements or numerical calculations on laminar flame quenching three configurations are used: head on quenching, side wall quenching and tube quenching. A graphical representation of these configurations is shown in Figure 3-8.

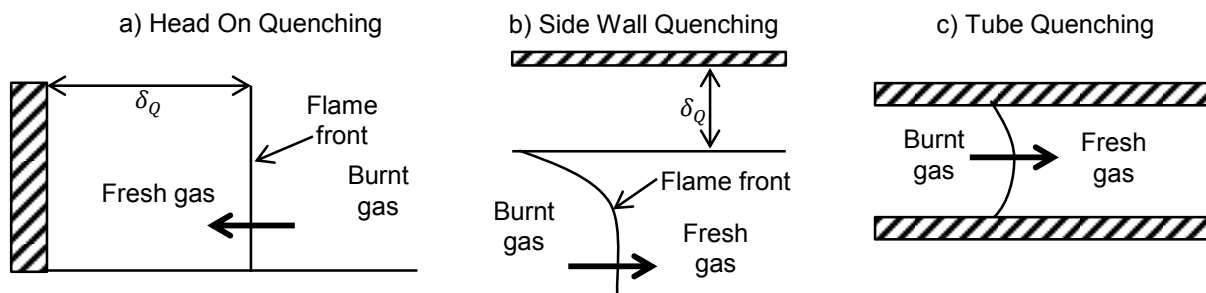


Figure 3-8: Configurations for flame wall interaction studies in laminar flows

Head on quenching (Figure 3-8.a) occurs when a flame impinges on a cold wall in the normal direction. This situation occurs in an SI combustion chamber when the flame front approaches the piston or the cylinder walls. When the flame distance becomes equal to or smaller than the quenching distance δ_Q , the flame globally extinguishes. The quenching distance is mostly controlled by the heat loss of the flame front [87]. This is an important parameter in SI combustion because it is the reason for massive flame quenching and a decrease in the heat release. A universal conclusion of experimental and numerical studies [87], [89], [91] is that the flame front suffers the impact of the wall before it arrives at the quenching distance (δ_Q). The heat released from the flame starts to decrease once the flame has passed a characteristic distance from the wall (δ_{inf}). For a distance greater than the wall

influence distance, the flame behaves as a fully developed turbulent flame and it is free from wall effects.

Side wall quenching (Figure 3-8.b) is only local. In an SI chamber it represents the flame which is in contact with the cylinder head whilst it propagates parallel to the wall. This phenomenon is of minor importance, as quenching is local and limited to the flame-wall contact region. Tube quenching (Figure 3-8.c) occurs when a flame quenches into a cylindrical configuration, if its diameter is sufficiently small. It represents the flame entering the cylinder-piston crevice volume in a SI engine. The limited level of accuracy of the geometric tool used in this work does not allow taking into account this situation, although crevice quenching is a substantial HC source at the exhaust.

3.9.2 Quenching of turbulent flames

Quenching of turbulent flames has many similarities with the quenching of laminar flames. As briefly described in the introduction, three main effects are involved in turbulent flame-wall interaction [91]: (i) The increased heat flux from the flame front towards the wall, which may cause local quenching; (ii) The confining effect of the combustion chamber geometry that creates obstacles to the turbulent flame thickness (flame brush); and (iii) the effect of a turbulent to laminar flow transition. The structure of the turbulent boundary layer is controlled by local viscous and highly dissipative effects. As a result, flame stretching (wrinkling) decreases and the flame area decreases, showing the importance of laminar flame-wall interaction configurations. In fact, they can be used to create a model that is valid for both kinds of flames.

In the 0D modeling approach implemented in this work, the controlling quantity of turbulent flame is the wrinkling factor (\mathcal{E}). When \mathcal{E} is greater than unity, the total flame surface increases. In our flame-wall interaction modeling approach the decrease in the heat release due to the wall will be attributed to the wrinkling factor, as it can describe this decrease in a global manner, regardless of any specific effect, as described in the previous section. This approach is consistent with the reduction in flame surface density (Σ) described in [91]. A schematic representation of the evolution of the wrinkling factor as the flame approaches the wall is shown in Figure 3-9. The flame is fully developed and it does not 'feel' the impact of the wall for a distance greater than the influence distance. The value of the wrinkling factor of a flame in this case is the global value given by equation (2-39). As the flame reaches the wall, its wrinkling is reduced. At some distance, the flame becomes laminar with $\mathcal{E} = 1$. Then, flame quenching continues until the flame reaches the quenching distance. Fractions of the laminar flame are eliminated and this is expressed by $\mathcal{E} < 1$. Beyond the quenching distance there is no flame. The part of the wrinkling factor (\mathcal{E}) between δ_Q and δ_{inf} constitutes an extinction function or a 'law of the wall' for flame-wall interaction. It must be specified that this law is not applied globally to the flame but is related to each flame fraction and its respective distance from the wall.

An algebraic formulation for the law of the wall must be derived for the law to be used in 0D modeling. Analysis of the properties of the flame at the quenching distance and at the influence distance requires that no flame exists at $\delta = \delta_Q$ and that flame wrinkling at δ_{inf} is equal to that of an unconstrained turbulent flame. Moreover, as shown in the experimental work by Foucher *et al.* [93], the slope (w) at $\delta = \delta_Q$ as well as the δ_{inf} value are quite con-

stant for various configurations. These results were used in our model, in order to set values for w and δ_{inf} . The influence distance is connected to the thickness of the turbulent flame and δ_{inf} changes with the turbulence of the flow. If a model for δ_{inf} is required, an expression which contains the laminar flame speed as well as the turbulent intensity can be used. An example of such an expression can be found in [94]. Thermal formulations were proposed in [88] to calculate δ_Q and they have been reported to agree with experimental measurements [95]. Given the comparison in [96], an experimental correlation [95] for the calculation of δ_Q as a function of cylinder pressure (p) was used here (equation (3-22)). Finally, the flame wrinkling is constant (and equal to the free flame wrinkling) for $\delta > \delta_{inf}$. These considerations are summarized in equation (3-23).

$$\delta_Q = 0.32 \cdot p^{-0.56} \quad (3-22)$$

$$\mathcal{E}(\delta_Q) = 0, \mathcal{E}(\delta_{inf}) = \mathcal{E}_{libre}, \mathcal{E}'(\delta_Q) = w, \mathcal{E}'(\delta_{inf}) = 0 \quad (3-23)$$

The law of the wall was defined based on the above analysis on flame wrinkling near the wall. In fact, a third order polynomial always satisfies the boundary conditions of equation (3-23). Typical values of δ_{inf} and w are 1.5 mm and $2 \cdot 10^{-4} \text{ m}^{-1}$. If we denote \mathcal{E}_w as the wrinkling factor near the wall, the form of the polynomial for $\delta_Q < \delta < \delta_{inf}$ is written (with δ being the distance from the wall):

$$\begin{aligned} \mathcal{E}_w(\delta) = w(\delta - \delta_Q) + \frac{3\mathcal{E} - 2(\delta_{inf} - \delta_Q)w}{(\delta_{inf} - \delta_Q)^2} (\delta - \delta_Q)^2 \\ + \frac{2(\delta_{inf} - \delta_Q)w - 2\mathcal{E}}{(\delta_{inf} - \delta_Q)^3} (\delta - \delta_Q)^3 \end{aligned} \quad (3-24)$$

3.9.3 Flame-wall interaction wrinkling for the entire flame

In the previous section a model of flame-wall interaction was proposed. The impact of head on quenching, which is the main configuration in SI combustion engines, was modeled in terms of a decrease in the heat release rate. At each time step, the mean flame surface has a spatially non-uniform distance from the wall (Figure 3-3). The final step for the 0D modeling of flame-wall interaction is to separate the flame into a number of small fractions (A_{fr}), calculate their distance from the wall and compute their wrinkling factor as a function of their distance from the wall.

A distribution of flame surface as a function of the distance from the wall was calculated by the tool presented in the section 3.6. The fractions, which have a distance $\delta > \delta_{inf}$, have a wrinkling factor equal to that of the free turbulent flame as calculated by equation (2-39). The fractions closer to the wall than δ_Q have no wrinkling (quenched flame). Finally the fractions within $\delta_Q < \delta < \delta_{inf}$ are assigned a wrinkling factor in agreement with their respective distances according to equation (3-24). The integral expression of the global wrinkling factor $\tilde{\mathcal{E}}$ is:

$$\tilde{\mathcal{E}} = \frac{1}{\delta_{inf}} \int_0^{\delta_{inf}} \mathcal{E}_w(\delta) A_{fr}(\delta) d\delta + \mathcal{E} A_{fr, \delta > \delta_{inf}} \quad (3-25)$$

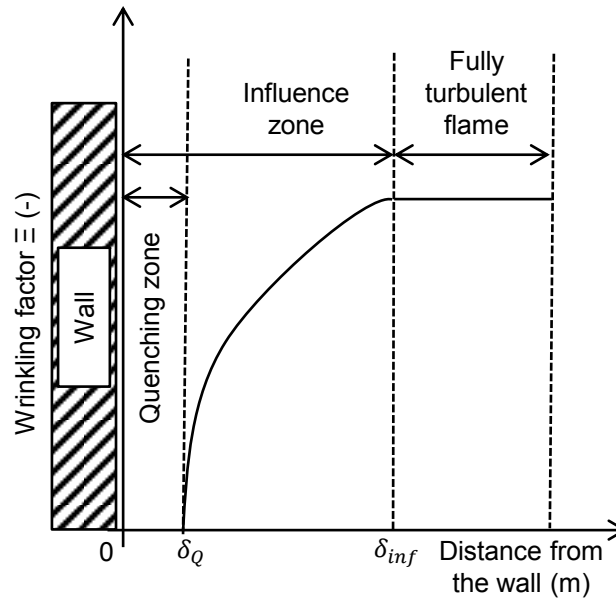


Figure 3-9: Schematic representation of the flame-wall interaction model. Impact of distance from the wall on the wrinkling factor of a flame fraction.

3.10 Validation of flame-wall interaction sub-model

3.10.1 Experimental setup

Experiments were carried out in single-cylinder SI engine characterized by a four-valve pent-roof chamber. Table 3-1 summarizes the main characteristics of the test engine. The engine was driven by an electric motor at a fixed engine speed, and equipped with an optical encoder mounted on the main shaft, giving a resolution of 0.1 crank angle degrees. A conventional sparkplug with an electrode space of 1 mm was used. A timer card ensured synchronization of the various trigger signals and data acquisition systems. The engine sucks in the air through a thermal mass flow-meter. The quantity of iso-octane was measured by using a 0-8 kg/h Brooks Quantim (QMBM) Coriolis mass flow meter. Before the intake pipe, the gases passed through a plenum volume, to avoid pressure oscillations inside the intake port. To provide a premixed fuel-air mixture inside the intake pipe, the liquid fuel was injected at inlet valve closure.

The cylinder pressure was recorded with a water-cooled AVL quartz pressure transducer connected to a charge amplifier at 0.1 deg resolution. Before the experiments, the transducer was calibrated with a Keller high pressure hydraulic calibrator. The absolute cylinder pressure was deduced by equalizing the in-cylinder pressure at 20 deg after inlet valve opening timing to the intake mean absolute pressure. 100 consecutive cycles of cylinder pressure data were acquired by a computer equipped with a National Instruments acquisition board.

The cylinder head is symmetric. Two sparkplug positions were tested, one centered in the cylinder head and the other shifted 14 mm from the cylinder head wall. In addition, two kinds of sparkplug were tested, a standard sparkplug and a 9.95 mm protruding tip sparkplug. Thus, for different engine operating conditions, two positions for the standard sparkplug and two positions for the protruding sparkplug were used. Several ignition timings were investi-

gated: for the centered position, the variation ranged from 25 to 41 degrees before TDC and in the lateral position, from 33 to 47 crank angle degrees before TDC with a 2 deg step between each operating point. The engine speed was 2000 rpm and the indicated mean effective pressure was about 5 bar. Figure 3-10 shows the cylinder head and the positions of the two sparkplug.

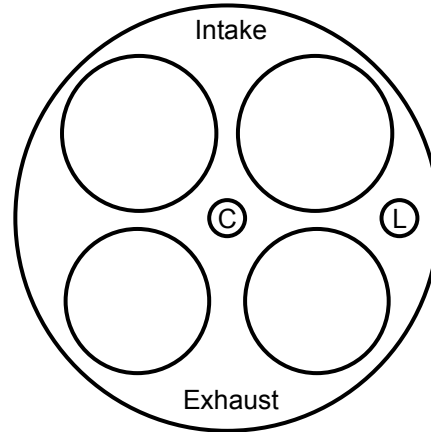


Figure 3-10: Cylinder head representation and sparkplug positions of test engine. The valve positions of the intake and exhaust sides are shown. Sparkplug positions are shown in circles with 'C' standing for centered and 'L' standing for lateral.

Table 3-1: Test engine characteristics for flame-wall interaction model validation

Bore (mm)	88
Stroke (mm)	80
Geometrical Compression Ratio (-)	9.5

3.10.2 Validation results

An overview of the quality of the model and of its predictive capacity is provided by observation of the distribution of the cumulative mean flame surface fraction during the combustion process. In Figure 3-11 and Figure 3-12, the distribution of the cumulative mean flame surface is given as a function of the crank angle for the centered (the spark advance angle is 31 crank angle degrees) and lateral position (the spark advance angle is 39 crank angle degrees) of the standard sparkplug. The maximum distance from the wall is limited to 1cm, in order to have a clear view of the situation near the walls. Figure 3-11 shows the distribution for the centered sparkplug position. During the flame development phase (ignition delay), 40% of the flame is up to 1 cm from the wall. At about -15 deg, the flame touches the wall and starts to propagate towards the cylinder walls. From this point, the wall-flame distance decreases. At 12 deg, the volume of burnt gases occupies 90% of the chamber volume. The whole flame is within 4 mm, since the cumulative flame fraction has reached unity. In the lateral sparkplug configuration, the flame follows a similar course to the flame of the centered sparkplug. It first touches the piston crown and then the cylinder head. The remaining flame crosses the chamber and reaches the opposite part of the cylinder liner much later (about 10 deg) than the centered sparkplug flame.

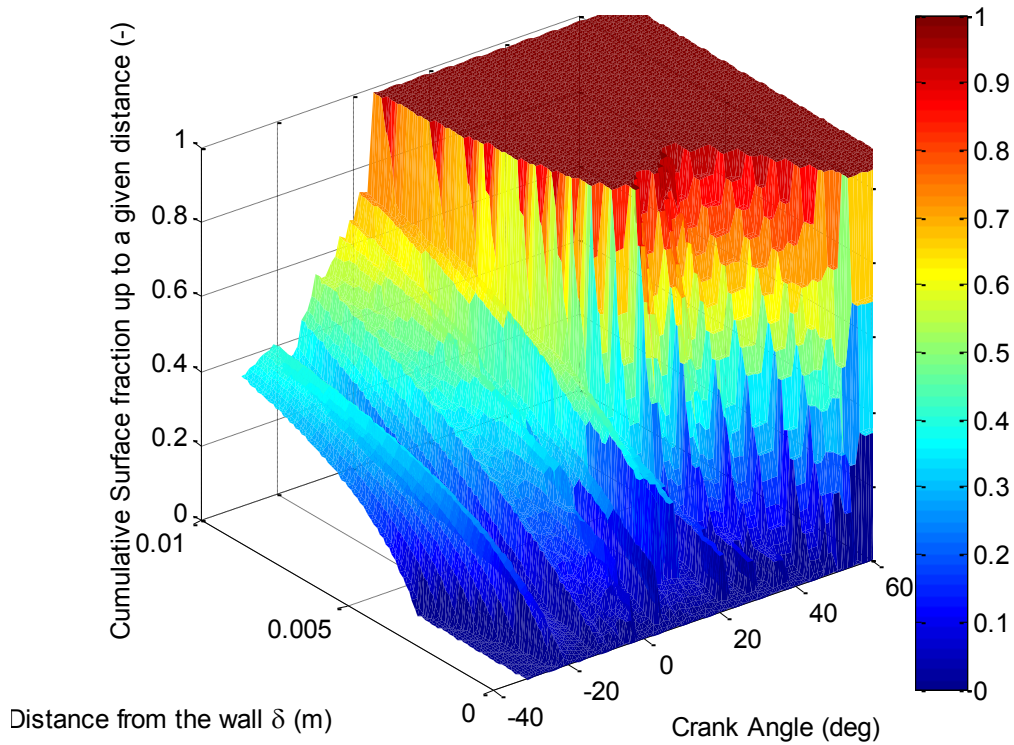


Figure 3-11: Flame surface fraction as a function of distance from the wall for various crank angles during combustion for central sparkplug position (standard length) (2000 RPM, IMEP: 5 bar, spark advance 31 deg)

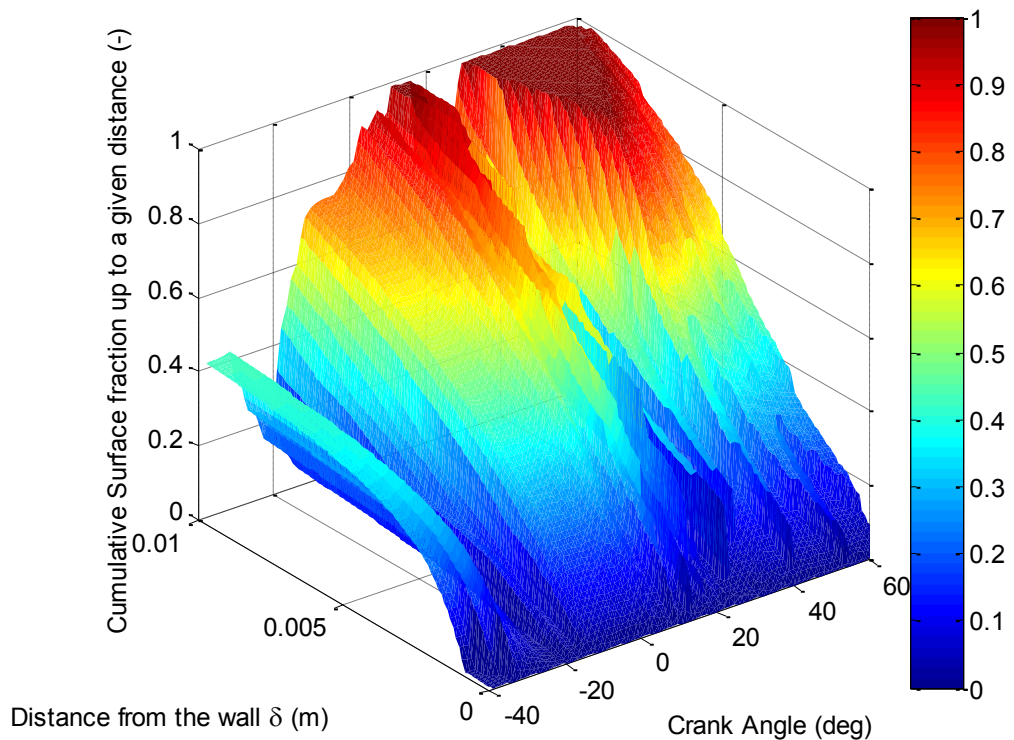


Figure 3-12: Flame surface fraction as a function of distance from the wall for various crank angles during combustion for lateral sparkplug position (standard length) (2000 RPM, IMEP: 5 bar, spark advance 39 deg)

When the flame front approaches the walls, it appears to stop as the piston descends (Figure 3-11). This abnormal behavior takes place between 10 to 30 crank angle degrees for

the centered sparkplug position and between 20 and 40 crank angle degrees for the lateral sparkplug position. The flames at those moments are very close to the wall (2 mm away for the centered sparkplug and 8 mm for the lateral sparkplug). This is in fact the result of a code artifact, which relies on the iterations to calculate the flame radius. At each time step, the burnt gas volume calculated by the two-zone thermodynamic model must be the same as the geometrical volume of the mean flame surface. The validity of the assumption of using a mean flame surface to describe the flame front during the very end of combustion (when the burnt gas volume has covered at least the 90% of the chamber) is questioned.

The Borghi-Peters diagram of premixed combustion can give qualitative information about the flame during the simulation. In order to assess the phenomenology of the structure of premixed flames as determined by their interaction with the turbulent flow field, the flames are positioned on the regime diagram of premixed turbulent combustion modes (Figure 3-13). In this diagram, initially postulated by Borghi [35] and later extended by Peters [36], the various modes of premixed turbulent combustion are identified by comparing turbulence and chemical characteristic time scales. Through chemical and flow phenomena, the nature and characteristics of combustion are revealed. All four flames (one for each sparkplug configuration) fall within the same dominant regime of 'corrugated flames'. The small differences are due to pressure changes, which affect the laminar flame speed s_L and the laminar flame thickness δ_L . In the 'corrugated flames' regime, the flame front is thin, has an inner structure close to that of a laminar flame and is wrinkled by turbulence motions. It is called the 'flamelet' regime. As the turbulent motion velocities, which are represented by the global turbulent intensity u' in our model, become larger than the flame speed s_L , turbulent motions become able to wrinkle the flame front up to flame front interactions, leading to the formation of pockets of fresh and burnt gases. This regime is identified as a 'thin flame regime with pockets' or 'corrugated flamelet regime' [17]. This description of combustion regimes is in accordance with the analysis of a set of Schlieren photographs illustrating the various stages of combustion in an SI engine, reported in [97]. The shape of the combustion chamber in [97] is similar to the shape of the test engine used in the present study and the sparkplug position is also lateral. As the main wrinkled flame front approaches the walls, combustion continues to take place through very thin flames. However, unburnt gas regions surrounded by a thin reaction zone of burnt gas exist. Although the existence of unburnt gas pockets in the burnt gases is not taken into account by the geometrical model, the mean flame surface may still be approximated by a spherical mean surface. The identification of the combustion regime through the Borghi-Peters diagram shows that the assumption of flamelet combustion is valid for typical operating points in SI engines and the use of a model with a mean flame surface and a wrinkling factor is also valid for all stages of combustion and for all four configurations tested.

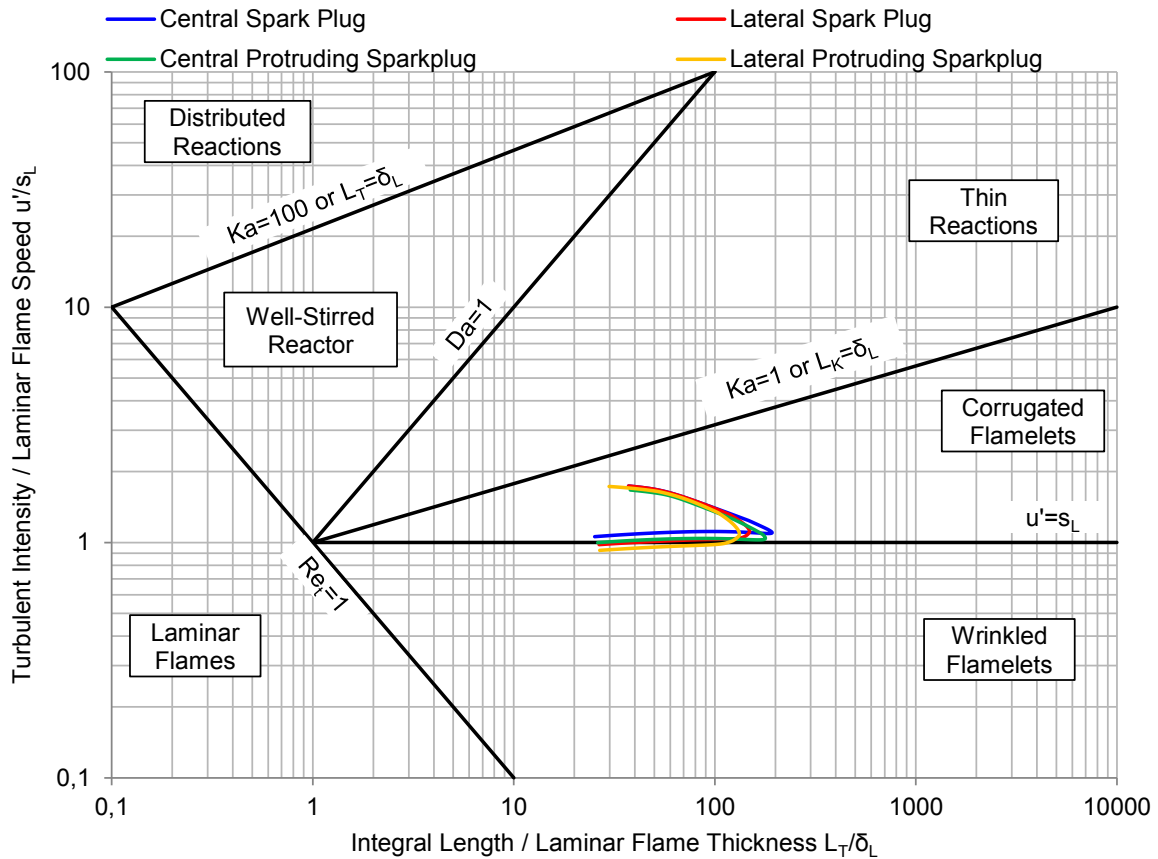


Figure 3-13: Borghi-Peters premixed combustion regime diagram for all four spark configurations. Centered standard sparkplug configuration is represented by the blue line and lateral standard sparkplug configuration by the red line. The respective positions of the protruding plug are represented by the green line and the orange line. The arrow indicates the direction of combustion evolution from spark ignition to extinction. The following dimensionless numbers appear: Karlovitz (Ka), Damköhler (Da), and turbulent Reynolds (Re_t)

The results of cylinder pressure for both centered and lateral normal sparkplug positions are shown in Figure 3-14 and Figure 3-15. The engine speed is 2000 rpm and the IMEP \sim 5 bar. The curves of measured pressure are compared with two simulations: one with the wall-flame interaction model and one without this model. A satisfactory matching of experiment and model for the compression phase is observed. The accurate description of the compression phase is important for the quality of the response of the combustion model with or without flame wall interaction. It was reported in [97] that the flame reaches the wall of the chamber at the crank angle of maximum pressure. This can also be observed on the two pressure figures. The deviation from the measured value observed for the maximum pressure of the case without the wall model is important, since it underlines the impact of the application of the flame wall interaction model. The correct evaluation of maximum cylinder pressure is crucial for many reasons and especially at full load when the engine is prone to knock. The expansion phase is not well predicted for the lateral sparkplug configuration in the case without flame-wall interaction. It has to be noted that the calibration coefficient of free flame wrinkling in equation (2-40), which is the sole coefficient of the combustion model, has not been readjusted for the simulation with wall-flame interaction. Nevertheless, the coefficient changes with the sparkplug position (it has different values for the central and for the lateral sparkplug position). This is expected, because the lateral sparkplug flame is not affected by turbulence in the same way as the central sparkplug flame.

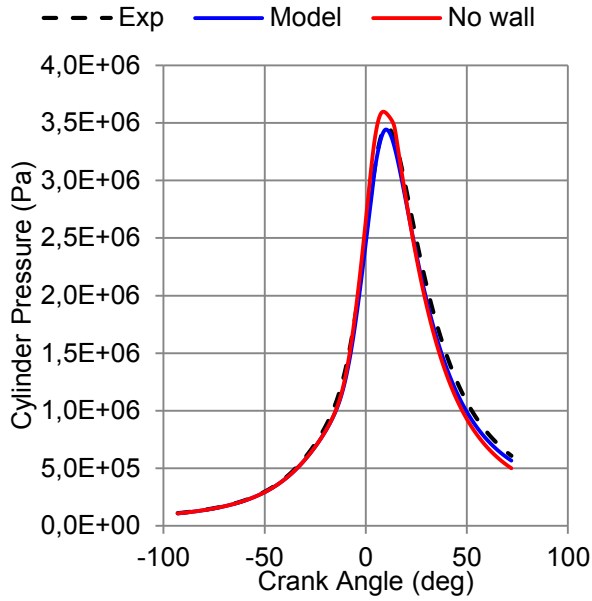


Figure 3-14: Cylinder pressure versus crank angle for centered sparkplug position (standard sparkplug)

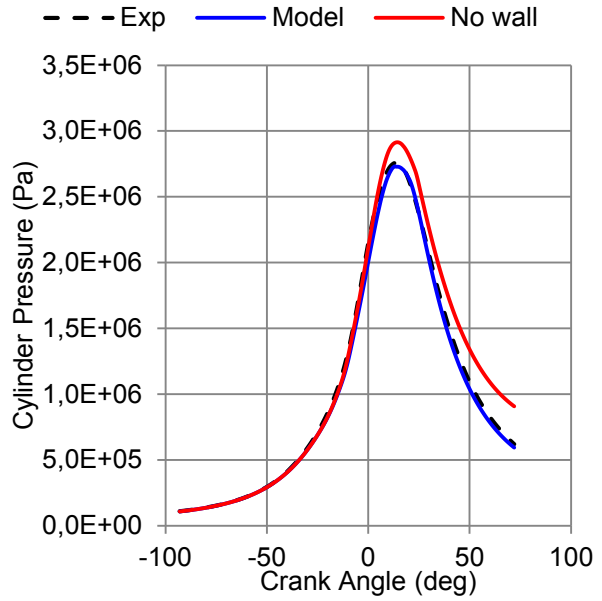


Figure 3-15: Cylinder pressure versus crank angle for lateral sparkplug position (standard sparkplug)

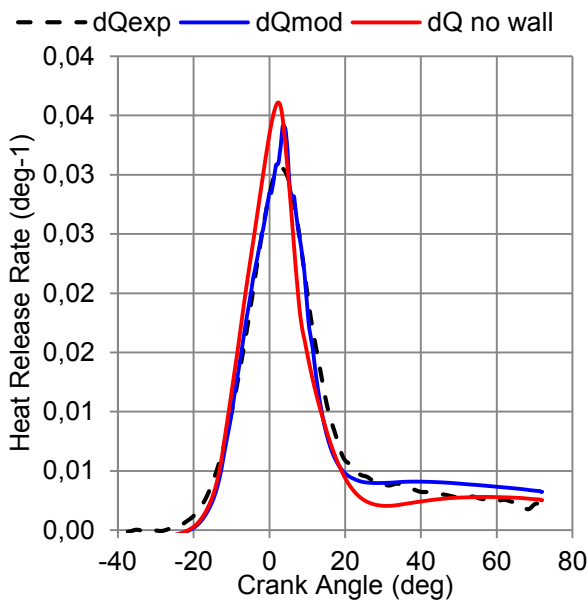


Figure 3-16: Heat Release Rate for centered sparkplug position (standard sparkplug)

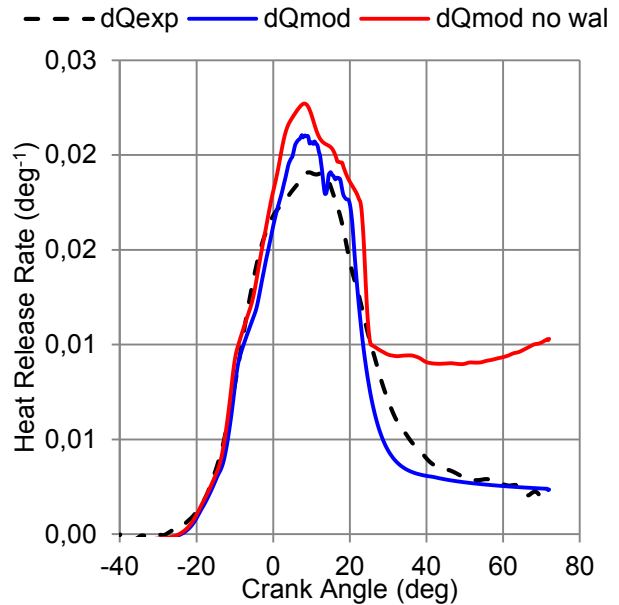


Figure 3-17: Heat Release Rate for lateral sparkplug position (standard sparkplug)

From the pressure figures, it is expected that the maximum of heat release rate will be different from the cases with and without flame wall interaction. Indeed, there is a slight difference in Figure 3-16 for the centered spark plug position and a greater one in the lateral position. The two characteristic distances of flame-wall interaction determine the magnitude of this heat release difference. If, for instance, the quenching distance δ_Q is higher, the impact on the wrinkling factor will also be higher. An example of such results may be found in [46]. The model without flame-wall interaction cannot manage the end of combustion in the lateral position (Figure 3-17): it gives an unphysical heat release rate after 20 degrees of crank angle. In the lateral sparkplug position, the flame front reaches the wall earlier than in the centered sparkplug position. For this reason, the influence of the flame-wall interaction model is

greater in the lateral sparkplug case. Higher heat transfer from the flame front to the wall would be needed in order to compensate for the elevated heat release and to ensure that the cylinder pressure is correct. Such a compensation would be artificial, since the heat transfer model was calibrated independently from the combustion model results. The proposed model takes into account the influence of geometry variations on flame-wall interaction in a predictive way.

The equilibrium wrinkling factor (\mathcal{E}_{equ}) of the centered sparkplug configuration (Figure 3-18) is higher than that of the lateral position (Figure 3-19). This was also observed in the calculated global wrinkling factor. In the wrinkling factor equation (2-39), the efficiency function Γ takes into account the influence of turbulence (the dominant factor). A more complete version of the efficiency function, proposed in [78], takes thermo-diffusive instabilities into account through the Lewis number. However, it is useful to note that even in the most updated efficiency function formulation the impact of flame stretch ($\kappa = \dot{A}/A$, where A is the flame surface) on the heat release rate during the first stage of the flame development phase is weak. During this phase, flame wrinkling is low since the flame is said to be laminar but flame stretching is maximal and modifies the laminar flame speed. The wrinkling factor starts to be affected by the wall after the flame development phase. During flame propagation, the impact of flame-wall interaction on wrinkling is small and becomes significant as the flame reaches the wall. For the central sparkplug position, after 20 crank angle degrees from ignition, 58% of the mean flame surface is found within 1 cm from the wall (Figure 3-11). This leads to a decrease of 10% in the flame wrinkling factor \mathcal{E} . This is consistent with the pressure and heat release results. The difference between the wall and no wall model depends on the value of δ_Q . The region of the impact is around the maximum cylinder pressure angle. When the flame is close enough to the walls, the wrinkling factor diminishes, as expected from the analysis of the cumulative mean flame surface distributions. It is also observed that for the respective wrinkling factors of the protruding spark configurations (Figure 3-20 and Figure 3-21), the flame kernel propagates freely (wall wrinkling is equal to free wrinkling) at the beginning of combustion due to the fact that the flame is further from the cylinder head. Apart from this observation, the protruding spark configurations show a similar behavior to the standard spark configurations.

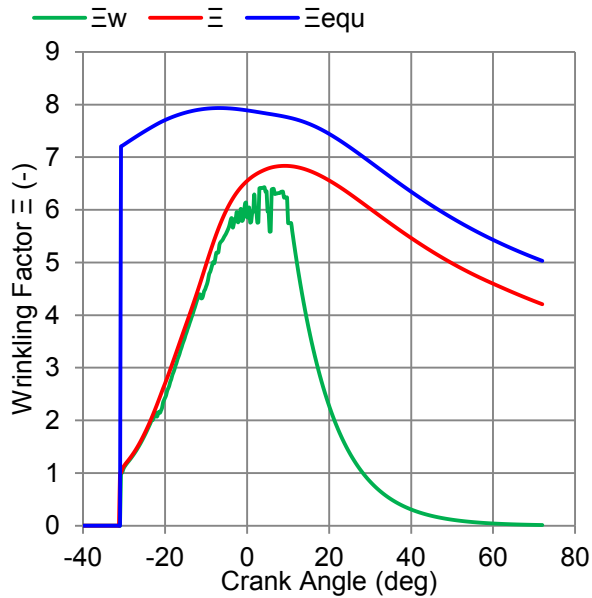


Figure 3-18: Wrinkling factors for central spark-plug position (standard sparkplug)

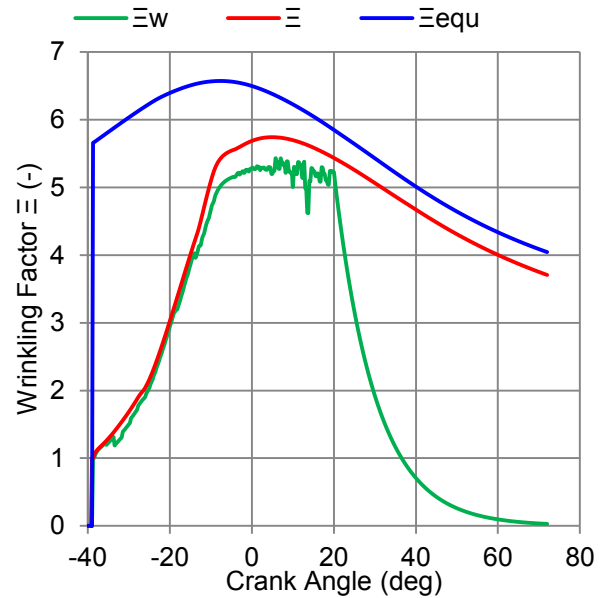


Figure 3-19: Wrinkling factors for lateral spark-plug position (standard sparkplug)

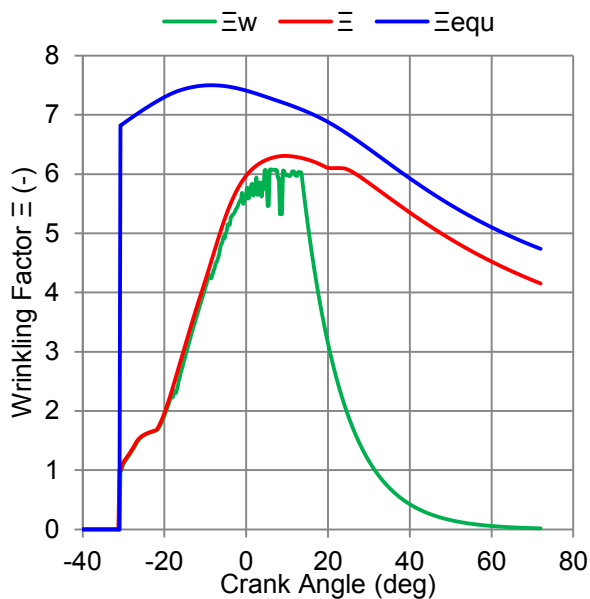


Figure 3-20: Wrinkling factors for central spark-plug position (projected spark)

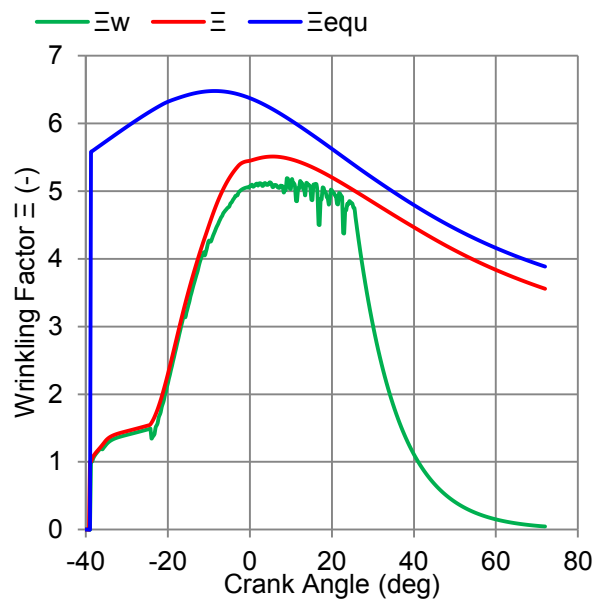


Figure 3-21: Wrinkling factors for lateral spark-plug position (projected spark)

3.11 Conclusion for the wall-flame interaction impact

In this section, a sub-model is conceived and added to the zero-dimensional combustion model. The sub-model describes the interaction of the flame front and the chamber wall as well as the quenching of the flame front. The basic configurations of flame quenching in laminar flames are also applicable in turbulent flames, which is the case in SI engines. A simplified geometric model was developed to calculate the mean flame surface, the flame volume and the distribution of flame surface as a function of the distance from the wall. In order to validate the predictive capacity of the model in terms of combustion chamber geometry, the flame-wall interaction takes into account the geometry of the combustion chamber and of the

flame, aerodynamic turbulence and the in-cylinder pressure and temperature conditions, through a phenomenological attenuation function. It calculates a modified global wrinkling factor as a function of the mean surface distance distribution from the wall. The impact of flame-wall interaction was simulated by varying the spark plug position and its length (four configurations were used). Results show that the position of the sparkplug has a greater influence than its length. The heat release rate is significantly altered in the lateral sparkplug case, when running the model with flame-wall interaction. In the case of the protruding spark plug, the impact of the wall on the initial flame kernel is delayed, since the flame is not close to the cylinder head. The maximum pressure is reduced when using the flame-wall interaction model for all four configurations. The attenuation of the wrinkling factor and of the mean flame surface at the end of combustion is captured by the model. The values measured for the four sparkplug positions configurations gave consistent results in terms of cylinder pressure and heat release.

3.12 Post flame reactions sub-model

3.12.1 Contribution of CO to the heat release rate

Chemical equilibrium does not usually occur during combustion in SI engines. This is due to lack of time, since the time scale of the engine cycle is smaller than the chemical scale of the major reactions. For example, some species like NO and CO, which are formed at high temperatures in burnt gases, are present in large amounts (greater than those of chemical equilibrium) during expansion. If the system were in an equilibrium state, their concentrations would be negligible. In fact, the equilibrium concentrations of these two species have “frozen” at a higher temperature and their evolution is kinetically controlled.

The non-negligible concentration of CO retains chemical energy that would be released if CO were in equilibrium state. Subsequently, it is necessary to model the concentration of CO controlled by kinetics and to find its impact on the heat release rate.

A simple chemical kinetics model was implemented here, in order to preserve the qualities (speed, simplicity) of the global 0D model. The most basic chemical equations, which control the kinetics of CO, according to [98], are the following (with k_f and k_b being the forward and backward rate constants):



A combination of equations (3-26) and 3-27 gives the total CO formation rate:

$$[\dot{CO}] = -k_{f,1}[CO][OH] + k_{b,1}[CO_2][H] + k_{f,2}[CO_2][O] - k_{b,2}[CO][O_2] \quad (3-28)$$

The parameters into brackets refer to molar concentration (mol/cm^3). In the following, the index ‘eq’ refers to equilibrium concentration. The species O, O_2 , OH, H and CO_2 are considered to be in partial equilibrium state, according to [14]. As a results, the CO formation rate can be expressed as [98], with $R_1 = k_{f,1}[CO]_{eq}[OH]_{eq} = k_{b,1}[CO_2]_{eq}[H]_{eq}$ and $R_2 = k_{f,2}[CO_2]_{eq}[O]_e = k_{b,2}[CO]_e[O_2]_{eq}$:

$$[\dot{CO}] = (R_1 + R_2) \left(1 - \frac{[CO]}{[CO]_{eq}} \right) \quad (3-29)$$

The reaction rate constants are described by Bowman [14]:

$$k_{f,1} \left[\frac{\text{cm}^3}{\text{mol} \cdot \text{sec}} \right] = 6.76 \cdot 10^{10} \exp \left(\frac{T_b}{1102} \right) \quad (3-30)$$

$$k_{f,2} \left[\frac{\text{cm}^3}{\text{mol} \cdot \text{sec}} \right] = 2.50 \cdot 10^{12} \exp \left(\frac{-24055}{T_b} \right)$$

Equation (3-29) can be equivalently written with mass fractions (Y) instead of mole concentrations:

$$\dot{Y}_{CO} = \frac{Y_{CO}^{eq} - Y_{CO}}{\tau_{CO}} \quad (3-31)$$

The characteristic kinetic time of CO (τ_{CO}) is:

$$\tau_{CO} = \frac{Y_{CO}^{eq}}{M_{CO}(R_1 + R_2)V} \quad (3-32)$$

where V is the chamber volume, and $M_{CO} = 28.01$ g/mol is the molar weight of CO. This time corresponds to a characteristic relaxation time for the Y_{CO} , which is not in equilibrium, to reach its equilibrium value Y_{CO}^{eq} . This time varies during the combustion phase, since it depends on the thermodynamic conditions. Equation (3-32) characterizes an exponential relaxation of the CO mass fraction, in accordance with the assumption made in [99]. It should be noted that τ_{CO} describes the behavior of the chemical kinetics scheme used. This approach is thus valid for schemes of varying complexity.

The two-zone thermodynamic model takes into account the energy contained in the equilibrium species, since the burnt gas zone contains several species (see section 3.3). However, it does not consider the energy retained by the CO kinetics. This loss of energy is introduced into the combustion model in the form of the second term of the right hand side in equation (3-19). It is useful to add this term during the late expansion stroke when the CO mass fraction starts to 'freeze', as shown in [63].

3.12.2 Contribution of HC to the heat release rate

The main causes of HC emissions in SI engines with well premixed and stoichiometric charge that have been proposed are [8]: (i) flame quenching when the flame approaches the wall, which leaves a layer of unburnt HC adjacent to the wall; (ii) incapacity of the flame to enter the crevice volumes; (iii) absorption and desorption in lubricant oil during intake and compression. All these mechanisms result in high HC concentrations adjacent to the walls.

As shown by experimental studies [8], quenching is a two-step process. The first step is extinction of the flame as described in the previous sections and the second step is the post-quench diffusion and oxidation of HC on a time scale of a few milliseconds after quenching. The diffusive-reactive mechanism decreases the mass of the initial quantity of HC due to quenching.

The impact of diffusion and oxidation on heat release can be shown by numerical analysis of the convective, diffusive and reactive phenomena, which occur during the expansion

stroke. Several studies [100]–[102] discussed the issue of unburnt HC based on numerical solutions of one-dimensional mass, species and energy conservation equations. The system considered in such studies consists of a layer of unburnt air-fuel mixture adjacent to the impermeable chamber wall maintained at a specified temperature. Since the engine bore is much larger than a typical unburnt hydrocarbon mixture layer, the diffusive-reactive process can be treated as a planar, one-dimensional configuration. A detailed explanation of the one-dimensional model is given in [100] with all its assumptions and equations.

The approach developed here consists in formulating an equivalent set of equations in the 0D domain, which contains the reactive-diffusive processes of the post oxidation phenomena. In our 0D model, the thermodynamics of the cylinder provides the burnt gas temperature as well as the fresh gas temperature. These two variables are uniform inside their respective zones. In addition, the aim of this effort is to take into account the post-oxidation of HC in the heat release rate.

The equation of species conservation in the one-dimensional modeling in [100] is:

$$\rho \left(\frac{\partial Y_i}{\partial t} + u \frac{\partial Y_i}{\partial x} \right) - \frac{\partial}{\partial x} \left(\rho D_i \frac{\partial Y_i}{\partial x} \right) - \dot{\omega}_i = 0 \quad (3-33)$$

where i is the species index, u is the flow velocity, x is the spatial dimension, D is the species diffusion coefficient and $\dot{\omega}$ is the reaction rate. From left to right one can read: the unsteady term, the convective term, the diffusive term and the reaction term. The flow in the region adjacent to the cylinder wall is highly viscous and diffusive phenomena are dominant (boundary layer). Consequently, the convective term can be neglected. This assumption is also validated by the results in [101]. The remaining terms are the chemical and the diffusion terms. A phenomenological analysis of the post oxidation phenomena revealed that the unburnt HC-air mixture diffuses from the cold boundary towards the burnt gases. This diffusion process results in an increase of the temperature of the mixture, until the local thermodynamic conditions for auto-ignition are reached.

The fuel consumption is controlled by a characteristic chemical time τ_{HC} , which can be defined as:

$$\dot{\omega}_{HC} = \rho \dot{Y}_{HC}^{ch} = -\rho \frac{Y_{HC}}{\tau_{HC}} \quad (3-34)$$

This characteristic time is short compared to the other characteristic time scales, so that the fuel is consumed very rapidly after auto-ignition. HC oxidation can be decomposed into two successive stages. Furthermore, if the chemical stage is fast in comparison with the mixing process of the fresh gases with the burnt gases, this mixing will control combustion.

The thermodynamic conditions as well as the physicochemical properties are considered uniform in the near-wall zone, which has a thickness δ_{HC} of only 0.2 mm, as proposed in [100]. As a result, a global species diffusion coefficient was used (D_{HC}). By taking into account the fact that the spatial variation of Y_{HC} is entirely controlled by diffusion and by adopting a change of variable $\xi = Y_{HC} - Y_{HC}^{ch}$, the conservation equation of HC is written:

$$\frac{\partial \xi}{\partial t} = D_{HC} \frac{\partial \xi}{\partial x^2} \quad (3-35)$$

This equation has an analytical solution in the form of separated variables:

$$\xi(\hat{x}, \hat{t}) = X(\hat{x})T(\hat{t}) \quad (3-36)$$

The dimensionless variables \hat{x} and \hat{t} appear:

$$\hat{x} = \frac{x}{\delta_{HC}}, \hat{t} = \frac{t}{\tau} \text{ with } \tau = \frac{\delta_{HC}^2}{D_{HC}} \quad (3-37)$$

The general form of $X(\hat{x})$ term is written:

$$X(\hat{x}) = A \cos(\sqrt{\lambda}\hat{x}) + B \sin(\sqrt{\lambda}\hat{x}) \quad (3-38)$$

The values of λ correspond to the eigenvalues of the Sturm-Liouville problem and the constants A and B are associated with the boundary conditions. The boundary conditions are as follows:

Mass flux is zero at the wall boundary:

$$X'(\hat{x} = 0) = 0 \quad (3-39)$$

If the fresh gases have diffused and reached the far-wall boundary, then they have been entirely consumed. The constants A and B can be calculated:

$$X(\hat{x} = 1) = 0 \quad (3-40)$$

These equations give:

$$X'(\hat{x} = 0) = 0 \rightarrow B\sqrt{\lambda} = 0 \rightarrow B = 0 \quad (3-41)$$

$$X(\hat{x} = 1) = 0 \rightarrow A \cos(\sqrt{\lambda}) = 0 \rightarrow \sqrt{\lambda} = \frac{\pi}{2}(2n - 1) \quad (3-42)$$

For each n , the solution is a function of all the eigenfunctions:

$$X_n(\hat{x}) = A_n \cos\left[\left(\frac{\pi}{2}(2n - 1)\hat{x}\right)\right] \quad (3-43)$$

The temporal term of the solution is of the form:

$$T_n(\hat{t}) = e^{-\lambda\hat{t}} = e^{-(2n-1)^2\frac{\pi^2}{4}\hat{t}} \quad (3-44)$$

Each function $\xi_n(\hat{x}, \hat{t})$ is a solution of equation (3-35) and is written:

$$\xi_n(\hat{x}, \hat{t}) = A_n \cos\left[\left(\frac{\pi}{2}(2n - 1)\hat{x}\right)\right] e^{-(2n-1)^2\frac{\pi^2}{4}\hat{t}} \quad (3-45)$$

In general, the $\xi_n(\hat{x}, \hat{t})$ functions do not verify the initial conditions individually. Consequently, the general solution is written as the sum of all elementary solutions:

$$\xi(\hat{x}, \hat{t}) = \sum_{n=1}^{\infty} \xi_n(\hat{x}, \hat{t}) \quad (3-46)$$

In this work, the region studied, i.e. the near-wall zone, can be considered as a thin system and a ‘‘lumped analysis’’ (spatial averaging) can be performed. The initial condition can be considered as homogeneous in the near wall zone. The initial value of the HC mass fraction comes from the combustion model. It is thus possible to respect the initial condition for a particular value of n ($n = 1$). The integration gives:

$$\int_0^1 \xi_1(\hat{x}, 0) d\hat{x} = \int_0^1 A_1 \cos\left(\frac{\pi}{2}\hat{x}\right) d\hat{x} = \langle Y_{HC}^0 \rangle \text{ with } A_1 = \frac{\pi}{2} \langle Y_{HC}^0 \rangle \quad (3-47)$$

By integrating in the studied domain for the temporal solution, we obtain:

$$\langle \xi(\hat{t}) \rangle = \int_0^1 \xi(\hat{x}, 0) d\hat{x} = \frac{\pi}{2} \langle Y_{HC}^0 \rangle e^{-\frac{\pi^2}{4} \hat{t}} \int_0^1 \cos\left(\frac{\pi}{2} \hat{x}\right) d\hat{x} = \langle Y_{HC}^0 \rangle e^{-\frac{\pi^2}{4} \hat{t}} \quad (3-48)$$

If the original variables $\hat{t} = \frac{D_{HC}}{\delta_{inf}^2} t$ and $\langle \xi \rangle = \langle Y_{HC} \rangle - Y_{HC}^{ch}$ are introduced, we obtain:

$$\langle Y_{HC} \rangle - Y_{HC}^{ch} = \langle Y_{HC}^0 \rangle \exp\left(-\frac{\pi^2 D_{HC}}{4 \delta_{HC}^2} t\right) \quad (3-49)$$

This expression can be written in differential form:

$$\langle \dot{Y}_{HC} \rangle = \frac{Y_{HC}^{ch} - \langle Y_{HC} \rangle}{\tau_{HC}} \quad (3-50)$$

with

$$\tau_{HC} = \frac{4 \delta_{HC}^2}{\pi^2 D_{HC}} \quad (3-51)$$

The characteristic time τ_{HC} corresponds to the relaxation time of the diffusion process. It represents the time necessary for the diffusion process to attain the favorable conditions for auto-ignition of the mixture. During the auto-ignition chemical process the fuel is consumed quasi-instantaneously.

For the chemical term Y_{HC}^{ch} a global HC kinetics equation from [103] was used:

$$\frac{d[HC]_{ch}}{dt} = -6.7 \cdot 10^{15} e^{\left(-\frac{18735}{T_u}\right)} X_{HC} X_{O_2} \left(\frac{p}{RT_u}\right) \quad (3-52)$$

The global fresh gas mixture diffusion coefficient D_{HC} was computed as described in [104]. The binary diffusion coefficients D_{jk} for the fresh gas species (fuel, CO₂, H₂O, O₂, N₂, H₂ and CO with $j, k = 1 \dots 7$) were calculated at a temperature equal to the fresh gas temperature (T_u), with the use of coefficients obtained after running the CHEMKIN™ Transport Package [105] for the fresh gas species. \bar{M} is the mean molar weight of the fresh gases.

$$D_{HC} = \frac{1 - Y_k}{\bar{M} \sum_{j \neq k}^7 X_j / D_{jk}} \quad (3-53)$$

3.13 Validation of post flame reactions sub-model

3.13.1 Experimental setup

Table 3-2: Test engine characteristics for post-flame model validation

Bore (mm)	72.2
Stroke (mm)	73.1
Connecting rod length (mm)	132
Geometric compression ratio	9.5

The facility used to acquire experimental data on CO and HC, was a single-cylinder test bed. This kind of experimental configuration enables tests for various technical definitions to be conducted more rapidly and at a lower cost than a test bed with a multi-cylinder engine. The characteristics of the test bed engine are presented in Table 3-2. A compressor was mounted on the intake section to simulate the operating points of a supercharged engine.

Coolant and oil temperature were monitored and regulated. Pressure sensors recorded the intake, exhaust and cylinder pressures. Emissions and Fuel-Air ratio were also monitored. These data are essential for the calculation of the burn rate, which was used to evaluate the response of each modeling approach.

For all the operating points, a typical gasoline fuel with 95 Research Octane Number (RON) and with a Lower Heating Value (LHV) of 43.12 MJ/kg was used. The equivalence ratio was 1. Data were acquired for the steady state operating points which are shown in Figure 3-22.

In addition to these tests, a special test of Air-Fuel ratio variation was conducted for the operating point with an engine speed of 1200 rpm and an IMEP of 3 bar.

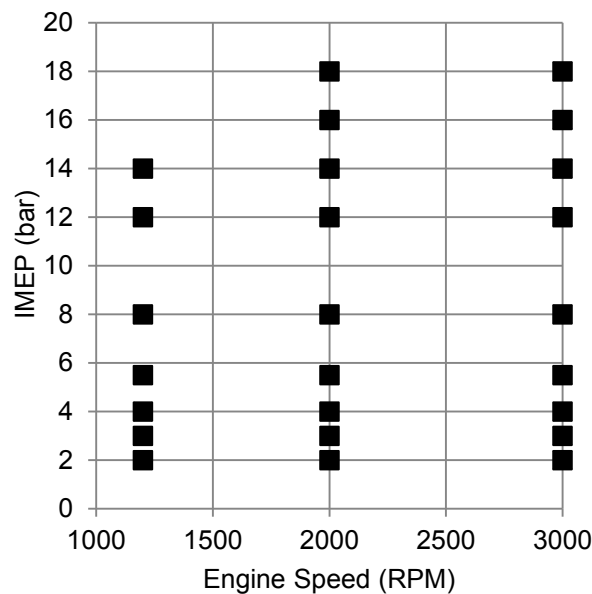


Figure 3-22: Available operating points from the test bed with Fuel-Air equivalence ratio $\phi=1.0$

3.13.2 Impact of CO on the heat release rate

To correctly assess the impact of CO on the heat release rate, a realistic CO emissions prediction is indispensable. In Figure 3-23 the results of the Air-Fuel ratio variation are presented. For all points there is an underestimation of the CO levels at the exhaust. The general behavior of the CO model is correct, since it predicts an increase in CO concentration with increasing Fuel-Air ratio. Indeed, when the Fuel-Air ratio increases, the available quantity of oxygen diminishes. The system is prone to incomplete combustion and CO creation cannot be avoided. In Figure 3-24 the characteristic kinetic reaction time of CO (equation (3-32)) is shown. With this expression, the chemical time of simple reactions was compared with the one calculated by complex chemistry tools as described in [99]. The characteristic time in [99] was calculated by tabulated chemical kinetics. With the approach proposed here, which is less complex and much less time consuming, the same description as with a complex chemistry of CO kinetics was obtained. However, this result does not occur for all operating points.

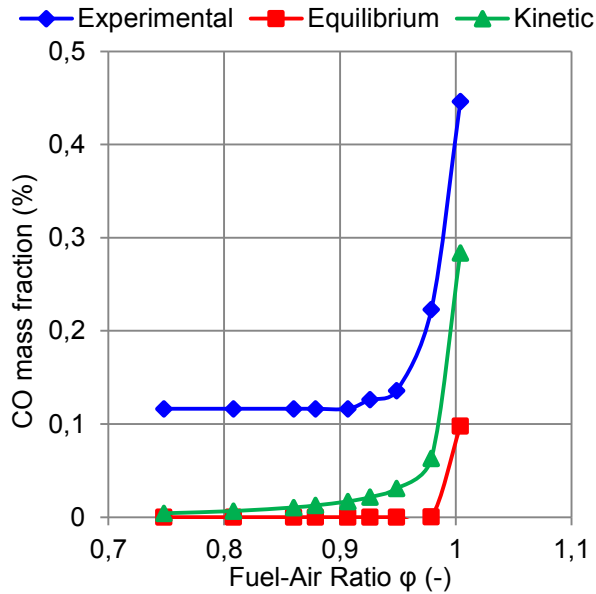


Figure 3-23: Model calculations for equilibrium and kinetic CO mass fraction along with experimental measurements from the test bed with varying Air-Fuel ratio. The values shown are at exhaust valve opening crank angle.

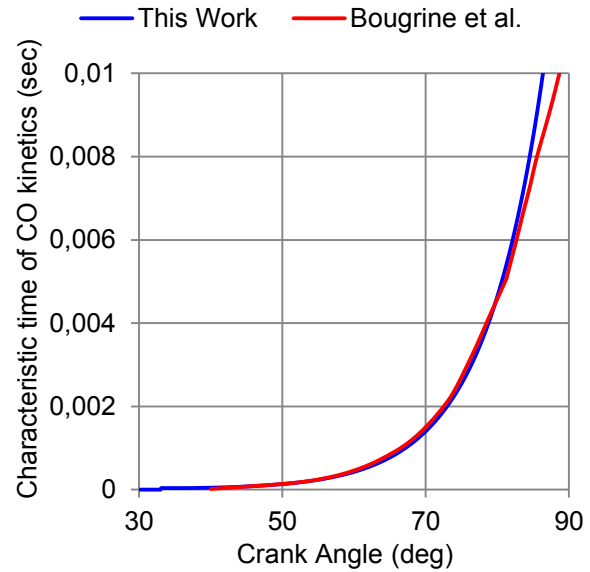


Figure 3-24: Characteristic time τ_{CO} of CO at 3000 rpm, IMEP 15bar and Fuel-Air equivalence ratio $\phi=1.0$. The 'Bougrine *et al.*' curve is from reference [99]

In Figure 3-25, the evolution of equilibrium and CO kinetics with crank angle can provide valuable information about the underestimation of the CO levels at the exhaust valve opening. During the first phase of combustion, the burnt gas temperature, which starts at the adiabatic flame temperature, increases and dissociation phenomena are enhanced. For these high temperatures, CO chemistry is quite fast and equilibrium is reached, as predicted by CO kinetics models, since both equilibrium and kinetic concentrations are essentially the same.

When the temperature decreases (2200 K for CO), τ_{CO} increases and the CO mass fraction begins to deviate from equilibrium. It can also be observed that the 'freezing' effect is naturally described by the present reduced chemistry model. At 1800 K, CO reactions become very slow and the change in CO mass fraction is negligible. This is a very important result, because the reduced chemistry reactions allow a physical description of the 'freezing' CO kinetics for low burnt gas temperatures. The existing amount of CO seems to be correctly oxidized in terms of crank angle evolution. A comparison of the CO emissions predicted by a simple model with a calibrated relaxation time and by a detailed tabulated chemistry model was reported in [99]. Unsurprisingly, the tabulated chemistry model predicted the accurate evolution of CO kinetics concentration. It also predicted a much higher maximum CO concentration during the cycle. However, the maximum CO concentration during the combustion cycle must be equal to the CO equilibrium concentration due to the high temperature, regardless of the modeling approach. Consequently, tabulated chemistry approaches calculate a much higher equilibrium concentration. As a result, when the burnt gases reach the characteristic temperature of 1800 K, the reactions freeze at a higher CO concentration and the results at the exhaust valve opening are closer to the measured values.

The underestimation of CO levels can be attributed to several causes. The closed valves simulation conducted in the present work does not take into account the scavenging phase nor any back flow phenomena. These phenomena impose temperature gradients in the

combustion chamber, which directly affect the reaction rates of unburnt HC, which may transform into CO when they react. For the closed valves period, the HC reactions are modeled (see section 3.12.2) but the remaining HC contribute only to the heat release rate. Neither the thermodynamic nor the chemical kinetics model take into account the intermediate reactions of partial burning of HC and the potential formation of CO when HC react. Burnt gas temperature stratification is a very important phenomenon and is not directly taken into account in this model. Multi-zone models have been used [106], [107] for NO predictions and it has been shown that three burnt zones were a good trade-off between computational time and accurate predictivity, since they contained most of the NO quantity. Since the slow kinetics of CO occurs in the whole volume of burnt gases, a similar multi-zone 0D approach could be a promising approach to a more accurate prediction of CO fractions. Another approach for the artificial creation of burnt gas temperature stratification may be the use of a presumed probability density function, enabling multi-zone effects to be recreated. The difficulty with this approach is to describe the physical evolution of the variance of the burnt gas temperature. This problem can be circumvented by an algebraic or even a fixed variance value. Such a solution was successfully adopted in [108] for lean natural gas premixed combustion applications.

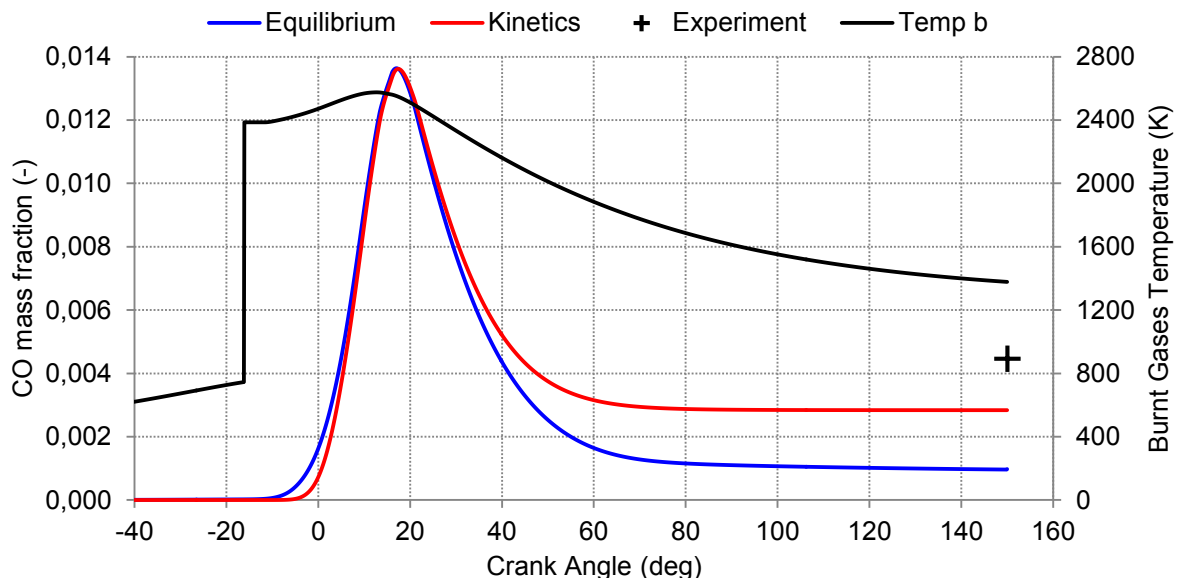


Figure 3-25: Evolution of equilibrium and kinetic CO mass fraction with crank angle along with burnt gas temperature. ‘Freezing’ of the CO reaction occurs at $T=1800\text{K}$. Operating point: Engine speed: 1200 rpm, IMEP: 3bar, Air-Fuel equivalence ratio $\varphi : 1.004$

In addition to the previous sources of error, another potential source could be that cycle-to-cycle variations are not modeled in this approach. The mean cycle, which we try to capture, may not correspond to the mean pollutant emissions. Although the engine stability (especially for the variation of Fuel-Air ratio) was satisfactory (3-5% standard deviation on IMEP), cyclic variations may be a cause of error for the CO concentration: RBG composition varies from cycle to cycle and it surely contains CO. In the thermodynamic model of this approach, the RBG composition is assumed to be that of the cold exhaust gas (CO_2 , H_2O , O_2 , N_2 , H_2 and CO). It will contain CO if and only if the global Fuel-Air ratio is in the rich region ($\varphi > 1$). Even if the quantity of RBG is correctly predicted by the implemented models, its composition in terms of CO may contain an error.

The impact of the remaining CO on the combustion efficiency at the end of combustion is important for rich mixtures, in which CO concentrations are high. The proposed model gives a fair quantitative prediction for the remaining CO mass fraction and the impact of CO (for a remaining 0.4% CO mass fraction, the impact on combustion inefficiency is 0.1%) on the heat release rate is calculated.

3.13.3 Impact of HC on the heat release rate

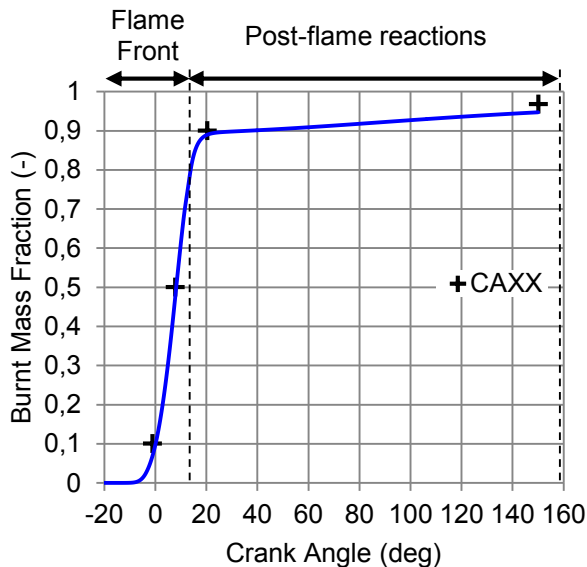


Figure 3-26: Burnt mass fraction as calculated by the model and the experimentally derived characteristic combustion angles CAXX (crosses at 10%, 50% and 90%). The last cross is the experimental combustion efficiency. The phases of flame front (rapid combustion) and of post flame reactions (slow combustion) are also depicted. Operating point: Engine Speed 2000 rpm, IMEP 8 bar, $\phi=1.0$.

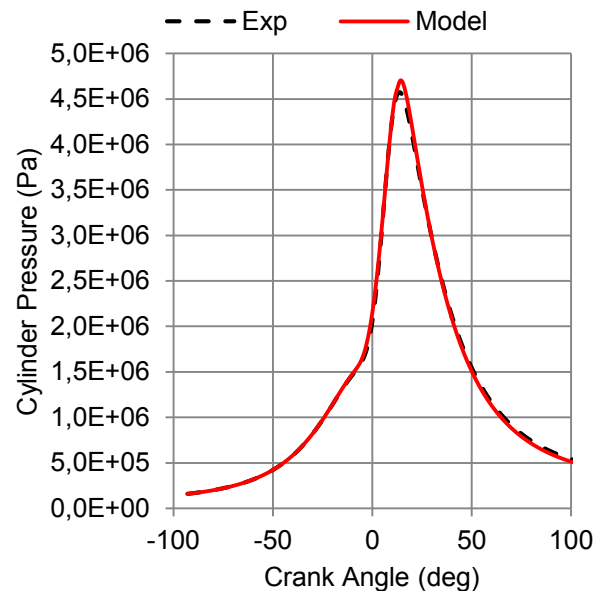


Figure 3-27: Measured and simulated cylinder pressure. Operating point: Engine Speed 2000 rpm, IMEP 8 bar, $\phi=1.0$.

The HC sub-model is activated as soon as the burnt gas volume reaches 90% of the total chamber volume, since the reactive-diffusive mechanism is activated when the flame is close enough to the wall. At this volume fraction, the flame radius R_f has passed the bore radius for all operating points and the percentage of the mean flame surface, which is within the influence zone of wall-flame interaction δ_{inf} , is near 90%. In Figure 3-26, two combustion phases can be distinguished. The first phase corresponds to the rapid propagation of the turbulent flame front. The second phase is characterized by a fuel consumption speed, which is much slower than the turbulent flame propagation speed, even if this speed is diminished by the wall-flame interaction model. This slow combustion phase corresponds to the post oxidation of unburnt HC and is described by the reaction/diffusion model in this work.

The HC model can quantify HC consumption during the expansion phase till the exhaust valve opening as well as the quantity of HCs that have not been consumed in terms of remaining fresh charge. The model correctly simulates the cylinder pressure for all the operating points investigated. Figure 3-27 shows a comparison between measured and simulated pressure for the operating point with engine speed at 2000 rpm and IMEP at 8 bar. In Figure 3-26 the simulated burnt mass fraction follows the trend of the experimentally derived one. The first three crosses represent the experimentally derived characteristic combustion an-

gles (CAXX) of 10%, 50% and 90% of burnt mass fraction. The calculated remaining fraction is 5.3% and the combustion inefficiency, based on HC and CO volume fractions measured at the exhaust is 3.2% (last cross in Figure 3-26). This difference was expected since the HC reactions continue after the exhaust valve opening. One limitation of this sub-model is that there is an uncertainty about the temperature used in the chemical equation as well as in the calculation of the species diffusivity. The chemical equation must be used for $850\text{ K} < T < 1250\text{ K}$, as reported in [103]. This is why the fresh gas temperature was used in this model. The temperature of the HC-air mixture, which diffuses into the burnt gases, corresponds neither to the burnt gas temperature nor to the fresh gas temperature. Ideally, a temperature distribution could have been used. Another drawback is the fact that it is not clear when the flame front reaction ceases to take place. In fact, there is certainly an overlap period during which minor flame front burn and reactive-diffusive HC processes coexist. The amount of fuel-air mixture which escapes the primary combustion mechanism and remains inside crevice volumes is not modeled. It is reported in [8] that the trapped charge in crevice volumes reenters the combustion chamber and also diffuses into the burnt gases and reacts. As a result, the addition of a crevice model could provide more unburnt mass in the HC sub-model during the expansion phase.

The capacity of the HC sub-model to capture the physics of the HC post-flame mechanisms can be assessed by comparing with the mass fractions of HC measured at the exhaust. No direct comparison was attempted, because the reactions after EVO are not modeled and the amount of HC in the RBG is not known. In Figure 3-28, the consumption of HC during the end of combustion in terms of mass fraction is shown for all the operating points, while Figure 3-29 depicts the HC mass fraction measured at the exhaust. The trends of the experimental results are correctly reproduced by the response of the physical HC model. For operating points near the low load region (2-4 bar), a low consumption of HC is predicted by the model, which leads to a high mass fraction at the exhaust. The same remark applies to the region of full load points (14-18 bar). For medium load points, the HC sub-model predicts a high consumption, which is also validated by the experimental measurements (low values at the exhaust). Both figures show an increase in HC consumption with increasing engine speed.

These two trends can be explained by the pressure and temperature conditions during the engine cycle. Pressure and temperature in the combustion chamber increase with engine speed. This has a direct impact on the chemical equation of the HC sub-model and the reactions are accelerated. Consequently, HC consumption increases with increasing engine speed. At low loads, the RBG fraction is high and the laminar flame speed is low. Combustion is slow and the pressure and temperature are low. HC reactions are not favored. For high loads, the heat transfers are high and late ignition, in order to avoid knocking, does not permit very high pressure and temperature to enhance HC reactions. The most favorable cases for low HC emissions can be found in medium loads when ignition starts early enough and heat transfers are moderate.

To sum up, the HC emissions are due to several phenomena. For a well-mixed, stoichiometric charge all these phenomena create HC adjacent to the walls or trapped in crevice volumes. The addition of the amount of HC which enters the crevice volumes during compression and reenters the bulk gas at the expansion stroke would be an improvement to the HC post-flame reactions. Our model helps in modeling these reactions in the bulk gas.

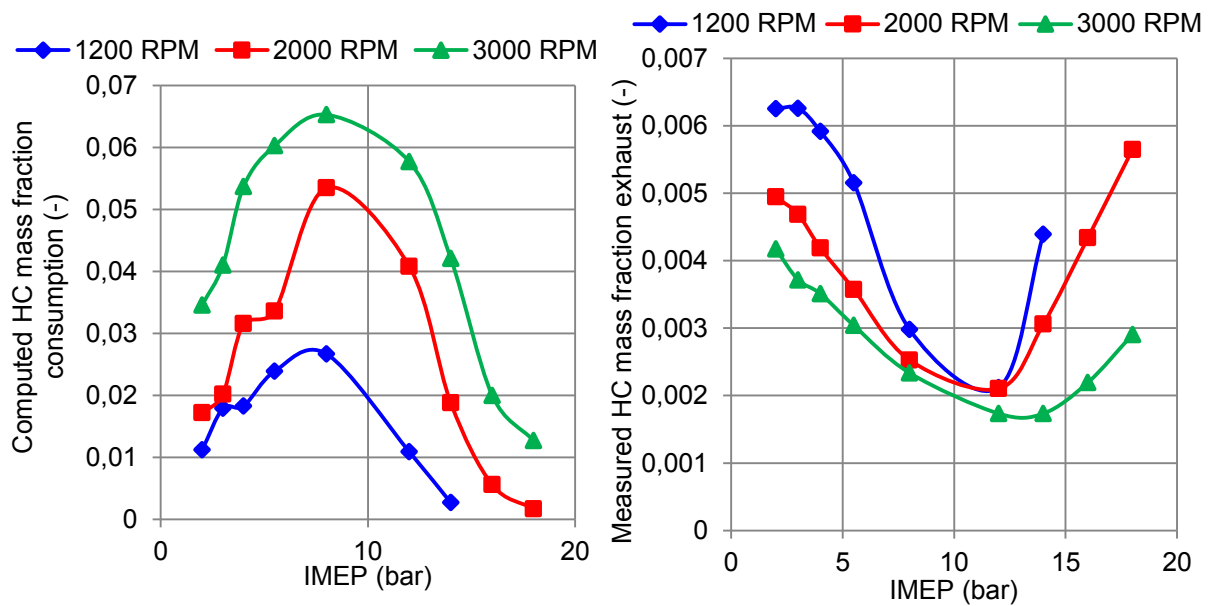


Figure 3-28: HC mass fraction consumed during the last stage of combustion as calculated by the HC sub-model. Air-Fuel ratio is constant ($\phi=1.0$) for all operating points.

Figure 3-29: HC mass fraction from measurements at the exhaust. Air-Fuel ratio is constant ($\phi=1.0$) for all operating points.

3.14 Conclusion for the post-flame reactions

A sub-model for the post flame reactions (CO and HC), based on equilibrium chemistry, reduced chemical kinetics and diffusion phenomena is proposed. The CO sub-model uses reduced chemistry equations in order to calculate the kinetic evolution of CO during the expansion phase. The model predicts a characteristic time of CO kinetics comparable to complex chemistry results, while it has the advantages of speed and simplicity. For high temperature values (2200 K) CO controlled by kinetics and equilibrium CO are almost equal. The 'freezing' temperature of 1800 K is captured, even if the adopted chemistry is reduced. Although the predicted CO values at the exhaust are consistently underestimated for the cases studied, the model has shown its capacity to reproduce the trends of CO kinetics. It has also been shown that an improved prediction of CO emissions requires a more accurate calculation of equilibrium values. The post-flame oxidation of unburnt HC is governed by a reaction/diffusion phenomenon. The approach developed here consists in decomposing the two processes and in introducing a relaxation time, which represents the time necessary for the mixture to reach auto-ignition conditions. HC reactions are dominant during the very late stage of combustion after the burning of 90% of the charge. Consistent results are found in light of the measured values for a variety of engine operating points. This modeling approach allows a more physical description of the near-wall post-flame reactions and their contribution to the total heat release rate, while remaining quick in terms of computational time and simple in terms of modeling theory.

3.15 Impact of flame stretch

In a previous study [74], the impact of the engine speed on the stretch rate levels and the dependence of different mixtures (air with isooctane, propane and methane at different

fuel/air equivalence ratios) to those stretch levels were studied. It has been shown that the flame stretch sensitivities observed in the laminar regime directly impact the combustion process inside the engine. In order to validate those results, the accurate study of the local flame has been performed and the results can be found in [76]. Different lean mixtures presenting almost the same unstretched laminar burning speed were selected. Those mixtures present also different Lewis numbers which is a relevant parameter to describe thermo-diffusive instabilities as well as flame stretch interactions. Global flame wrinkling and local flame curvature were also studied.

The 0D combustion model is enhanced with a sub-model for the stretch of the laminar flame. The mean flame surface is considered to be a sphere, which intersects with the chamber wall. The model calculates a flame radius as well as a flame wrinkling factor and is coupled with a two-zone thermodynamic model. The aim of this section is to reproduce the previously referred experimental results [74] through 0D modeling, clarify in which combustion stage flame stretching is important, reveal in which way the stretched laminar burning speed must be taken into account in SI combustion models.

The laminar flame speed has been calculated with the equation (2-25) for isooctane and propane, with the following constants:

Table 3-3: Constant for laminar flame correlation of isooctane and propane [24]

	Isooc- tane	Pro- pane
B_m (m/s ec)	0.263	0.342
B_φ (m/s ec)	-1.387	-0.847
φ_0 (-)	1.13	1.08
α (-)	2.18 - 0.8($\varphi - 1$)	
β (-)	-0.16 + 0.22($\varphi - 1$)	

For methane, a calculation as simple as equation (2-25) does not adequately correlate the laminar burning speed data over the range of pressure and temperature relevant to engines, as it is reported in [8]. However laminar burning speed data from a spherical constant volume bomb experiment are obtained along an unburnt gas isentropic path, as the pressure in the bomb rises during combustion. Variation in laminar burning speed with a power law [8]:

$$s_L^0 = s_{L,CH_4}^{00} \left(\frac{\rho_u}{\rho_0} \right)^\varepsilon, s_{L,CH_4}^{00} = 0.3 \text{ m/sec}, \varepsilon = 0.4 \quad (1)$$

The stretched laminar flame speed can be calculated with the aid of the Markstein (Ma) number, of the flame stretch (κ) and of the dimensional laminar flame thickness (δ_L^0), as it is proposed in [77]. This laminar flame thickness is equal to the thermal diffusivity of the fresh gases divided by the unstretched laminar flame speed (equation (2-3)).

$$\kappa = \frac{2}{R_f} \quad (3-54)$$

$$s_L = s_L^0 (1 - Ma \cdot \delta_L^0 \cdot \kappa) \quad (3-55)$$

The strain rate is reported to have a minor contribution on the modification of burning speed in comparison with the mean curvature [77]. According to Bechtold and Matalon [109], the Markstein number (Ma) can be calculated as follows:

$$Ma = \alpha - (\sigma - 1) \frac{\gamma_1}{\sigma} \quad (3-56)$$

With

$$\alpha = \gamma_1 + 0.5Ze(Le - 1)\gamma_2 \quad (3-57)$$

$$\gamma_1 = \frac{2\sigma}{\sqrt{\sigma} + 1} \quad (3-58)$$

$$\gamma_2 = \frac{4}{\sigma - 1} \{ \sqrt{\sigma} - 1 - \ln[0.5(\sqrt{\sigma} + 1)] \} \quad (3-59)$$

The Zeldovitch number Ze is calculated following [110], with T_0 defined in [111] and

$$Ze = 4 \frac{T_b - T_u}{T_b - T_0} \quad (3-60)$$

$$T_0 = - \frac{E}{\ln \frac{p}{B}} \quad (3-61)$$

The constants (E and B) have been taken from [110] and their values are shown in Table 3-4 :

Table 3-4: Constants (taken from [110]) for the calculation of T_0 temperature for all three fuels

	Isooctane	Propane	Methane
$E(K)$	20906	17223.5	23873
$B(\text{bar})$	$3.8 \cdot 10^7$	$2.2501 \cdot 10^6$	$3.1557 \cdot 10^8$

3.16 Validation of flame stretch sub-model

3.16.1 Experimental setup for flame stretch impact

The results obtained from the 0D model are compared to experimental results obtained in [4]. The experimental set-up has been fully described in several references [74], [76], [85], [93]. Optical Engine specifications are summarized in Table 3-5. In [4], experimental results were deduced from images obtained with Mie-Scattering Tomography. The 0.5mm laser sheet was created through the cylinder head thanks to a Nd:YAG laser with a 12.5 kHz frequency. Images were recorded through the piston thanks to a Photron SA5 high speed camera synchronized with the laser.

Table 3-5: Test engine characteristics for the validation of stretch model

Displaced volume (cm^3)	499
Bore (mm)	88
Stroke (mm)	82
Connecting rod length (mm)	127
Geometric compression ratio	9.5

Number of valves	4
Spark advance (crank angle degrees before TDC)	30

3.16.2 Validation results for flame stretch impact

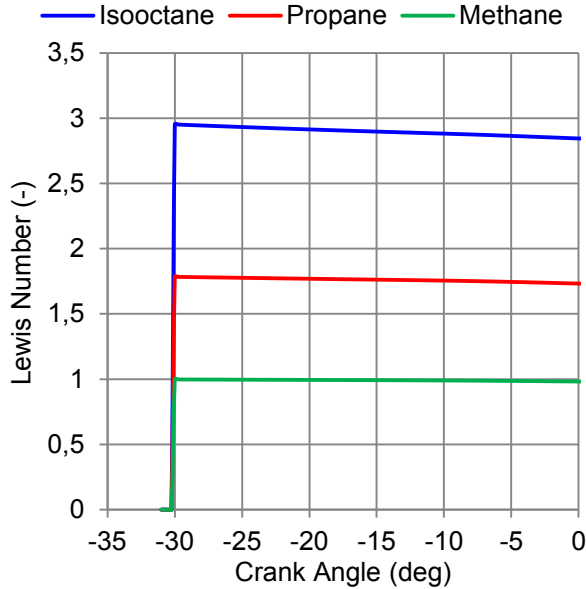


Figure 3-30: Lewis number during the combustion phase for all three fuels.

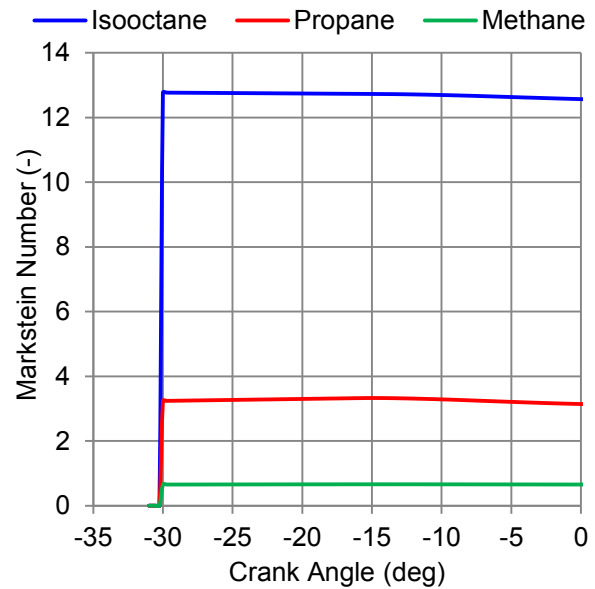


Figure 3-31: Markstein number during the combustion phase for all three fuels.

A basic validation of the simulations consists in calculating the characteristic non-dimensional numbers of combustion, check whether they agree with already published results and to explore their evolutions during the engine cycle, during which pressure and temperature evolve. In Figure 3-30, the Lewis numbers for all three fuels have been plotted during the combustion cycle. They remain almost constant during combustion and their values match with the ones calculated by CHEMKIN at 6.1 Bar and 565.5 K (0.99, 1.82 and 2.85 for methane, propane and isooctane respectively) in the publication with the experimental results for the three fuels [76]. The Markstein number results for all three fuels are shown in Figure 3-31. Following the trend for the Lewis number, the Markstein number remains quasi-constant during the combustion process. The values of the Markstein number for all three fuels are in agreement with the derived values in [76] (0.6, 3.0 and 12.8 for methane, propane and isooctane respectively). The consistency of the calculated Markstein and Lewis number as well as the fact that they remain quasi constant during the cycle allows continuing to the physical interpretation of the simulated results.

The results of the model for the laminar burning speeds of three fuels (equation 3-55) are presented in Figure 3-32. The presented unstretched laminar burning speeds have been calculated with the adopted correlations in section 2.5 (dashed line). The values of unstretched laminar burning speed, which have been calculated by the use of CHEMKIN™ and they have already been presented in [76], are superposed in the figure. The unstretched laminar burning speed is indeed almost identical for all three fuels no matter how it was computed (correlation or CHEMKIN™). It varies from 0.45 to 0.7 m/sec for the first crank angle degrees of combustion. The values of the correlations are sufficiently close to the experimental results. This confirms that the correlation of unstretched laminar flame is valid for the three fuels. Discrepancies for the laminar burning speed are observed between the

CHEMKIN and the correlations results. A discussion on the quality of the correlation or of the CHEMKIN results would not be pertinent, since the objective of Figure 3-32 is to prove that the unstretched laminar burning speed is almost similar for the three fuels regardless of the way of its calculation.

The stretched laminar burning speed for the three fuels is smaller than the unstretched laminar burning speed. This observation was expected since the Markstein numbers for all fuels are positive. On spark ignition, the stretched laminar burning speed is diminished by 40% for the isooctane, 13% for propane and 2% for methane. Therefore, isooctane is much more sensitive to flame stretching than propane and methane.

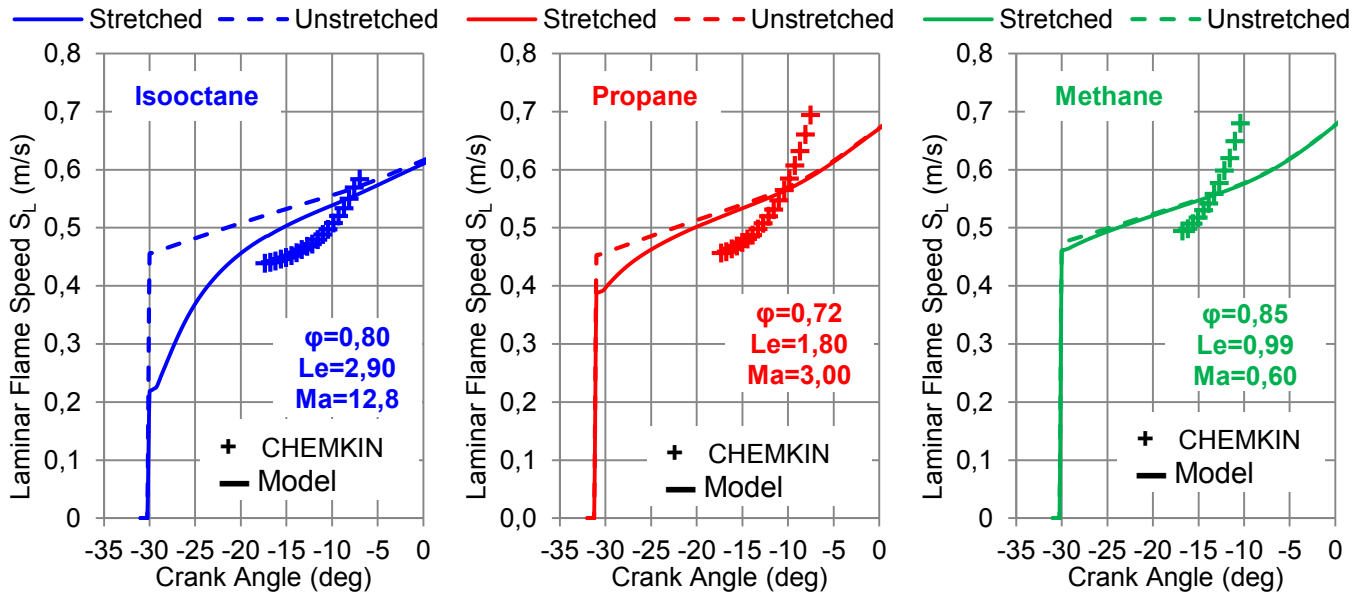


Figure 3-32: Stretched (s_L) and unstretched (s_L^0) laminar flame speeds after spark ignition along with calculated values (+) with CHEMKIN™ for the experimental pressure and temperature conditions. The calculated values have already appeared in [76].

Another important observation is that for all fuels the impact of flame stretch is dominant at the beginning of combustion. The fact that the flame stretch is preponderant during the beginning of a premixed expanding spherical flame is expected, since it is inversely proportional to the flame radius, as it is shown in [17] for laminar premixed spherically expanding flames. As a consequence of the laminar and highly stretched flame, the modeling of the stretched laminar burning speed is important to predict with more accuracy the beginning of combustion.

The tracing of the combustion regime of the turbulent flame of each fuel mixture will provide valuable insight on the discussion of flame wrinkling and stretch. Turbulence characteristics (turbulent intensity u' and integral length scale L_T) are the same for all three fuels. This assumption is based on the fact that the turbulent charge motion is fuel independent and it rather depends on the geometrical characteristics of the combustion chamber and of the intake duct [8]. The laminar burning speed, used for the determination of the combustion regime, is the unstretched laminar burning speed. Examples of its use can be found in [35], [36].

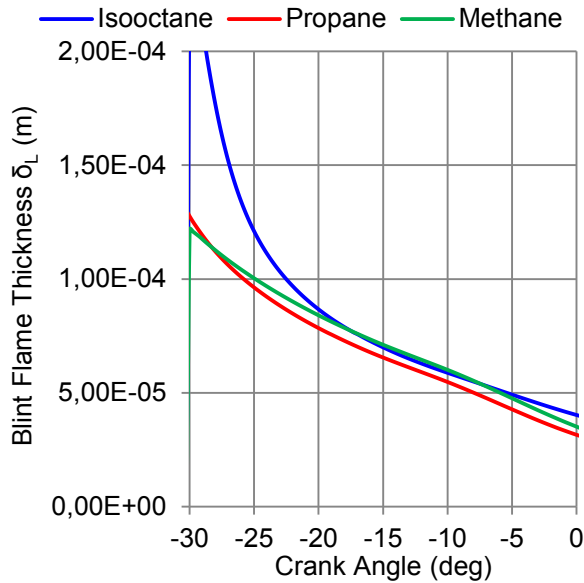


Figure 3-33: Laminar flame thickness calculated with Blint's correlation [21].

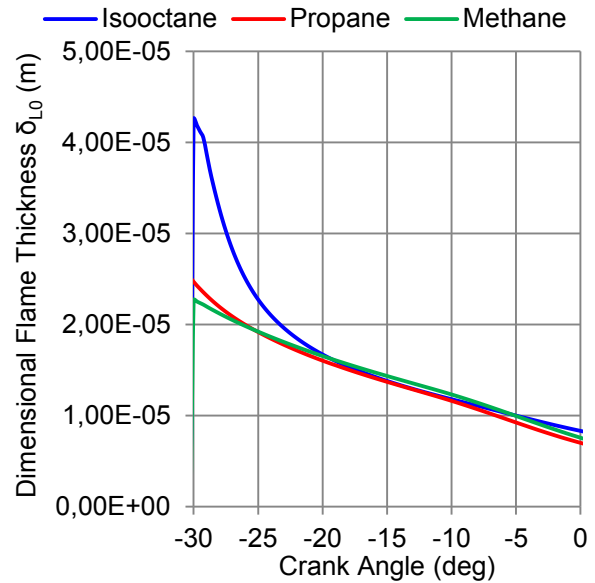


Figure 3-34: Diffusive laminar flame thickness.

As it has already been shown, the selection of the mixtures has been intentionally fixed to ensure identical unstretched laminar burning speed is the same for all three fuels. Therefore, the laminar flame characteristic which will change is the flame thickness. The laminar flame thickness for all three fuels is shown in Figure 3-33 (equation (2-4)) and in Figure 3-34 (equation (2-3)). The main observation in those figures is that propane and methane have almost the same laminar flame thickness. This is explained by the fact that the thermal diffusivities of both fuels are really close. On the contrary, the flame thickness of isooctane is 40% greater than the other two fuels. This difference will have an impact on the efficiency function and on the flame wrinkling. However, the laminar flame thickness is sufficiently small, in order that all turbulent scales are able to wrinkle the flame front. Consequently, it is expected that the flame thickness difference of isooctane will have a minor effect on the flame wrinkling.

The Borghi-Peters diagram of premixed combustion may provide qualitative information about the flame during the simulation. In order to assess the phenomenology of the structure of premixed flames as determined by their interaction with the turbulent flow field, these are positioned on the regime diagram of premixed turbulent combustion modes (Figure 3-35). In this diagram, initially postulated by Borghi [35] and later extended by Peters [36], the various modes of premixed turbulent combustion are identified, by comparing turbulence and chemical characteristic time scales. Through chemical and flow phenomena, the nature and characteristics of combustion are revealed. All three fuel mixtures are found in the same combustion regimes of "thin flames" and "corrugated flames". Propane and methane mixtures show an almost identical combustion regime and it can be expected that their wrinkling will also be similar.

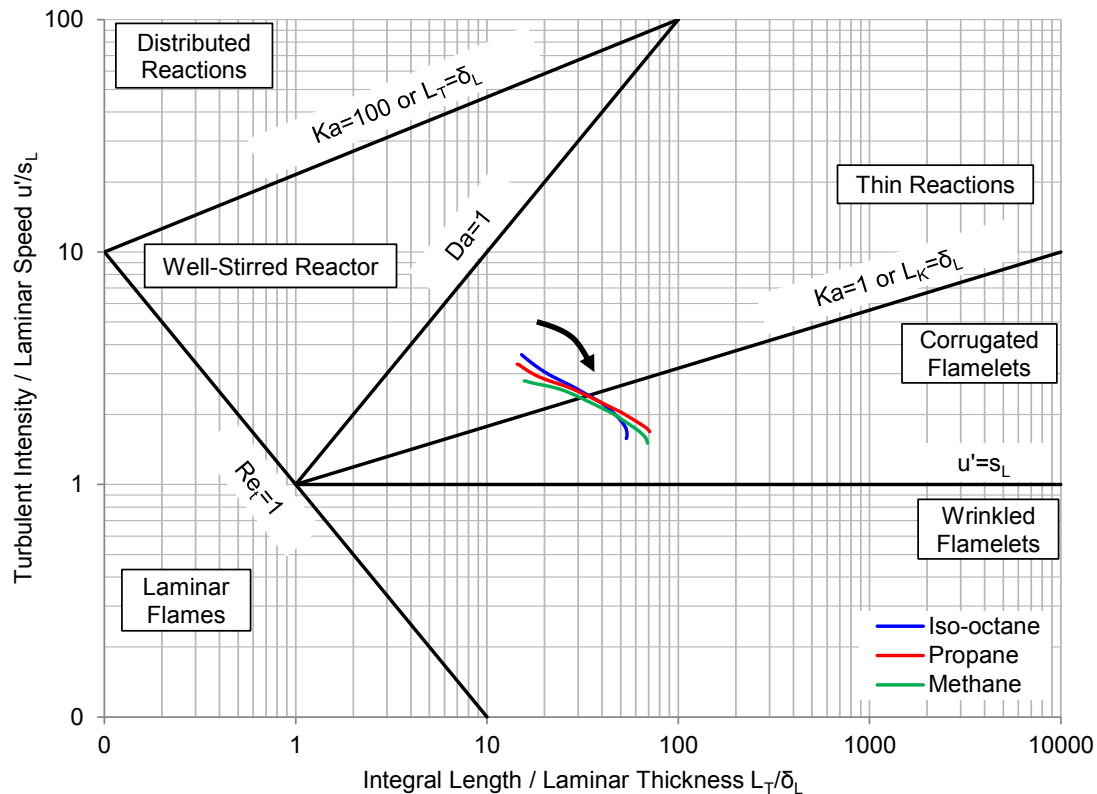


Figure 3-35: Borghi-Peters diagram showing the combustion regimes for all three fuels. The black arrow shows the direction of the combustion process. The unstretched laminar flame speed and the Blint's [21] laminar flame thickness have been used for the calculation of the combustion regime.

The efficiency function, used in this 0D model (equation in [16]), has been calculated by Meneveau and Poinot equation [16] with an one-step chemistry of an Arrhenius law for the description of the combustion process (Lewis number equal to 1.2). Notwithstanding the constant Lewis number upon the calculation of the efficiency function, fuel dependence exists through the use of the laminar flame thickness. An updated version of the efficiency function has been proposed by Bougrine *et al.* in [78]. It contains a 4-step kinetic scheme dedicated to the combustion of methane-hydrogen and propane-hydrogen fuel blends. Finally, a new efficiency function is proposed, which contains a correction term in function of Lewis number. In the discussion of the results of Figure 3-32 (stretched and unstretched speed), it has been shown that the Lewis number effects have a significant impact on the beginning of combustion. This impact of fuel composition on the flame is not taken into account by the updated efficiency function, since the efficiency function describes the turbulence-flame interaction of a fully turbulent flame rather than the flame after ignition. As a consequence, modeling of the stretched laminar burning speed is needed even if of a turbulence-flame interaction model takes into account fuel composition effects by the Lewis number.

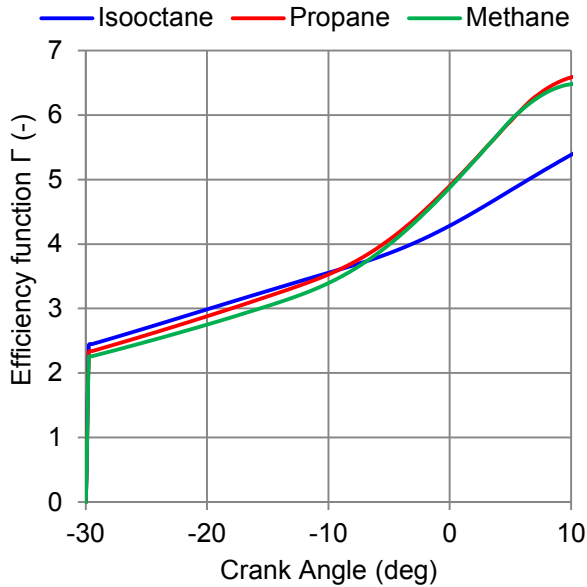


Figure 3-36: Efficiency function Γ for all three fuels. It is calculated by the relation in [16].

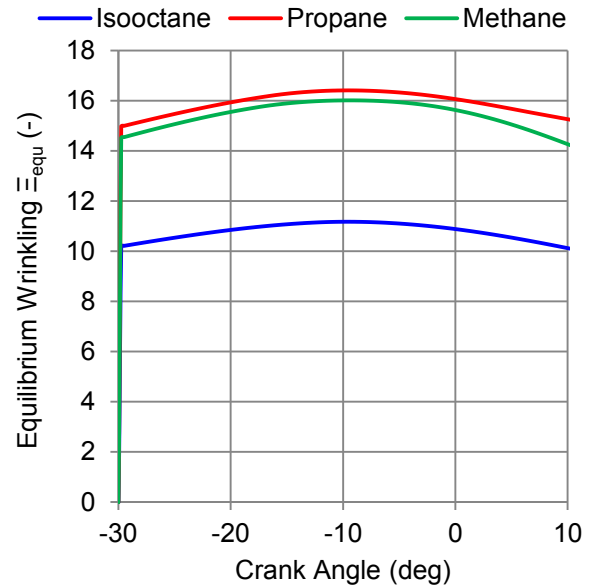


Figure 3-37: Equilibrium wrinkling factor (Ξ_{equ}) during the combustion phase for all three fuels.

In Figure 3-36 the efficiency function for all three fuels is shown. As it is expected after the discussion on laminar flame thickness the efficiency function is similar for propane and methane. The isooctane efficiency function is also close to the ones of the other two fuels at the beginning of combustion and it finally becomes lower. This decrease is due to the decrease of the ratio L_T/δ_L . Similar trends are found for the equilibrium wrinkling factor (Ξ_{equ}) in Figure 3-37: propane and methane mixtures have almost identical equilibrium wrinkling factors, with a maximum value of 16. On the contrary, isooctane mixture has a lower maximum value (about 11). Besides that the equilibrium wrinkling factor is adjusted with the model coefficient for each fuel, its trend is the same as the one of the efficiency function. It is expected that this trend will appear in the wrinkling factor as well.

The flame radius evolution for all three fuels along with the experimental measurements (acquired from [76]) is plotted in Figure 3-38. The simulation curves are close to the experimental points and they have the same ranking: methane propagates more rapidly, propane follows and isooctane has the slowest propagation. The same trend was observed in [74], [75]. The simulation radii are always lower than the experimental ones. This divergence is probably due to the difference of calculation process of the flame front radius in the model and in the experiment. Indeed, in the experimental study, the flame radius is deduced from tomographic images. This means that the flame radius was obtained from a surface and does not take into account the three-dimensional shape of the flame unlike the model. On the other hand, the simulation radius is calculated so as that the thermodynamic burnt gas volume V_b is equal to the volume V_L , which is enclosed by the mean flame surface.

The flame propagation speed as defined by equation (3-18) is shown in Figure 3-39, as function of flame radius. As the slow evolution of isooctane radius has already been identified, the propagation speed of isooctane mixture is the lowest in both modeling and experimental results. Methane mixture propagates faster than the propane one in the experiments, while they seem to have the same propagation speed in modeling results. An inflexion point on all three modeling curves appear between 0.009 and 0.010 m of flame radius. At this point the spherical flame surface touches the piston and continues to expand towards the

cylinder wall. This inflexion point is not visible on experimental data again due to the optical diagnostic used in [4]. The tomographic image was taken with a laser sheet parallel to the piston plane thus implying that the moment when the flame rises the piston is not visible.

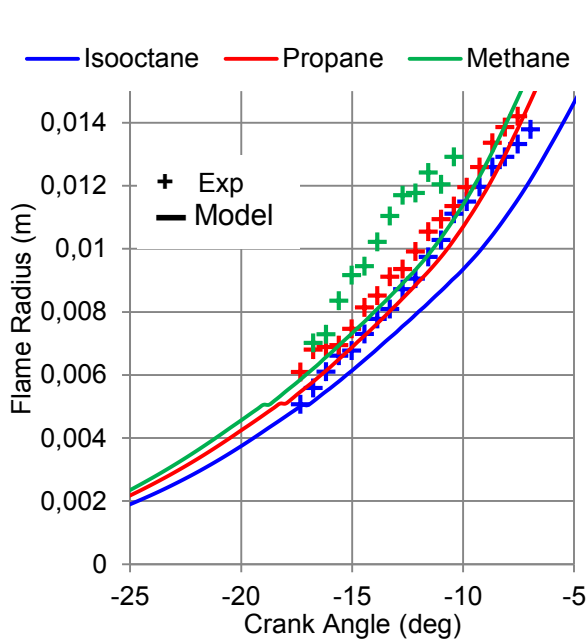


Figure 3-38: Flame Radius (R_f) during the combustion phase for all three fuels along with the experimentally derived values (+) acquired from [76].

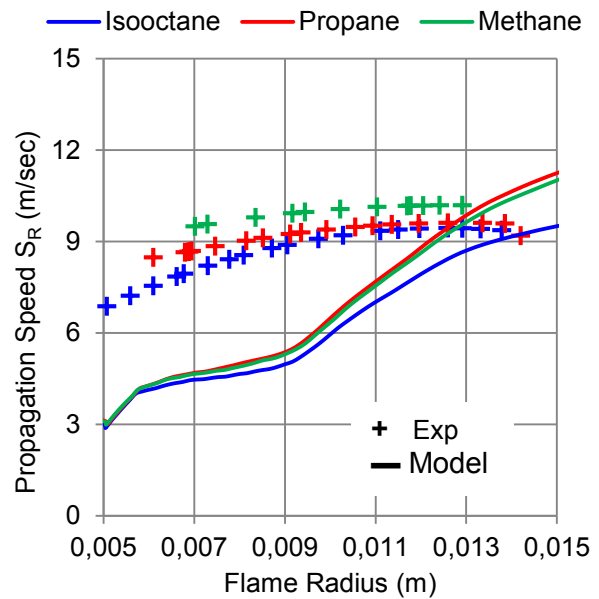


Figure 3-39: Equivalent propagation speed (s_R) during the combustion phase for all three fuels along with the experimentally derived values (+) acquired from [76].

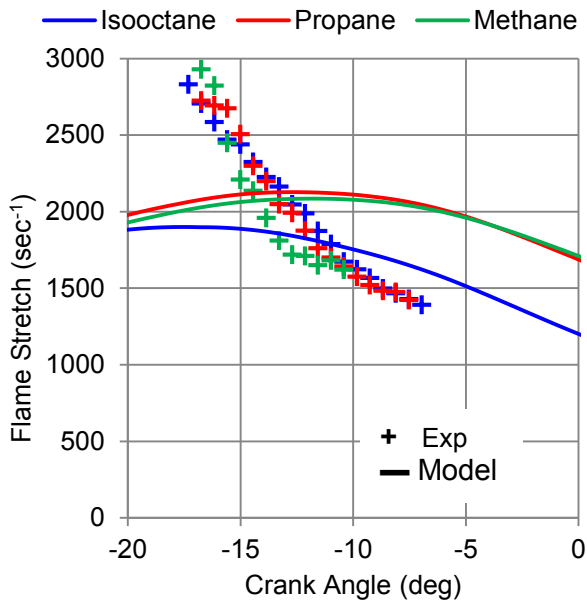


Figure 3-40: Flame stretch (κ) during the combustion phase for all three fuels along with the experimentally derived values (+) acquired from [76].

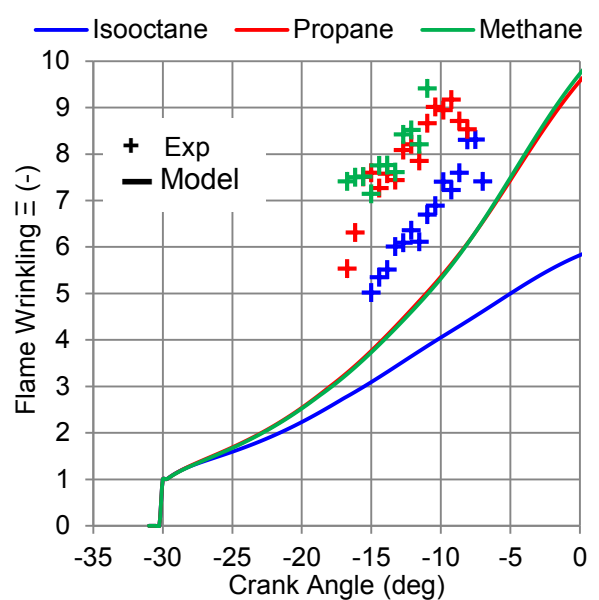


Figure 3-41: Simulated wrinkling factor (Ξ) during the combustion phase for all three fuels along with the experimentally derived values (+) acquired from [76].

Flame stretch, as it has been calculated by equation (2-39), is plotted for all three fuel mixtures in Figure 3-40. Numerical and experimental results are in the same order of magnitude and for both, the three fuels have almost the same stretch.

The global wrinkling of the three mixtures from modeling is shown along with the experimental results in Figure 3-41. Both numerical and experimental results expose an augmentation of flame wrinkling during the first part of combustion. The wrinkling factor starts in the model at spark advance timing with a unity value in order to simulate the laminar nature of the flame kernel [57] and during 10 crank angle degrees the simulated wrinkling value is similar for all models. This is expected since the flame front starts to be affected by turbulence, when the flame kernel becomes larger than the integral length scale ($L_T = 1.9$ mm at spark advance in all computations) [25]. Both simulated and numerical results give similar wrinkling for propane and methane mixtures and lower for isooctane case. As it is explained in [76] and observed in Figure 3-40, the most stretch sensitive mixture, i.e. isooctane mixture one presents the less wrinkled flame front. The Lewis number, being equal or larger than unity, ensures thermodiffusive stability for all three fuels. Moreover, hydrodynamic (Darrieus–Landau) instabilities have a minor impact since the impact of the highly turbulent flow on flame wrinkling is preponderant. These considerations lead to the fact that the decreased wrinkling for isooctane is due to local flow-flame interactions. These local interactions, which are different for each mixture, are not identified by the used 0D wrinkling model. Nevertheless, they are taken into account globally and a correct flame wrinkling is calculated.

At -10 crank angle degrees, the simulated wrinkling of all three fuel mixtures reaches at 64% of the experimental value. From the observation of experimental and simulated flame wrinkling results, it can be noted that the derivation of the wrinkling factor from tomographic images by the use of radii gives higher wrinkling than the usual values for such low load operating points. Another possible explication of the discrepancy between the simulated and experimentally derived wrinkling is the difference of the flame stretch, as it was explained in the previous paragraph. In fact, higher stretch at the beginning of combustion leads to lower stretched laminar burning speed. Therefore, if the modeled stretched laminar burning speed was lower, flame wrinkling would have been higher and thus closer to the experimental values.

As reported in [25], if it is assumed that the flame thickness is clearly smaller than the flame radius, the following relation, which is a consumption speed, can be deduced:

$$s_c = \frac{\rho_b}{\rho_u} \frac{1}{\bar{\epsilon}} \frac{dR_f}{dt} \quad (3-62)$$

This consumption speed gives information on the global reaction rate but is unable to provide information on the local development of the flame front, as it is explained in [25]. In Figure 3-42, this consumption speed has been calculated by both simulation and experimental results and compared with the stretched laminar burning speed for all fuel mixtures. For Lewis numbers superior or equal to unity ($Le \geq 1$), the expected trend is to obtain a lower consumption speed than the unstretched laminar burning speed, as in [25]. For propane and methane mixtures both simulated and numerical results are very close. The observed discrepancies are due to the different flame radius evolution between the model and the experiment (see discussion of Figure 3-38). The consumption speeds for those mixtures are always smaller than the stretched laminar burning speed. The difference between these both speeds decrease as function of the Le number increase. Therefore, the experimental results are closer to the stretched laminar burning speed rather than the consumption speed, as for propane and methane mixtures.

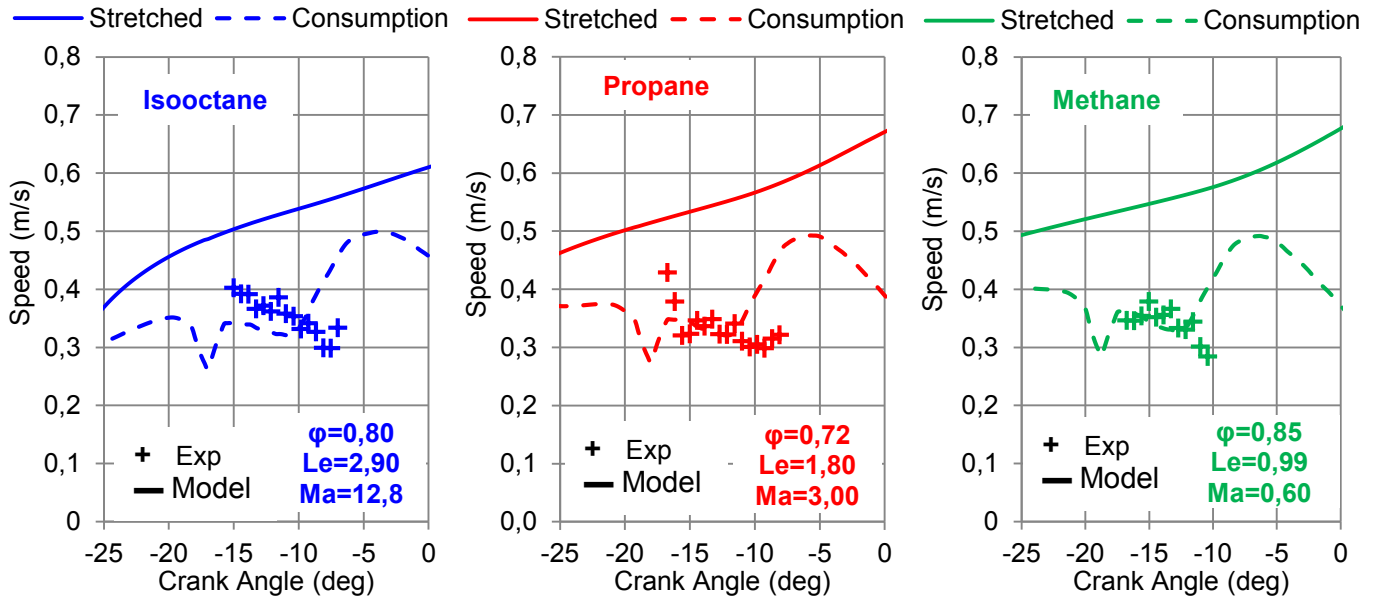


Figure 3-42: Consumption speed (s_c) compared with simulated stretched laminar flame speed along with the experimentally derived values (+) acquired from [76].

Figure 3-43 exposes the burnt mass fraction up to 0.50 for all three mixtures. As it has been already discussed in [76], mixtures do not burn with the same speed with the isooctane mixture being the slowest and methane mixture the fastest. With the help of the simulation results, the impact of thermo-diffusive effects through the Lewis number is visible. For methane the two burnt mass fraction traces are almost identical, since the stretched and unstretched laminar burning speeds are similar. The Lewis number effect starts to be visible for propane (unstretched trace is 2.5 degrees ahead of stretched at 50%). The greatest impact is found for the isooctane mixture with the unstretched Le trace being 7.5 crank angle degrees ahead of the stretched trace at 50%.

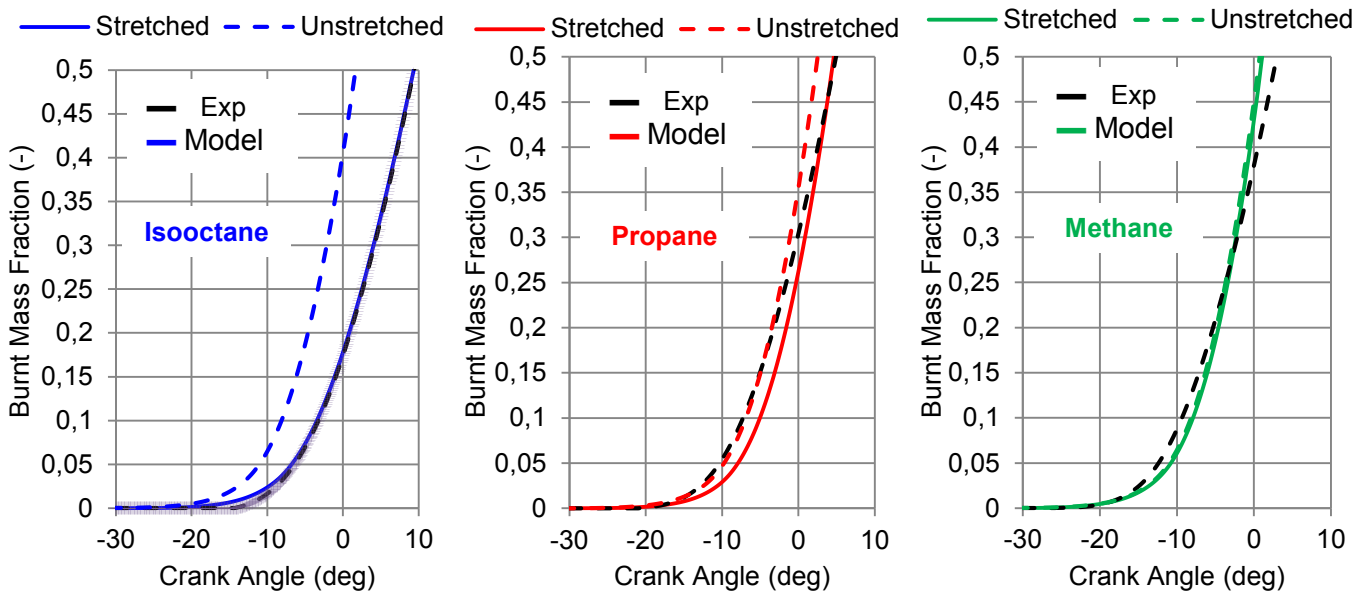


Figure 3-43: Burnt mass function compared with simulated stretched and unstretched laminar flame.

3.17 Conclusion for impact of flame stretch

The 0D Spark Ignition combustion model, which has been developed on the basis of the 0D Flame Surface Density equation, has been enhanced with a sub-model for the stretching of the laminar flame. Simulation results are compared against previously published experimental results, of different lean mixtures (isooctane, propane and methane) presenting almost the same unstretched laminar burning speed during the beginning of combustion.

The Lewis and Markstein numbers remain almost constant during the combustion cycle. Their values are in accordance with already published values for the same fuel/air equivalence ratio, pressure and temperature conditions. The adopted correlation for the unstretched laminar burning speed preserve the equality of the unstretched flame speeds of each mixture. The stretched speeds are ranked from low to high as follows: Isooctane (Le: 2.9), Propane (Le: 1.80) and Methane (Le: 0.99).

The adopted model for the stretched laminar burning speed is an indispensable addition in a physical combustion model because it adapts the laminar burning speed to the high stretch rate at the beginning of combustion, while during this stage flame wrinkling is low. The turbulent efficiency function takes partially into account the fuel composition through the laminar flame thickness but does not incorporate the effect of stretch even it is corrected by the Lewis number.

Flame radius and flame propagation speed simulations show almost the same trends with the experimental results. Methane mixture propagates faster than the propane in the experiments, while they seem to have the same propagation speed in modeling results. The differences in the simulated and experimental flame radius and propagation speeds are due to the different manner of calculation of flame radius through two-dimensional tomographic images in the experiments and by spherical surfaces in the model. Flame wrinkling trend is also recovered by the model with propane and methane having almost identical wrinkling, while isooctane has lower values. The absolute values of the experiments are greater than those of simulations, due to the greater flame radii in experiments. Flame stretch is rather similar for all three mixtures for simulations and experiments.

Finally, the impact of the stretched flame speed in function of the thermo-diffusive effects is visible in the burnt mass fraction. The difference in combustion speed is not visible for methane, since its stretched speed is close to the unstretched one. Stretch impact becomes visible for propane, while it is dominant in isooctane. This conclusion underlines the need of flame stretch modeling for the first stage of combustion and offers insight for a future study on the various parameters, which affect flame stretch, such as RBG fraction, engine speed and engine load. If a more detailed flame stretch model becomes available, the impact of strain to the total flame stretch may be also reconsidered.

Chapter 4 Model validation for different engine configurations

In this chapter the proposed model will be validated against experimental data from various engine configurations. The purpose of this validation is to trace the predictive capacity of the model as well as the limitations of its sub-models. In the following section the general technical characteristics of the engine are given and the range of operating points is shown. A list of special tests, which will enlighten the impact of operating conditions on the different sub-models, is also proposed. The most interesting results, which are derived from this validation plan, will be discussed.

4.1 Test bed engine description

The basic technical characteristics of the test bed engine are presented in Table 4-1. The test bed is equipped with a SI PFI four-stroke engine. Inlet pressure can be greater than atmospheric pressure and turbocharged operating points can be achieved. The experimental facility (Figure 4-1) allows running at loads of a supercharged engine thanks to a compressor mounted on the intake section. Air intake temperature as well as cooling and oil temperature are regulated and recorded; pressure sensors are recording the instantaneous intake, exhaust and in-cylinder pressure. These data are necessary to perform pressure analysis and calculate heat release rate that will be subsequently used for evaluation of our combustion model. The cooling water and lubricant oil temperatures regulated at 363.15 K. The typical fuel, which used in this engine, is a gasoline fuel with Research Octane Number (RON) of 95. Its lower heating value (LHV) is 43.12 MJ/kg.

Table 4-1: Characteristics of the engine, which has been used for engine validation.

Engine type:	Spark Ignition, PFI, four-stroke, turbo-charged
Number of cylinders	1
Bore (mm)	72.2
Stroke (mm)	73.1
Connecting rod length (mm)	123.5
Geometric compression ratio (-)	9.3
IVO (crank angle degrees before TDC) ¹	23
IVC (crank angle degrees after BDC) ¹	55
EVO (crank angle degrees before BDC) ¹	53
EVC (crank angle degrees after TDC) ¹	19
Fuel/air equivalence ratio φ (-)	1.0

The basic set of test bed experiments contains several operating points. Engine speed varies from 1200 PRM to 3000 RPM and engine load varies from 2 to 18 bar of IMEP. A

¹ Opening and closing angles of valves are given at zero valve lift.

summary of the simulated operating points is shown in Figure 4-2. The IMEP is the one, which has been calculated by the pressure measurements. The optimal ignition advance angles of those points are shown in Figure 4-3. The fuel/air equivalence ratio φ was kept constant and equal to unity for all operating points. The spark advance angle of spark ignition was set so as that the engine delivers the maximum effective efficiency. In the turbo-charged operating points the limiting factor of knocking occurrence did not allow optimal thermodynamic spark timing.

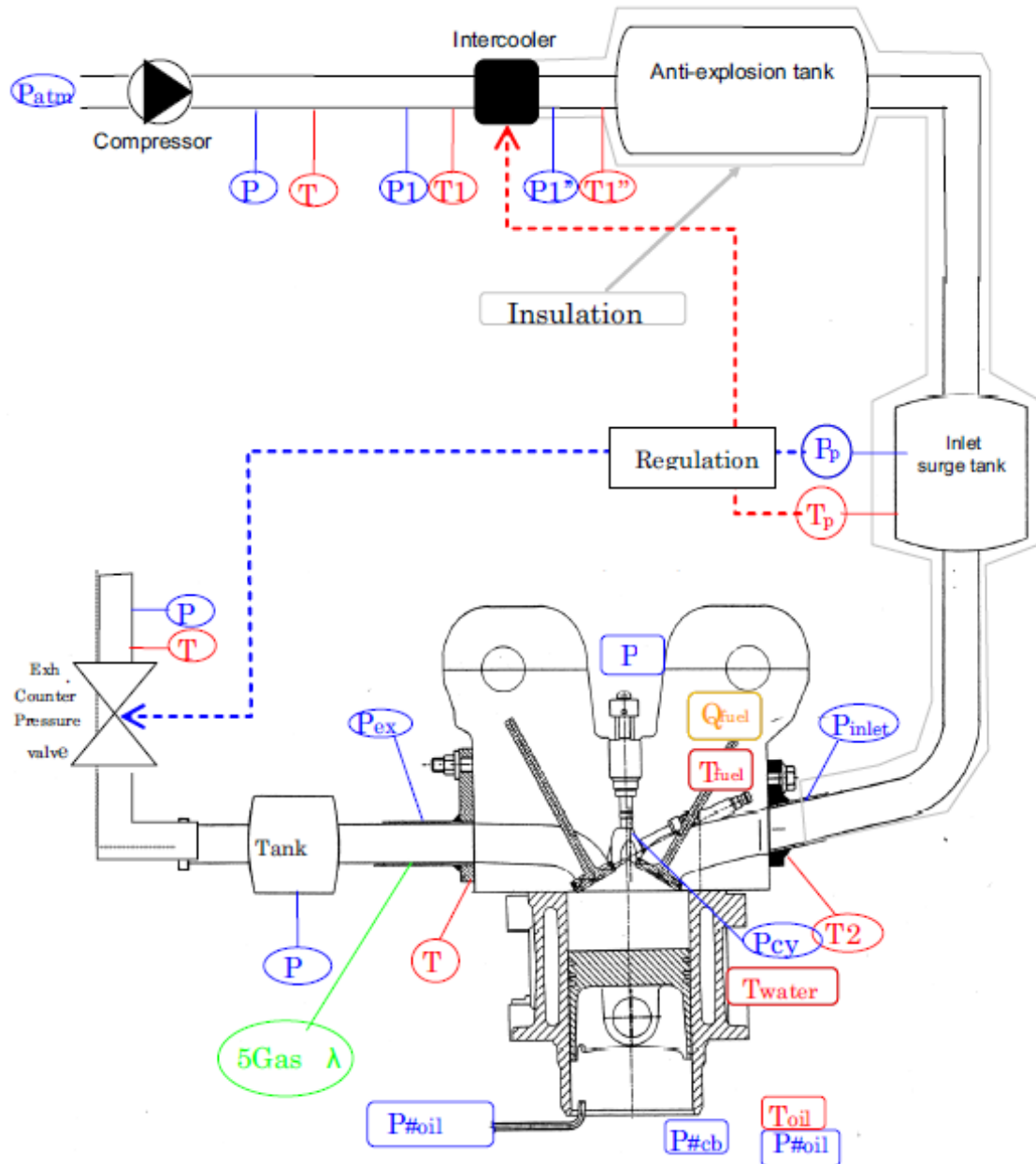


Figure 4-1: Single cylinder engine as it is used in the test bed.

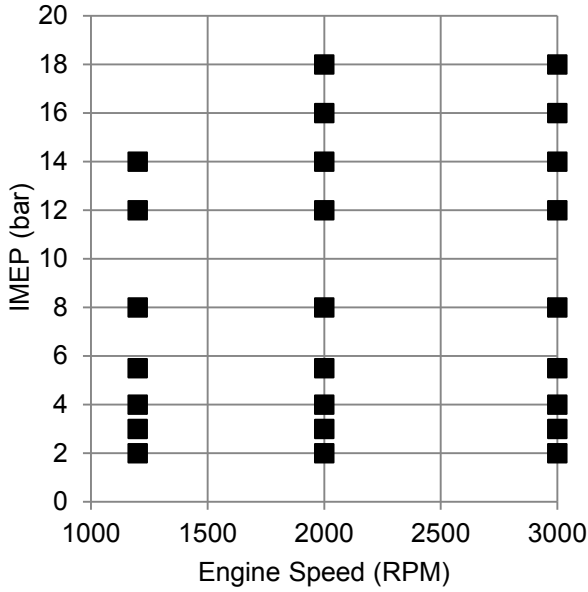


Figure 4-2: Operating points of engine test bed results. The spark advance angle was set to the optimal value of maximum efficiency. This value is limited for the turbocharged points by the occurrence of knocking.

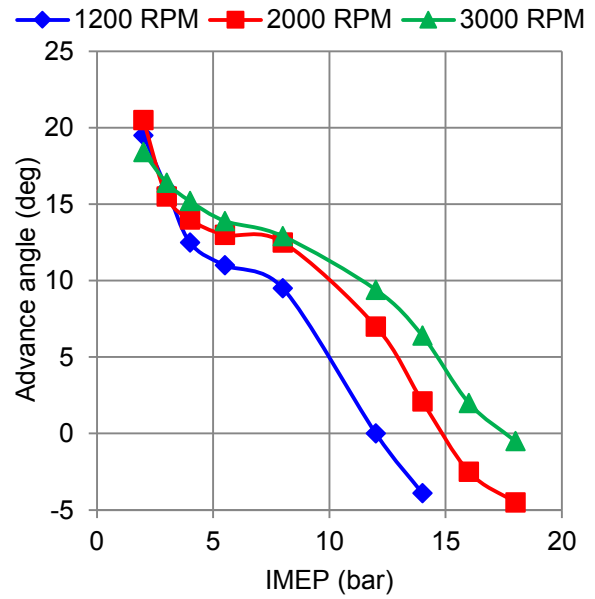


Figure 4-3 : Ignition advance angle for all operating points. Advance angle is given in crank angle degrees before TDC.

Cylinder pressure measurements allow the reconstruction of an energy balance inside the combustion chamber while the valves are closed. The total heat release during combustion Q_{comb} consists of the work term, the internal energy term and the heat transfer term, as it can be observed in equation 3-17. The ratio of heat capacities γ is calculated through the mean gas temperature in the chamber. No mass loss into crevice volumes is considered so any change in the internal energy is made by temperature variation. Like in the previous chapters, a Woschni model is used for the calculation of heat transfer. For each operating point a wall temperature is set for the cylinder liner, piston crown and cylinder head. The models constants are calibrated in order that the total heat release during combustion is the same with the converted fuel energy ($\eta_{comb}m_{fuel}LHV_{fuel}$). The total RBG mass fraction at inlet valve closing can be estimated by the semi-empirical relations proposed in [81], [112] in function of the compression ratio, the valve overlap period, the fuel/air equivalence ratio and the intake and exhaust pressures.

$$\frac{dQ_{comb}}{d\theta} = \frac{\gamma}{\gamma - 1} p \frac{dV}{d\theta} + \frac{1}{\gamma - 1} V \frac{dp}{d\theta} + \frac{dQ}{d\theta} \quad (3-17)$$

The combustion efficiency η_{comb} is calculated by equation (4-1). This equation uses the measured values of unburnt HC as well as of the remaining CO. It also employs the approximation that the lower heating value of CO, which is equal to 10.1 MJ/kg, is equal to the 25% of the heating value of unburnt HC (which is not well defined, since the exact composition of unburnt HC is not known). Any other species (H_2) or soot particles, which may contribute to the heat release rate, are considered negligible in SI engines. Moreover, the lower heating value of unburnt HC is directly comparable with the one of the fuel. The previously described process permits the calculation of the characteristic angles of 10%, 50% and 90% of burnt charge. All in all, pressure measurements as well as unburnt HC and CO measurements lead to the assessment of an experimentally derived heat release rate, which will be called “experimental” in the following figures.

$$\eta_{comb} = 1 - \frac{m_{HC}LHV_{HC}}{m_{fuel}LHV_{fuel}} - \frac{m_{CO}LHV_{CO}}{m_{fuel}LHV_{fuel}} = 1 - \frac{m_{HC}}{m_{fuel}} - 0.25 \frac{m_{CO}}{m_{fuel}} \quad (4-1)$$

The cylinder pressure measurement has been conducted for several cycles for a given operating point. Due to the phenomenon of cyclic variation, there is an important difference between the pressure traces of cycles. The pressure trace of the mean cycle is used but data on 300 cycles allow as calculating standard deviations of the maximum pressure and the angle of appearance of maximum pressure. After the reconstruction of heat release rates of the 300 cycles, the standard deviation of the maximum value of heat release rate of the mean cycle is also calculated. A respective estimation of the standard deviation of the characteristic combustion angles is also performed. These results appear in the form of error bars on the pressure and heat release figures with a total width of two standard deviations. It has to be noted, that they do not constitute an error estimation of pressure measurements, since the pressure difference, which appears on different cycles, is a physical phenomenon and not an error-induced artifact.

4.2 Comparison with optimal advance angle engine test bed results

Table 4-2: Variation of engine variables in function of engine speed and load. Increasing and diminishing trends are denoted by ▲ and ▼ respectively. No change is denoted by —.

	▲ Engine speed: N	▲ Engine load: $imep$
Spark Advance angle (AA)	▲	▼
RBG	▼	▼
Heat transfer (% fuel energy)	▲	▼
p_{max}	▲ ²	▲, $\eta_v < 1$ —, $\eta_v \geq 1$
$T_{u,max}$ $T_{b,max}$	▲	▲, $\eta_v < 1$ ▼, $\eta_v \geq 1$
CA10	▼	▲
CA50	— ³	—, $\eta_v < 1$ ▲, $\eta_v \geq 1$
CA90	▼	▲, $\eta_v < 1$ ▼, $\eta_v \geq 1$
Maximum Heat Release (divided by the fuel energy)	—	▲, $\eta_v < 1$ ▼, $\eta_v \geq 1$

In Table 4-2 the qualitative variation of different engine variables, which are related to the combustion process, is shown. The variables behavior is the result of the different physical phenomena taking place during or before combustion. This analysis is helpful for the understanding of the response of the model for the different operating points. This is the reason why the evolution of the variables has been expressed in function of engine speed and load.

² Constant for very high engine speed.

³ Apart from the points, which are prone to knock.

In order to get the most out the fuel energy, combustion must take place as fast as possible (combustion is ideally instantaneous) at TDC piston position. Spark ignition must occur neither early (when compression stroke is still taking place and the initial pressure of combustion would be low) nor too late during the expansion stroke. Indeed, combustion must take place around the top dead center. The efficiency of the combustion cycle is a trade-off between the heat transfer losses (too early spark advance) and the combustion speed (too late spark advance). It is expected that the maximum pressure for the optimal spark advance to appear some degrees after the TDC. Experimental testing has revealed that for low and medium engine loads this thermodynamically optimal spark advance angle (in terms of efficiency 13 crank angle degrees after the TDC. An equivalent version of this rule is that 50% of combustion has been completed at about 8 crank angle degrees after TDC. This rule does not hold for the cases of full load due to knocking. A new optimal spark advance angle is found for such operating points. This new value is a value at which knocking slightly occurs and is smaller than the optimal thermodynamic value. Spark advance increases with engine speed because combustion has almost the same duration in seconds ($\Delta\theta = 6N\Delta t$), even if turbulence increases with engine speed. It decreases with engine load since combustion takes place faster (less RBG leads to higher laminar flame speed). Heat transfer as a percentage of the fuel energy increases with engine speed, since it is a function of mean piston speed. It decreases with engine load. Maximum pressure increases for low and medium speeds and from low and medium loads. Due to late spark ignition, it remains constant for turbocharged points. Both burnt and fresh gas temperatures increase with engine speed and increase for low to medium loads but decrease for turbocharged operating points. CA10 decreases with engine speed since spark advances takes place earlier and RBG decreases. It increases with engine load, since spark advance is retarded. CA50, as discussed earlier, remains constant for all operating points due to optimal spark timing except for the points, which are prone to knock. CA90 comes earlier when engine speed increases and it has the same evolution with engine load apart from the turbocharged points.

Table 4-3: Turbulence evolution. In this work, the dependence on engine speed and on engine load is of particular interest. The assessment of the evolutions is observed in results of the 0D turbulence model presented previously as it is calculated by 3D CFD commercial code.

	▲ Engine speed: N	▲ Engine load: $imep$
Turbulent intensity (maximum value): u'	▲	—, ▲
Integral length scale (maximum value): L_T	—	—

As it has already been shown in Chapter 2, turbulent intensity has a very strong impact in SI combustion, since it controls flame wrinkling. It is important to know the evolution of turbulence and of the integral length scale inside a cycle as well as its variation with engine speed and load. Turbulent intensity is connected with the mean piston speed. Its maximum value during a cycle is proportional to the engine speed [113], [114]. It remains constant with engine load, although a moderate increase is observed for turbocharged points. In Figure 4-4 and in Figure 4-5 these considerations are obvious. In Figure 4-6 for an engine speed of

3000 RPM the difference between the maximum turbulence through the different loads is smaller than in the other engine speeds.

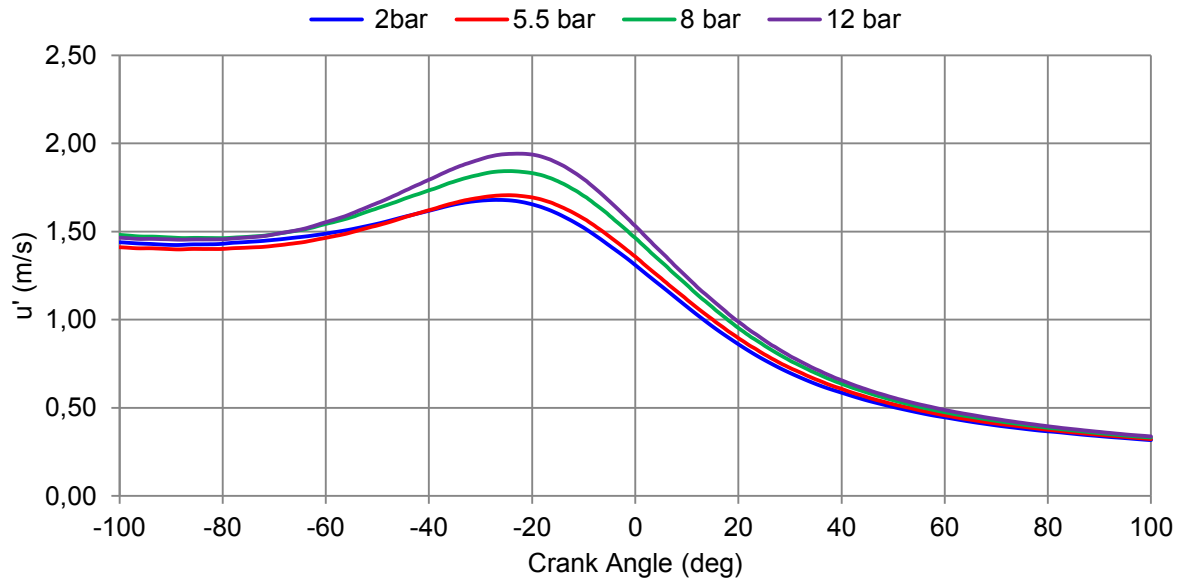


Figure 4-4: Turbulent intensity for several operating points of engine speed 1200 RPM in function of engine load as it was calculated by 3D CFD commercial code.

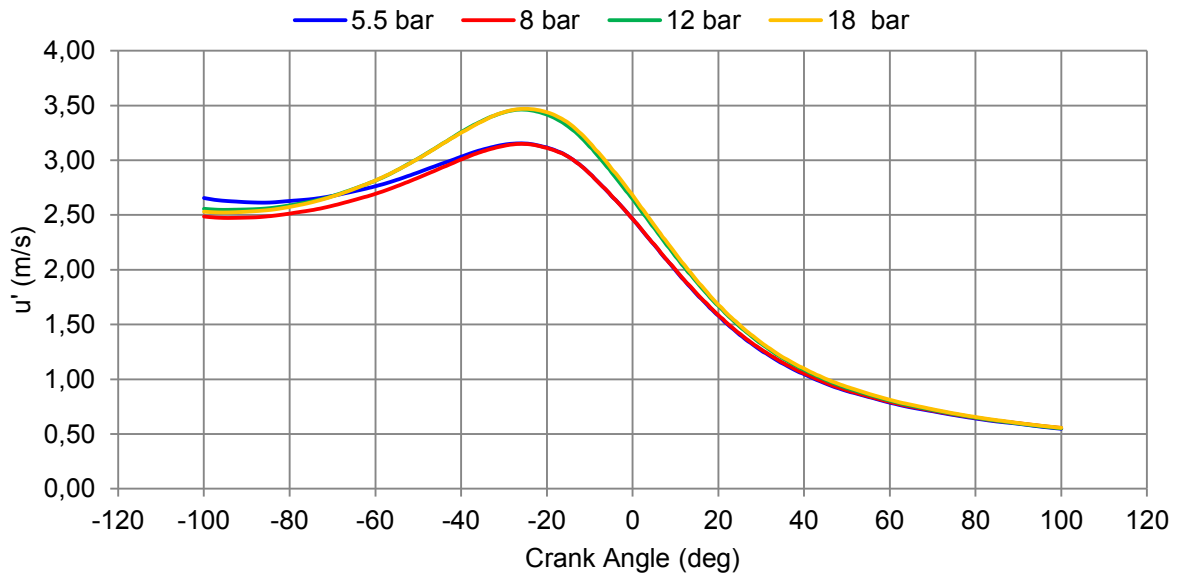


Figure 4-5: Turbulent intensity for several operating points of engine speed 2000 RPM in function of engine load as it was calculated by 3D CFD commercial code.

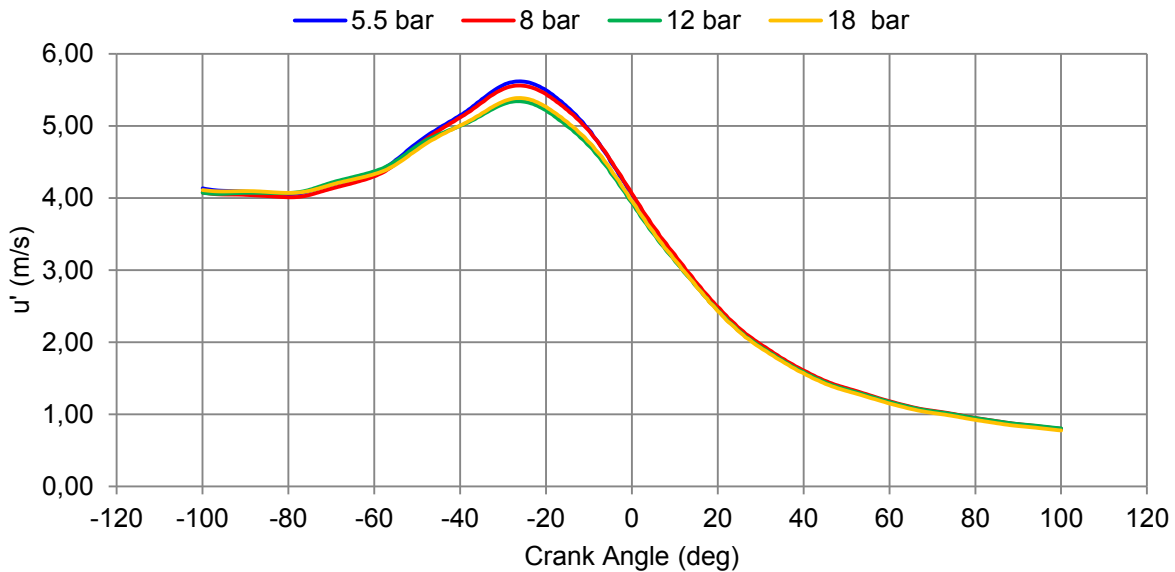


Figure 4-6: Turbulent intensity for several operating points of engine speed 3000 RPM in function of engine load as it was calculated by 3D CFD commercial code.

The integral length scale is linked with the distance between the intake valve tip and the cylinder head and it is controlled by the chamber geometry, as explained in [115]. It has its maximum early during compression and it becomes lower while the pistons goes to the TDC (compression: $L_T = C_{LT} V^{1/3}$). After TDC its decay continues (expansion: $L_T = L_T^{TDC} \exp(-\theta/100)$). This is why it is modeled as a function of chamber volume during compression. A comparison with 3D CFD results showed that the integral length scale barely changes in function of engine loads and speed. The outcome of the considerations about turbulent intensity and integral length scale is summarized in Table 4-3. Turbulence behavior is very important for the trends of the coefficient of the model. The discussion on turbulence evolution is presented before discussing the combustion process in itself since in this level of physical modeling turbulence is not affected by the combustion process.

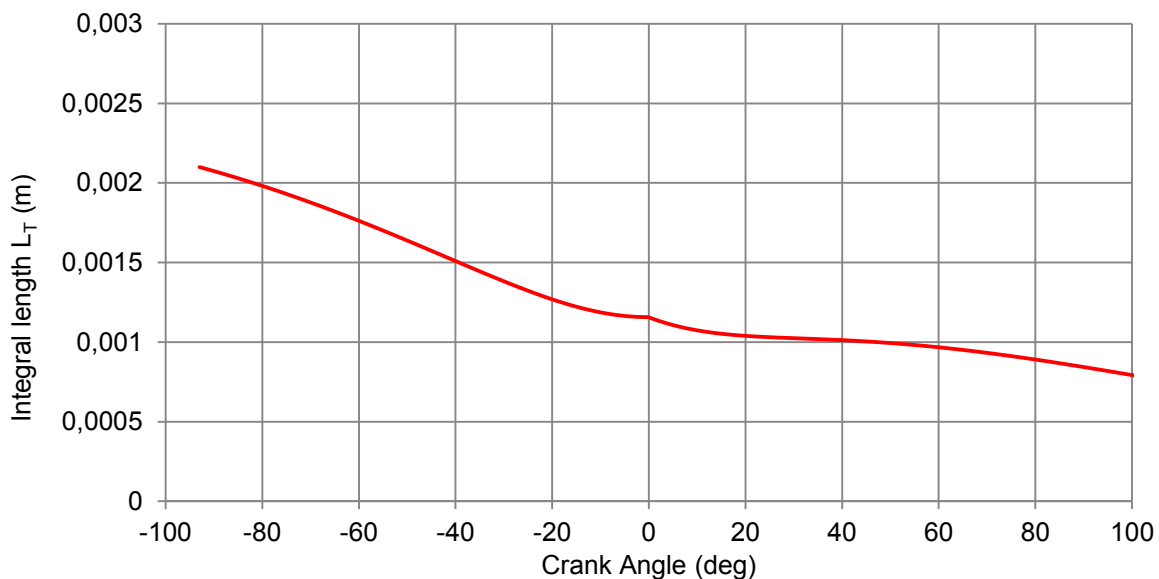


Figure 4-7: Integral length scale for the typical point of engine speed 2000 RPM and IMEP of 8 bar.

4.2.1 Typical evolutions of combustion variables in a cycle

The burnt mass evolution is a function of the density of the fresh gases ρ_u , of the laminar flame speed s_L , of the mean flame surface A_L and of the wrinkling factor \mathcal{E} . The evolution of these variables is analyzed through the model results. The consistency of these results underlines the quality of the model as well as its predictive capacity. A typical point operating with engine speed at 2000 RPM and engine load (IMEP) at 8 bar will be analyzed. For this operating point the cylinder pressure is correctly modeled by the model, as it can be observed in Figure 4-8. The pressure agreement is the fundament for the rest of the variables.

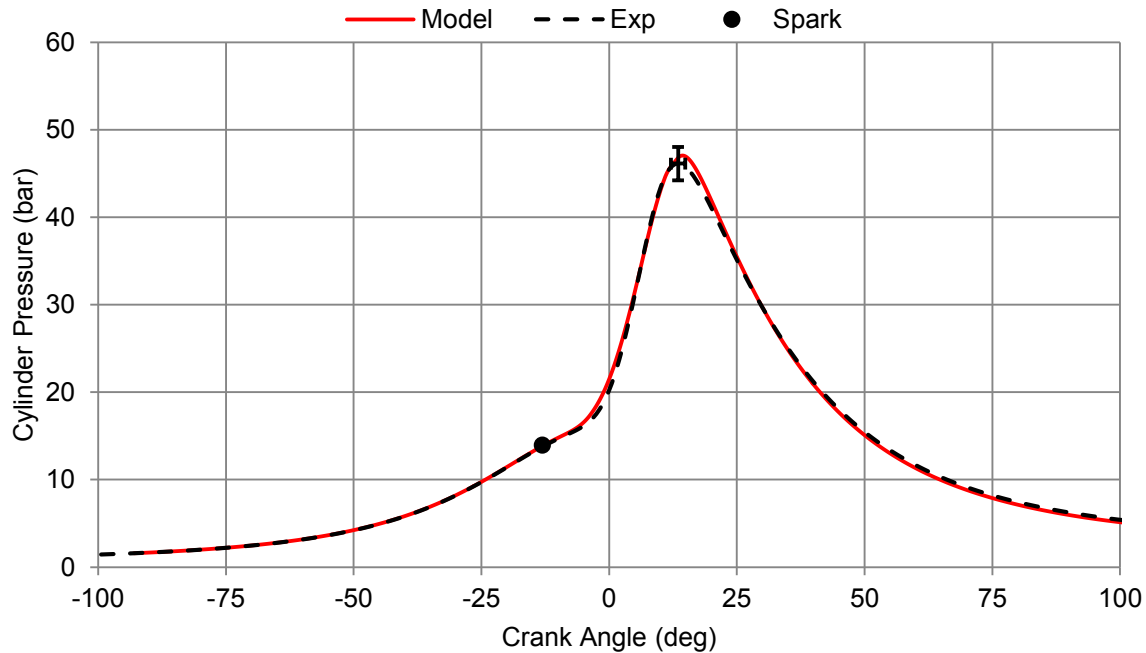


Figure 4-8: Cylinder pressure evolution for the typical point of engine speed 2000 RPM and IMEP of 8 bar.

The variation of fresh and burnt gas temperature is shown with engine load variation (Figure 4-9) and with engine speed variation (Figure 4-10). The results for engine load as well as engine speed variation are in agreement with the expected trends (Table 4-2). The crank angle of maximum value of gas temperature is the same with the crank angle of the maximum cylinder pressure. The fresh gas temperature evolution also follows the pressure evolution for load and engine speed variation. The effect of late spark timing is visible in the engine load variation for the operating point of 2000 RPM and 12 bar. The increase of fresh gas temperature with engine speed was expected, since the overall combustion speed increases due to turbulence increased levels, when engine speed rises. Those two phenomena lead to increased combustion speed.

The density variations with engine load show a clear rising trend due to the increase of the cylinder charge total mass (Figure 4-11). The late spark advance effect for the point of 2000 RPM, 12 bar is also evident, as it was for the temperature evolution. The typical value (about 4) for the fresh/burnt gas ratio is recovered for the beginning of combustion. In the case of engine speed variation (Figure 4-12), a decline of fresh gas density is observed. The density is proportional to pressure/temperature ratio (Table 4-4). Cylinder pressure increases but the fresh gas temperature increases, as it was shown before. The final result leads to a decrease of the fresh gas density.

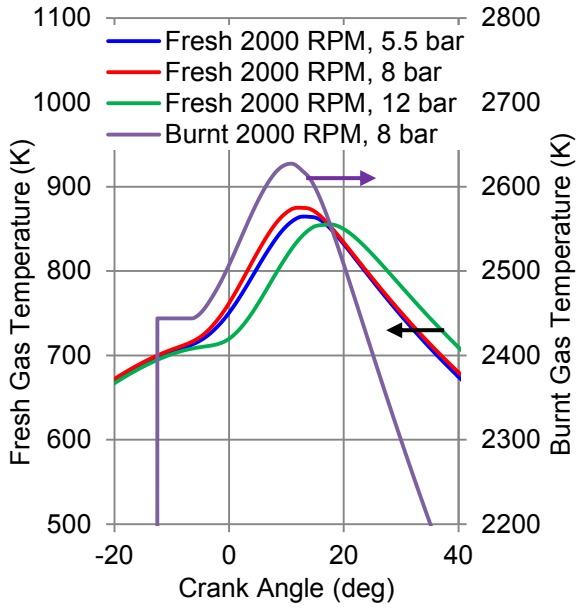


Figure 4-9: Burnt and fresh gas temperature (right and left Y axis respectively) for the typical point of engine speed 2000 RPM and IMEP of 8 bar with additional engine load variation results.

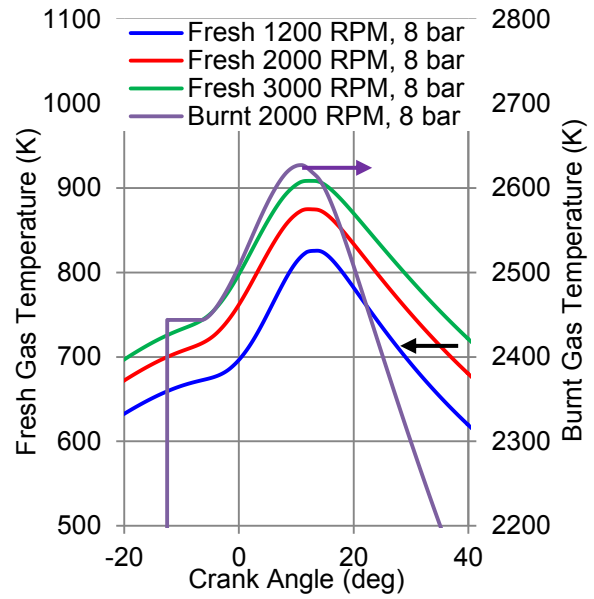


Figure 4-10: Burnt and fresh gas temperature (right and left Y axis respectively) for the typical point of engine speed 2000 RPM and IMEP of 8 bar with additional engine speed variation results.

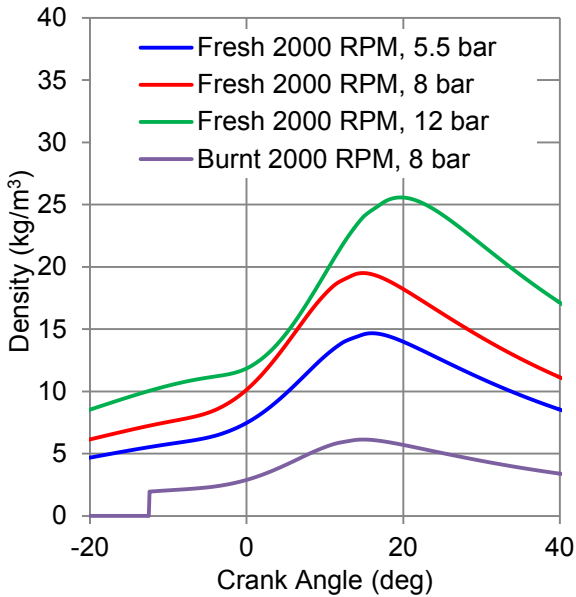


Figure 4-11: Burnt and fresh gas densities for the typical point of engine speed 2000 RPM and IMEP of 8 bar with additional engine load variation results.

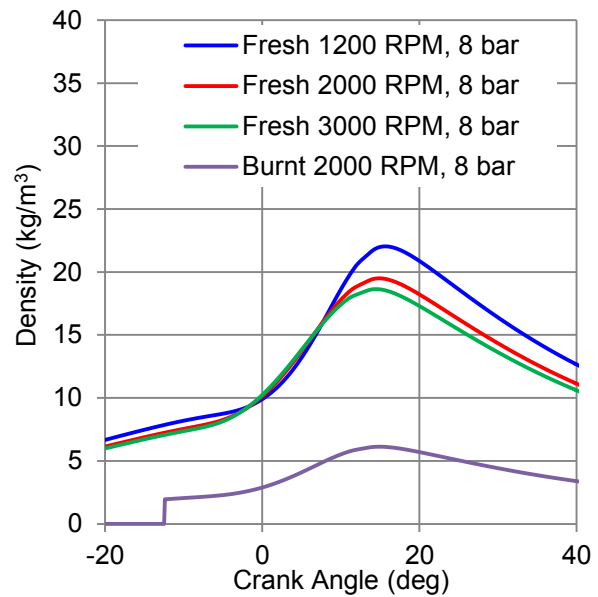


Figure 4-12: Burnt and fresh gas densities for the typical point of engine speed 2000 RPM and IMEP of 8 bar with additional engine speed variation results.

Table 4-4: Unburnt gas density evolution

	▲ Pressure: p	▲ Unburnt gas temperature: T_u
Unburnt gas density: $\rho_u \propto \frac{p}{T_u}$	▲	▼

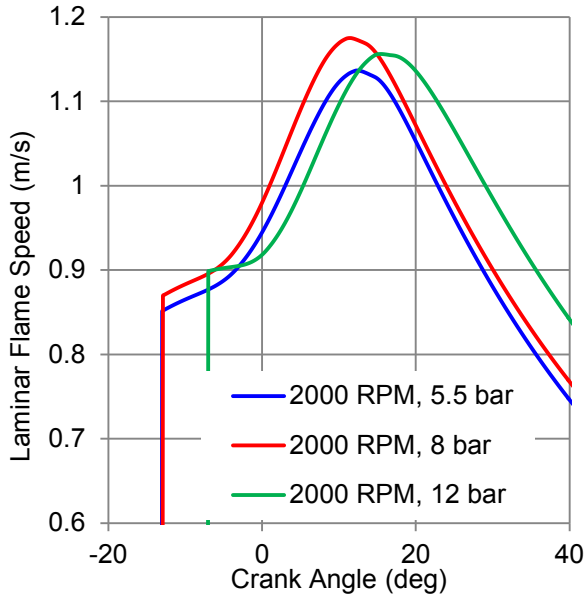


Figure 4-13: Laminar flame speed for the typical point of engine speed 2000 RPM and IMEP of 8 bar with additional engine load variation results.

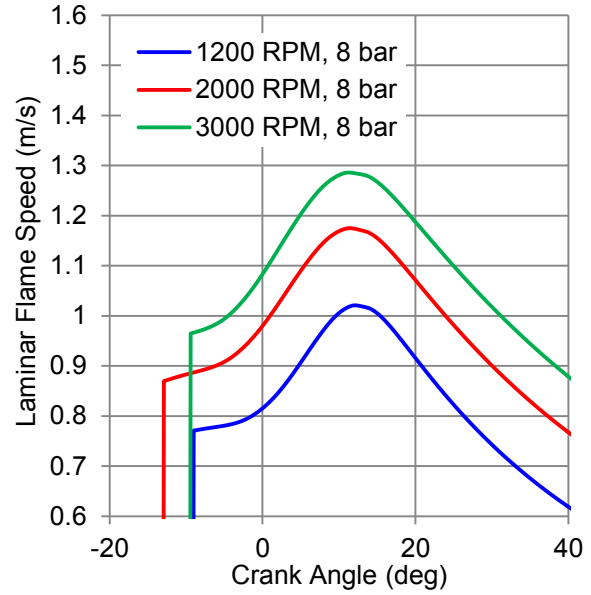


Figure 4-14 Laminar flame speed for the typical point of engine speed 2000 RPM and IMEP of 8 bar with additional engine speed variation results.

The laminar flame speed is connected with several parameters. In a typical SI engine configuration, in which fuel/air equivalence ratio ϕ is equal to unity, laminar flame speed is affected by the RBG fraction, pressure and fresh gas temperature. An increase of the laminar flame speed is observed from low to medium loads due to the decrease of RBG fraction (Figure 4-15). Beyond the RBG dominated load region, the impact of temperature is preponderant an increase of laminar flame speed is observed. The effect of late spark advance is also observed as it was expected. The laminar flame speed has a strong dependence on temperature. This dependence becomes evident in Figure 4-14, in which laminar flame speed rises with engine speed following the similar trend of fresh gas temperature (Figure 4-10).

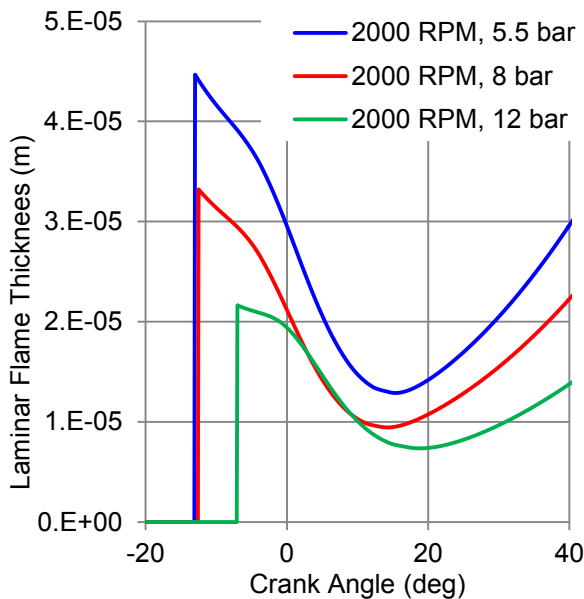


Figure 4-15 : Laminar flame thickness for the typical point of engine speed 2000 RPM and IMEP 8 bar with additional engine load variation results.

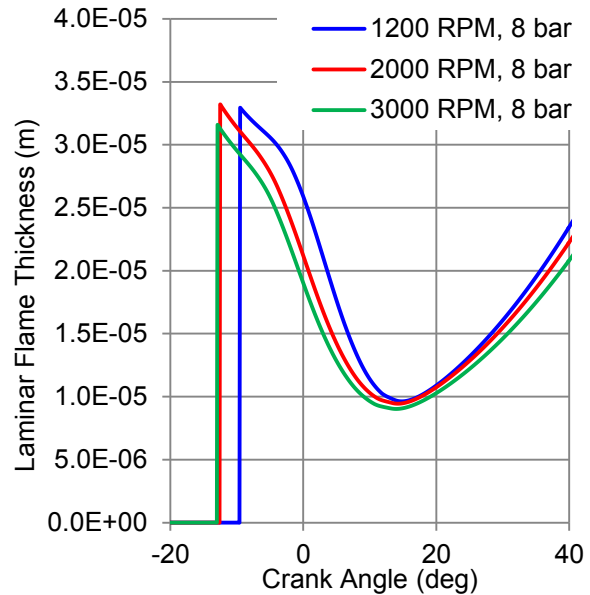


Figure 4-16 : Laminar flame thickness for the typical point of engine speed 2000 RPM and IMEP of 8 bar with additional engine speed variation results.

The laminar flame thickness is calculated by the thermal conductivity and the laminar flame speed. It diminishes when pressure and temperature increase and it rises when RBG fraction augments. Its strong dependence on pressure is shown on the load variation in Figure 4-15. A much smaller diminution is observed in the case of engine speed variation (Figure 4-16) even if the laminar flame speed varies significantly with engine speed. This fact leads to the conclusion that the laminar flame thickness is strongly connected to the fresh gas density, which is used for the calculation of thermal diffusivity. A summary of laminar flame characteristics (speed and thickness) is found in Table 4-5.

Table 4-5 : Laminar flame characteristics evolution

Isooctane	Fuel/air equivalence ratio: φ	▲ Pressure: p	▲ Unburnt gas temperature: T_u	▲ Molar RBG fraction: X_{RBG}
Laminar flame speed: s_L	▲, $0 < \varphi < 1.05$ ▼, $1.05 < \varphi$	▼	▲	▼
Laminar flame thickness: δ_L	▼, $0 < \varphi < 1.05$ ▲, $1.05 < \varphi$	▼	▼	▲

The evolution of the characteristics of the laminar flame as well as the evolution of the turbulent intensity and integral length scale permits the reconstruction of the Borghi-Peters diagram of combustion regimes (Figure 4-17). The typical operating point of engine speed 2000 RPM and IMEP 8 bar is presented from the spark ignition moment till the end of combustion. An arrow shows the direction of the curve from spark to termination. In general, the flame moves from thicker to thinner flames or from corrugated flamelets to pure flamelets. The course of the curve is explained by the form of laminar flame speed and turbulent intensity curves as well as from the laminar flame and integral length scale evolution.

The increase of u'/s_L ratio explains the upward movement of the Borghi-Peters curve when the engine regime increases. The combustion regimes moves from thin wrinkled flamelets towards thin flames when engine speed increases. The variation of engine load has a direct impact on the laminar flame thickness and the Borghi-Peters curve moves horizontally towards the corrugated flame regime, while laminar flame thickness diminishes with increasing load. For low load points with high flame thickness due to high RBG fraction and low turbulence and laminar flame speed, the spark ignition may appear in the “well stirred reactor” regime. The dashed rectangle in Figure 4-17, shows the region, in which all the operating points lie. The placement of the operating points inside the Borghi-Peters diagram justifies the use of a thin flamelets model for the usual SI premixed combustion, although a large part of the flame front evolution lies in the “thin reactions” regime.

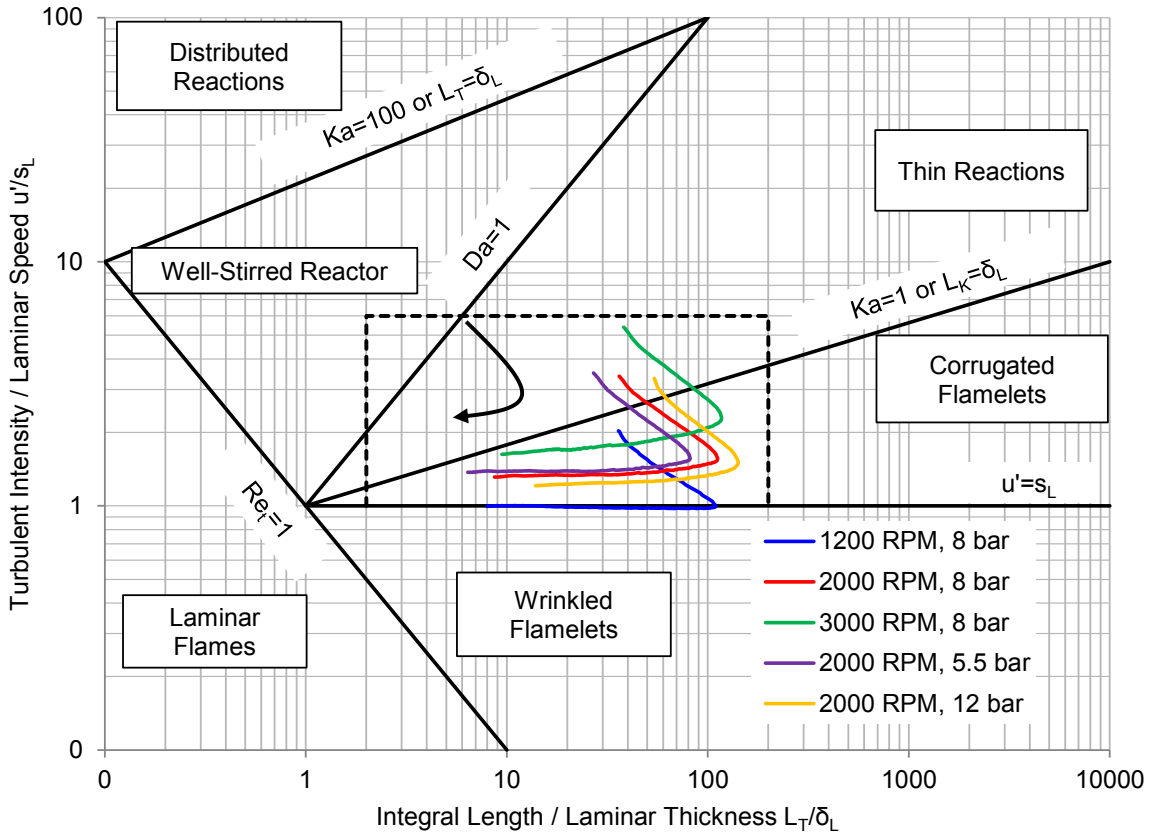


Figure 4-17: Borghi-Peters combustion diagram for the typical point of engine speed 2000 RPM and IMEP of 8 bar (red line) with additional engine load variation results (purple and orange lines) as well as engine speed variation results (blue and green lines). The black dashed rectangle (---) shows the region of in which all the operating points lie. The black arrow shows the direction of the curves from spark ignition towards the end of combustion. The combustion regime lies mostly in thin reactions or flamelets regions.

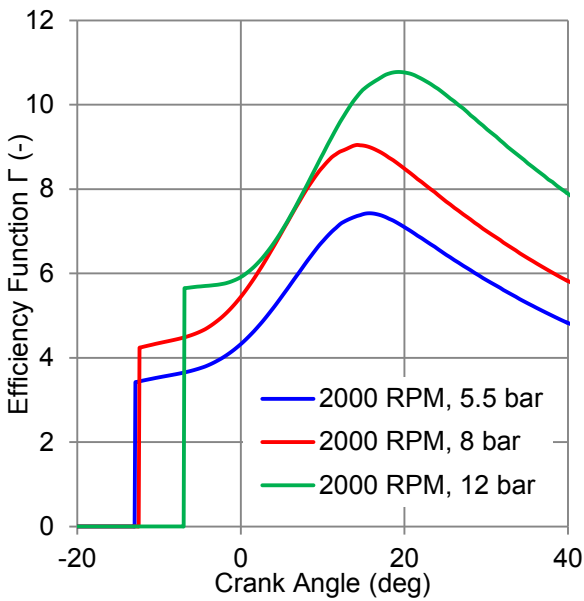


Figure 4-18: Turbulence efficiency function (Γ) for the typical point of engine speed 2000 RPM and IMEP of 8 bar with additional engine load variation results.

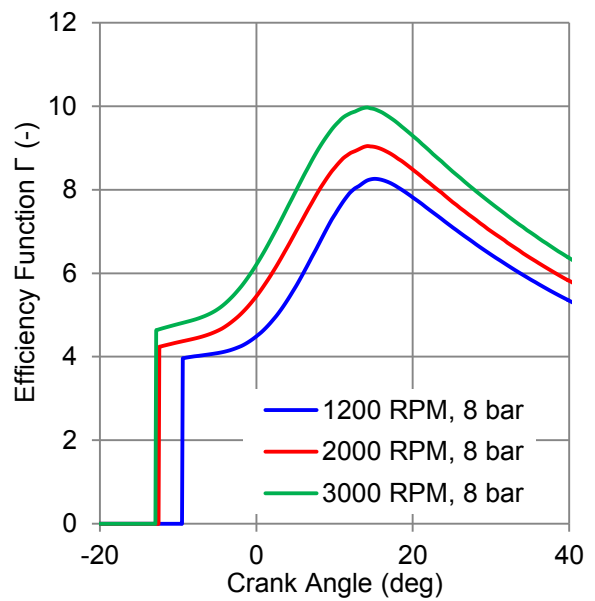


Figure 4-19: Turbulence efficiency function (Γ) for the typical point of engine speed 2000 RPM and IMEP of 8 bar with additional engine speed variation results.

Table 4-6: Efficiency function evolution

	▲ Turbulent intensity / Laminar speed: $\frac{u'}{s_L}$	▲ Integral scale / laminar thickness: $\frac{L_T}{\delta_L}$
Turbulent efficiency function: Γ	▲	▲

The impact of turbulence in the flame front is taken into account by the turbulent efficiency function Γ . As it is explained in [17], the efficiency function takes in the reduced ability of small vortices to wrinkle the flame front. When the length scale ratio L_T/δ_L tends towards zero, the efficiency function also decreases and reduces the effective strain rate. It depends weakly on the velocity ratio u'/s_L and it shows a modest increase, when u'/s_L increases. In Figure 4-18, in which the load variation of efficiency function is shown, the impact of the diminution of the laminar flame thickness is preponderant and leads to an increase of the efficiency function. An increase of this magnitude is also observed in Figure 4-19, in which turbulent intensity increases more than the laminar flame speed. The dependence of the efficiency function on the velocity and length scale ratios is summarized in Table 4-6.

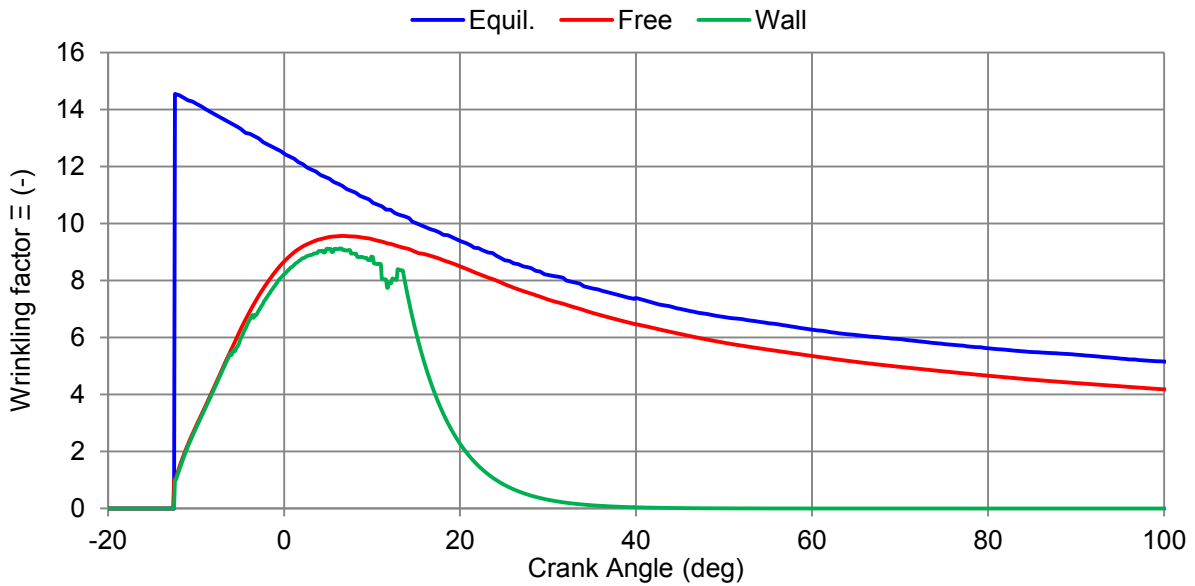


Figure 4-20: Wrinkling factor (ε) for the typical point of engine speed 2000 RPM and IMEP of 8 bar.

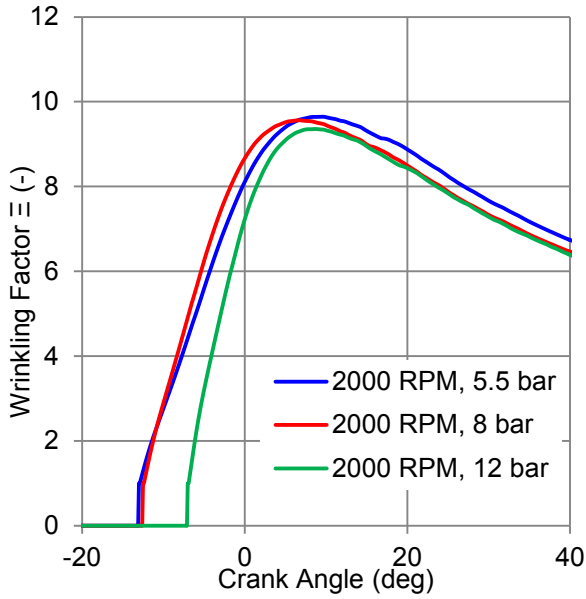


Figure 4-21: Wrinkling factor (Ξ) of free flame for the typical point of engine speed 2000 RPM and IMEP of 8 bar with additional engine load variation results.

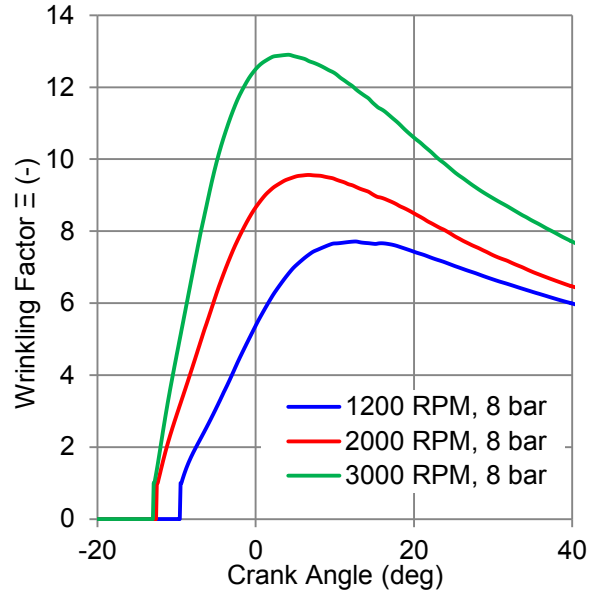


Figure 4-22: Wrinkling factor (Ξ) of free flame for the typical point of engine speed 2000 RPM and IMEP of 8 bar with additional engine speed variation results.

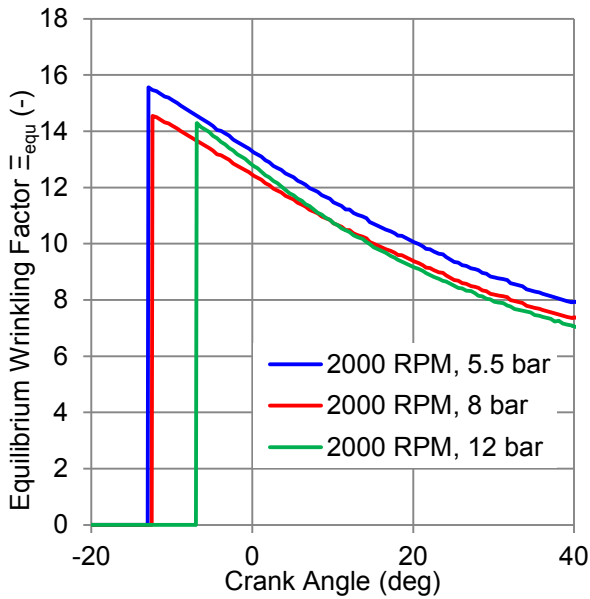


Figure 4-23: Equilibrium wrinkling factor (Ξ_{equ}) for the typical point of engine speed 2000 RPM and IMEP of 8 bar with additional engine load variation results.

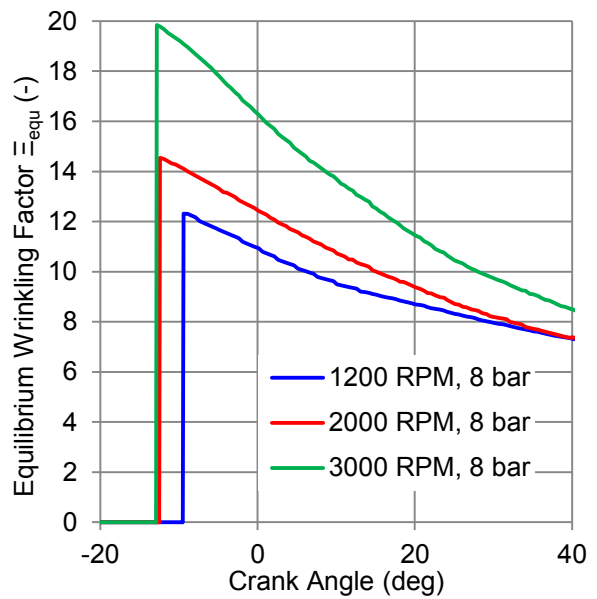


Figure 4-24: Equilibrium Wrinkling factor (Ξ_{equ}) for the typical point of engine speed 2000 RPM and IMEP of 8 bar with additional engine speed variation results.

The evolution of the wrinkling factor in its three forms (equilibrium wrinkling factor Ξ_{equ} , free flame wrinkling factor Ξ and wall wrinkling factor Ξ_w) is presented in Figure 4-20. An extended discussion about the trends of the wrinkling factor has been done in Chapter 3. In this section the dependence of the wrinkling factors on the engine load and speed variation is discussed.

The wrinkling factor does not change significantly with engine load as it is presented in Figure 4-21 and Figure 4-23. If the spark advance delay is not taken into account, the wrinkling factor diminishes with engine load. This observation shows that even if the total mass in the combustion chamber rises with engine load, the wrinkling factor stays mainly constant.

This remark is important and it will be used to explain the trends of the coefficient of the proposed model, which lies in the equilibrium wrinkling factor. Moreover, this remark cannot be considered as globally valid, because its derivation is based on specific models values of the laminar flame speed and of the turbulent intensity.

Table 4-7: Equilibrium wrinkling factor evolution

	▲ Turbulent intensity / Laminar speed: $\frac{u'}{s_L}$	▲ Schmidt number (constant for all points): Sc	▲ Turbulent efficiency function: Γ
Equilibrium wrinkling: \mathcal{E}_{equ}	▲	▼	▲

Table 4-8: Wrinkling factor evolution

	▲ Turbulent intensity / Laminar speed: $\frac{u'}{s_L}$	▲ Equilibrium wrinkling factor: \mathcal{E}_{equ}	▲ Turbulent efficiency function: Γ
Wrinkling factor: \mathcal{E}	▲	▲	▲

Wrinkling factor (both equilibrium and free flame) increases with engine speed. The combined effect of turbulent intensity and efficiency function rise appears also in Figure 4-23 and in Figure 4-24. The variation of the equilibrium wrinkling factor \mathcal{E}_{equ} is summarized in Table 4-7. It must be noted that the Schmidt number mostly depends on the fuel and on the fuel/air equivalence ratio φ and it remains mainly constant during a combustion cycle as well as throughout the operating points.⁴ The variation of the wrinkling factor of free flame is summarized in Table 4-8.

In Table 4-9, the evolution of mean flame surface in a cycle is given. It shows a peak value for a flame radius value equal to the 2/3 of the bore radius. If the spark ignition difference between the operating points is omitted, the mean flame surface does not seem to change either with engine load (Figure 4-25) or with engine speed (Figure 4-26). The piston position is the same for all operating points and depends on the crank angle θ . Flame radius evolution is almost constant with engine load (Figure 4-27) and engine speed (Figure 4-28) (with spark ignition difference excluded). In the engine speed variation combustion duration is the same in terms of crank angle degrees but it diminishes in terms of time ($\Delta\theta = 6N\Delta t$). This behavior is also shown in [32], in which simulated and experimentally derived flame radius results are presented and discussed.

⁴ Schmidt number remains constant throughout the operating points as long as $\varphi = 1$. This may not be true in high engine speeds and loads where the mixture tends to be rich in order to increase laminar flame speed and thus achieve maximum torque.

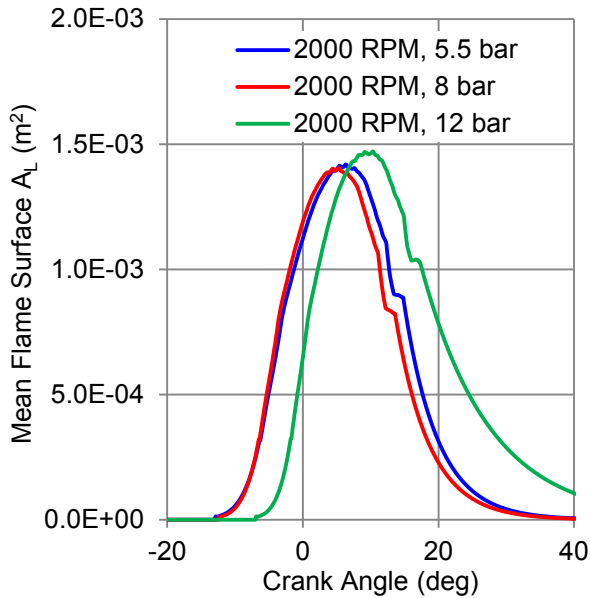


Figure 4-25: Mean flame surface for the typical point of engine speed 2000 RPM and IMEP of 8 bar with additional engine load variation results.

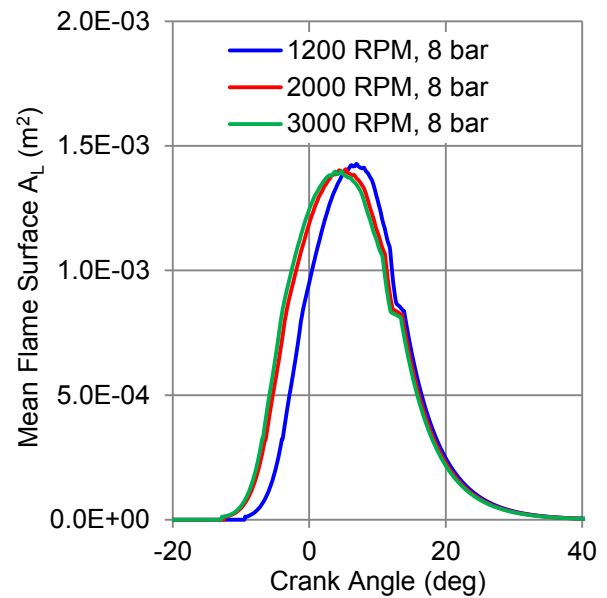


Figure 4-26: Mean flame surface for the typical point of engine speed 2000 RPM and IMEP of 8 bar with additional engine speed variation results.

Table 4-9: Mean flame surface and volume evolution. R_f^0 is the critical value, for which mean flame surface reaches its maximal value.

	▲ Flame radius: R_f	▲ Piston position: H_p
Mean flame surface: A_L	▲, $0 < R_f < R_f^0$ ▼, $R_f > R_f^0$	▲ ⁵
Volume of mean flame surface: V_L	▲	▲

The last variable, which is a part of the burnt mass evolution equation, is the mean flame surface A_L . This variable is a function of the piston position H_p and of the flame radius R_f .

Flame radius evolution starts with the value of 0.5 mm. This happens at spark ignition advance angle, when the initial flame kernel is deployed between the electrodes of the flame. After the flame radius has passed the bore radius and the enclosed volume by the flame has reached 90% of the combustion chamber, in most operating points, the burnt gas volume calculated by the geometric model (V_L) does not coincide with the calculated by the thermodynamic model burnt gas volume (V_b) while the flame radius is increasing. This explains the abrupt and unphysical increase of the flame radius in Figure 4-27 and in Figure 4-28. In this case, the wall flame interaction model takes into account the increase of flame radius for the calculation of the wall corrected wrinkling factor. It would not be unjustified to allow the decrease of the flame radius, when it crossed the bore radius, since the actual wrinkled flame surface is not actually known. Finally, the radius inconsistency of this kind takes place the burnt mass fraction has always passed 75% and the volume fraction has passed 90%, the post HC reactions model is enabled.

⁵ If the flame does not intersect with the piston, its value is constant for a constant flame radius.

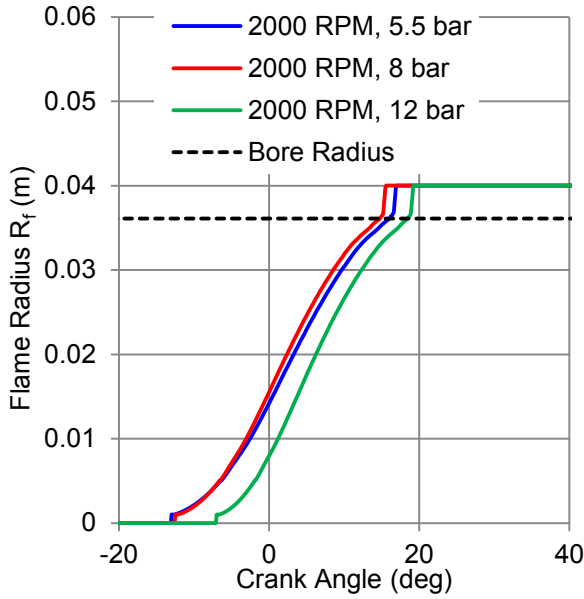


Figure 4-27: Flame radius for the typical point of engine speed 2000 RPM and IMEP of 8 bar with additional engine load variation results.

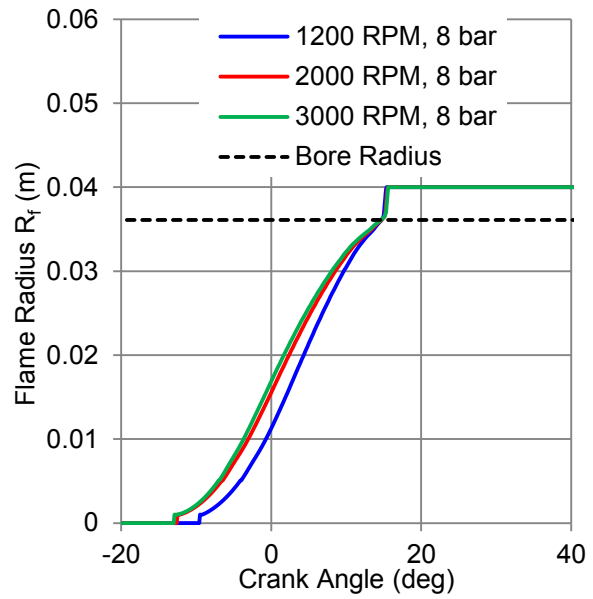


Figure 4-28: Flame radius for the typical point of engine speed 2000 RPM and IMEP of 8 bar with additional engine speed variation results.

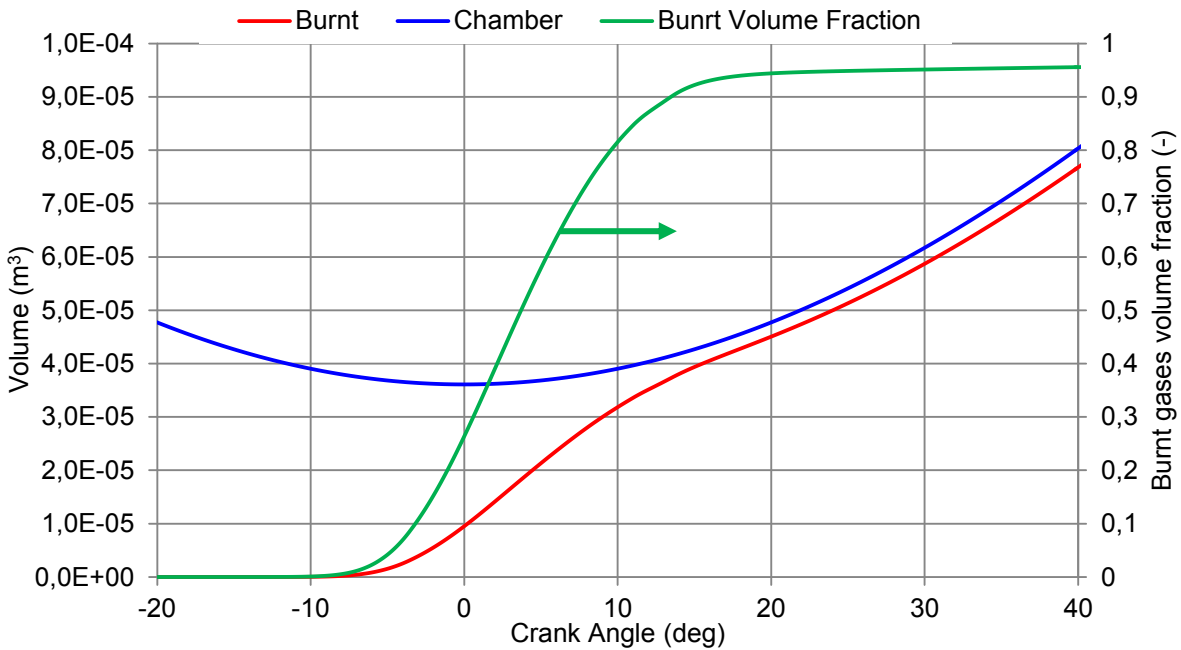


Figure 4-29: Volume of burnt gases for the typical point of engine speed 2000 RPM and IMEP of 8 bar. The burnt gas volume fraction is presented on the secondary Y axis on the right.

The burnt gas volume evolution is shown in Figure 4-29. Burnt gas volume follows the increase of flame radius and it tends asymptotically to the chamber volume value. This fact is also shown by the green line, which represents the fraction of the burnt gases volume divided by the chamber volume. It is useful to note that the burnt volume fraction is greater than the burnt mass fraction and they are connected with the following relation:

$$x_b = \left[1 + \frac{\rho_u}{\rho_b} \left(\frac{1}{y_b} - 1 \right) \right]^{-1} \quad (4-2)$$

In Figure 4-30 the mass fractions of the major species are presented, as they were calculated by the thermodynamic model. The mean temperature of the chamber is also presented on the secondary Y axis. Nitrogen (N_2) remains quasi constant since only a small amount of it reacts with oxygen and produces NO_x (see the discussion in Chapter 1). Carbon dioxide (CO_2) and water (H_2O) which are the main products of combustion follow the consumption of fuel and oxygen (O_2). The maximum carbon monoxide (CO) fraction is of the order of 0.01 and hydrogen concentrations are very low with an order of magnitude of 10^{-4} . When the mean flame temperature reaches its maximum value (at about 18 deg), the reactions continue but with a very low rate.

In Figure 4-31 the mass fractions of the minor species are presented, as they were calculated by the thermodynamic model. The burnt temperature of the chamber is also presented on the secondary Y axis. An estimation of the minor species is essential. Especially in this work, in which kinetic schemes are used for the calculation of CO and unburnt HC an estimation of some species (OH for example) is indispensable. The maximum concentration of NO and OH appears for a burnt gas temperature 2550 K. Maximum concentrations of monoatomic hydrogen (H) and monoatomic nitrogen (N) are of the order of 10^{-5} and 10^{-8} respectively.

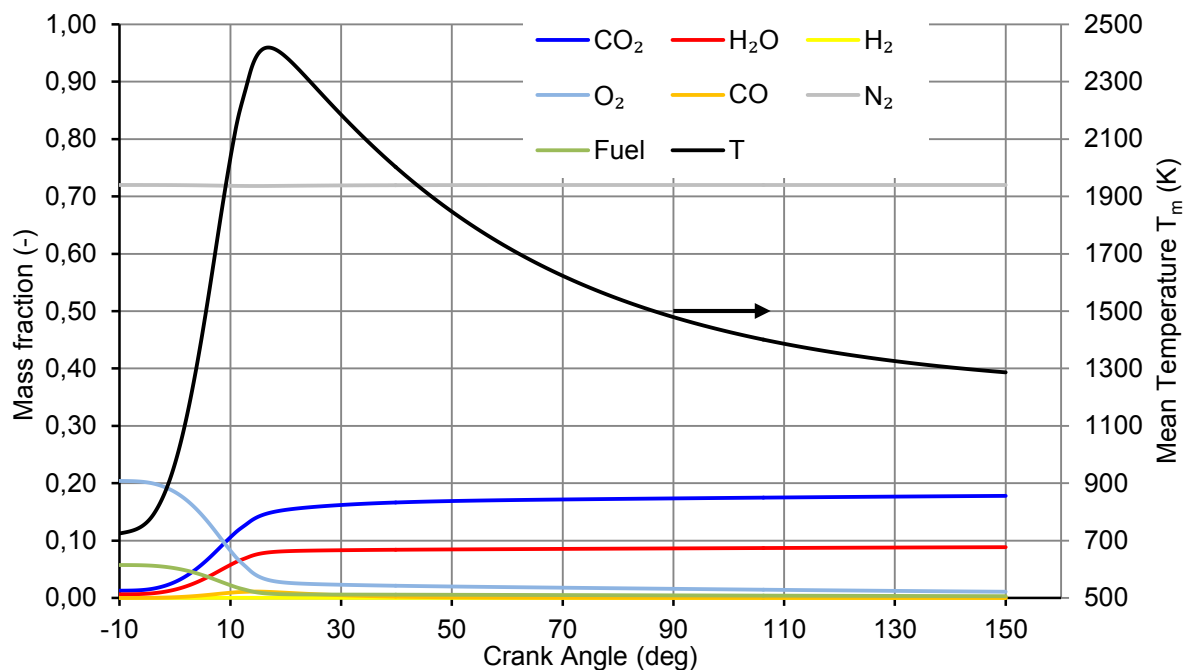


Figure 4-30: Mass fractions of major species in equilibrium as calculated by the thermodynamic model for the typical point of engine speed 2000 RPM and IMEP of 8 bar. The mean temperature of the chamber is presented on the secondary Y axis on the right.

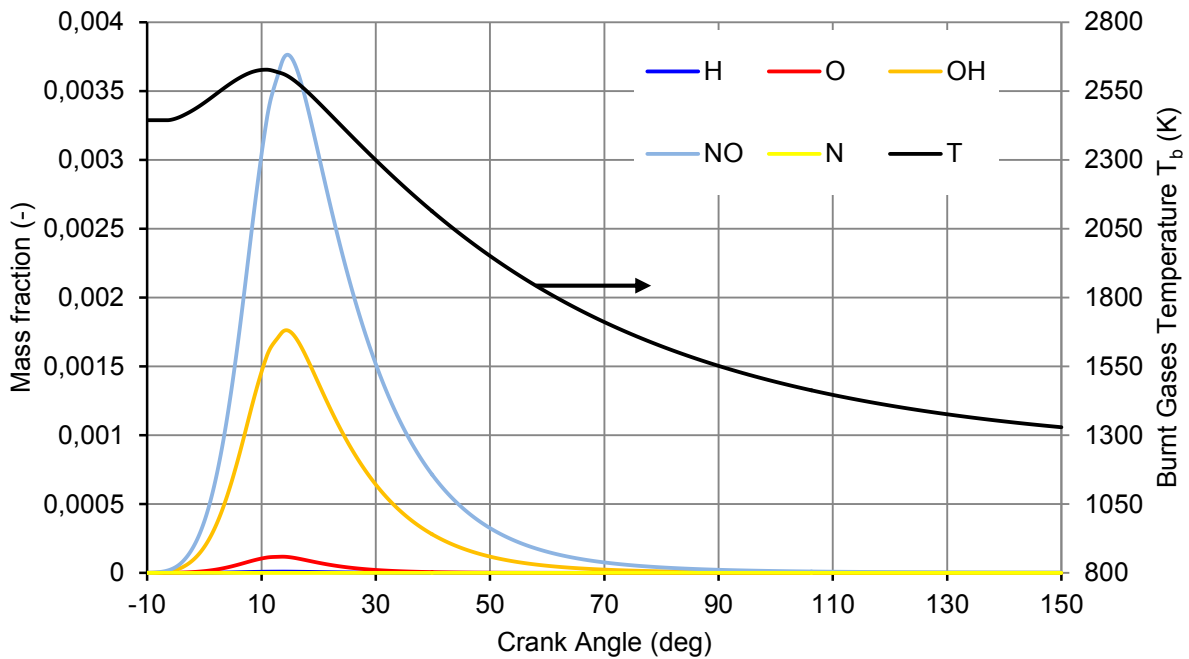


Figure 4-31: Mass fractions of minor species in equilibrium as calculated by the thermodynamic model for the typical point of engine speed 2000 RPM and IMEP of 8 bar. The burnt gases temperature is presented on the secondary Y axis on the right.

In Figure 4-32 the experimentally derived and the model heat release are compared for the operating point of engine speed 2000 RPM and of IMEP 8 bar. The model response follows the trends of the experimental curve. In Figure 4-33 the model burnt mass fraction is superposed on the characteristic combustion angles of the same operating point. The combustion efficiency, as computed by equation (4-1), is also in the figure at the crank angle of the exhaust valve opening. Apart from CA90 angle, the model captures correctly the evolution of combustion. The maximum heat release rate crank angle is the same as the maximum wrinkling angle, as is evident in Figure 4-20.

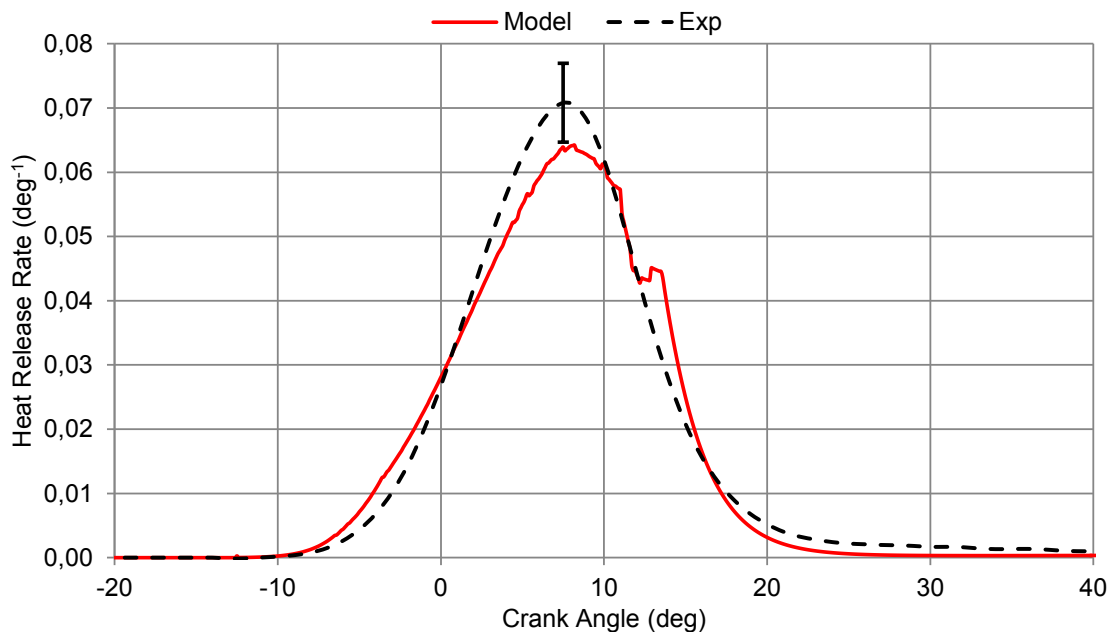


Figure 4-32 : Heat release rate (\dot{x}_b) for the typical point of engine speed 2000 RPM and IMEP of 8 bar.

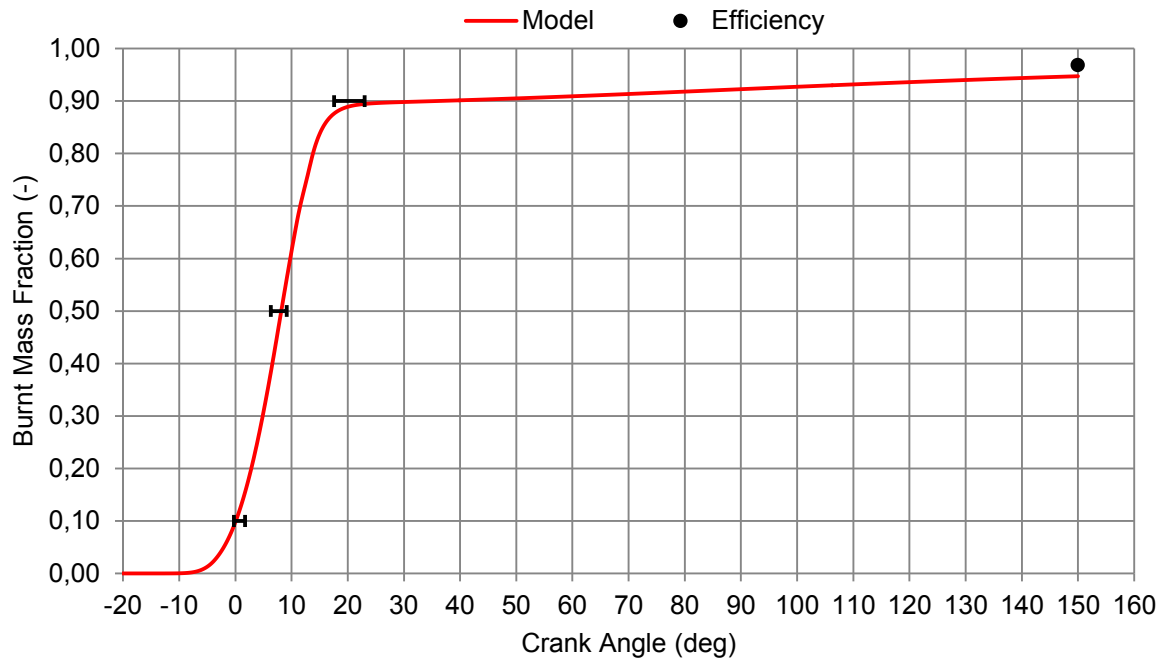


Figure 4-33: Burnt mass fraction for the typical point of engine speed 2000 RPM and IMEP of 8 bar.

4.2.2 Operating points of particular interest

In this section the results of two operating points with particular interest are presented: A low load operating point (engine speed 1200 RPM and IMEP 3 bar) and a high load operating point (engine speed 3000 RPM and IMEP 16 bar).

In the low load case, the maximum pressure of the simulation curve is offset from the expected point of 13 crank angle degrees by 4 degrees (Figure 4-34). This is explained by the heat release results (Figure 4-35), in which it is evident that the combustion model starts correctly but it cannot follow the experimental curve. The experimental maximum of heat release rate is found at 7.5 degrees as expected, whereas the model maximum heat release point is at 12.5 deg. The same remark can be made on the burnt mass fraction curve (Figure 4-36), in which the CA50 is missed by the model. The maximum heat release angle is the same as the maximum wrinkling factor angle (Figure 4-37), as discussed in the previous section. The reason for this delay of the wrinkling factor can be found in the nature of the wrinkling factor equation, which does not include a spark ignition and beginning of combustion model. Consequently, it is expected that in some operating points the beginning of combustion is not taken into account correctly. An attempt to correct this problem is to slightly change the spark advance angle, so as that maximum pressure crank angle reaches the expected value of 13 degrees (low and medium loads). In the pressure, heat release and burnt mass fraction figures of this low load point operating points, results with modified spark ignition advance are shown (spark advance happens 2 degrees earlier than the actual angle).

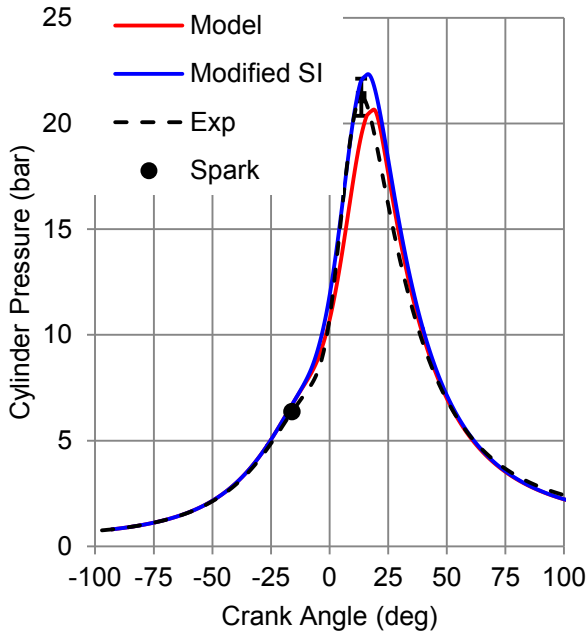


Figure 4-34: Pressure evolution for the low load operating point of engine speed 1200 RPM and IMEP of 3 bar.

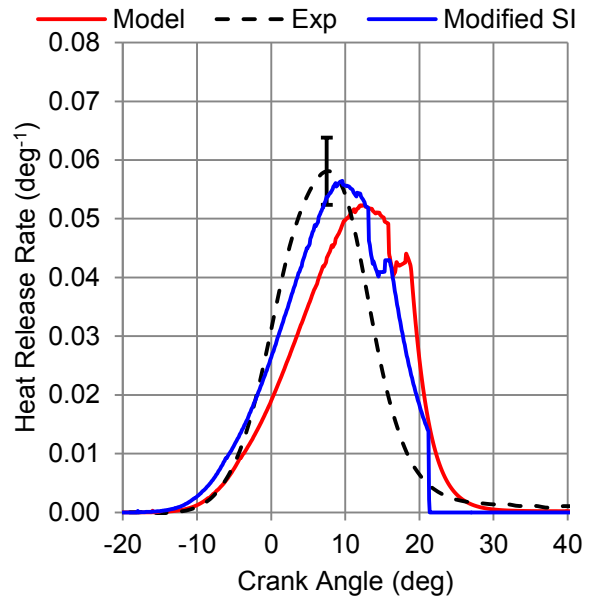


Figure 4-35: Heat release rate (\dot{x}_b) for the low load operating point of engine speed 1200 RPM and IMEP of 3 bar.

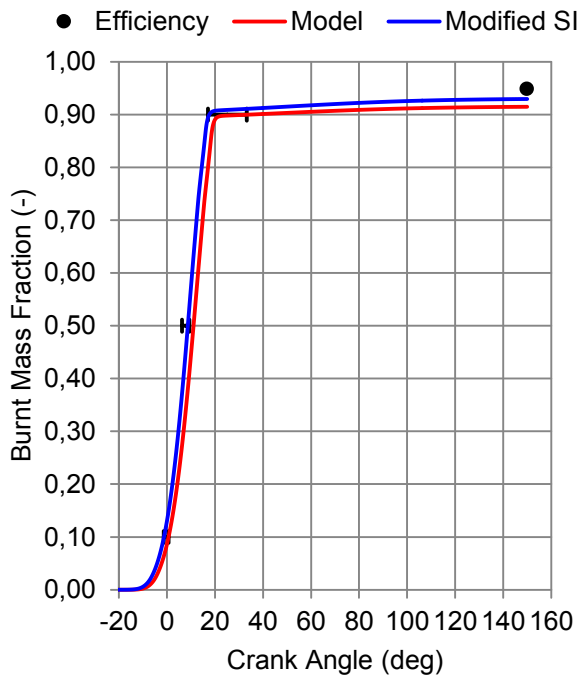


Figure 4-36: Burnt mass fraction for the low load point of engine speed 1200 RPM and IMEP of 3 bar.

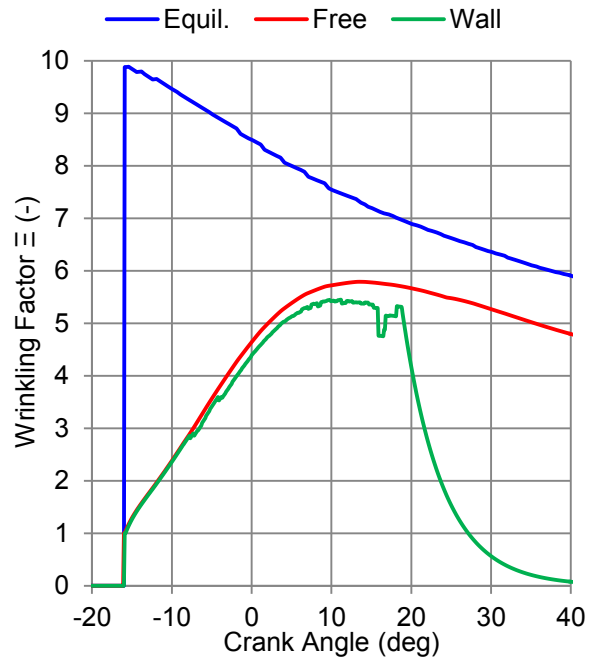


Figure 4-37: Wrinkling factor (ξ) for the low load operating point of engine speed 1200 RPM and IMEP of 8 bar.

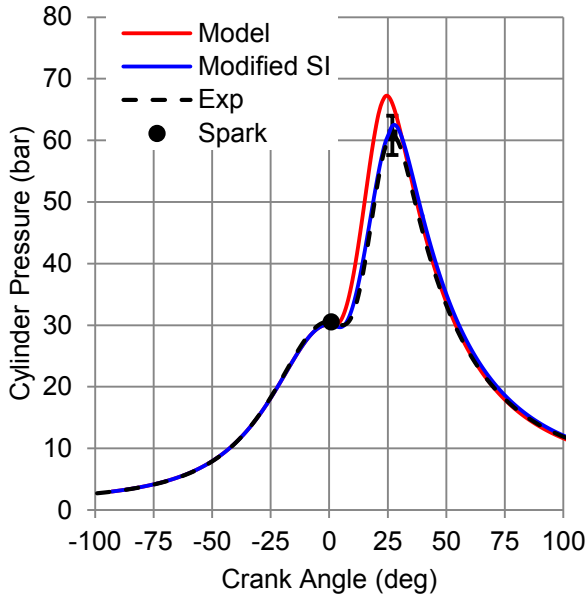


Figure 4-38: Pressure evolution for the full load operating point of engine speed 3000 RPM and IMEP of 16 bar.

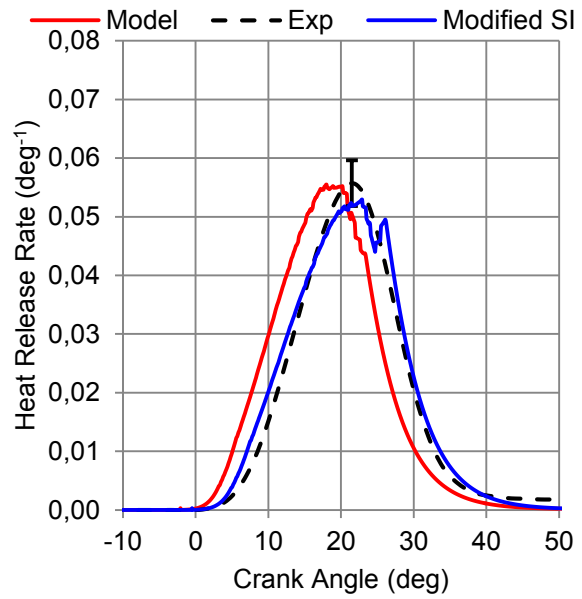


Figure 4-39: Heat release rate (x_b) for the full load operating point of engine speed 3000 RPM and IMEP of 16 bar.

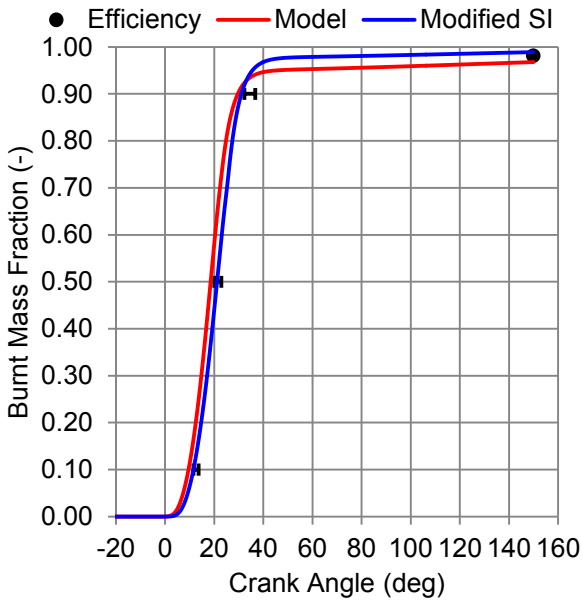


Figure 4-40: Burnt mass fraction for the full load operating point of engine speed 3000 RPM and IMEP of 16 bar.

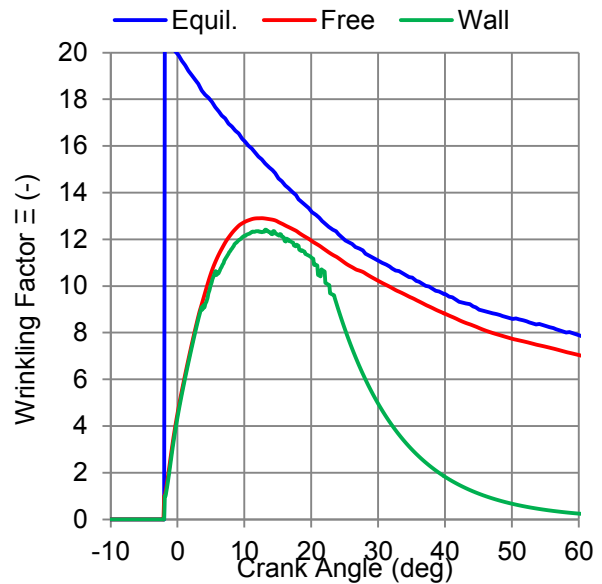


Figure 4-41: Wrinkling factor (\mathcal{E}) for the full load operating point of engine speed 3000 RPM and IMEP of 16 bar.

The same phenomenon, but in the opposite direction, appears for a high load point of 3000 RPM and IMEP 16 bar: When the model runs with the same spark advance with the experiment, modeled combustion is much faster than the experimental one. This is evident in the pressure comparison (Figure 4-38) as well as in the heat release and burnt mass fraction figures (Figure 4-39 and Figure 4-40). A modified spark advance (delay of 1.5 deg from the original advance) is also applied in order to correct this problem. The uncertainty in the high load case is that the maximum pressure angle does not appear at 13 degrees because of the late spark advance imposed by knocking.

4.2.3 Results for all operating points

Table 4-10: Results for the wrinkling factor in function of engine load for an engine speed of 2500RPM taken from [52]. Flame wrinkling increases with engine load in this case.

Engine speed (RPM)	2500	2500	2500	2500
IMEP (bar)	3.5	8	14	19
Maximum flame wrinkling ε (-)	7.5	10	12	15

In this section the values of the calibrating coefficient (Figure 4-42) of the model are presented for all the operating points of Figure 4-2. The spark advance of the simulations is slightly different from the experimental spark advance. This change is applied in order to obtain a good agreement of CA50. The correct calculation of CA50 will serve as a solid base for the calculation of the end of combustion. The pressure, heat release, burnt mass fraction and wrinkling factor figures for all operating points, which have not been presented in this chapter are shown in Appendix D with the original spark advance values. The coefficient varies with engine speed and engine load. This variation in function of engine load is caused by the turbulence which is not the exactly the same as the load varies as well as from the behavior of the efficiency function, which increases with engine load (Figure 4-18), while the wrinkling is almost the same for all operating points of the same engine speed (the effect of turbulence, which increases with engine speed, is preponderant and there is small change in function of engine load). It must be noted, that in [52], results of flame wrinkling are given and the wrinkling factor is not constant with engine load but is shows an increasing trend. Those results are summarized in Table 4-10. This behavior does not agree with the results of this work. Such a difference can be justified by the different laminar flame speed equation, which is used in the model of [52] or from differences in the turbulence values, which are not shown in that work.

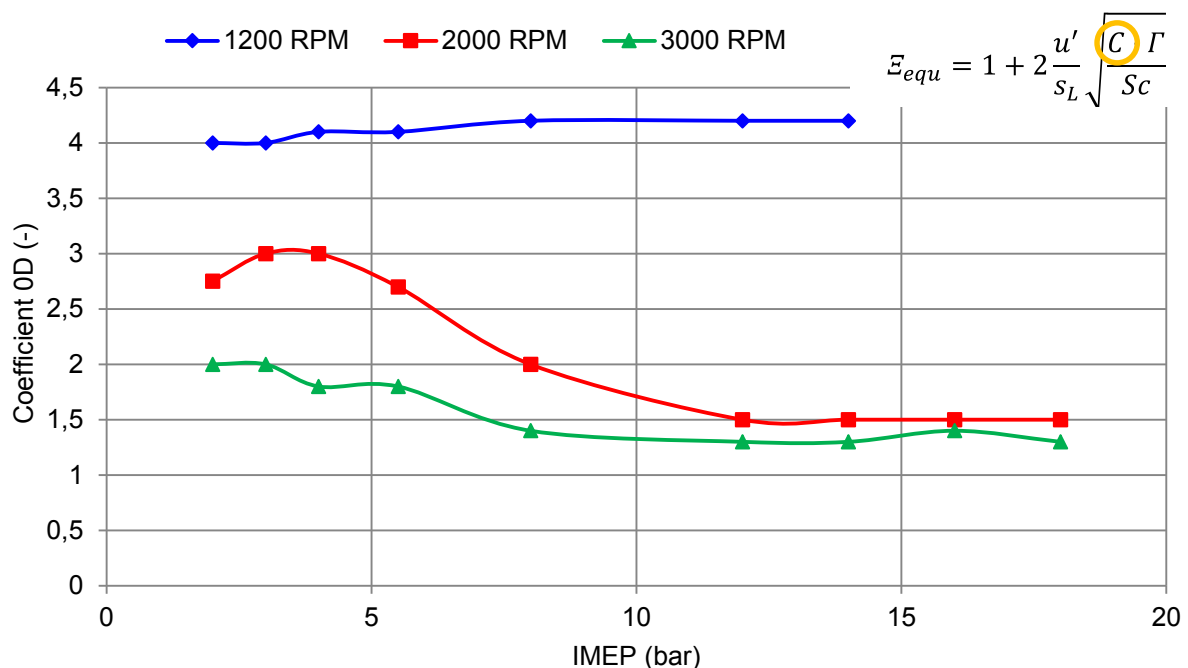


Figure 4-42: Coefficient of the FSD model in the equilibrium wrinkling factor for all operating points. The coefficient is underlined by the orange circle in the ε_{equ} equation.

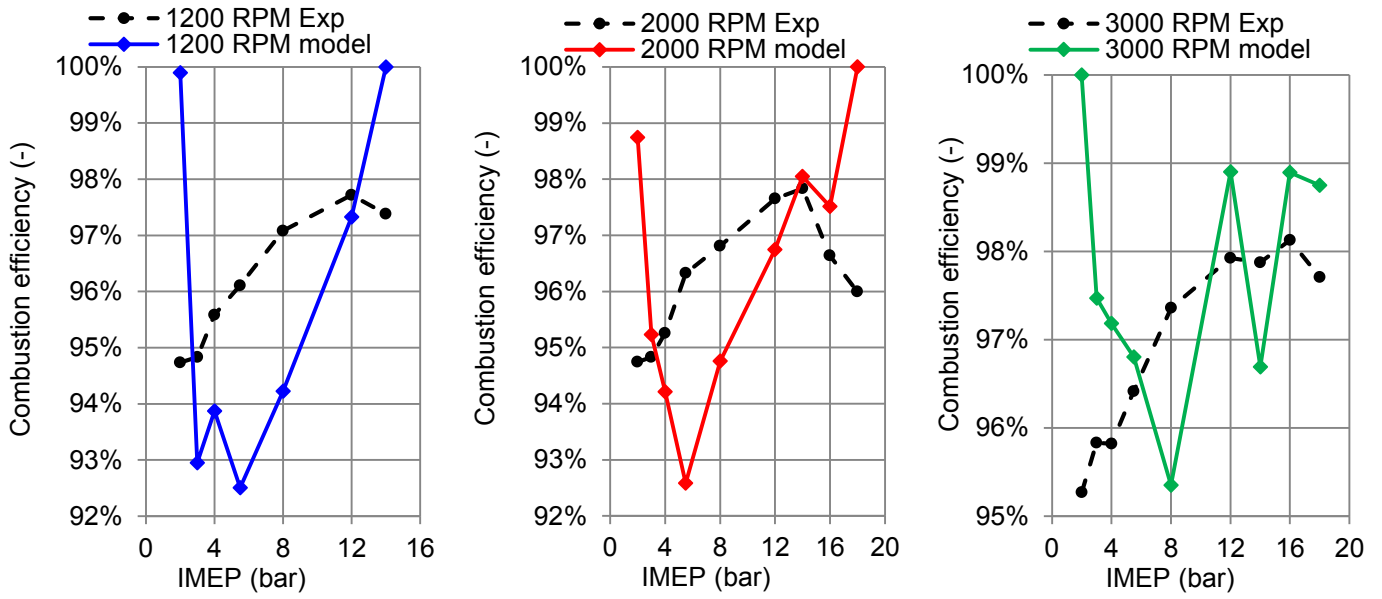
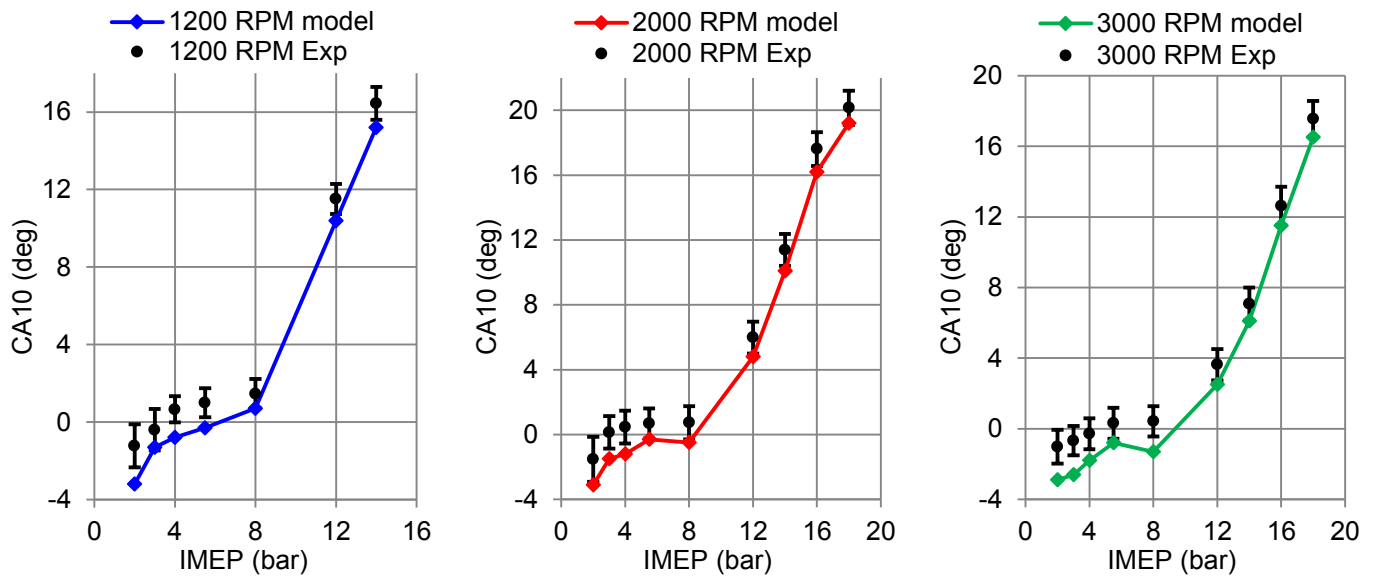


Figure 4-43: Combustion efficiency for all operating points.



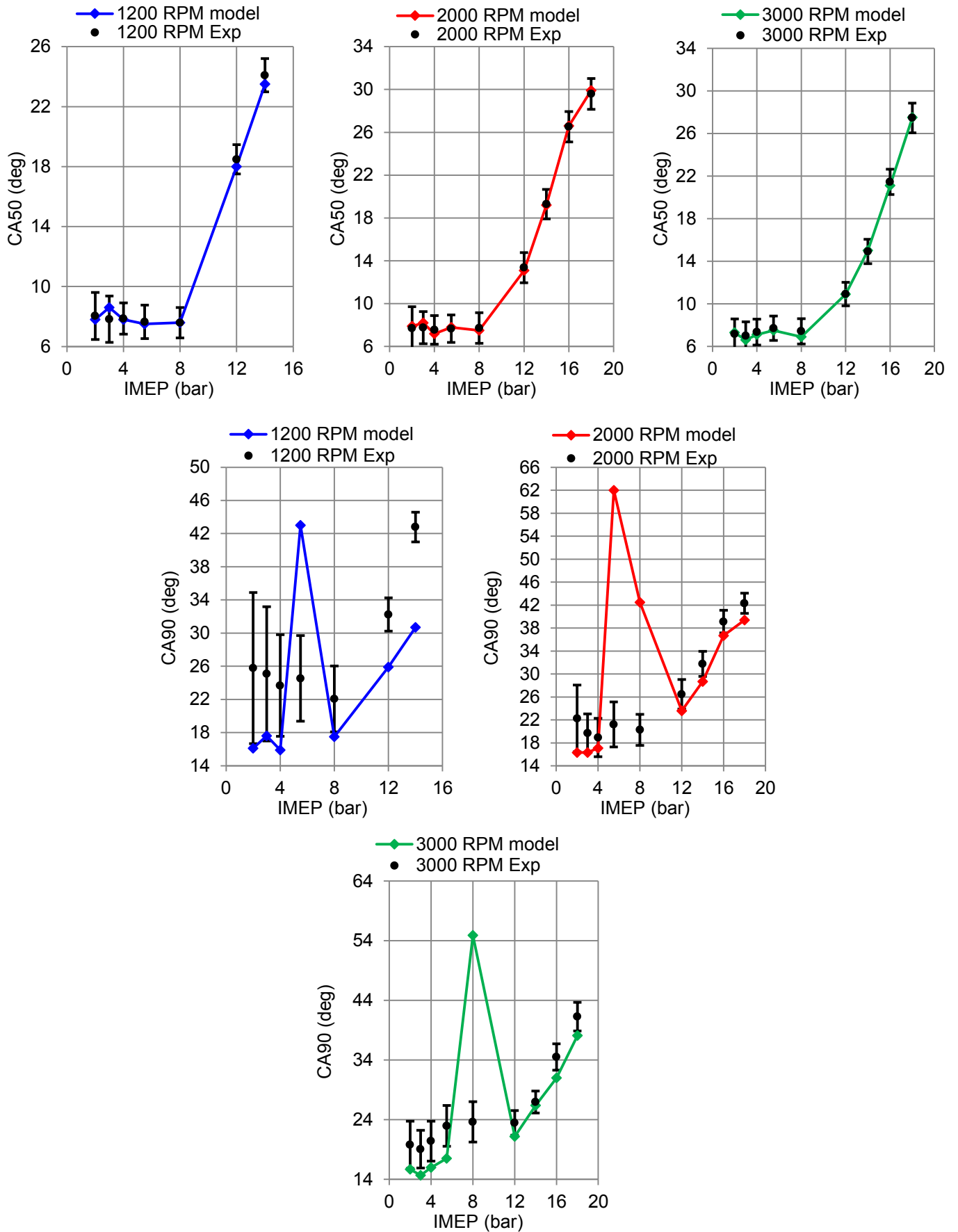


Figure 4-44: Characteristic combustion angles for all operating points.

Simulation results and experimental measurements are compared in Figure 4-43. The combustion model reaches a level of more than 94% of burnt mass for all operating points. In some points the entire fuel mass is consumed. As it was shown in the analysis of the post flame reaction model (section 3.10), the model takes into account the latest stage of combustion and in function of temperature and diffusion characteristics of the fresh gases. It is difficult to discern the source (post flame reaction or flame front) of misestimation of the combustion efficiency. For the operating point of engine speed 2000 RPM and IMEP 18 bar, the experimental CA90 is at 31.8 crank angle degrees whereas the simulation CA90 is at 28.5 degrees (see Figure 4-44 for the characteristic combustion angles of all operating points). Yet the combustion efficiency for this point is essentially the same between experiment and simulation (97.8% and 97.9% respectively). For the operating point of engine speed 2000 RPM and IMEP 18 bar the experimental values and the simulation results almost coincide for the end of combustion (CA90: 42.3 – 42.9 and efficiency 96.0% - 95.7% respectively). This observation leads to the conclusion that when the termination of flame front combustion is correctly simulated (correct CA90 in this case), the combustion efficiency is correctly calculated.

The inconsistency of the flame wall interaction model results with the experimental values of CA90 combustion angle as well as combustion efficiency is due to its limitation of calculating the flame front mean surface correctly during the last stage of combustion. In order to clarify the nature of the flame front shape at the last stage of combustion a calculation with 3D CFD RANS model has been performed for the operating point of engine speed 2000 RPM and IMEP 8 bar.

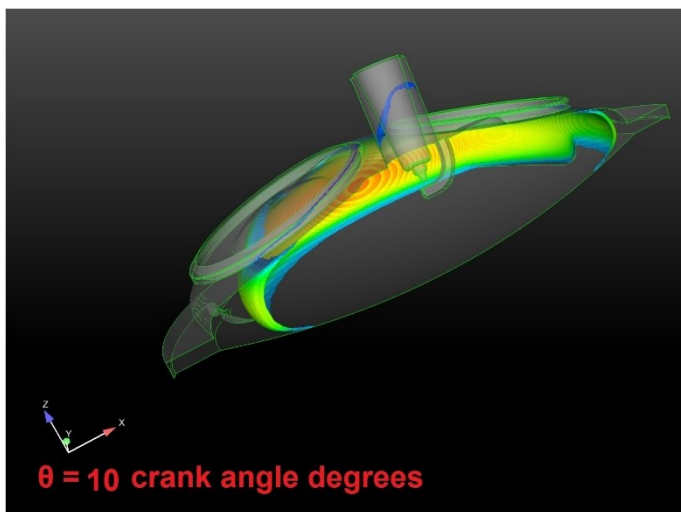


Figure 4-45: CFD combustion calculation of the operating point with engine speed 2000 RPM and IMEP 8 bar. Flame front is shown at CA50 angle.

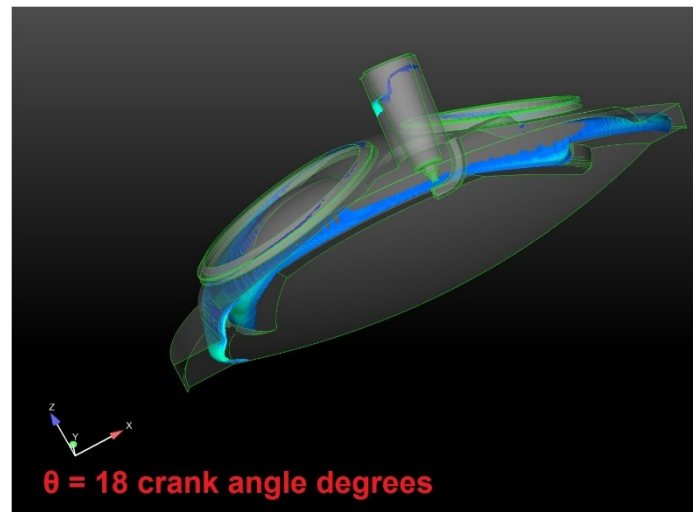


Figure 4-46: CFD combustion calculation of the operating point with engine speed 2000 RPM and IMEP 8 bar. Flame front is shown at CA90 angle.

The combustion process is simulated with a G-equation model. In Figure 4-45 the flame front at CA50 angle is shown. It can be observed that the flame front is rather elliptical spherical, as it is assumed in this 0D combustion model. This shape is imposed by the turbulent boundary layer (highly diffusive and low mean velocity region adjacent to the wall). In Figure 4-46, the flame front is shown at CA90 angle. It can be observed that the assumption of the spherical flame front is no longer valid for the last stage of combustion. After the threshold of the burnt mass fraction of 0.80 (valid for most operating points), the geometrical spherical surface will become equal to zero due to very high radius. In such cases, the wall-flame

model cannot calculate correctly the burning rate, although the flame front exists as it shown in CFD results. This limitation of the model explains the inconsistencies of the CA90 and combustion efficiencies simulation results.

4.3 Specific tests for sub-model validation

In this section, the experimental results of several specific test engine configurations will be used for the validation of the combustion model. In fact, each test employs the alteration of a physical variable in the model and puts into question the capabilities of the global model and the response of the basic sub-models (laminar flame characteristics, coefficient of wrinkling factor).

The sub-models of the laminar flame characteristics (speed and thickness) as well as the turbulent flame (flame wrinkling) can be validated. Three configurations are employed:

1. Variation of the fuel air equivalence ratio from lean to stoichiometric conditions.
2. Use of a gasoline-ethanol blend E85 fuel (85% ethanol volume fraction).
3. Earlier IVO and IVC, which increase the RBG fraction of the cylinder charge.

The validation test cases as well as their impact on combustion and on the model coefficient are summarized in Table 4-11.

Table 4-11: Special test in order to validate the various sub-models of the combustion model.

Type of test	Impact on combustion	Comment
<u>Fuel/air equivalence ratio ϕ (-)</u> : 0.75 – 1 Engine speed: 2000 RPM, IMEP: 3bar	Ignition delay ($\phi \nabla$) Combustion instabilities ($\phi \nabla$)	Coefficient of optimal spark advance
<u>Ethanol-gasoline blend (E85): Spark timing variation</u> Engine Speed 1200 RPM, IMEP: 3 bar	New correlation for laminar speed for high ethanol content fuels	Coefficient of optimal spark advance
<u>Intake VVT⁶</u> : standard configuration and 40 advance of IVO and IVC Engine speed: 1200 and 2000 RPM, IMEP: 3-18 bar	▲ RBG (due to wider valve overlap), ▲ Ignition delay	Coefficient will surely change

⁶ This particular test configuration has been performed in a three-cylinder engine, with the same characteristics of the single-cylinder engine, which is described in section 4.1. In general, the variation of valve timing in the single-cylinder engine test bed is manual and therefore difficult to employ. On the contrary, variable valve timing is easier in the multi-cylinder engine.

4.3.1 Fuel/air equivalence ratio variation

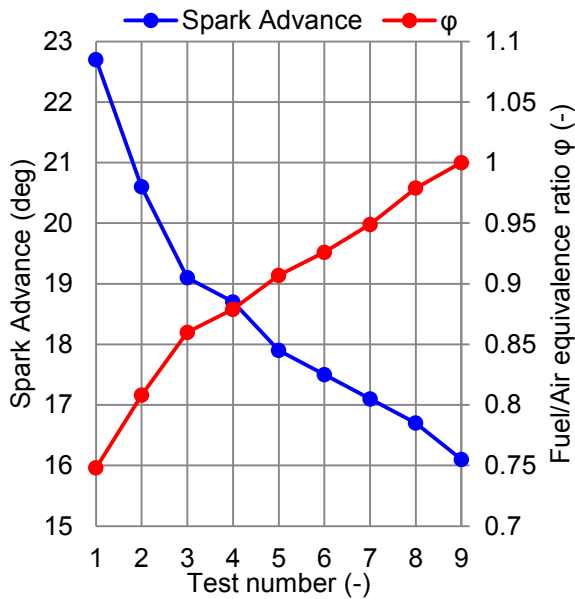


Figure 4-47: Spark advance angle (left Y axis) and fuel/air equivalence ratio ϕ (right Y axis) for engine speed 2000 RPM and IMEP 3 bar operating points.

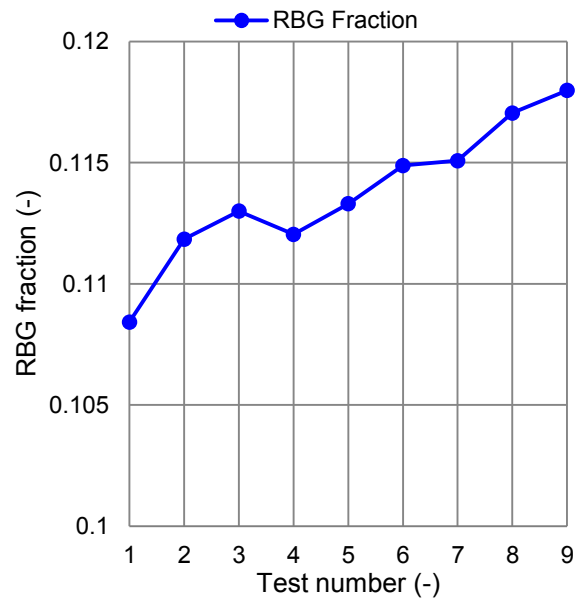


Figure 4-48: RBG fraction for engine speed 2000 RPM and IMEP 3 bar operating points. It is essentially constant.

The fuel/air equivalence ratio ϕ is a fundamental variable of the laminar flame. It is, of course, a fundamental variable for the engine performance and efficiency but, in this discussion, the impact on laminar flame speed will be enlightened. For this test, a fuel/air equivalence ratio variation from lean to stoichiometric conditions for the operating point of engine speed 2000 RPM and IMEP 3 bar and has been chosen. The values of spark advance as well as the fuel/air equivalence ratio values are presented in Figure 4-47. Since the IMEP must be always equal to 3 bar, the spark advance diminishes as long as the fuel/air equivalence ratio increases. This decrease is expected since the laminar flame speed is higher, when the $\phi \rightarrow 1$ (see Table 4-5). The estimated RBG fraction (Figure 4-48) for all testing points rests between 0.105 and 0.12. This confinement of RBG fraction values ensure that the laminar flame speed will not be affected by RBG fraction. The thermo-diffusive characteristics of the flame, as they are expressed by the Lewis number, do not vary significantly for the lean to stoichiometric values of fuel/air equivalence ratio. Finally, pressure and temperature conditions remain the same for all tests since the operating point is the same (2000RPM, 3 bar). The laminar flame increase, while moving from lean to stoichiometric conditions is apparent in Figure 4-49.

The model coefficient is the same for the operating point of 2000 RPM and 3 bar (see Figure 4-42). It is expected to retrieve an increase of flame wrinkling when moving from stoichiometric to lean conditions, since wrinkling is a function of the u'/s_L ratio and u' remains constant. This expected evolution of flame wrinkling is retrieved in Figure 4-50. The wrinkling level of the stoichiometric point ($\phi = 1.004$), is the same as the one of the optimal spark advance case of engine speed 2000 RPM and IMEP 3 bar (see Appendix D).

In Figure 4-51, the experimental and simulated heat release rate are compared and in Figure 4-52 the simulated burnt mass fraction along with the experimentally derived characteristic combustion angles are shown for the leanest case of $\phi = 0.748$. The behavior of the

heat release rate is similar to the characteristic operating point, which was presented in section 4.2.2. The simulated ignition delay time is lower (earlier CA10 for the model) but the main flame development phase is slower in the model (later CA50 for the model). The heat release after the CA50 is elevated and the total burnt mass fraction reaches unity, while the combustion efficiency is 0.944.

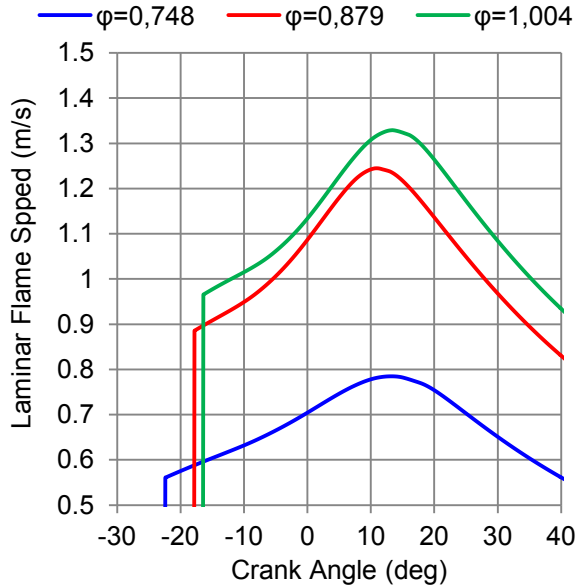


Figure 4-49: Laminar flame speed for fuel/air equivalence ratio ϕ variation.

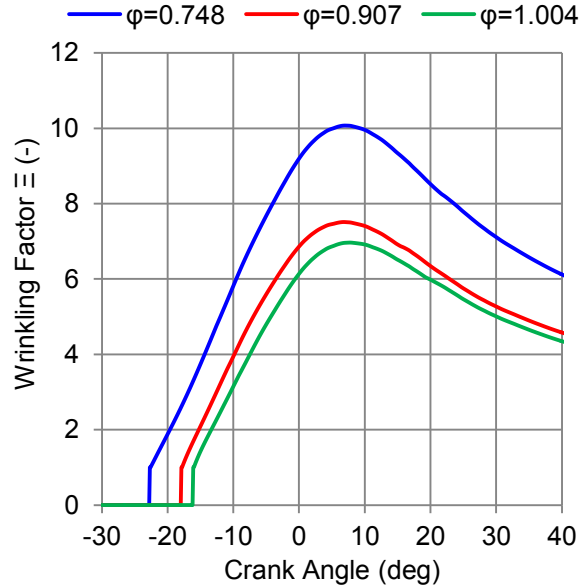


Figure 4-50: Wrinkling factor Ξ for fuel/air equivalence ratio variation.

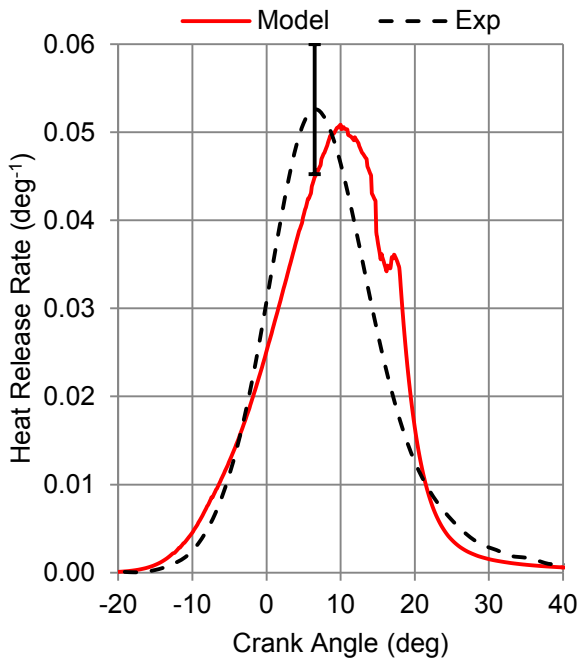


Figure 4-51: Experimental and simulated heat release rate at engine speed 1200 RPM, IMEP 3 bar, $\phi=0.748$

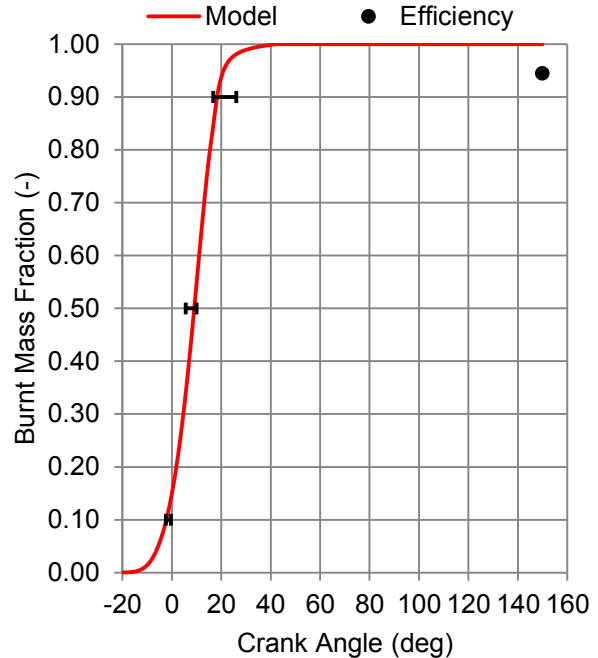


Figure 4-52: Experimental and simulated burnt mass fraction at engine speed 1200 RPM, IMEP 3 bar, $\phi=0.748$

Experimental and simulated CA10 and CA50 combustion angles are shown in Figure 4-53 and Figure 4-54 respectively. In all operating points the simulated CA10 angle is lower (lower ignition delay time). Simulated CA50 arrives later than the experimental one in most

of the points. In general, the operating point of engine 2000 RPM and IMEP 3 bar, has been difficult to calibrate in the optimal spark advance angle case as well. A conclusion for the fuel/air equivalence ratio variation is that the laminar flame speed correlation takes into account its variation and that the same coefficient of the turbulent combustion model may be used in similar cases.

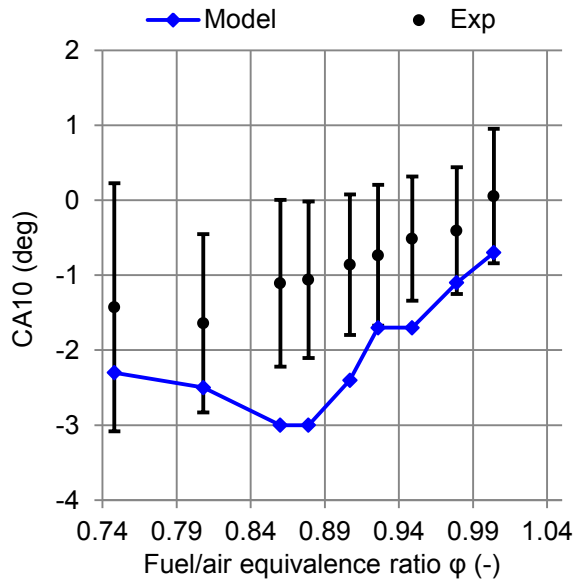


Figure 4-53: Experimental and simulated CA10 angle for fuel/air equivalence ratio ϕ variation.

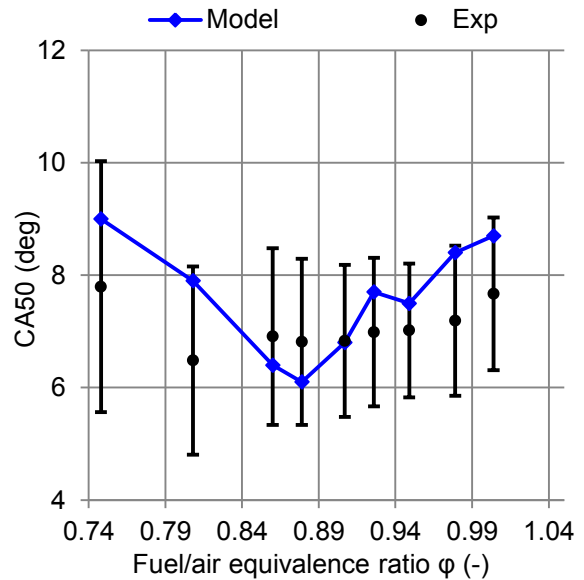


Figure 4-54: Experimental and simulated CA50 angle for fuel/air equivalence ratio ϕ variation.

4.3.2 Gasoline/Ethanol fuel

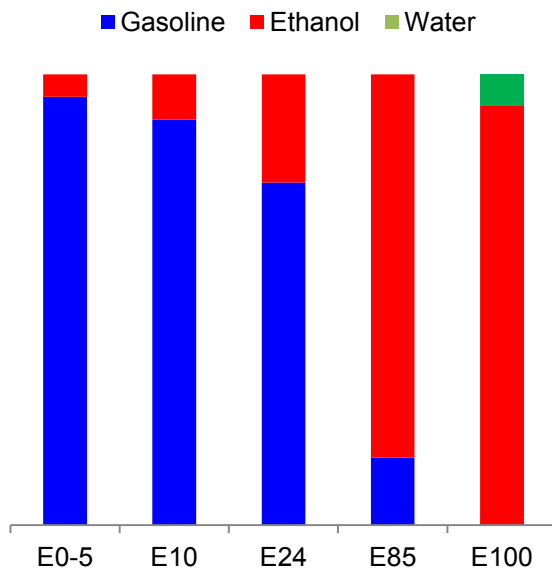


Figure 4-55: List of various gasoline-ethanol blends, which are used throughout the world. [116]

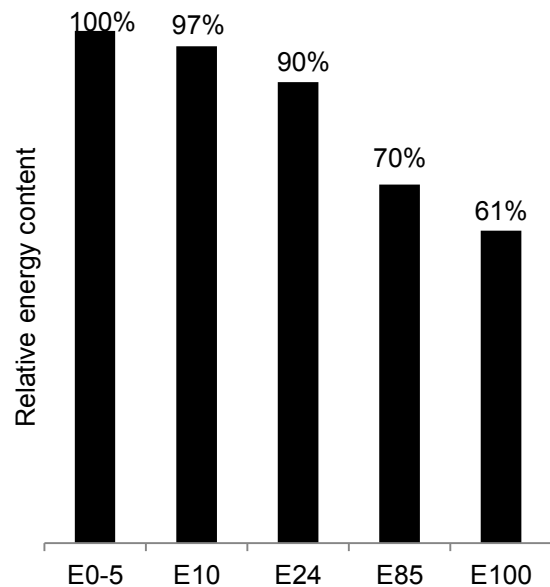


Figure 4-56: Comparison of energy content (LHV) of various gasoline-ethanol blends. 100% is for pure gasoline. [116]

Ethanol (derived from biomass) is a form of quasi-renewable energy that can be produced from agricultural feedstock. It is used as an additive in typical gasoline fuel or it can be used as the sole fuel of an engine. The typical gasoline-ethanol blends, which are in use throughout the world are presented in Figure 4-55. As it has already been mentioned in sec-

tion 1.5.4, modern (after 2000) SI engines may run on a gasoline/ethanol blend with 10% ethanol volume fraction without modifications. Concerning its use in SI engines, it provides further advantages. Ethanol fuel has the following advantages:

- High latent heat of vaporization, which leads to a cooler fuel/air mixture less prone to auto-ignite. [117]
- Higher Research Octane Number (RON) than typical gasoline, which helps in avoiding knocking.[118]

The above advantages allow the use of spark advance angles, which can be closer or equal to the thermodynamic optimal advance angle. However, ethanol has low vaporization rate and this may lead to cold-start problems. Furthermore, the energy content of gasoline/ethanol blend is not the same with a pure 100% gasoline fuel (Figure 4-56). These issues may demand a redesign of the combustion system concept, when blends with high ethanol content need to be used.

In order to simulate the laminar flame of gasoline /ethanol blends, a different laminar flame speed correlation was chosen from [119]. This correlation has been chosen among others (such as the proposed correlation in [120]), because it has been created up to an 69% ethanol volume fraction and it permits to simulate the E85 fuel (blend with 15% gasoline and 85% ethanol). The proposed correlation is a result of fitting among numerically calculated speeds, through the use of CHEMKIN™ commercial software.

$$s_L = s_L^0 \left(\frac{T_u}{T_0} \right)^\alpha \left(\frac{p_{cyl}}{p_0} \right)^\beta (1 - aX_{RBG})^b \quad (4-3)$$

The term of s_L^0 depends on the fuel/air equivalence ratio φ and on the ethanol content:

$$s_L^0 = (1 + 0.07E^{0.35})0.4658\varphi^{-0.326}e^{-4.48(\varphi-1.075)^2} \quad (4-4)$$

The coefficients α , β , a , b , are given in Table 4-12 for an increasing ethanol mole fraction. In order to simulate the gasoline/ethanol E85 blend fuel, extrapolation must be made.

Table 4-12: Coefficients for gasoline-ethanol blend correlation for laminar flame speed for several ethanol mole fractions. Extrapolation is used for the fuel of E85 (85% ethanol volume fraction) in this work.

E (mole fraction %)	E (volume fraction %)	s_L^0	α	β	a	b
0	0	0.454	1.85	-0.41	1.37	2.34
20	9	0.468	1.85	-0.42	1.40	2.26
40	20	0.472	1.85	-0.42	1.43	2.18
60	37	0.477	1.86	-0.41	1.39	2.25
85	69	0.482	1.90	-0.38	1.50	2.03

The special test for this case was a spark advance variation around the TDC for the engine speed of 1200 RPM and IMEP 3 bar. This test is an attempt to simulate the cold start of an engine, which burns the gasoline/ethanol blend fuel. The goal is to delay the spark ignition, so as that the combustion arrives later and the burnt gases are hotter at the moment of EVO. In this manner, the catalyst will be heated faster. It is reminded that the temperature of the catalyst must be high in order to achieve high efficiency. While the spark advance is reduced (Figure 4-57) the, the IMEP is kept constant at 3 bar. In order to maintain it constant, the throttle opens and the charge mass is increased. This is the reason why the RBG fraction diminishes in this test (Figure 4-58). Its values fall in the interval from 0.115 to 0.15 for most operating points.

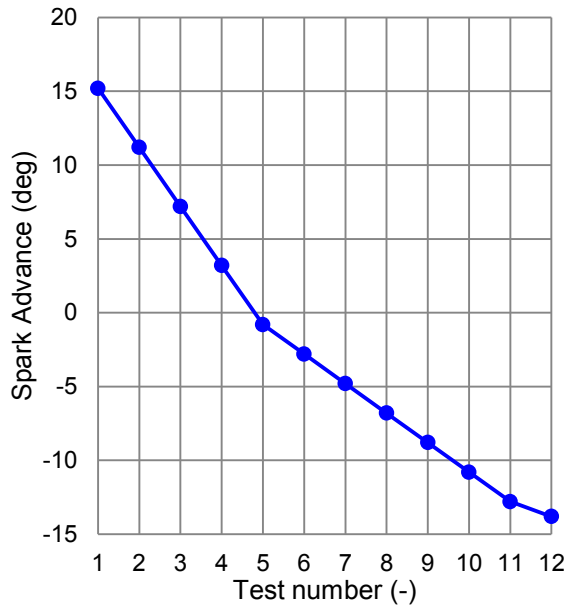


Figure 4-57: Spark advance angle for engine speed 1200 RPM and IMEP 3 bar operating points. (Gasoline-ethanol blend with 85% vol. of ethanol)

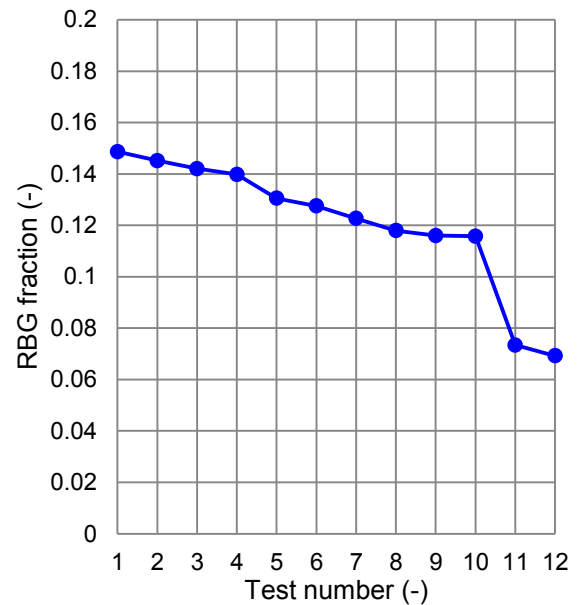


Figure 4-58: RBG fraction for engine speed 1200 RPM and IMEP 3 bar operating points. (Gasoline-ethanol blend with 85% vol. of ethanol)

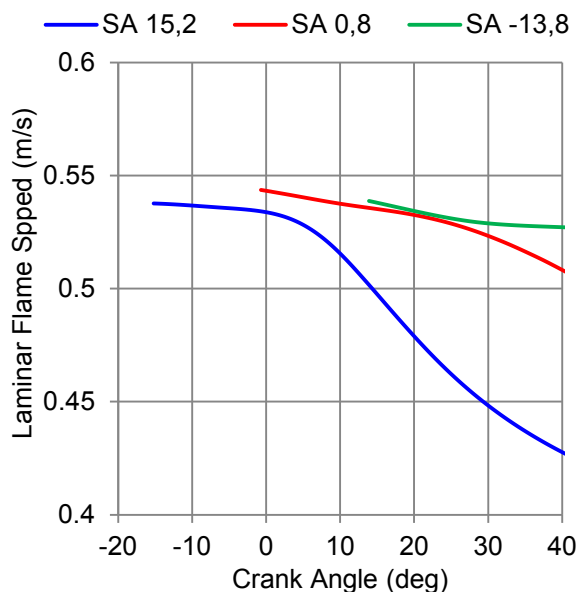


Figure 4-59: Laminar flame speed for various spark advances. (Gasoline-ethanol blend with 85% vol. of ethanol)

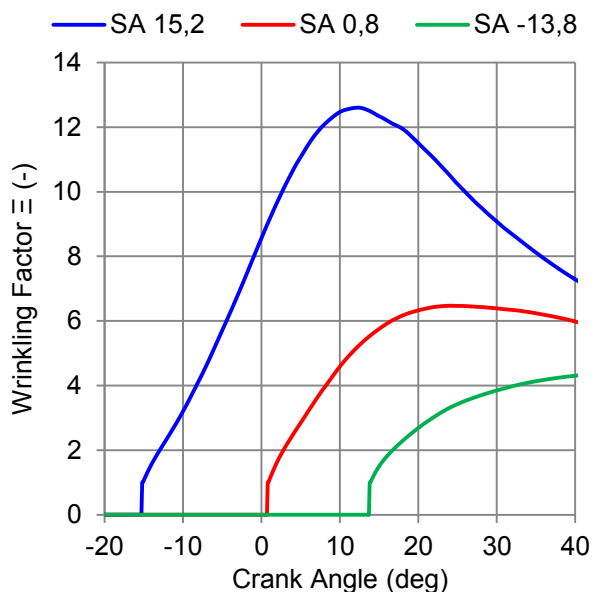


Figure 4-60: Wrinkling factor for various spark advances. (Gasoline-ethanol blend with 85% vol. of ethanol)

The laminar flame speed for three spark advance angles is shown in Figure 4-59. The gasoline/ethanol correlation shows a different behavior during a combustion cycle: It remains quasi-constant for a large period of the combustion process and it finally decreases. This behavior is different with the usual laminar flame speed, which was used for gasoline (see Figure 4-14). This difference is explained by the exponents for temperature and pressure, which vary in the two relations (Table 4-13). The impact of the RBG may be excluded, because the RBG correction term does not vary during the cycle. The wrinkling factor Ξ for the same three test points is presented in Figure 4-60. Wrinkling diminishes with the diminution of the spark advance. This trend is expected since wrinkling is a function of the u'/s_L ratio.

The laminar flame speed s_L remains quasi-constant but the turbulent intensity diminishes in function of the crank angle.

Table 4-13: Comparison of exponents for laminar flame speed correlations (isooctane with $\phi=1$)

	α (Temperature term)	β (Pressure term)
Metgalchi and Keck [43]	2.18	-0.16
Syed and others (SAE 2010-01-0620) [119]	1.85	-0.41

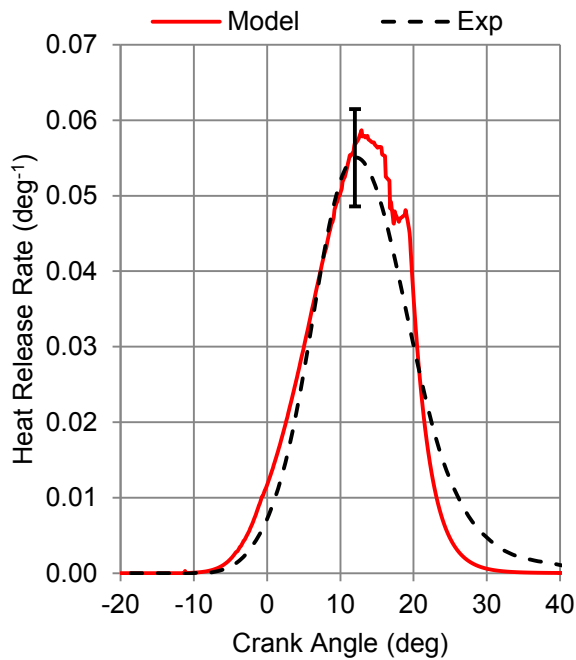


Figure 4-61: Experimental and simulated heat release rate for the operating point of engine speed 1200RPM, IMEP 3 bar and spark advance 11,2 deg before TDC. (Gasoline-ethanol blend with 85% vol. of ethanol)

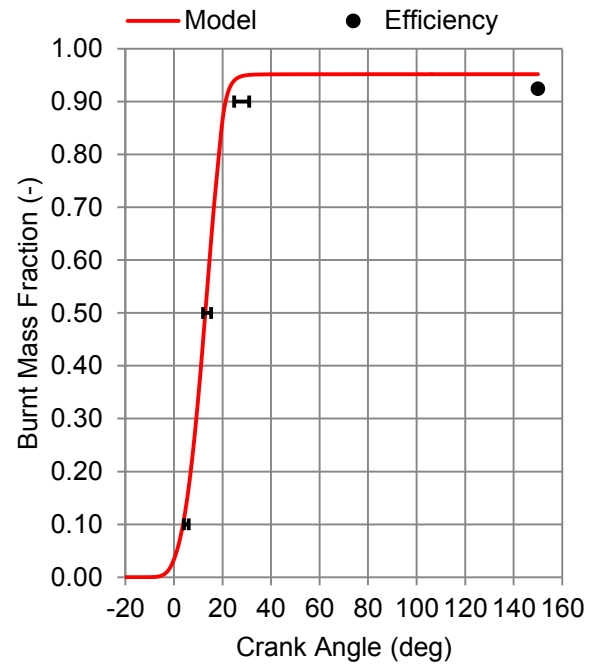


Figure 4-62: Experimental and simulated burnt mass fraction rate for the operating point of engine speed 1200RPM, IMEP 3 bar and spark advance 11,2 deg before TDC. (Gasoline-ethanol blend with 85% vol. of ethanol)

The coefficient for turbulent combustion, which has been used in this test case was the same with the one for the operating point of engine speed 1200 RPM and IMEP 3 bar⁷. In Figure 4-61, the experimental and simulated heat release rate are compared and in Figure 4-62 the simulated burnt mass fraction along with the experimentally derived characteristic combustion angles are shown for the leanest case of spark advance of 11.2 degrees before TDC. The behavior of the heat release rate is similar to the characteristic operating point, which was presented in section 4.2.2. The simulated ignition delay time is lower (earlier CA10 for the model) but the main flame development phase is correctly predicted by the model (almost equal CA50 for model and experiment). The CA90 is reached earlier for the model and the combustion efficiency is higher for the model than (0.952) the experiment (0.924).

⁷ The calculation of a Schmidt and Lewis number for the gasoline/ethanol/air mixture has been avoided for the sake of simplicity. If a Schmidt number is computed then the model coefficient must be corrected by the ratio of the pure gasoline/blend fuel Schmidt numbers.

Experimental and simulated CA10 and CA50 combustion angles are shown in Figure 4-63 and Figure 4-64 respectively. In all operating points the simulated CA10 angle is lower (lower ignition delay time). Simulated CA50 arrives also earlier than the experimental one in most of the points. The points with very late spark advance are not correctly modeled. This behavior may be linked with high wrinkling for the flame development phase, which is present in all operating points (early CA10 for model) and a higher laminar flame speed for the last points of the test due to the diminution of RBG fraction.

A conclusion for the gasoline/ethanol blend fuel is that the combustion model, as it has been enhanced with the proposed laminar flame speed correlation takes into account its variation and that the same coefficient of the turbulent combustion model may be used in similar cases.

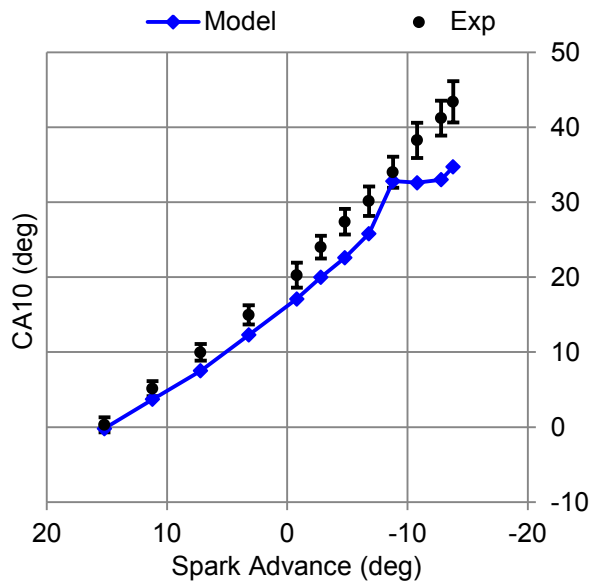


Figure 4-63: Experimental and simulated CA10 angle for spark advance variation. (Gasoline-ethanol blend with 85% vol. of ethanol)

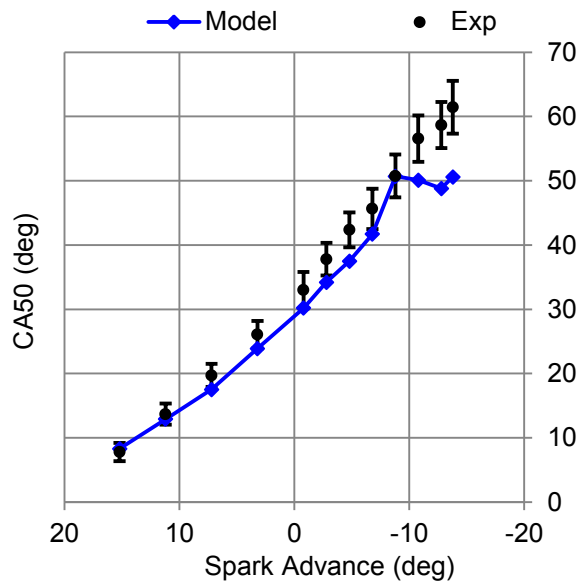


Figure 4-64: Experimental and simulated CA50 angle for spark advance variation. (Gasoline-ethanol blend with 85% vol. of ethanol)

4.3.3 Variable valve timing

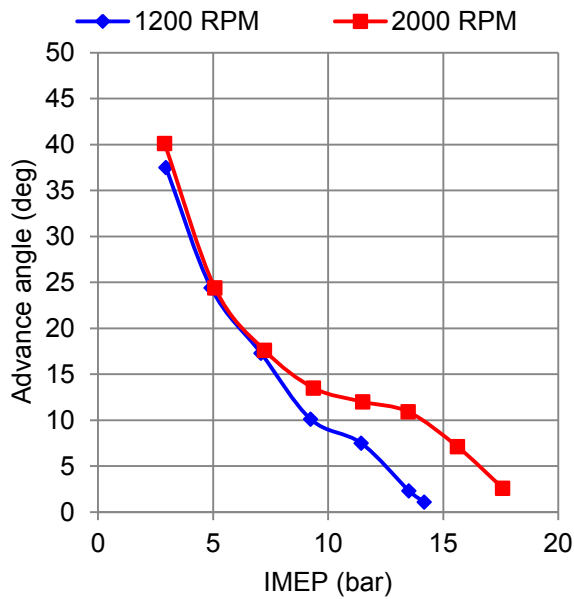


Figure 4-65: Spark advance angle for the VVT40 configuration by using the experimental pressure and measurements. Those values are used also in simulations.

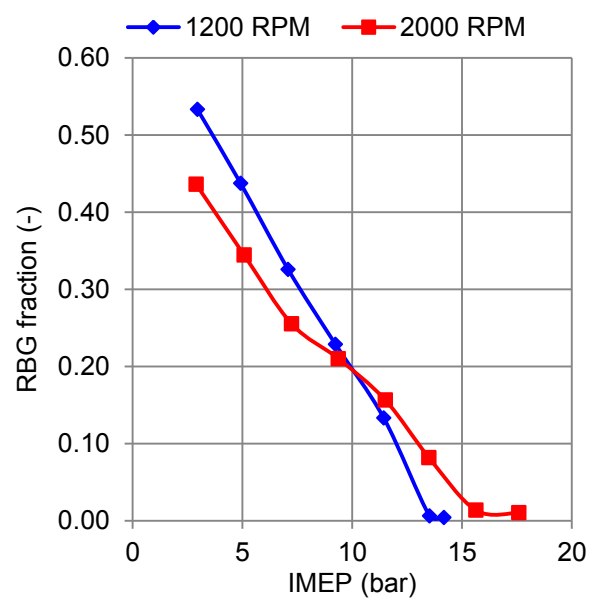


Figure 4-66: Estimated RBG for the VVT40 configuration by using the experimental pressure and measurements.

The RBG fraction X_{RBG} has an impact on laminar flame since it affects directly the laminar flame speed and thickness. It is, of course, a fundamental variable for the engine performance and efficiency since it connected with the valve overlap period and the pressure difference between the intake and the exhaust. Nevertheless, in this discussion the impact on laminar flame speed will be enlightened. For this test, an optimal spark advance with delayed (40 crank angle degrees) IVO and IVC has been chosen. This offset increases valve overlap period and, consequently, the RBG fraction rises. The values of spark advance for the engine speeds of 1200 RPM and 2000 RPM are shown in Figure 4-65 engine loads from 3 bar to 18 bar if IMEP. The estimated RBG fraction from pressure measurements is shown for all the operating points of this configuration in Figure 4-66.

Table 4-14: RBG correction term for both laminar flame correlations along with the associated constants.

Isooctane	Metgalchi and Keck [43]	Syed and others (SAE 2010-01-0620) [119]
RBG correction	$(1 - aX_{RBG}^b)$	$(1 - aX_{RBG})^b$
a	2.06	1.37
b	0.733	2.34
Range of RBG experiment	0 - 20%	0 - 32%

The presence of RBG inside the combustion chamber diminishes the laminar flame speed. This diminution is taken into account by a correction term, as it appears in Table 4-14. The correction term is of the same nature for the two laminar flame speed correlations, which has been used in this work for gasoline or gasoline/ethanol fuel. This remark underlines the interest of testing both correlations for this RBG fraction configuration test. The

RBG correction term can be tested beforehand its use in the simulation of high RBG fraction operating points by tracing its dependence on RBG fraction. Both the RBG correction terms, which are used in this configuration, are presented in function of RBG fraction in Figure 4-67. The dashed (- - -) lines represent the results for RBG fractions, which are beyond the range of each experiment. In the X axis the RBG fraction increases from zero (no RBG) to unity (extreme case, with no combustion). For a unity value of the Y axis, the laminar flame speed is equal with the speed without RBG presence (zero X axis). The drop of laminar flame fraction is steeper with the Metgalchi and Keck correction. For a RBG fraction of 0.1, the laminar flame speed is already lowered by 40% of the one with zero RBG fraction, whereas in the correlation of [119] the diminution of laminar flame speed fraction is limited to 30%. A noteworthy remark is that the Metgalchi and Keck correlation gives an unphysical negative correction (intentionally omitted in the figure) beyond almost 0.363 RBG fraction, notwithstanding the fact that combustion takes place for a RBG diluted charge higher than this limit. On the contrary, the correlation of [119] gives a correction value, which is never inferior to zero. For the limiting value of the Metgalchi and Keck correlation, the correlation of [119] gives a laminar speed diminution of 0.796 (still almost 20% of the no RBG flame speed exists). A premature conclusion may be that the Metgalchi and Keck correlation may be used till 36% of RBG and the correlation of [119] may be used till 60% of RBG, where the value of laminar flame is at 1.5% of the initial speed. The subsequent simulation results will prove the validity of this consideration.

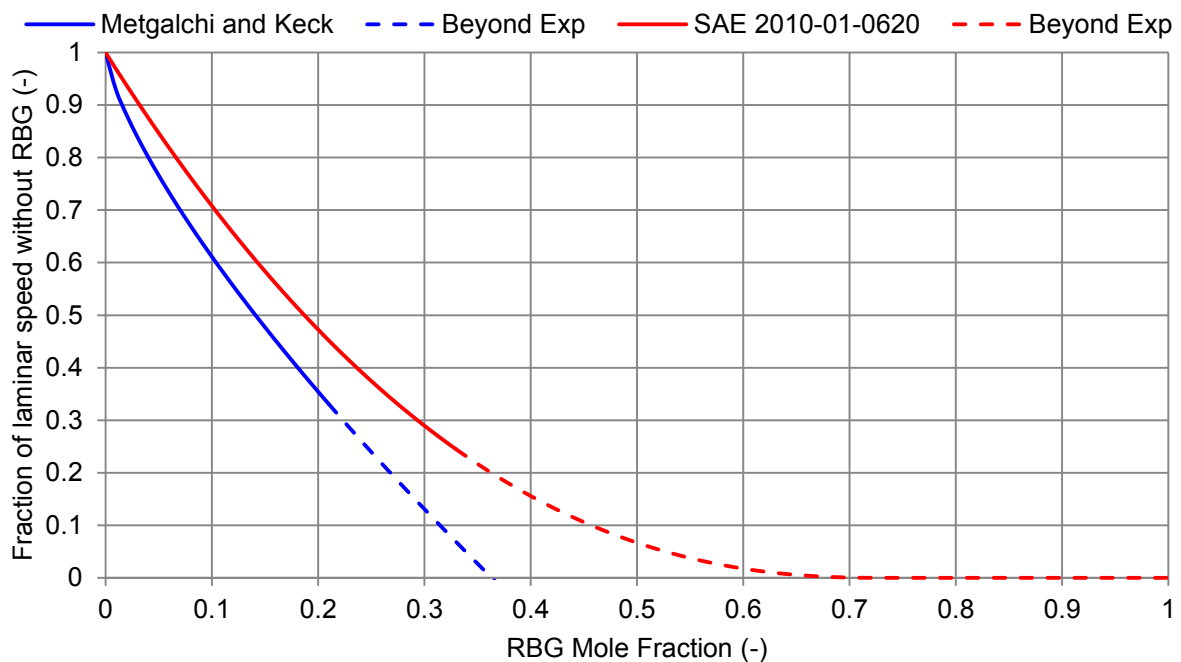


Figure 4-67: Comparison of the RBG term of the two correlations used in this work. In the Y axis the diminution of the flame speed from the value with zero RBG fraction is shown.

An emerging question for the high RBG combustion is whether the combustion regime is in accordance with flamelet modeling. As it has been shown previously (see Figure 4-17), the positioning of an operating point in the Borghi-Peters diagram requires values of turbulence properties as well as laminar flame characteristics. In [45] turbulence results (three dimensional RANS simulations) for a VVT00 and VVT20 (20 crank angle degrees of IVO and IVC offset) cases, turbulent intensity is the essentially the same for both configurations. Therefore, turbulent intensity u' as well as integral length scale L_T are kept equal to the

VVT00 configuration (see section 4.2.1). The drop of laminar flame speed with increasing RBG fraction in addition to the thickening of the flame (see Table 4-5) lead the flame in a “well-stirred reactor” regime, as it is shown in Figure 4-68 for the VVT40 operating points if engine speed 1200 RPM and engine load of 5 bar (RBG at 44%). It is expected that the model will not simulate correctly the combustion because of the very low laminar flame speed. Moreover, the pertinence of a flamelet model, such as the FSD model, for this kind of high diluted combustion is questioned.

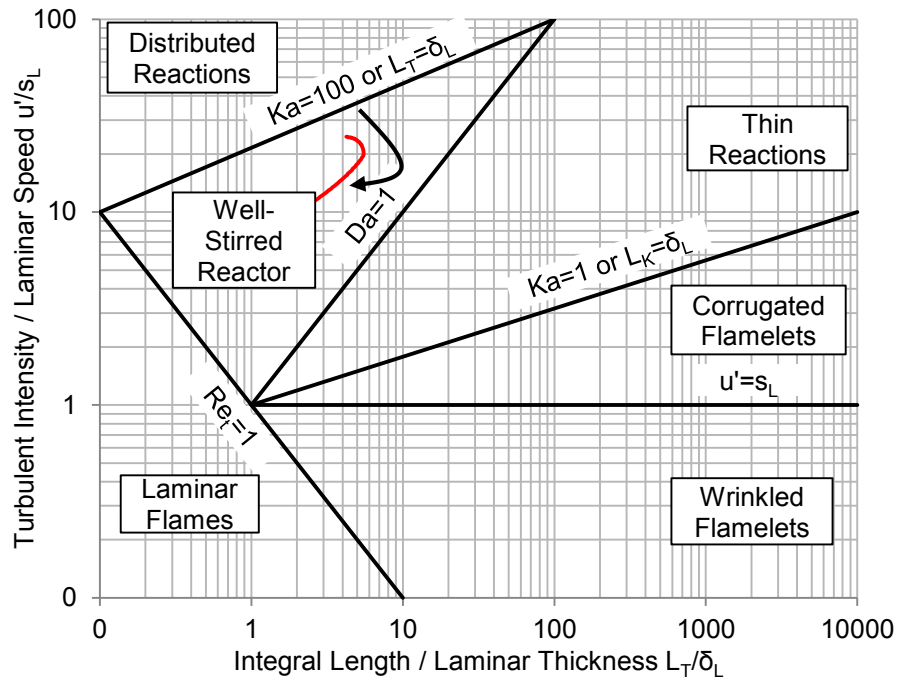


Figure 4-68: Borghi-Peters diagram of engine speed 1200 RPM and IMEP of 5 bar. Estimated RBG fraction is at 44%. The combustion is not in the flamelet regime. (laminar speed correlation of [119])

In Figure 4-69 and Figure 4-70 the heat release and the laminar flame speed of the operating point of engine speed 2000 RPM and loads of 5 bar of IMEP are shown. The estimated RBG fraction at 34% for this medium load case and the laminar flame speed is at 5% of the speed without RBG for the Metgalchi and Keck correlation and at 23% for the correlation in [119]. Combustion takes place slowly due to the very low laminar flame speed and none of the models may predict correctly the heat release rate.

On the other hand, in the high load case (heat release: Figure 4-71 and laminar flame speed: Figure 4-72) with only 8% of RBG, the heat release rate is correctly simulated with the Metgalchi and Keck correlation. The coefficient of the wrinkling factor equation is the same with the respective operating points in the optimal spark advance configuration (VVT00). On the contrary, the correlation in [119] gives a lower laminar speed value under the ignition pressure and temperature conditions. This remark is also valid in the medium load case. Since this correlation consistently gives a lower laminar flame speed, it is expected that it will not predict correctly the combustion process with the same coefficient of the optimal spark advance configuration.

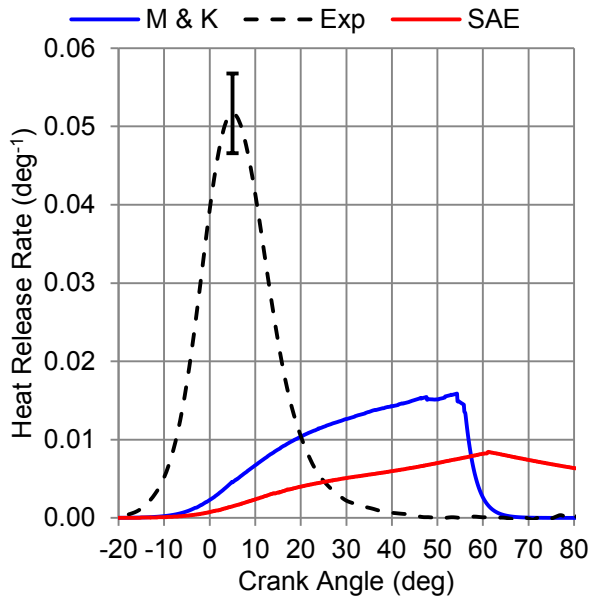


Figure 4-69: Heat release rate of the operating point with engine speed 2000 RPM and IMEP 5 bar. Simulated results from both laminar flame speed correlations are presented. Estimated RBG fraction at 34%.

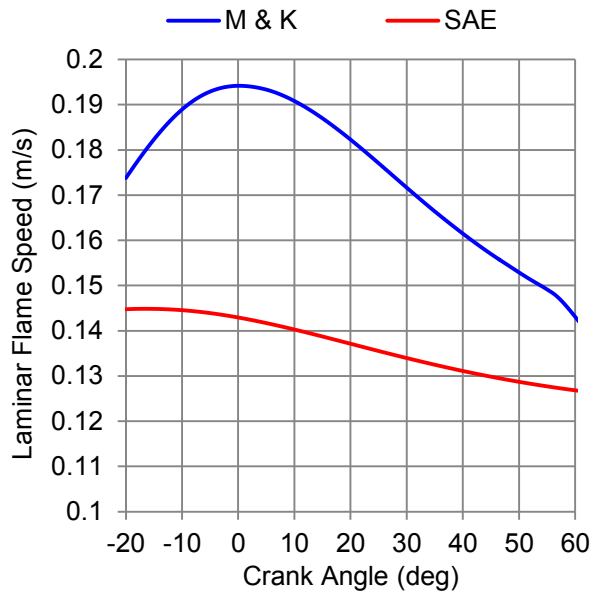


Figure 4-70: Laminar flame speed correlations for the operating point with engine speed 2000 RPM and IMEP 5 bar. Estimated RBG fraction at 34%.

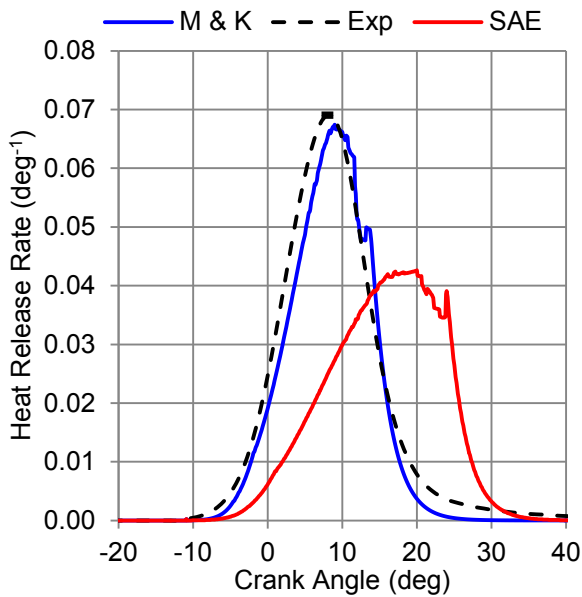


Figure 4-71: Heat release rate of the operating point with engine speed 2000 RPM and IMEP 13 bar. Simulated results from both laminar flame speed correlations are presented. Estimated RBG fraction at 8%.

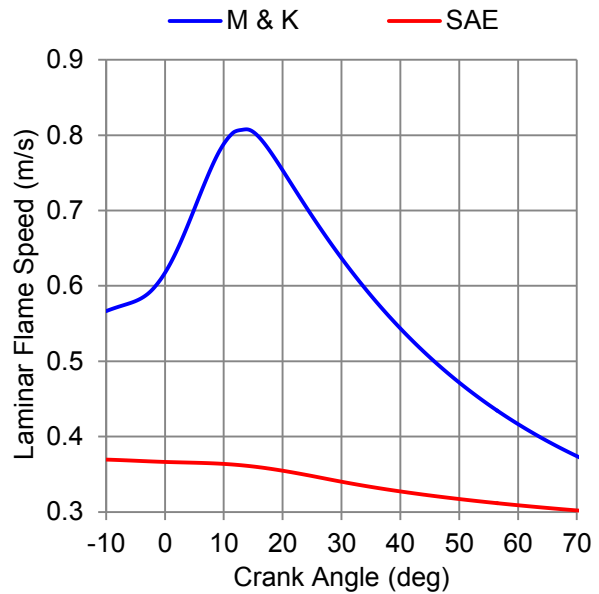


Figure 4-72: Laminar flame speed correlations for the operating point with engine speed 2000 RPM and IMEP 13 bar. Estimated RBG fraction at 8%.

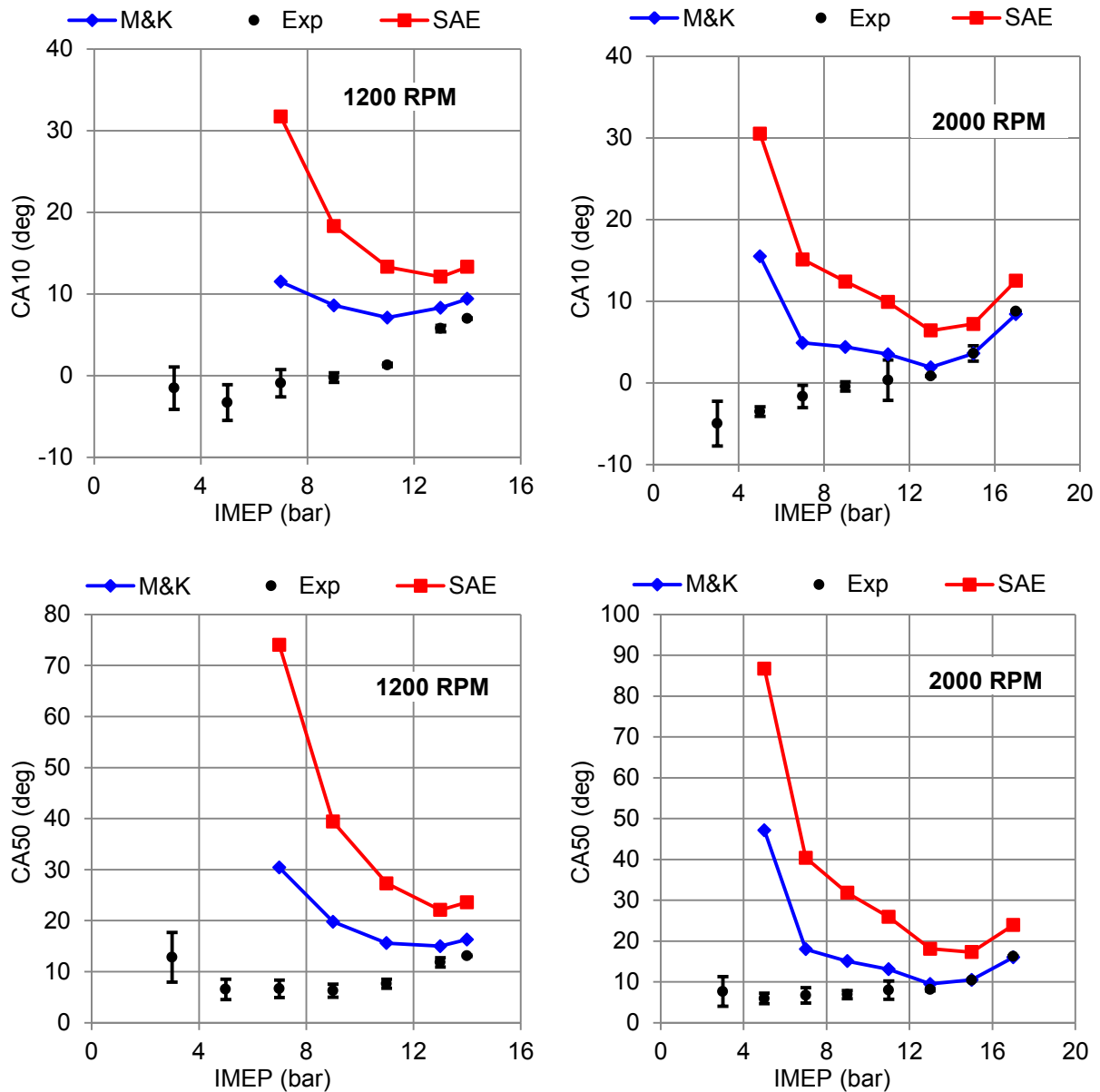


Figure 4-73: Characteristic combustion angles (CA10, CA50) for both laminar speed correlations in comparison with experimental results for all tested operating points.

In Figure 4-73 the characteristic combustion angles (CA10 and CA 50) are presented. For the operating points of engine speed 1200 RPM and IMEP 3 and 5 bar no simulated results are shown either because the Metgalchi and Keck correlation could not be used (RBG 36%) or because the correlation of [119] gave a laminar flame speed close to zero and the heat release was negligible.

A conclusion for the Metgalchi and Keck relations is that the results for the points with RBG fraction from 0% to 15% are correctly modeled with the coefficient of the optimal spark advance. Finally, for the correlation of [119] it can be observed that even if its RBG correction is less heavy than the Metgalchi and Keck relation, it cannot be used for gasoline fuel with the same coefficients with the optimal spark advance. This result is due to the lower values of laminar speed for the same pressure and temperature conditions.

Chapter 5 Conclusion and Perspective

The development of spark ignitions engines with low fuel consumption, regulated emissions and sufficient performance is achieved by the combination of various technological solutions. There is a need to diminish the cost of evaluation of such technologies. Computer simulation set-ups are a promising and much less expensive alternative to the traditional engine test bed.

One dimensional engine modeling is an established industrial practice among various simulations techniques. It provides a sufficiently accurate calculation of the gas exchange process. This simulation technique is completed by phenomenological zero-dimensional combustion models, which take into account various aspects of spark ignition combustion such as the laminar flame characteristics, the aerodynamic turbulence and its impact on the flame.

In this work, in order to create a zero-dimensional combustion model, which can be able to describe correctly the physics of combustion, the following steps have been followed:

- The key aspects of laminar and turbulent premixed combustion are identified.
- Three versions of typical combustion models are compared in terms of physical description of the combustion process. The result of this comparison indicates the most physically pertinent model (the Flame Surface Density model).
- The retained Flame Surface Density model is enhanced with physical modeling of the several phenomena, which affect the heat release rate and are not contained in the initial model. Those phenomena are:
 - Wall-flame interaction
 - Post-flame reactions (Carbon monoxide and Hydrocarbons)
 - Flame stretch
- Finally, the proposed model is validated for several engine configurations. Each configuration has an impact on a specific engine parameter. This analysis shows which are the confidence intervals and the limitations of the proposed model.

The specific conclusions of the works, which have been described in the previous paragraph, are elaborated in the following sections. The future work opportunities, which are opened by the results of this work, are presented in the last section of this chapter.

5.1 Comparison of turbulent premixed combustion models

Three 0D SI combustion models (Eddy Burn Up, Fractal, FSD) were coded as user models in a GT-POWER™ single cylinder engine and simulations were performed.

- Cylinder pressure results were very satisfactory for all models.
- Calibration under low load conditions was difficult for all models.
- The FSD model is retained, since:
 - It simulates a unity wrinkling factor at the beginning of combustion, when the flame is quasi-laminar.
 - It describes physically the turbulence-flame interaction through its efficiency function.

- The retained model must be enhanced in terms of wall-flame interaction and post-flame reactions.

5.2 Flame-wall interaction

A phenomenological model is developed for the simulation of wall-flame interaction and the diminution of flame wrinkling.

It integrates the impact of (i) the diminution of the flame front temperature, (ii) the confinement by the chamber geometry and (iii) the impact of boundary layer. A modified global wrinkling factor is computed in function of the mean surface distance distribution from the wall.

- Four alternative geometrical configurations (varying sparkplug position and length) are tested.
- The diminution of flame wrinkling and mean flame surface is captured by the model.
- Sparkplug position is more influencing than sparkplug length in terms of flame wall-interaction.
- The impact of wall-flame interaction is more evident in the lateral spark plug position than in the central sparkplug position.
- Pressure and heat release simulation results agree with experimental results for all configurations.

5.3 Post flame reactions

The post flame reactions (CO and HC) sub-model, based on equilibrium chemistry, reduced chemical kinetics and diffusion phenomena is used to ameliorate the simulation of the heat release rate.

- The characteristic time of CO kinetics is comparable to complex chemistry results, while its calculations remains quick and simple.
- The “freezing” (CO fraction remains almost constant) effect is captured by the model.
- The trends of measured CO values at the exhaust are captured by the model, when a fuel/air equivalence ratio variation is performed.
- The final stage of combustion is dominated by the slow HC diffusion reaction process.
- A relaxation time is used to decompose the diffusion/reaction process of the HC post oxidation.
- The consumed HC quantity during this stage is found consistent in comparison with the measured HC quantity at the exhaust for a variety of operating points.
- The proposed HC post oxidation model offers a realistic description of the final stage of combustion, while remaining quick and relatively simple.

5.4 Impact of flame stretch on heat release

The assessment of the flame stretch model has been conducted with the aid of previously published experimental results. The impact of flame stretch is taken into account in the stretched laminar flame speed through the thermodiffusive characteristics of the fuel/air mixture. The comparison of experiments with simulations showed:

- The trends of flame radius and flame propagation speed are similar in both experiments and simulations. Variations between simulated and experimental flame radius and propagation speeds rely on the different geometrical considerations, which are assumed in simulation and experiments.
- Simulated flame wrinkling follows the same trend as in experiments: It diminishes for an increasing Lewis number. Experimental wrinkling values are higher than simulated ones, since the experimental flame radii are higher than the simulated radii.
- Flame stretch is rather similar for all three mixtures for simulations and experiments.
- The impact of flame stretch becomes more visible on the burnt mass fraction, as the Lewis number increases.

5.5 Model validation for different engine configurations

The comparison of model simulation results with a series of experimental measurements of several operating points at the optimal spark advance and other configurations showed:

- The calibration coefficient of the FSD model is very sensitive to the ratio of turbulent intensity to the laminar flame speed (u'/s_L).
- The trends of CA10 and CA50 are retrieved by the model even if a modification of the spark advance is needed, since the first stage of combustion is not physically modeled.
- During the very last stage of the combustion, the model cannot calculate a flame front radius. The shape of the flame front may be not accurately described by the spherical flame front. This uncertainty explains why the trends of CA90 and combustion efficiency are partially retrieved.
- The optimal spark advance coefficients of the wrinkling factor can be conserved in the case of fuel/air mixture equivalence ratio variation.
- Similarly, the optimal spark advance coefficients of the wrinkling factor can be conserved in the case of the gasoline/ethanol fuel blend fuel with a different laminar flame speed correlation than the one for typical gasoline fuels.
- In the operating points of high RBG fraction, achieved with intake variable valve timing, the optimal spark advance coefficients can be used up to 15% of RBG.

5.6 Perspective

Interesting paths for future works have been indicated during the research for the enhancement of the phenomenological 0D combustion model:

The wall-flame interaction model simulates the diminution of flame wrinkling based on physical experimental and numerical results. However, the contribution of the flow impact (laminar flow in the boundary layer) as well as the contribution of heat transfer (elevated heat transfer from the hot flame towards the cold wall) are not distinguished in the proposed model. A potential amelioration could be the implementation of a more detailed heat transfer model, which would simulate the intense heat release from the flame to the wall. A possible stratification, by means of a Probability Density Function (PDF) for example, of the fresh gas temperature (T_u) would also be applicable. The reduced temperature in the vicinity of the wall would impact the characteristics of the laminar flame (thickness δ_L and speed s_L). Moreover, the boundary layer region can possibly be modeled, even for the 0D geometry, with the appropriate “law of the wall for the flow velocity” (u^+, y^+ formulation proposed by von Karman). This modeling would have an impact on the turbulent flame characteristic (turbulent intensity u' and length scale L_T).

The post-flame interaction of carbon monoxide and unburnt Hydro Carbons is taken into account by the proposed models. The fundamental magnitudes, which affect these two post-flame reactions are the fresh and burnt gases temperature (T_u and T_b), the mass of unburnt charge (m_u) as well as the equilibrium values of the fresh and burnt gases mass fractions species (Y_i). The fresh gas temperature estimation can be improved as it has been discussed in the previous paragraph. The burnt gas temperature can be modeled by means of a multi-zone thermodynamic model. The resulting temperature stratification in the burnt gases region, will allow calculating in a more detailed manner the carbon monoxide concentration. A more detailed manner for calculating the equilibrium concentrations (notably of CO concentration) would improve the estimation of CO at exhaust valve opening. In addition, a crevice model can be implemented in the combustion model. Fuel/air mixture which enters the crevice volume during compression and reenters in the combustion chamber during expansion would decrease the burnt mass in the flame front and would possibly raise the post-flame consumed HC. Finally, a more detailed chemistry for the post oxidation of HC would possibly result in the increase of CO mass fractions.

The impact of flame stretch on the laminar flame speed is very important especially on the first stage of combustion. In this work, the impact of stretch is modeled by only one of its components. In other words, only flame curvature is taken into account by the flame stretch model. The omission of the strain component has been based on conclusions of other researchers. An interesting perspective would be to explore under which circumstances the flame strain can be of significant impact. Its importance can be revealed either by dedicated experiments or by DNS simulation with flames of varying Lewis number and sufficiently small length scales, as it is the case on spark ignition. A physical modeling of the ignition process would also provide a more accurate prediction of the initial flame surface and would improve the input of the flame stretch model.

Appendix A Thermodynamic model

A.1 System of differential equations

For a control volume, containing the enclosed charge in the combustion chamber, the energy conservation equation can be written in differential form. The crank angle θ intervenes as independent variable.

$$m \frac{du}{d\theta} + u \frac{dm}{d\theta} = -p \frac{dV}{d\theta} + \frac{dQ}{d\theta} - h_f \frac{\dot{m}_f}{\omega_{eng}} \quad (\text{A-1})$$

The angular engine speed ω is defined by the following relation:

$$\omega_{eng} = \frac{d\theta}{dt} = 6N \quad (\text{A-2})$$

The burnt mass fraction x_b is defined during the cycle:

$$x_b = \frac{m_b}{m} \quad (\text{A-3})$$

The burnt mass fraction is calculated by the combustion model and is considered an entry of the thermodynamic model. The total specific internal energy u of the system can be expressed by the following form:

$$u = \frac{U}{m} = x_b u_b + (1 - x_b) u_u \quad (\text{A-4})$$

with u_b being the specific internal energy of the burnt gases, calculated at the temperature T_b , and u_u being the specific internal energy calculated at the temperature T_u . Similarly, the total specific volume of the charge is written:

$$v = \frac{V}{m} = x_b v_b + (1 - x_b) v_u \quad (\text{A-5})$$

A system of ordinary differential equations will be written, in function of the system's thermodynamic variables pressure p , burnt gases temperature T_b and fresh gas temperature T_u . Every system variable may be written in function of these basic variables. For example, the specific burnt gases volume is written:

$$v_b = v_b(T_b, p) \quad (\text{A-6})$$

The derivative of this relation in function of the crank angle degree gives:

$$\frac{dv_b}{d\theta} = \frac{\partial v_b}{\partial T_b} \frac{dT_b}{d\theta} + \frac{\partial v_b}{\partial p} \frac{dp}{d\theta} \quad (\text{A-7})$$

For the calculation of the thermodynamic properties of each zone, it is useful to reveal the terms with the natural logarithms:

$$\frac{dv_b}{d\theta} = \frac{v_b}{T_b} \frac{\partial \ln v_b}{\partial \ln T_b} \frac{dT_b}{d\theta} + \frac{v_b}{p} \frac{\partial \ln v_b}{\partial \ln p} \frac{dp}{d\theta} \quad (\text{A-8})$$

A similar expression may be extracted for the fresh gases zone:

$$\frac{dv_u}{d\theta} = \frac{v_u}{T_u} \frac{\partial \ln v_u}{\partial \ln T_u} \frac{dT_u}{d\theta} + \frac{v_u}{p} \frac{\partial \ln v_u}{\partial \ln p} \frac{dp}{d\theta} \quad (\text{A-9})$$

A similar expression can be written for the specific internal energy:

$$u_b = u_b(T_b, p) \quad (\text{A-10})$$

By applying a crank angle derivative:

$$\frac{du_b}{d\theta} = \frac{\partial u_b}{\partial T_b} \frac{dT_b}{d\theta} + \frac{\partial u_b}{\partial p} \frac{dp}{d\theta} \quad (\text{A-11})$$

By using in this equation the relation for enthalpy (A-12), internal energy (A-13) as well as the fourth Maxwell equation (A-14):

$$h_b = u_b + p v_b \quad (\text{A-12})$$

$$du_b = T_b dS_b - p dv_b \quad (\text{A-13})$$

$$\left(\frac{\partial S_b}{\partial p}\right)_{T_b} = -\left(\frac{\partial v_b}{\partial T_b}\right)_p \quad (\text{A-14})$$

We obtain:

$$\frac{du_b}{d\theta} = \left(\frac{\partial h_b}{\partial T_b} - p \frac{\partial v_b}{\partial T_b}\right) \frac{dT_b}{d\theta} - \left(T_b \frac{\partial v_b}{\partial T_b} + p \frac{\partial v_b}{\partial p}\right) \frac{dp}{d\theta} \quad (\text{A-15})$$

By revealing the terms of the logarithmic derivatives, we get:

$$\frac{du_b}{d\theta} = \left(C_{Pb} - \frac{p v_b}{T_b} \frac{\partial \ln v_b}{\partial \ln T_b}\right) \frac{dT_b}{d\theta} - v_b \left(\frac{\partial \ln v_b}{\partial \ln T_b} + \frac{\partial \ln v_b}{\partial \ln p}\right) \frac{dp}{d\theta} \quad (\text{A-16})$$

The same equation can be written for the fresh gases:

$$\frac{du_u}{d\theta} = \left(C_{Pu} - \frac{p v_u}{T_u} \frac{\partial \ln v_u}{\partial \ln T_u}\right) \frac{dT_u}{d\theta} - v_u \left(\frac{\partial \ln v_u}{\partial \ln T_u} + \frac{\partial \ln v_u}{\partial \ln p}\right) \frac{dp}{d\theta} \quad (\text{A-17})$$

If we consider the energy conservation equation (A-1) and by using equation (A-4), the first left hand side term is written:

$$m \frac{du}{d\theta} = m \left[x_b \frac{du_b}{d\theta} + (1 - x_b) \frac{du_u}{d\theta} + (u_b - u_u) \frac{dx_b}{d\theta} \right] \quad (\text{A-18})$$

By substitution of the equations (A-16) and (A-17), equation (A-18) becomes:

$$\begin{aligned} m \frac{du}{d\theta} = & m x_b \left(C_{Pb} - \frac{p v_b}{T_b} \frac{\partial \ln v_b}{\partial \ln T_b} \right) \frac{dT_b}{d\theta} + m (1 - x_b) \left(C_{Pu} - \frac{p v_u}{T_u} \frac{\partial \ln v_u}{\partial \ln T_u} \right) \frac{dT_u}{d\theta} \\ & - \left[m x_b v_b \left(\frac{\partial \ln v_b}{\partial \ln T_b} + \frac{\partial \ln v_b}{\partial \ln p} \right) + m (1 - x_b) v_u \left(\frac{\partial \ln v_u}{\partial \ln T_u} + \frac{\partial \ln v_u}{\partial \ln p} \right) \right] \frac{dp}{d\theta} \\ & + m (u_b - u_u) \frac{dx_b}{d\theta} \end{aligned} \quad (\text{A-19})$$

In equation (A-1), \dot{m}_f represents the mass losses. This mass rate is considered to go toward the exterior environment. The mass conservation equation applied to the control volume is written:

$$\frac{dm}{d\theta} = -\frac{\dot{m}_f}{\omega} \quad (\text{A-20})$$

A blow-by coefficient is considered, with unit sec^{-1} . This coefficient is characterized by the geometry of the combustion chamber and the segments of the piston:

$$C = \frac{\dot{m}_f}{m} \quad (\text{A-21})$$

The second term of the left hand side becomes:

$$u \frac{dm}{d\theta} = -[x_b u_b + (1 - x_b) u_u] \frac{Cm}{\omega} \quad (\text{A-22})$$

The exchanged heat of the system with the external environment in the right hand side of equation (A-1) represents the heat losses due to energy transfer from the burnt and fresh gases towards the wall.

$$\frac{dQ}{d\theta} = -\frac{\dot{Q}_P}{\omega} = -\frac{\dot{Q}_{P,b} + \dot{Q}_{P,u}}{\omega} \quad (\text{A-23})$$

In SI engines, the heat losses between the gas and the chamber walls can be considered as convective:

$$\dot{Q}_{P,b} = h_{g,b} A_b (T_b - T_p) \quad (\text{A-24})$$

$$\dot{Q}_{P,u} = h_{g,u} A_u (T_u - T_p) \quad (\text{A-25})$$

In these expressions, the wall temperature T_p is considered constant and equal to 453 K. A_b and A_u are the instantaneous surfaces of the wall and the burnt and fresh gases respectively. The heat transfer coefficients are estimated by the equations of Woschni:

$$h_{g,b} = 3.26B^{-0.2} p^{0.8} T_b^{-0.55} T_b w^{0.8} \quad (\text{A-26})$$

$$h_{g,u} = 3.26B^{-0.2} p^{0.8} T_u^{-0.55} T_b w^{0.8} \quad (\text{A-27})$$

$$w = \left[C_1 \bar{v}_p + C_2 \frac{V_d T_r}{p_r V_r} (p - p_m) \right]$$

The coefficients C_1 and C_2 are adjusted experimentally in function of the engine's operating conditions. The pressure of the motored engine is used (p_m).

The surface of the cylinder liner in contact with the cylinder charge is of cylindrical form:

$$A_{cylinder} = \frac{4V}{D} \quad (\text{A-28})$$

The contact surfaces of the piston crown as well as of the cylinder head are considered as cylindrical:

$$A_{piston} + A_{head} = \frac{\pi D^2}{2} \quad (\text{A-29})$$

The total exchange surface between the gas and the walls is written:

$$A = \frac{\pi D^2}{2} + \frac{4V}{D} \quad (\text{A-30})$$

In order to calculate the exchange surfaces, which correspond to the fresh and burnt gases, it is assumed that the burnt gases surface contact A_b and the fresh gases surface contact A_u are expressed in function of the square root of the burnt mass fraction $x_b^{0.5}$:

$$A_b = \left(\frac{\pi D^2}{2} + \frac{4V}{D} \right) x_b^{0.5} \quad (\text{A-31})$$

$$A_u = \left(\frac{\pi D^2}{2} + \frac{4V}{D} \right) (1 - x_b^{0.5}) \quad (\text{A-32})$$

The equations (A-31) and (A-32) are empirical functions, in which the wetted chamber surface is proportional to the square root of the burnt mass fraction. These expressions are based on the fact that the burnt gases density is four times lower than the fresh gases density. Consequently, for an equivalent mass, the burnt gases occupy a greater volume fraction of the cylinder than the fresh gases. In a more rigorous manner, the surfaces A_b and A_u

could have been calculated by making an assumption of the flame front form. In practice, the exponent of x_b can be considered as a free parameter and can be adjusted in function of experimental measurements. The chosen value (0.5) in equations (A-31) and (A-32) is currently the most employed for modeling wall heat losses [31].

The enthalpy losses due to blow-by effects are modeled with the following empirical relation:

$$h_f = x_b^2 h_b + (1 - x_b^2) h_u \quad (\text{A-33})$$

This relation implies that at the beginning of combustion ($x_b = 0$) the fresh gases are concerned by the losses, while the burnt gases are concerned at the end of combustion ($x_b = 1$). In addition, for a given crank angle, the fraction of the fresh gases, which is contained in the losses is more important than the fresh gases fraction in the combustion chamber.

When the equations (A-19), (A-22), (A-23) and (A-33) are replaced in (A-1), the energy conservation equation is finally written:

$$\begin{aligned} & mx_b \left(C_{pb} - \frac{pv_b}{T_b} \frac{\partial \ln v_b}{\partial \ln T_b} \right) \frac{dT_b}{d\theta} + m(1 - x_b) \left(C_{pu} - \frac{pv_u}{T_u} \frac{\partial \ln v_u}{\partial \ln T_u} \right) \frac{dT_u}{d\theta} \\ & - \left[mx_b v_b \left(\frac{\partial \ln v_b}{\partial \ln T_b} + \frac{\partial \ln v_b}{\partial \ln p} \right) + m(1 - x_b) v_u \left(\frac{\partial \ln v_u}{\partial \ln T_u} + \frac{\partial \ln v_u}{\partial \ln p} \right) \right] \frac{dp}{d\theta} \\ & + m(u_b - u_u) \frac{dx_b}{d\theta} - [x_b u_b + (1 - x_b) u_u] \frac{Cm}{\omega} \\ & = -\frac{1}{\omega} \left(\frac{\pi D^2}{2} + \frac{4V}{D} \right) [h_{g,b} x_b^{0.5} (T_b - T_p) + h_{g,u} (1 - x_b^{0.5}) (T_u - T_p)] \\ & - p \frac{dV}{d\theta} - \frac{Cm}{\omega} [x_b^2 h_b + (1 - x_b^2) h_u] \end{aligned} \quad (\text{A-34})$$

If the burnt mass fraction x_b from an empirical function or a phenomenological model, the differential equation (A-34) can be written in the following form:

$$f \left(\theta, \frac{dp}{d\theta}, \frac{dT_b}{d\theta}, \frac{dT_u}{d\theta}, p, T_b, T_u \right) = 0 \quad (\text{A-35})$$

Two supplementary differential equations can be written in function of the thermodynamic magnitudes of the combustion chamber system: pressure p , burnt gases temperature T_b and fresh gases temperature T_u , in order to obtain a system of ordinary differential equations like the following one:

$$\begin{aligned} \frac{dp}{d\theta} &= f_1(\theta, p, T_b, T_u) \\ \frac{dT_b}{d\theta} &= f_2(\theta, p, T_b, T_u) \\ \frac{dT_u}{d\theta} &= f_3(\theta, p, T_b, T_u) \end{aligned} \quad (\text{A-36})$$

One of these equation can be written by differentiation of the volume conservation equation (A-5):

$$\frac{1}{m} \frac{dV}{d\theta} - \frac{V}{m^2} \frac{dm}{d\theta} = x_b \frac{dv_b}{d\theta} + (1 - x_b) \frac{dv_u}{d\theta} + (v_b - v_u) \frac{dx_b}{d\theta} \quad (\text{A-37})$$

By the use of equations (A-8), (A-9) et (A-20) it is obtained:

$$\frac{1}{m} \frac{dV}{d\theta} + \frac{VC}{m\omega} = x_b \frac{v_b}{T_b} \frac{\partial \ln v_b}{\partial \ln T_b} \frac{dT_b}{d\theta} + (1-x_b) \frac{v_u}{T_u} \frac{\partial \ln v_u}{\partial \ln T_u} \frac{dT_u}{d\theta} \quad (\text{A-38})$$

$$\left[x_b \frac{v_b}{p} \frac{\partial \ln v_b}{\partial \ln p} + (1-x_b) \frac{v_u}{p} \frac{\partial \ln v_u}{\partial \ln p} \right] \frac{dp}{d\theta} + (v_b - v_u) \frac{dx_b}{d\theta}$$

The last differential equation can be written with the use of the entropy conservation equation of the fresh gases. Those gases are considered as an open system, which loses mass by the combustion and the losses and exchanges heat with the environment. (See figure A-1).

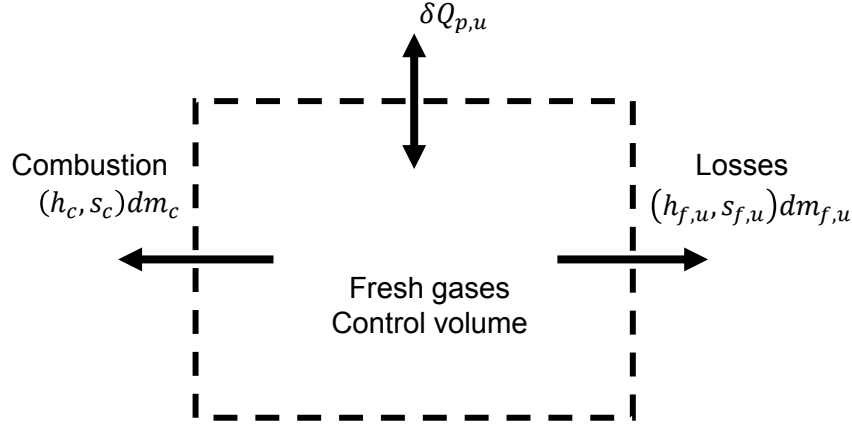


Figure A-1: Entropy conservation of the fresh gases.

The application of the entropy conservation (second law of thermodynamics), it is obtained:

$$dS_u = dS_{received} + dS_{created} + \sum_i s_i dm_i \quad (\text{A-39})$$

The entropy of the system is expressed in terms of the specific entropy:

$$dS_u = d(m_u s_u) = s_u dm_u + m_u ds_u \quad (\text{A-40})$$

By using the mass conservation equation, the previous expression is written:

$$dS_u = -(dm_c + dm_{f,u})s_u + m_u ds_u \quad (\text{A-41})$$

The fresh gases are not chemically transformed, which means that the system is in chemical equilibrium at each instant. The system's transformation can be considered as reversible:

$$dS_{created} = 0 \quad (\text{A-42})$$

The entropy by heat transfer is given:

$$dS_{reçu} = -\frac{\delta Q_{p,u}}{T_u} \quad (\text{A-43})$$

The first term of the right hand side of equation (A-39) corresponds to the entropy of mass exchange. It is assumed that the lost gas through the losses happens at the fresh gas temperature T_u . It is obtained:

$$\sum_i s_i dm_i = -(dm_c + dm_{f,u})s_u \quad (\text{A-44})$$

By replacing all the previously calculated terms in the conservation equation (A-39), the following results is obtained:

$$m_u ds_u = -\frac{\delta Q_{P,u}}{T_u} \quad (\text{A-45})$$

A division by dt , the employment of equation (A-2) and the relation $m_u = (1 - x_b)m$, leads to the relation:

$$-\dot{Q}_{P,u} = m\omega(1 - x_b)T_u \frac{ds_u}{d\theta} \quad (\text{A-46})$$

The equation, which links the entropy, pressure and temperature, is:

$$s_u = s_u(T_u, p) \quad (\text{A-47})$$

From this equation, it is deduced:

$$\frac{ds_u}{d\theta} = \frac{\partial s_u}{\partial T_u} \frac{dT_u}{d\theta} + \frac{\partial s_u}{\partial p} \frac{dp}{d\theta} \quad (\text{A-48})$$

By using one more time, in this equation the expressions of enthalpy (A-12), of internal energy (A-13) as well as the fourth Maxwell equation (A-14) and by introducing the logarithmic derivatives, it is obtained:

$$\frac{ds_u}{d\theta} = \frac{C_{P,u}}{T_u} \frac{dT_u}{d\theta} - \frac{v_u}{T_u} \frac{\partial \ln v_u}{\partial \ln T_u} \frac{dp}{d\theta} \quad (\text{A-49})$$

By substituting the equation (A-49) in (A-46), the second ordinary differential equation of the system is obtained:

$$C_{P,u} \frac{dT_u}{d\theta} - v_u \frac{\partial \ln v_u}{\partial \ln T_u} \frac{dp}{d\theta} = -\frac{h_{g,u}}{\omega m} \left(\frac{\pi D^2}{2} + \frac{4V}{D} \right) \frac{(1 - x_b^{0.5})}{(1 - x_b)} (T_u - T_P) \quad (\text{A-50})$$

The equations (A-34), (A-38) and (A-50) will be manipulated in order that they are written in the form of the system of differential equations (A-36).

The equations of energy conservation (A-34), of total specific volume (A-38) are added. In the resulting relation, the term $dT_u/d\theta$ extracted by equation (A-50), and the total volume from equation (A-5) are replaced:

$$\begin{aligned} \frac{dT_b}{d\theta} = & -\frac{h_{g,b}x_b^{0.5}}{\omega m x_b C_{P,b}} \left(\frac{\pi D^2}{2} + \frac{4V}{D} \right) (T_b - T_P) + \frac{v_b}{C_{P,b}} \frac{\partial \ln v_b}{\partial \ln T_b} \frac{dp}{d\theta} \\ & + \frac{h_u - h_b}{x_b C_{P,b}} \left[\frac{dx_b}{d\theta} - (x_b - x_b^2) \frac{C}{\omega} \right] \end{aligned} \quad (\text{A-51})$$

The expressions of $dT_u/d\theta$ et $dT_b/d\theta$ are replaced in equation (A-38), and the result is:

$$\begin{aligned} \frac{dp}{d\theta} \left[x_b \frac{v_b}{p} \frac{\partial \ln v_b}{\partial \ln p} + x_b \frac{v_b^2}{C_{P,b} T_b} \left(\frac{\partial \ln v_b}{\partial \ln T_b} \right)^2 + (1 - x_b) \frac{v_u}{p} \frac{\partial \ln v_u}{\partial \ln p} \right. \\ \left. + (1 - x_b) \frac{v_u^2}{C_{P,u} T_u} \left(\frac{\partial \ln v_u}{\partial \ln T_u} \right)^2 \right] = \end{aligned} \quad (\text{A-52})$$

$$\frac{1}{m} \left(\frac{dV}{d\theta} - \frac{VC}{\omega} \right) - (v_b - v_u) \frac{dx_b}{d\theta} - v_b \frac{\partial \ln v_b}{\partial \ln T_b} \frac{h_u - h_b}{T_b C_{P,b}} \left[\frac{dx_b}{d\theta} - (x_b - x_b^2) \frac{C}{\omega} \right]$$

$$\begin{aligned}
 & + \frac{1}{\omega m} \left(\frac{\pi D^2}{2} + \frac{4V}{D} \right) \left[\frac{h_{g,b} v_b}{C_{Pb}} \left(\frac{\partial \ln v_b}{\partial \ln T_b} \right) x_b^2 \frac{(T_b - T_P)}{T_b} \right. \\
 & \quad \left. + \frac{h_{g,u} v_u}{C_{Pu}} \left(\frac{\partial \ln v_u}{\partial \ln T_u} \right) (1 - x_b^{0.5}) \frac{(T_u - T_P)}{T_u} \right]
 \end{aligned}$$

By posing the following variables:

$$\beta_1 = \frac{1}{m} \left(\frac{dV}{d\theta} - \frac{VC}{\omega} \right) \quad (\text{A-53})$$

$$\begin{aligned}
 \beta_2 = \frac{1}{\omega m} \left(\frac{\pi D^2}{2} + \frac{4V}{D} \right) & \left[\frac{h_{g,b} v_b}{C_{Pb}} \left(\frac{\partial \ln v_b}{\partial \ln T_b} \right) x_b^{0.5} \frac{(T_b - T_P)}{T_b} \right. \\
 & \left. + \frac{h_{g,u} v_u}{C_{Pu}} \left(\frac{\partial \ln v_u}{\partial \ln T_u} \right) (1 - x_b^{0.5}) \frac{(T_u - T_P)}{T_u} \right] \quad (\text{A-54})
 \end{aligned}$$

$$\beta_3 = -(v_b - v_u) \frac{dx_b}{d\theta} - v_b \frac{\partial \ln v_b}{\partial \ln T_b} \frac{h_u - h_b}{T_b C_{Pb}} \left[\frac{dx_b}{d\theta} - (x_b - x_b^2) \frac{C}{\omega} \right] \quad (\text{A-55})$$

$$\beta_4 = x_b \frac{v_b}{p} \frac{\partial \ln v_b}{\partial \ln p} + x_b \frac{v_b^2}{C_{Pb} T_b} \left(\frac{\partial \ln v_b}{\partial \ln T_b} \right)^2 \quad (\text{A-56})$$

$$\beta_5 = (1 - x_b) \frac{v_u}{p} \frac{\partial \ln v_u}{\partial \ln p} + (1 - x_b) \frac{v_u^2}{C_{Pu} T_u} \left(\frac{\partial \ln v_u}{\partial \ln T_u} \right)^2 \quad (\text{A-57})$$

The system of differential equations, in which the expressions of mechanical work of heat transfers and of the enthalpy losses are integrated, is finally written:

$$\frac{dp}{d\theta} = \frac{\beta_1 + \beta_2 + \beta}{\beta_4 + \beta_5} \quad (\text{A-58})$$

$$\begin{aligned}
 \frac{dT_b}{d\theta} = -\frac{h_{g,b} x_b^{0.5}}{\omega m x_b C_{Pb}} & \left(\frac{\pi D^2}{2} + \frac{4V}{D} \right) (T_b - T_P) + \frac{v_b}{C_{Pb}} \frac{\partial \ln v_b}{\partial \ln T_b} \left(\frac{\beta_1 + \beta_2 + \beta}{\beta_4 + \beta_5} \right) \\
 & + \frac{h_u - h_b}{x_b C_{Pb}} \left[\frac{dx_b}{d\theta} - (x_b - x_b^2) \frac{C}{\omega} \right] \quad (\text{A-59})
 \end{aligned}$$

$$\begin{aligned}
 \frac{dT_u}{d\theta} = -\frac{h_{g,u}}{\omega m C_{Pu}} & \left(\frac{\pi D^2}{2} + \frac{4V}{D} \right) \frac{(1 - x_b^{0.5})}{(1 - x_b)} (T_u - T_P) \\
 & + \frac{v_u}{C_{Pu}} \frac{\partial \ln v_u}{\partial \ln T_u} \left(\frac{\beta_1 + \beta_2 + \beta}{\beta_4 + \beta_5} \right) \quad (\text{A-60})
 \end{aligned}$$

$$\frac{dW}{d\theta} = p \frac{dV}{d\theta} \quad (\text{A-61})$$

$$\begin{aligned}
 \frac{dQ_P}{d\theta} = \frac{1}{\omega} & \left(\frac{\pi D^2}{2} + \frac{4V}{D} \right) \left[h_{g,b} x_b^{0.5} (T_b - T_P) \right. \\
 & \left. + h_{g,u} (1 - x_b^{0.5}) (T_u - T_P) \right] \quad (\text{A-62})
 \end{aligned}$$

$$\frac{dH_f}{d\theta} = \frac{Cm}{\omega} [x_b^2 h_b + (1 - x_b^2) h_u] \quad (\text{A-63})$$

If the system of differential equations (A-58) to (A-63) is analyzed, it is observed that:

- The magnitudes D and ω_{eng} are characteristics of the engine geometry and of the operating point. Similarly, the blow-by coefficient C is representative of the piston segments and is considered constant.
- The transfer coefficients $h_{g,b}$ and $h_{g,u}$ are estimated by the Woschni correlation in function of the thermodynamic variables p , T_b and T_u .
- The instantaneous chamber volume V depends on the piston position and is expressed in function of the crank angle θ :

$$V(\theta) = V_c \left[1 + \frac{\varepsilon - 1}{2} \left(1 + R_L - \cos \theta - \sqrt{R_L^2 - \sin^2 \theta} \right) \right] \quad (\text{A-64})$$

The total mass m contained in the combustion chamber, is considered as a known function of the crank angle θ and is obtained by integrating equation (A-20):

$$m = m_{init} e^{\left[\frac{C(\theta - \theta_{IVC})}{\omega} \right]} \quad (\text{A-65})$$

Where m_{init} is the mass inside the chamber at the moment of IVC at θ_{IVC} crank angle? As it was noted previously, the burnt mass fraction x_b with the aid of a phenomenological model. Therefore, it is a common function θ and maybe of the thermodynamic properties as well.

The other variables

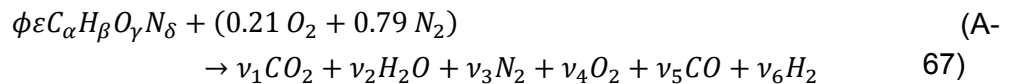
$$C_{pb}, C_{pu}, u_b, u_u, v_b, v_u, h_b, h_u, \frac{\partial \ln v_b}{\partial \ln T_b}, \frac{\partial \ln v_u}{\partial \ln T_u}, \frac{\partial \ln v_b}{\partial \ln p}, \frac{\partial \ln v_u}{\partial \ln p} \quad (\text{A-66})$$

Are thermodynamic properties and are calculated in function of p , T_b and T_u in the following sections.

A.2 Composition of fresh gases zone

In internal combustion engines, the total chamber mass in the combustion chamber on the moment of inlet valve closing is comprised by the admitted fresh gas mass and a fraction of residual gases from the previous cycle (RBG). For SI engines, typical values of RBG fraction vary from 20% at low loads to 7% for a full load of a naturally aspirated engine [8]. In some engine configurations, a part of the burnt gases is recirculated in the fresh gases intake, in order to diminish NO_x emissions. The presence of RBG on combustion is a diluent of the reactants. It has an impact on the laminar flame speed and on the chemical reactions of species.

The composition of RBG in the fresh gases can be calculated by considering the combustion chemical equation of a fuel of the form $C_\alpha H_\beta O_\gamma N_\delta$ at low temperature (as it is the case for exhaust gases).



Coefficient ε is determined by a reaction at stoichiometry:

$$\varepsilon = \frac{0.21}{\alpha + \frac{\beta}{4} - \frac{\gamma}{2}} \quad (\text{A-68})$$

The terms v_i are calculated by the atom conservation:

$$\begin{array}{l}
 C \quad \phi \varepsilon \alpha = v_1 + v_5 \\
 H \quad \phi \varepsilon \beta = 2v_2 + 2v_6 \\
 O \quad \phi \varepsilon \gamma + 0.42 = 2v_1 + v_2 + 2v_4 + v_5 \\
 N \quad \phi \varepsilon \delta + 1.58 = 2v_3
 \end{array} \quad (A-69)$$

Some approximations are considered in function of the fuel/air equivalence ratio ϕ :

$$\begin{array}{l}
 \phi < 1, v_5 = v_6 = 0 \\
 \phi > 1, v_4 = 0
 \end{array} \quad (A-70)$$

The solution of the system of equations (A-69) is given in Table A-1 for both cases of lean and rich mixtures.

Table A-1: Stoichiometric coefficients of low temperature combustion products

i	Species	$\phi \leq 1$	$\phi > 1$
1	CO ₂	$\alpha \phi \varepsilon$	$\alpha \phi \varepsilon - v_5$
2	H ₂ O	$\beta \phi \varepsilon / 2$	$0.42 - \phi \varepsilon (2\alpha - \gamma) + v_5$
3	N ₂	$0.79 + \delta \phi \varepsilon / 2$	$0.79 + \delta \phi \varepsilon / 2$
4	O ₂	$0.21 (1 - \phi)$	0
5	CO	0	v_5
6	H ₂	0	$0.42 (1 - \phi) - v_5$

For the case of a lean or stoichiometric mixture, the equations of atom conservation are enough for the solution of the system. For a rich mixture, an equilibrium constant is introduced, which comes from the following reaction:



$$K = \frac{v_2 v_5}{v_1 v_6} \quad (A-72)$$

The value de v_5 is thus given by the solution of a quadratic equation:

$$v_5 = \frac{-b + \sqrt{b^2 - 4ac}}{2a} \quad (A-73)$$

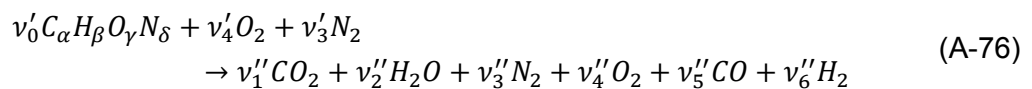
The constants a, b and c are:

$$\begin{array}{l}
 a = 1 - K \\
 b = 0.42 - \phi \varepsilon (2\alpha - \gamma) + K [0.42 (\phi - 1) + \alpha \phi \varepsilon] \\
 c = -0.42 \alpha \phi \varepsilon (\phi - 1) K
 \end{array} \quad (A-74)$$

$K(T)$ is determined by an approximation of values given in JANAF tables [80] by the following function: Temperature T is expressed in K :

$$\ln K = 2.743 - \frac{1.761 \cdot 10^3}{T} - \frac{1.611 \cdot 10^6}{T^2} + \frac{0.2803 \cdot 10^9}{T^3} \quad (A-75)$$

Let's un now write the combustion equation (A-67) in the following form:



ν_i' are the stoichiometric coefficients of reactants and ν_i'' , the stoichiometric coefficients of products. By introducing the mass fractions f of RBG, the mass fraction of each species are written:

$$Y_i = (1 - f)Y_i' + f Y_i'' \quad (\text{A-77})$$

The mole fractions are given:

$$X_i = (1 - x_r) X_i' + x_r X_i'' \quad (\text{A-78})$$

The RBG mole fraction is written x_r :

$$x_r = \left[1 + \frac{M''}{M'} \left(\frac{1}{f} - 1 \right) \right]^{-1} \quad (\text{A-79})$$

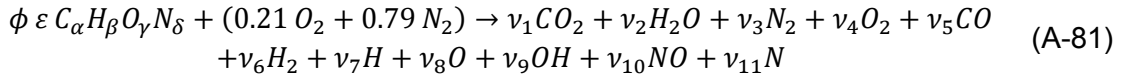
With M'' being the molar mass of products and M' being the molar mass of reactants:

$$M'' = \sum_{i=1}^6 X_i'' M_i \quad (\text{A-80})$$

$$M' = \sum_{i=1}^6 X_i' M_i$$

A.3 Composition of burnt gases zone

The temperature of the burnt gases often exceeds 2500 K in the combustion chamber of an engine. At this temperature dissociation and recombination phenomena among the species have a significant intervention. Ferguson [31] showed that the products of combustion are mainly composed of 11 species for $\varphi < 3$. The burnt gases are composed of the combustion products: CO_2, H_2O, O_2 and N_2 as well as of the dissociation and recombination products: CO, H_2, H, O, OH, NO and N . The equation of combustion is thus written:



The mole fractions of species X_i are expressed through the atom conservation:

$$\text{C: } \phi \varepsilon \alpha = (X_1 + X_5) N \quad (\text{A-82})$$

$$\text{H: } \phi \varepsilon \beta = (2X_2 + 2X_6 + X_7 + X_9) N \quad (\text{A-83})$$

$$\text{O: } \phi \varepsilon \gamma + 0.42 = (2X_1 + X_2 + 2X_4 + X_5 + X_8 + X_9 + X_{10}) N \quad (\text{A-84})$$

$$\text{N } \phi \varepsilon \delta + 1.58 = (2X_3 + X_{10} + X_{11}) N \quad (\text{A-85})$$

with N being the total mole number : $N = \sum_{i=1}^{11} \nu_i$, and by definition:

$$\sum_{i=1}^{11} X_i = 1 \quad (\text{A-86})$$

Seven equilibrium constants corresponding to the reactions of dissociation and recombination of species are used in order to complete the system of equations:

$$\frac{1}{2} H_2 \rightleftharpoons H, \quad K_1 = \frac{X_7 (p/p_0)^{1/2}}{X_6^{1/2}} \quad (\text{A-87})$$

$$\frac{1}{2}O_2 \rightleftharpoons O, \quad K_2 = \frac{X_8(p/p_0)^{1/2}}{X_4^{1/2}} \quad (\text{A-88})$$

$$\frac{1}{2}H_2 + \frac{1}{2}O_2 \rightleftharpoons OH, \quad K_3 = \frac{X_9}{X_4^{1/2}X_6^{1/2}} \quad (\text{A-89})$$

$$\frac{1}{2}O_2 + \frac{1}{2}N_2 \rightleftharpoons NO, \quad K_4 = \frac{X_{10}}{X_4^{1/2}X_3^{1/2}} \quad (\text{A-90})$$

$$H_2 + \frac{1}{2}O_2 \rightleftharpoons H_2O, \quad K_5 = \frac{X_2}{X_4^{1/2}X_6(p/p_0)^{1/2}} \quad (\text{A-91})$$

$$CO + \frac{1}{2}O_2 \rightleftharpoons CO_2, \quad K_6 = \frac{X_1}{X_4^{1/2}X_5(p/p_0)^{1/2}} \quad (\text{A-92})$$

$$\frac{1}{2}N_2 \rightleftharpoons N, \quad K_7 = \frac{X_{11}}{X_3^{1/2}}(p/p_0)^{1/2} \quad (\text{A-93})$$

The reference pressure p_0 is the atmospheric. For the temperature interval of $600 < T < 4000$ K, Olikara et Borman approximated the equilibrium constants given in JANAF tables [80] by a function of the following form.

$$\log K_j = A \ln(T/1000) + B/T + C + DT + ET^2 \quad (\text{A-94})$$

The coefficients are given in Table A-2:

Table A-2: Coefficients of equilibrium constants according to Olikara and Borman [83]

	<i>A</i>	<i>B</i>	<i>C</i>	<i>D</i>	<i>E</i>
K_1	0.432168E+00	-0.112464E+05	0.267269E+01	-0.745744E-04	0.242484E-08
K_2	0.310805E+00	0.129540E+05	0.321779E+01	-0.738336E-04	0.344645E-08
K_3	-0.141748E+00	-0.213308E+04	0.853461E+00	0.355015E-04	-0.310227E-08
K_4	0.150879E-01	-0.470959E+04	0.646096E+00	0.272805E-05	-0.154444E-08
K_5	-0.752364E+00	0.124210E+05	-0.260286E+01	0.259556E-03	-0.162687E-07
K_6	-0.415302E-02	0.148627E+05	-0.475746E+01	0.124699E-03	-0.900227E-08
K_7	+0.38972E+00	-0.245828E+05	-0.31422E+01	-0.963730E-04	+0.585643E-08

The integration of the six equations with the atom conservation equation and with the equation of total mole number leads to a non-linear system of eleven equations with ten unknown variables, which are the species mole fractions. After a recasting of the equations, this system may be resolved by an iterative method. The initial values of species mole fractions can be taken from a calculation without dissociation. The mole fractions of N_2 , O_2 , CO and H_2 are given by the relations in Table A-1. All mole fractions, which appear in equations (A-87) to (A-93), will be expressed as a function of the unknown variables X_3 , X_4 , X_5 and X_6 .

$$X_7 = c_1 X_6^{1/2}, \quad c_1 = K_1/(p/p_0)^{1/2} \quad (\text{A-95})$$

$$X_8 = c_2 X_4^{1/2}, \quad c_2 = K_2/(p/p_0)^{1/2} \quad (\text{A-96})$$

$$X_9 = c_3 X_4^{1/2} X_6^{1/2}, \quad c_3 = K_3 \quad (\text{A-97})$$

$$X_{10} = c_4 X_4^{1/2} X_3^{1/2}, \quad c_4 = K_4 \quad (\text{A-98})$$

$$X_2 = c_5 X_4^{1/2} X_6, \quad c_5 = K_5 (p/p_0)^{1/2} \quad (\text{A-99})$$

$$X_1 = c_6 X_4^{1/2} X_5, \quad c_6 = K_6 (p/p_0)^{1/2} \quad (\text{A-100})$$

$$X_{11} = c_7 X_3^{1/2}, \quad c_7 = K_7 (p/p_0)^{1/2} \quad (\text{A-101})$$

The total mole number can be eliminated by the division of equations (A-83), (A-84) and (A-85) by (A-82). The following equations are obtained:

$$2X_2 + 2X_6 + X_7 + X_9 - d_1(X_1 + X_5) = 0 \quad (\text{A-102})$$

$$2X_1 + X_2 + 2X_4 + X_5 + X_8 + X_9 + X_{10} - d_2(X_1 + X_5) = 0 \quad (\text{A-103})$$

$$2X_3 + X_{10} + X_{11} - d_3(X_1 + X_5) = 0 \quad (\text{A-104})$$

$$\text{where} \quad d_1 = \frac{\beta}{\alpha} \quad d_2 = \frac{\gamma}{\alpha} + \frac{0.42}{\varepsilon\phi\alpha} \quad d_3 = \frac{\delta}{\alpha} + \frac{1.58}{\varepsilon\phi\alpha}$$

By substituting the equations (A-95) to (A-101) in equations (A-102) to (A-104) and in equation (A-86) the system is reduced in a non-linear system of four equations with four unknown variables X_3, X_4, X_5 and X_6 , which is written in the form:

$$f_j(X_3, X_4, X_5, X_6) = 0, j = 1, 2, 3, 4 \quad (\text{A-105})$$

This system is resolved by the Newton-Raphson method. By using matrix notation, the system is linearized as follows:

$$\begin{aligned} & X_3^{(0)}, X_4^{(0)}, X_5^{(0)}, X_6^{(0)} \\ & J^{(k)} \Delta X + f^{(k)} = 0 \\ & X^{(k+1)} = X^{(k)} + \Delta X \end{aligned} \quad (\text{A-106})$$

In this system, the initial values of $X_3^{(0)}, X_4^{(0)}, X_5^{(0)}, X_6^{(0)}$ of the mole fractions of N_2, O_2, CO and H_2 are calculated in function of the equations of Table A-1. The components of the Jacobian matrix are:

$$X_3^{(0)}, X_4^{(0)}, X_5^{(0)}, X_6^{(0)} \quad (\text{A-107})$$

In order to simplify the mathematic notations, the following partial derivatives are introduced:

$$\begin{aligned} D_{ij} &= \frac{\partial X_{i(i=1, 2, 7, 8, 9, 10, 11)}}{\partial X_{j(j=3, 4, 5, 6)}} \\ D_{jj} &= \frac{\partial X_j}{\partial X_j} = 1 \end{aligned}$$

From relations (A-95) to (A-101), the non-zero values of the derivatives are obtained:

$$\begin{aligned} D_{76} &= \frac{1}{2} \frac{c_1}{X_6^{1/2}} & D_{84} &= \frac{1}{2} \frac{c_1}{X_4^{1/2}} & D_{94} &= \frac{1}{2} \frac{c_3 X_6^{1/2}}{X_4^{1/2}} & D_{96} &= \frac{1}{2} \frac{c_3 X_4^{1/2}}{X_6^{1/2}} & D_{104} &= \frac{1}{2} \frac{c_4 X_3^{1/2}}{X_4^{1/2}} \\ D_{103} &= \frac{1}{2} \frac{c_4 X_4^{1/2}}{X_3^{1/2}} & D_{26} &= c_5 X_4^{1/2} & D_{24} &= \frac{1}{2} \frac{c_5 X_6}{X_4^{1/2}} & D_{14} &= \frac{1}{2} \frac{c_6 X_5}{X_4^{1/2}} & D_{15} &= c_6 X_4^{1/2} \end{aligned}$$

And

$$D_{113} = \frac{1}{2} \frac{c_7}{X_3^{1/2}}$$

The Jacobian matrix is written:

$$\begin{bmatrix}
 1 + D_{103} + D_{113} & D_{14} + D_{24} + 1 + D_{84} + D_{94} + D_{104} & 1 + D_{15} & D_{26} + 1 + D_{76} + D_{96} \\
 0 & 2D_{24} + D_{94} - d_1 D_{14} & -d_1(D_{15} + 1) & 2D_{26} + 2 + D_{76} + D_{96} \\
 D_{103} & (2 - d_2)D_{14} + D_{24} + 2 + D_{84} + D_{94} + D_{104} & 2D_{15} + 1 - d_2(D_{15} + 1) & D_{26} + D_{96} \\
 2 + D_{103} + D_{113} & D_{104} - d_3 D_{14} & d_3(D_{15} - 1) & 0
 \end{bmatrix}$$

A.4 Thermodynamic properties of zones

The gas mixture in the combustion chamber is usually treated as a mixture of perfect gases:

$$pV = mRT \quad (\text{A-108})$$

R is the mass perfect gas constant calculated for each species in function of the universal perfect gas constant \bar{R} and of the molar mass of the respective species:

$$R = \frac{\bar{R}}{M} \quad (\text{A-109})$$

According to equation (A-106), the internal energy u as well as the enthalpy h of the gas is a function of temperature:

$$u = u(T) \quad (\text{A-110})$$

$$h = h(T) \quad (\text{A-111})$$

The specific heats at constant volume c_V and constant pressure c_P of a perfect gas are defined:

$$c_V = \left(\frac{\partial u}{\partial T} \right)_V = \frac{du}{dT} \quad (\text{A-112})$$

$$c_P = \left(\frac{\partial h}{\partial T} \right)_P = \frac{dh}{dT} \quad (\text{A-113})$$

$$c_P - c_V = \bar{R} \quad (\text{A-114})$$

In general, these expressions of internal energy and enthalpy of a perfect gas at temperature T are connected to the internal energy and enthalpy at the reference temperature T_0 :

$$u = u_0 + \int_{T_0}^T c_V(T) dT \quad (\text{A-115})$$

$$h = h_0 + \int_{T_0}^T c_P(T) dT \quad (\text{A-116})$$

The entropy expression at T, v and p in connection with the entropy at the reference state T_0, v_0 and p_0 is obtained by the relations:

$$ds = \frac{C_V}{T} dT + R \frac{dv}{v} = \frac{C_P}{T} dT - R \frac{dp}{p} \quad (\text{A-117})$$

Or in intergral form:

$$s = s_0 + \int_{T_0}^T \frac{C_V}{T} dT + R \ln \frac{v}{v_0} \quad (\text{A-118})$$

$$s = s_0 + \int_{T_0}^T \frac{C_P}{T} dT - R \ln \frac{p}{p_0} \quad (\text{A-119})$$

The thermodynamic properties of a mixture of perfect gases are obtained by the following relations:

$$M = \sum_i X_i M_i \quad (\text{A-120})$$

$$u = \sum_i Y_i u_i, \quad h = \sum_i Y_i h_i, \quad s = \sum_i Y_i s_i \quad (\text{A-121})$$

In practice, the calculation of thermodynamic properties is done by polynomial regressions [82], on two different temperature intervals $\langle T_{inf}|T_{med} \rangle$ and $\langle T_{med}|T_{sup} \rangle$. Typical values for the limiting temperatures are $T_{inf} = 300$ K, $T_{med} = 1000$ K and $T_{sup} = 5000$ K.

$$\frac{C_{P,i}^0}{R} = a_1^i + a_2^i T + a_3^i T^2 + a_4^i T^3 + a_5^i T^4 \quad (\text{A-122})$$

$$\frac{H_i^0}{RT} = a_1^i + \frac{a_2^i}{2} T + \frac{a_3^i}{3} T^2 + \frac{a_4^i}{4} T^3 + \frac{a_5^i}{5} T^4 + \frac{a_6^i}{T} \quad (\text{A-123})$$

$$\frac{S_i^0}{R} = a_1^i \ln T + a_2^i T + \frac{a_3^i}{2} T^2 + \frac{a_4^i}{3} T^3 + \frac{a_5^i}{4} T^4 + a_7^i \quad (\text{A-124})$$

The values for the coefficients a_k^i for the considered species are given in Table A-3.

Fresh gases

By introduction of equation (A-121) in equation (A-113), the specific heat at constant pressure of fresh gases, which are composed of air, fuel and RBG is given by the relation:

$$C_P = \left(\frac{\partial h}{\partial T} \right)_p = \frac{1}{M} \sum_{i=0}^6 \left(X_i C_{P,i}^0 + H_i^0 \frac{\partial X_i}{\partial T} \right) \quad (\text{A-125})$$

In order to calculate the second term of the right hand side, equation (A-78) is derived by the temperature T , by using the fact that X_i' and x_r do not depend on temperature :

$$\frac{\partial X_i}{\partial T} = x_r \frac{\partial X_i''}{\partial T} \quad (\text{A-126})$$

In Table A-1, it is observed that the sum of v_i does not depend on temperature regardless of the fuel/air equivalence ratio:

$$\frac{\partial X_i}{\partial T} = x_r \frac{1}{\sum_i v_i''} \frac{\partial v_i''}{\partial T} \quad (\text{A-127})$$

Table A-1 also shows that none of v_i of a lean mixture depends on temperature. This is not the case in rich mixtures, where the v_i are expressed in function of the temperature dependent v_5 , which depends on temperature through equation (A-73):

$$\begin{aligned} \frac{\partial X_i}{\partial T} &= 0, \quad (\varphi \leq 1) \\ \frac{\partial X_i}{\partial T} &= x_r \frac{1}{\sum_i v_i} \frac{\partial v_i}{\partial v_5} \frac{\partial v_5}{\partial K} \frac{\partial K}{\partial T}, \quad (\varphi > 1) \end{aligned} \quad (\text{A-128})$$

In order to calculate the specific heat under constant pressure of the fresh gases, the following partial derivatives are extracted:

$$\begin{aligned} \frac{\partial v_5}{\partial K} &= \frac{v_5^2 - v_5 [0.42 (\phi - 1) + \alpha \phi \varepsilon] + 0.42 \alpha \phi \varepsilon (\phi - 1)}{2 v_5 a + b} \\ \frac{\partial K}{\partial T} &= K \left(\frac{1.761 \cdot 10^3}{T^2} + \frac{3.222 \cdot 10^6}{T^3} + \frac{0.8409 \cdot 10^9}{T^4} \right) \end{aligned} \quad (\text{A-129})$$

Burnt Gases

The system of ordinary differential equations (A-58) to (A-63), which characterizes the system's thermodynamic state (p , T_b and T_u) in function of thermodynamic magnitudes, contains partial derivatives of thermodynamic properties, which are shown in relation (A-66) and are calculated in this section.

The specific heat under constant pressure, composed of the ten species of the combustion reaction (A-81), is given by:

$$C_P = \left(\frac{\partial h}{\partial T} \right)_P = \frac{1}{M} \left[\sum_{i=1}^{11} \left(X_i C_{P,i}^0 + H_i^0 \frac{\partial X_i}{\partial T} \right) - \frac{H^0 M_T}{M} \right] \quad (\text{A-130})$$

With M_T :

$$M_T = \frac{\partial M}{\partial T} = \sum_{i=1}^{11} M_i \frac{\partial X_i}{\partial T}, \quad H^0 = \sum_{i=1}^{10} X_i H_i^0 \quad (\text{A-131})$$

By introducing equation (A-109) in the perfect gas equation (A-108) and by deriving by the temperature, it is obtained:

$$\left(\frac{\partial \ln v}{\partial \ln T} \right)_P = 1 - \frac{T M_T}{M} \quad (\text{A-132})$$

Similarly, by deriving by pressure:

$$\left(\frac{\partial \ln v}{\partial \ln p} \right)_T = -1 - \frac{p M_P}{M} \quad (\text{A-133})$$

With M_P

$$M_P = \frac{\partial M}{\partial p} = \sum_{i=1}^{11} M_i \frac{\partial X_i}{\partial p} \quad (\text{A-134})$$

From the equations (A-95) to (A-101) it is known that all mole fractions may be expressed in function of the independent variables X_3, X_4, X_5 and X_6 . For the complete determination of

expressions (A-130), (A-132) and (A-133), the following partial derivatives must be evaluated:

$$\frac{\partial X_i}{\partial T}, \quad i = 3, 4, 5, 6 \quad (\text{A-135})$$

The evaluation is obtained by the resolution of the system of partial derivatives, which appears after the derivation by temperature T of the system (A-103):

$$\frac{\partial f_j}{\partial T} + \frac{\partial f_j}{\partial X_3} \frac{\partial X_3}{\partial T} + \frac{\partial f_j}{\partial X_4} \frac{\partial X_4}{\partial T} + \frac{\partial f_j}{\partial X_5} \frac{\partial X_5}{\partial T} + \frac{\partial f_j}{\partial X_6} \frac{\partial X_6}{\partial T} = 0 \quad (\text{A-136})$$

$$j = 3, 4, 5, 6$$

Which is written in matrix form:

$$J \frac{\partial X}{\partial T} + \frac{\partial f}{\partial T} = 0 \quad (\text{A-137})$$

With J being the Jacobian matrix in section A-3. For the evaluation of the second right hand side term, the following variable change is obtained:

$$x_i = \frac{X_i}{c_{i-6}}, \quad i = 7, 8, 9, 10, 11$$

$$x_1 = \frac{X_1}{c_6} \quad (\text{A-138})$$

$$x_2 = \frac{X_2}{c_7}$$

According to equations (A-95) à (A-101), les X_i are functions of the independent variables X_3, X_4, X_5 and X_6 exclusively. By replacing (A-138) in the equations (A-86) and (A-102) to (A-104), and by deriving by T , we get:

$$\frac{\partial f_1}{\partial T} = \frac{\partial c_6}{\partial T} x_1 + \frac{\partial c_5}{\partial T} x_2 + \frac{\partial c_1}{\partial T} x_7 + \frac{\partial c_2}{\partial T} x_8 + \frac{\partial c_3}{\partial T} x_9 + \frac{\partial c_4}{\partial T} x_{10} + \frac{\partial c_7}{\partial T} x_{11} \quad (\text{A-139})$$

$$\frac{\partial f_2}{\partial T} = 2 \frac{\partial c_5}{\partial T} x_2 + \frac{\partial c_1}{\partial T} x_7 + \frac{\partial c_3}{\partial T} x_9 - d_1 \frac{\partial c_6}{\partial T} x_1 \quad (\text{A-140})$$

$$\frac{\partial f_3}{\partial T} = 2 \frac{\partial c_6}{\partial T} x_1 + \frac{\partial c_5}{\partial T} x_2 + \frac{\partial c_2}{\partial T} x_8 + \frac{\partial c_3}{\partial T} x_9 + \frac{\partial c_4}{\partial T} x_{10} - d_2 \frac{\partial c_6}{\partial T} x_1 \quad (\text{A-141})$$

$$\frac{\partial f_4}{\partial T} = \frac{\partial c_4}{\partial T} x_{10} + \frac{\partial c_7}{\partial T} x_{11} - d_3 \frac{\partial c_6}{\partial T} x_1 \quad (\text{A-142})$$

In these four equations, the expressions of $\partial c_i / \partial T$ are determined from equations (A-95) to (A-101):

$$\frac{\partial c_1}{\partial T} = \frac{1}{(p/p_0)^{1/2}} \frac{dK_1}{dT}$$

$$\frac{\partial c_2}{\partial T} = \frac{1}{(p/p_0)^{1/2}} \frac{dK_2}{dT}$$

$$\frac{\partial c_3}{\partial T} = \frac{dK_3}{dT}$$

$$\frac{\partial c_4}{\partial T} = \frac{dK_4}{dT}$$

$$\frac{\partial c_5}{\partial T} = (p/p_0)^{1/2} \frac{dK_5}{dT}$$

$$\frac{\partial c_6}{\partial T} = (p/p_0)^{1/2} \frac{dK_6}{dT}$$

And

$$\frac{\partial c_7}{\partial T} = \frac{1}{(p/p_0)^{1/2}} \frac{dK_7}{dT}$$

The derivative of the equilibrium constants are deduced by equation (A-94):

$$\frac{dK_j}{dT} = 2.302585 K_i \left(\frac{A}{T} - \frac{B}{T^2} + D + 2ET \right) \quad (\text{A-143})$$

The partial derivatives of other species are calculated by the following relations, which have been obtained by temperature derivation of equations (A-95) to (A-101):

$$\frac{\partial X_7}{\partial T} = X_6^{1/2} \frac{\partial c_1}{\partial T} + D_{76} \frac{\partial X_6}{\partial T} \quad (\text{A-144})$$

$$\frac{\partial X_8}{\partial T} = X_4^{1/2} \frac{\partial c_2}{\partial T} + D_{84} \frac{\partial X_4}{\partial T} \quad (\text{A-145})$$

$$\frac{\partial X_9}{\partial T} = X_4^{1/2} X_6^{1/2} \frac{\partial c_3}{\partial T} + D_{94} \frac{\partial X_4}{\partial T} + D_{96} \frac{\partial X_6}{\partial T} \quad (\text{A-146})$$

$$\frac{\partial X_{10}}{\partial T} = X_4^{1/2} X_3^{1/2} \frac{\partial c_4}{\partial T} \quad (\text{A-147})$$

$$\frac{\partial X_2}{\partial T} = X_4^{1/2} X_6^{1/2} \frac{\partial c_5}{\partial T} + D_{24} \frac{\partial X_4}{\partial T} + D_{26} \frac{\partial X_6}{\partial T} \quad (\text{A-148})$$

$$\frac{\partial X_1}{\partial T} = X_4^{1/2} X_5 \frac{\partial c_6}{\partial T} + D_{14} \frac{\partial X_4}{\partial T} + D_{15} \frac{\partial X_5}{\partial T} \quad (\text{A-149})$$

$$\frac{\partial X_{11}}{\partial T} = X_3^{1/2} \frac{\partial c_7}{\partial T} + D_{113} \frac{\partial X_3}{\partial T} \quad (\text{A-150})$$

The mole fraction variations terms in function of pressure are obtained by a similar process, by simply replacing $\partial/\partial T$ with $\partial/\partial p$ in equations (A-133) to (A-147) and by using the following relations:

$$\frac{\partial c_1}{\partial p} = -\frac{1}{2} \frac{c_1}{(p/p_0)}$$

$$\frac{\partial c_2}{\partial p} = -\frac{1}{2} \frac{c_2}{(p/p_0)}$$

$$\frac{\partial c_3}{\partial p} = 0$$

$$\frac{\partial c_4}{\partial p} = 0$$

$$\frac{\partial c_5}{\partial p} = \frac{1}{2} \frac{c_5}{(p/p_0)}$$

$$\frac{\partial c_6}{\partial p} = \frac{1}{2} \frac{c_6}{(p/p_0)}$$

And

$$\frac{\partial c_7}{\partial p} = -\frac{1}{2} \frac{c_7}{(p/p_0)}$$

Table A-3: Coefficients a_k^i of relations (A-122) to (A-124) according to [80]⁸

	a_1	a_2	a_3	a_4	a_5	a_6	a_7
CO₂							
300-1000 K	2.35677352E+00	8.98459677E-03	-7.12356269E-06	2.45919022E-09	-1.43699548E-13	-4.83719697E+04	9.90105222E+00
1000-5000 K	3.85746029E+00	4.41437026E-03	-2.21481404E-06	5.23490188E-10	-4.72084164E-14	-4.87591660E+04	2.27163806E+00
H₂O							
300-1000 K	4.19864056E+00	-2.03643410E-03	6.52040211E-06	-5.48797062E-09	1.77197817E-12	-3.02937267E+04	-8.49032208E-01
1000-5000 K	3.03399249E+00	2.17691804E-03	-1.64072518E-07	-9.70419870E-11	1.68200992E-14	-3.00042971E+04	4.96677010E+00
N₂							
300-1000 K	0.03298677E+02	0.14082404E-02	-0.03963222E-04	0.05641515E-07	-0.02444854E-10	-0.10208999E+04	0.03950372E+02
1000-5000 K	0.02926640E+02	0.14879768E-02	-0.05684760E-05	0.10097038E-09	-0.06753351E-13	-0.09227977E+04	0.05980528E+02
O₂							
300-1000 K	3.78245636E+00	-2.99673416E-03	9.84730201E-06	-9.68129509E-09	3.24372837E-12	-1.06394356E+03	3.65767573E+00
1000-5000 K	3.28253784E+00	1.48308754E-03	-7.57966669E-07	2.09470555E-10	-2.16717794E-14	-1.08845772E+03	5.45323129E+00
CO							
300-1000 K	3.57953347E+00	-6.10353680E-04	1.01681433E-06	9.07005884E-10	-9.04424499E-13	-1.43440860E+04	3.50840928E+00
1000-5000 K	2.71518561E+00	2.06252743E-03	-9.98825771E-07	2.30053008E-10	-2.03647716E-14	-1.41518724E+04	7.81868772E+00
H₂							
300-1000 K	2.34433112E+00	7.98052075E-03	-1.94781510E-05	2.01572094E-08	-7.37611761E-12	-9.17935173E+02	6.83010238E-01
1000-5000 K	3.33727920E+00	-4.94024731E-05	4.99456778E-07	-1.79566394E-10	2.00255376E-14	2.00255376E-14	-3.20502331E+00
H							
300-1000 K	2.50000000E+00	7.05332819E-13	-1.99591964E-15	2.30081632E-18	-9.27732332E-22	2.54736599E+04	-4.46682853E-01
1000-5000 K	2.50000001E+00	-2.30842973E-11	1.61561948E-14	-4.73515235E-18	4.98197357E-22	2.54736599E+04	-4.46682914E-01
O							
300-1000 K	3.16826710E+00	-3.27931884E-03	6.64306396E-06	-6.12806624E-09	2.11265971E-12	2.91222592E+04	2.05193346E+00
1000-5000 K	2.56942078E+00	-8.59741137E-05	4.19484589E-08	-1.00177799E-11	1.22833691E-15	2.92175791E+04	4.78433864E+00
OH							
300-1000 K	3.99201543E+00	-2.40131752E-03	4.61793841E-06	-3.88113333E-09	1.36411470E-12	3.61508056E+03	-1.03925458E-01
1000-5000 K	3.09288767E+00	5.48429716E-04	1.26505228E-07	-8.79461556E-11	1.17412376E-14	3.85865700E+03	4.47669610E+00
NO							
300-1000 K	0.42184763E+01	-0.46389760E-02	0.11041022E-04	-0.93361354E-08	0.28035770E-11	0.98446230E+04	0.22808464E+01
1000-5000 K	0.32606056E+01	0.11911043E-02	-0.42917048E-06	0.69457669E-10	-0.40336099E-14	0.99209746E+04	0.63693027E+01
N							
300-1000 K	0.25000000E+01	0.00000000E+00	0.00000000E+00	0.00000000E+00	0.00000000E+00	0.56104637E+05	0.41939087E+01
1000-5000 K	0.24159429E+01	0.17489065E-03	-0.11902369E-06	0.30226245E-10	-0.20360982E-14	0.56133773E+05	0.46496096E+01
CH₄							
300-1000 K	5.14987613E+00	-1.36709788E-02	4.91800599E-05	-4.84743026E-08	1.66693956E-11	-1.02466476E+04	-4.64130376E+00
1000-5000 K	7.48514950E-02	1.33909467E-02	-5.73285809E-06	1.22292535E-09	-1.01815230E-13	-9.46834459E+03	1.84373180E+01
C₃H₈							
300-1000 K	0.93355381E+00	0.26424579E-01	0.61059727E-05	-0.21977499E-07	0.95149253E-11	-0.13958520E+05	0.19201691E+02
1000-5000 K	0.75341368E+01	0.18872239E-01	-0.62718491E-05	0.91475649E-09	-0.47838069E-13	-0.16467516E+05	0.17892349E+02
C₈H₈							
300-1000 K	-2.78349926E-01	9.13960795E-02	-4.92090542E-05	1.02668363E-08	-1.55748743E+04	-3.05715407E+04	2.72162000E+01
1000-5000 K	-	-	-	-	-	-	-
C₂H₅OH							
300-1000 K	3.51755641E+00	1.99987424E-02	-6.00148466E-06	0.00000000E+00	0.00000000E+00	-3.03013079E+04	8.01623000E+00
1000-5000 K	-	-	-	-	-	-	-

⁸ For isooctane (C₈H₈) and ethanol (C₂H₅OH) values from Heywood [8] are used.

Appendix B Geometric model

The geometry of the chamber has a very important role for combustion. During the calculations of the cycle, flame geometry has a direct impact of combustion as it was shown in previous chapters. The flame front is considered as a spherical surface, limited by the piston, the cylinder head and the cylinder. It is common practice to use 3D CAD applications in order to calculate the surface and the volume of the flame. Nevertheless, a digital representation of the combustion chamber is not always available for a given engine. In addition, the calculation of flame surface distribution in connection with the distance from the chamber walls, which is needed for the combustion model, cannot be calculated by a quick and straightforward manner by the 3D CAD tools. A parametric model of simplified geometry has been created which can calculate the surface, the volume and the surface distribution in function of the distance of the flame from the wall.

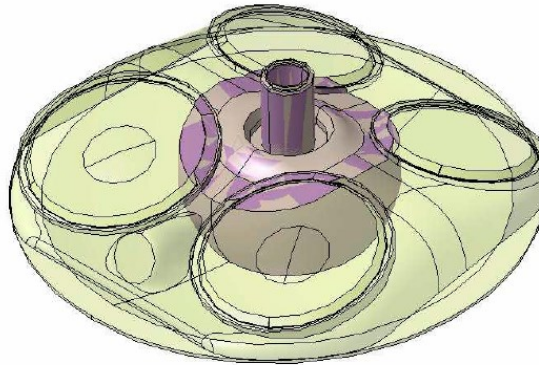


Figure B-1: Cylinder head, spark plug and spherical flame (3D CAD environment)

The simplified model consists of two planes which correspond to intake and exhaust valves (denoted with a and e). The top of the cylinder head may be offset by the symmetry axis of the cylinder. Thus, a pent-roof cylinder head is formed. A gap exists between each plane and the cylinder. It is closed by prolonging the cylinder. This detail can be shown in Figure B-2.

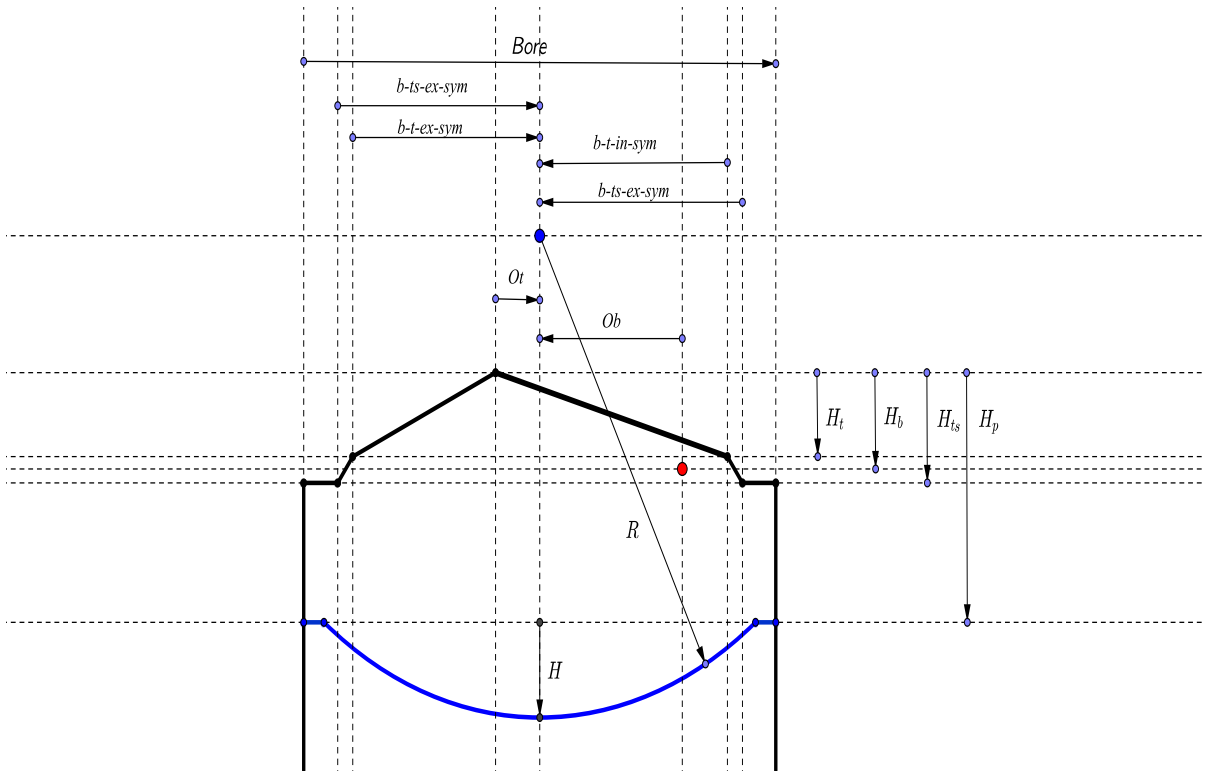


Figure B-2: Simplified chamber geometry in 2D cut section

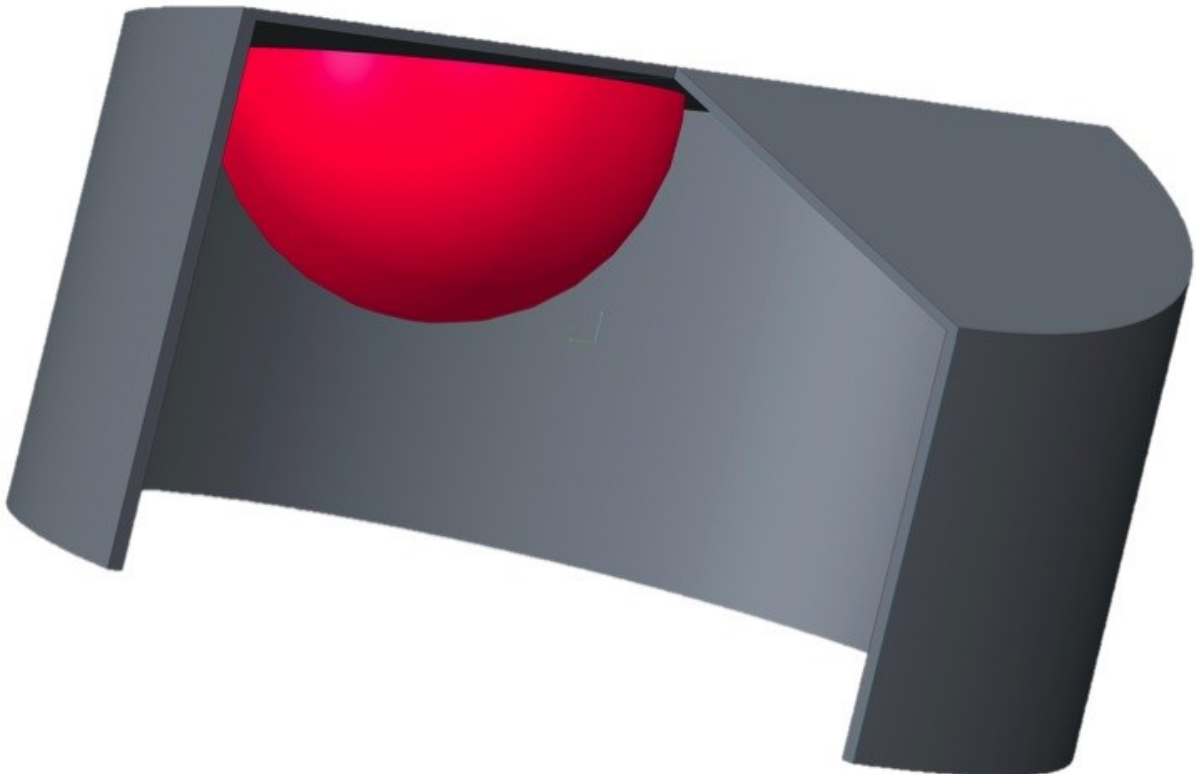


Figure B-3: Simplified chamber geometry in 3D vision

B.1 Burnt gas volume calculation

Spherical flame

When the flame does not intersect with the chamber walls, its volume is given by the fundamental relation (with R_f being the flame radius):

$$V = \frac{4}{3}\pi R_f^3 \quad (\text{B-1})$$

Flame intersects with one plane

In the case of an interaction of the flame with one head plane, a calculation of the volume of the outer spherical cap (Figure B-4) is needed. Afterwards, this volume is subtracted by the volume of the sphere. The volume of the spherical cap is given by the relation with h being the height of the outer cap:

$$V_{cap} = \frac{1}{3}\pi h^2(3R_f - h) \quad (\text{B-2})$$

The volume, which is enclosed by the flame, becomes:

$$V = \frac{4}{3}\pi R_f^3 - V_{cap} \quad (\text{B-3})$$

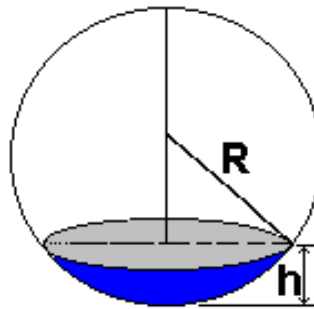


Figure B-4: Spherical cap

Flame intersects with both planes

When the flame intersects with both planes, the form of the volume is shown in Figure B-6. In this case, we calculate the inner part of the volume in the following manner: We calculate the volume of two caps with the aid of equation (B-3) and we subtract them from the sphere volume. The volume of the fourth part must be calculated.

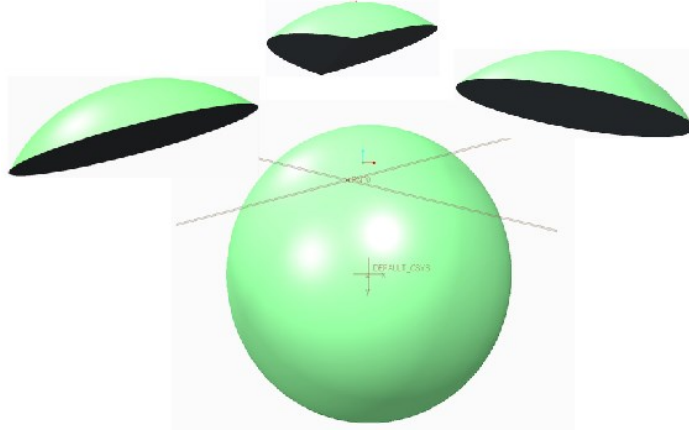


Figure B-5: Intersection of the flame with both planes

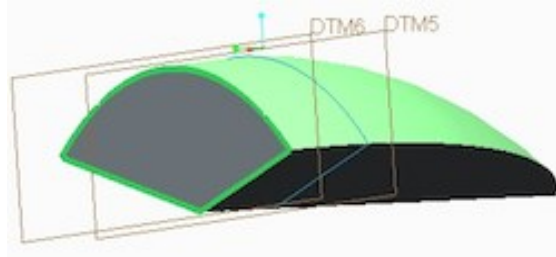


Figure B-6: Irregular part in the case of sphere intersecting with both planes (3D view)

We consider that the volume of this part is an accumulation of surfaces (Figure B-6). We suppose that there exist parallel to XZ planes. Consequently, we can find the volume by integrating those surfaces along the y direction. In the general case when a sphere intersects with a plane, their contact surface is a circle with radius r :

$$r = \sqrt{R_f^2 - y^2} \quad (\text{B-4})$$

In any other case, the interface surface must be identified. If this interface is denoted as $S = f(r)$, its volume is:

$$V_{int} = \int_{y_{min}}^{y_{max}} f(r) dr \quad (\text{B-5})$$

In the case of this geometry, we will use this procedure to calculate the volume of the irregular part (2D representation in Figure B-7). The equations of the two planes are:

$$\begin{aligned} A_{in}x + B_{in}y + C_{in}z + D_{in} &= 0 \\ A_{ex}x + B_{ex}y + C_{ex}z + D_{ex} &= 0 \end{aligned} \quad (\text{B-6})$$

The coefficients $A_{in,ex}$, $B_{in,ex}$, $C_{in,ex}$ and $D_{in,ex}$ represent the constants in the plan equation. $B = 0$ in the case when the planes are perpendicular to XZ plane. The intersection of the two plans is:

$$x = \frac{D_{ex}C_{in} - C_{ex}D_{in}}{A_{in}C_{ex} - A_{ex}C_{in}} \quad z = \frac{D_{ex}A_{in} - D_{in}A_{ex}}{A_{ex}C_{in} - A_{in}C_{ex}} \quad (\text{B-7})$$

We denote $x = a$ and $z = b$ in order to simplify the following equations. Then, we can calculate the y coordinates of intersection points of the planes and the sphere:

$$y_{max,min} = \pm \sqrt{R_f^2 - a^2 - b^2} \quad (B-8)$$

At this point, the surface for the volume integration can be computed:

$$F_3 = F_{1,2,3} - F_1 - F_2 \quad (B-9)$$

The angles α and β are equal to:

$$\cos \alpha = \frac{r^2 + a^2 + b^2 - \left(\sqrt{r^2 - d_i^2} - \sqrt{a^2 + b^2 - d_i^2} \right)^2}{2r\sqrt{a^2 + b^2}} \quad (B-10)$$

$$\cos \beta = \frac{r^2 + a^2 + b^2 - \left(\sqrt{r^2 - d_e^2} - \sqrt{a^2 + b^2 - d_e^2} \right)^2}{2r\sqrt{a^2 + b^2}} \quad (B-11)$$

With those angles we may calculate the surface:

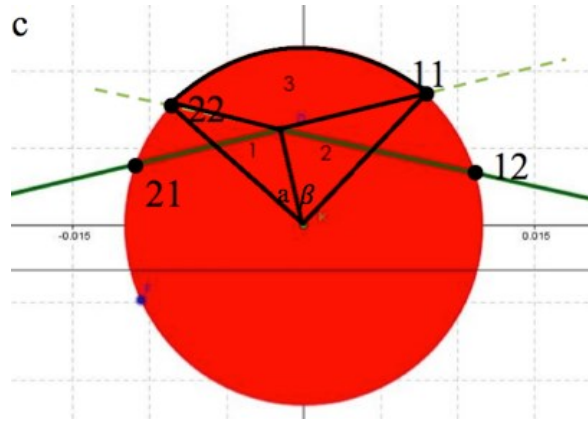


Figure B-7: Irregular part in the case of sphere intersecting with both planes (2D view)

$$F_{1,2,3} = \pi r^2 \frac{\alpha + \beta}{2\pi} \quad (B-12)$$

$$F_1 = 0.5 \sin \alpha \cdot r\sqrt{a^2 + b^2} \quad (B-13)$$

$$F_2 = 0.5 \sin \beta \cdot r\sqrt{a^2 + b^2} \quad (B-14)$$

$$F_2 = 0.5 \sin \beta \cdot r\sqrt{a^2 + b^2} \quad (B-15)$$

Thus the volume of the irregular section finally becomes:

$$V_3 = \int_{y_{min}}^{y_{max}} (F_{1,2,3} - F_1 - F_2) dy \quad (B-16)$$

Finally, we may calculate the enclosed volume by the flame:

$$V = \frac{4}{3} \pi R_f^3 - V_1 - V_2 + V_3 \quad (B-17)$$

Flame is between primary and secondary plane

In this case, the flame has passed the primary plane. The form of the volume is shown in Figure B-8. The volume can be divided in two parts. We have to calculate the small irregular volume.

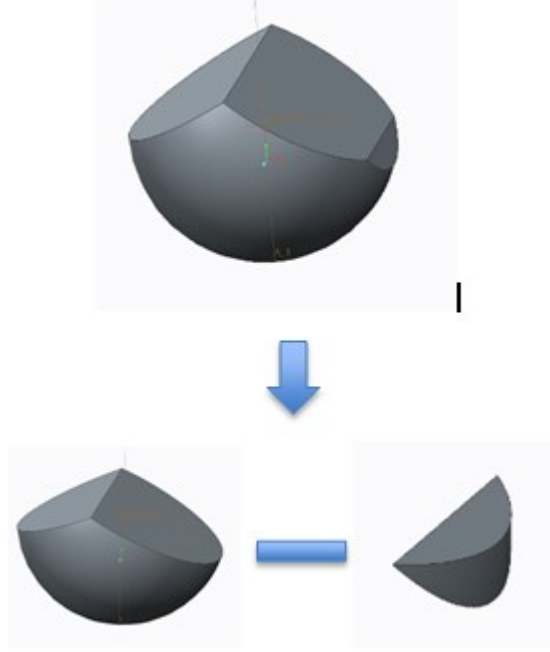


Figure B-8: Equivalence of volume when flame is between the two planes (primary and secondary)

For the small part of the volume we will use the XZ plane geometry (Figure B-9). We define the coordinates of points A,B and C as

$$A (b_{t,in}, H_b - H_t); B (x_{12}, z_{12}); C (x_{12s}, z_{12s})$$

The following vectors are defined:

$$\overline{AB} = (x_{12} - b_{t,in}, z_{12} - H_b + H_t) \quad (\text{B-18})$$

$$\overline{AC} = (x_{12s} - b_{t,in}, z_{12s} - H_b + H_t) \quad (\text{B-19})$$

The surface of the triangle ABC is calculated.

$$\begin{aligned} F_{ABC} &= 0.5 \overline{AB} \times \overline{AC} \\ &= 0.5(x_{12} - b_{t,in}) \cdot (z_{12s} - H_b + H_t) \\ &\quad - (z_{12} - H_b + H_t) \cdot (x_{12s} - b_{t,in}) \end{aligned} \quad (\text{B-20})$$

We also have to calculate the small spherical cap, defined by the angle $\angle BOC$

$$\angle BOC = \cos^{-1} \left(\frac{\overline{OB} \cdot \overline{OC}}{|\overline{OB}| \cdot |\overline{OC}|} \right) \quad (\text{B-21})$$

$$F_{cap} = 0.5 \angle BOC \cdot r^2 - 0.5(x_{12} \cdot z_{12s} - z_{12s} \cdot x_{12s}) \quad (\text{B-22})$$

Finally, we calculate the volume:

$$\begin{aligned} V_{e2} &= 2 \int_0^{y_1} (F_{ABC} + F_{cap}) dy \\ y_1 &= \sqrt{R_f^2 - b_{t,in}^2 - (H_b - H_t)^2} \end{aligned} \quad (\text{B-23})$$

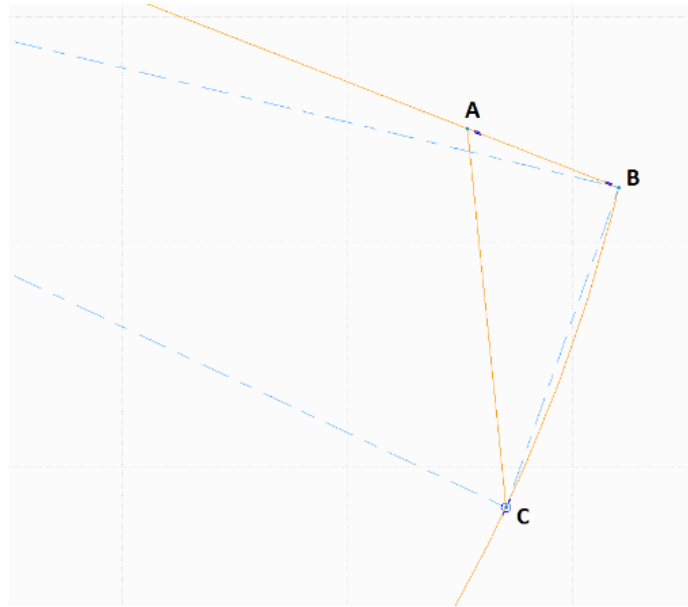


Figure B-9: XZ plane for flame between primary and secondary plane

Flame has passed secondary plane

By using a similar reasoning, we get the enclosed volume by the flame, when it passes the secondary plane (Figure B-10).

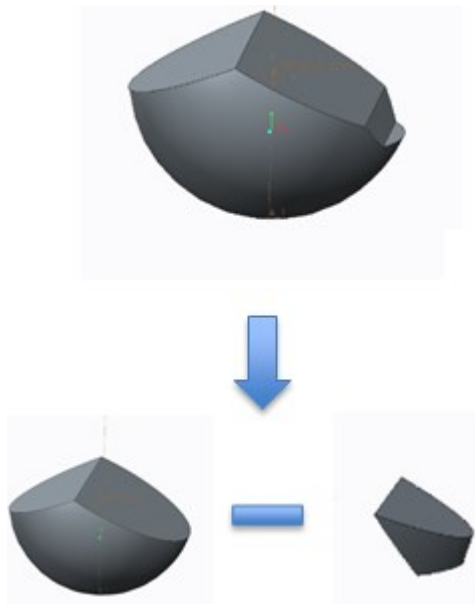


Figure B-10: Equivalence of volume when flame is between has passed secondary plane

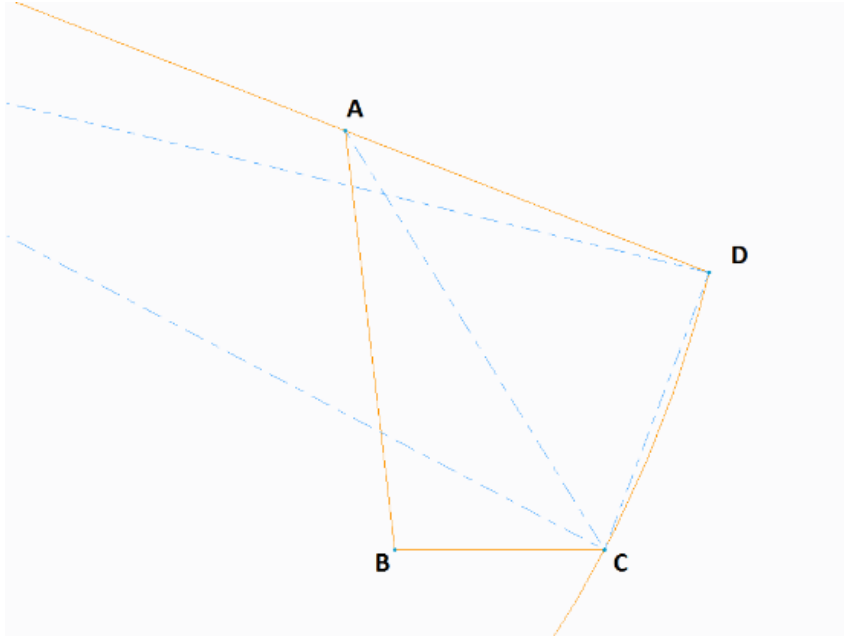


Figure B-11: XZ plane for flame between primary and secondary plane

We define the coordinates of points A, B and C as

$$A(b_{t,in}, H_b - H_t), B(b_{ts,in}, H_b - H_{ts}), C(x_i, H_b - H_{ts}), D(x_{12}, z_{12})$$

The following vectors are defined:

$$\vec{AB} = (b_{ts,in} - b_{t,in}, H_t - H_{ts}) \quad (B-24)$$

$$\vec{AC} = (x_i - b_{t,in}, H_t - H_{ts}) \quad (B-25)$$

$$\vec{AD} = (x_{12} - b_{t,in}, H_t - H_b) \quad (B-26)$$

The surface of the triangles ABC and ACD are calculated.

$$F_{ABC} = 0.5 \vec{AB} \times \vec{AC} \quad (B-27)$$

$$F_{ACD} = 0.5 \vec{AC} \times \vec{AD} \quad (B-28)$$

We also have to calculate the small spherical cap, defined by the angle $\angle COD$

$$\angle COD = \cos^{-1} \left(\frac{\vec{OC} \cdot \vec{OD}}{|\vec{OC}| \cdot |\vec{OD}|} \right) \quad (B-29)$$

$$F_{cap} = 0.5 \angle COD \cdot r^2 - 0.5(x_i \cdot z_{12} - (H_b - H_{ts}) \cdot x_{12}) \quad (B-30)$$

Finally, we calculate the volume ($F = F_{ABC} + F_{cap}$):

$$V_{e3} = 2 \left(\int_0^{y_1} F' dy + \int_{y_1}^{y_2} F dy \right) \quad (B-31)$$

$$y_1 = \sqrt{R_f^2 - b_{t,in}^2 - (H_b - H_t)^2}$$

$$y_2 = \sqrt{R_f^2 - b_{ts,in}^2 - (H_b - H_{ts})^2}$$

Flame has already intersected with the cylinder walls

There exist two cases to be analyzed (Figure B-12 and Figure B-13):

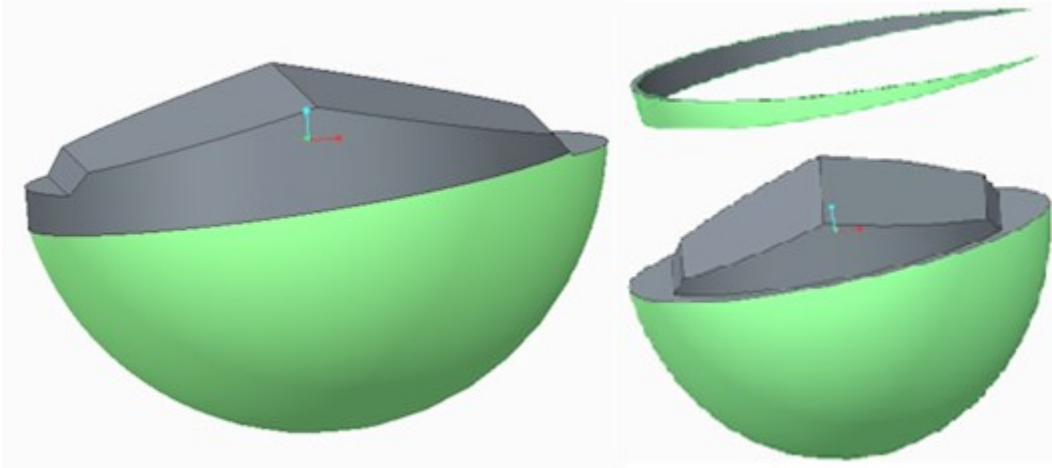


Figure B-12: First case of flame touching the walls ($x \leq 0.5B - O_b$)

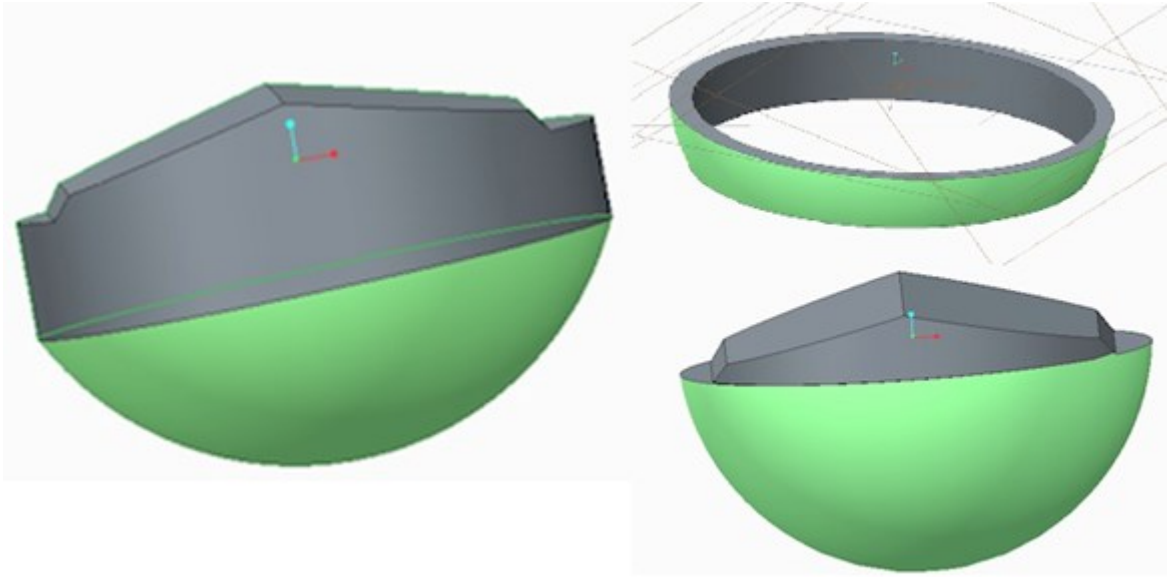


Figure B-13: Second case of flame touching the walls ($x > 0.5B - O_b$)

For the first case, the computation of this volume is easy if we know the volume of the cylinder head and the extra volume. The cylinder head volume will be calculated in a following section. The extra volume can be calculated as in the previous sections. We have to find the surface which must be integrated (Figure B-14).

This orange surface is calculated with the following equation:

$$F' = \pi R^2 \frac{2\alpha}{2\pi} - \cos \alpha \sin \alpha R^2 \quad (\text{B-32})$$

The surface, that must subtracted, is:

$$F_{sub} = r^2(\alpha - \sin \alpha \cos \alpha) - 0.25B^2(\beta - \sin \beta \cos \beta) \quad (\text{B-33})$$

With B being the cylinder bore and $r = \sqrt{R_f^2 - z^2}$, $\cos \alpha = \frac{0.25B^2 + O_b^2 - r^2}{B \cdot O_b}$, $\cos \beta = \frac{(0.5B + O_b)^2 + r^2 - 0.5B^2(1 - \cos \alpha)}{2(0.5B + O_b) \cdot r}$

Then we will integrate the subtracted surface between:

$$z_{min} = -\sqrt{R_f^2 - (0.5B + O_b)^2} \quad (\text{B-34})$$

$$z_{max} = -(H_t - H_b) \tag{B-35}$$

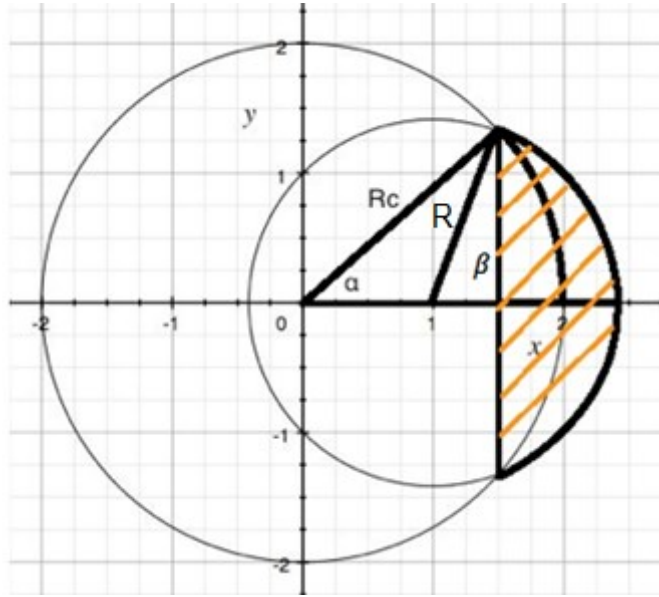


Figure B-14: XZ plane for flame between primary and secondary plane

We obtain:

$$V_{sub} = \int_{z_{min}}^{z_{max}} S_{sub} dz \tag{B-36}$$

The spherical part is calculated by the following equation:

$$V_{sphere} = \frac{2}{3}\pi R_f^3 - \pi R_f^2(H_t - H_b) + \frac{1}{3}\pi(H_t - H_b)^3 \tag{B-37}$$

For the second case, we will calculate the subtracted volume in two parts as shown in the equation hereafter ($z_0 = -\sqrt{R_f^2 - (0.5B + O_b)^2}$):

$$V_{sub} = \int_{z_{min}}^{z_0} F_{sub} dz + \pi \int_{z_0}^{z_{max}} (R_f^2 - z^2 - 0.25B^2) dz \tag{B-38}$$

Volume covered by the cylinder head

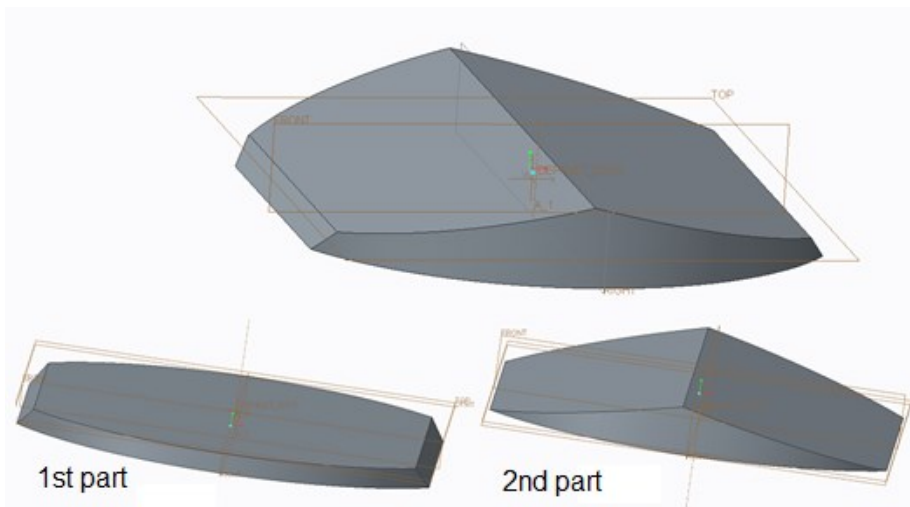


Figure B-15: Volume of the cylinder head

We must divide this volume in two parts as shown in Figure B-15. For the 1st part we have:

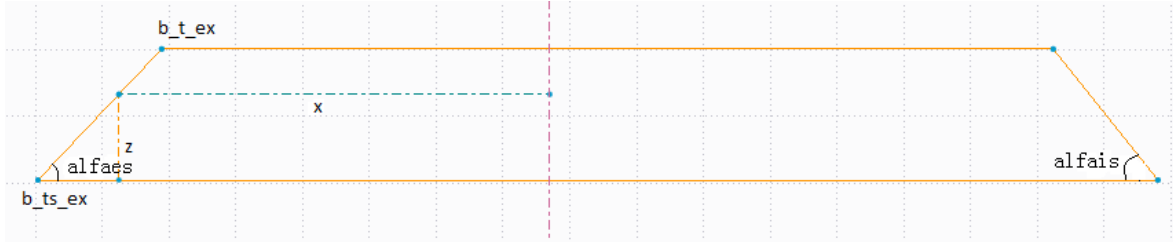


Figure B-16: 1st part of cylinder head volume (XZ plane)

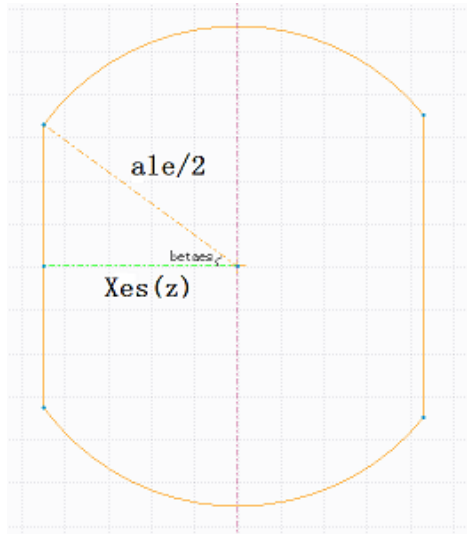


Figure B-17: 1st part of cylinder head volume (XY plane)

With the aid of Figure B-16 and Figure B-17, we obtain (intake and exhaust sides):

$$\beta_{es} = \cos^{-1} \frac{x_{es}}{0.5B} \quad (\text{B-39})$$

$$F_{es} = \beta_{es} \left(\frac{B}{2}\right)^2 - \sin \beta_{es} x_{es} \frac{B}{2} \quad (\text{B-40})$$

$$\beta_{is} = \cos^{-1} \frac{x_{is}}{0.5B} \quad (\text{B-41})$$

$$F_{is} = \beta_{is} \left(\frac{B}{2}\right)^2 - \sin \beta_{is} x_{is} \frac{B}{2} \quad (\text{B-42})$$

The surface of the section becomes:

$$F_1 = \pi \left(\frac{B}{2}\right)^2 - F_{is} - F_{es} \quad (\text{B-43})$$

The volume of the first part becomes:

$$V_1 = \int_0^{H_{ts}-H_t} F_1 dz \quad (\text{B-44})$$

For the 2nd part, we have:

$$\beta_e = \cos^{-1} \frac{b_{tex} + O_b + \frac{zC_e}{A_e}}{0.5B} \quad (\text{B-45})$$

$$\beta_i = \cos^{-1} \frac{b_{tin} - O_b + \frac{zC_i}{A_i}}{0.5B} \quad (\text{B-46})$$

$$F_{ex} = \beta_e \left(\frac{B}{2}\right)^2 - \sin \beta_e \left(b_{tex} + O_b + \frac{zC_{ex}}{A_{ex}}\right) \frac{B}{2} \quad (\text{B-47})$$

$$F_{in} = \beta_i \left(\frac{B}{2}\right)^2 - \sin \beta_i \left(b_{tin} - O_b + \frac{zC_{in}}{A_{in}}\right) \frac{B}{2} \quad (\text{B-48})$$

The volume is written as:

$$V_2 = \int_0^{H_t} \pi \left(\frac{B}{2}\right)^2 - F_{in} - F_{ex} dz \quad (\text{B-49})$$

And the total cylinder head volume is:

$$V_{head} = V_1 + V_2 \quad (\text{B-50})$$

B.2 Mean flame surface calculation in function of the distance from the wall

The general idea for the calculation of flame surface and distance distribution is to mesh the spherical surface and calculate the individual surface and distance from the wall of each mesh. In order to achieve this goal, we need to express all the points in spherical coordinates. For a sphere, the equivalence between the spherical coordinates and the Cartesian coordinates (Figure B-18) is:

$$\begin{aligned} x &= R_f \sin \theta \cos \varphi \\ y &= R_f \sin \theta \sin \varphi \\ z &= R_f \cos \theta \end{aligned} \quad (\text{B-51})$$

$$0 \leq \theta \leq \pi, 0 \leq \varphi \leq 2\pi$$

Similar equations can be extracted for the cylinder head, the piston and the cylinder:

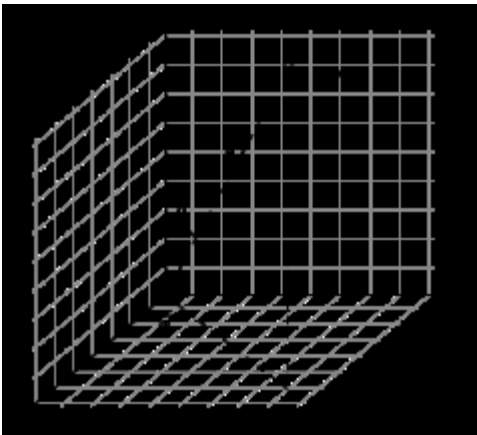


Figure B-18: Spherical coordinates

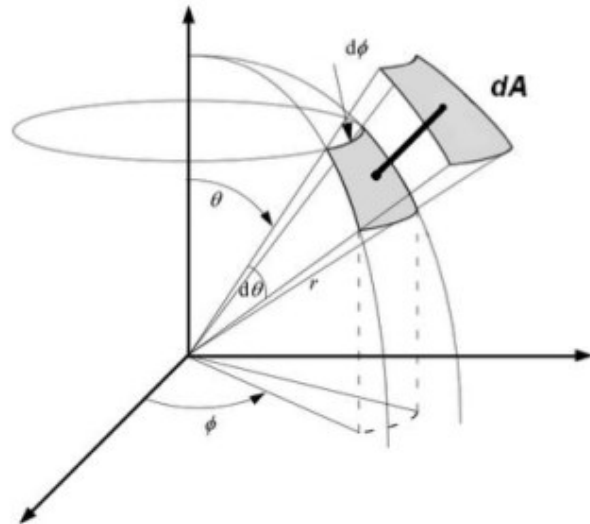


Figure B-19: Elementary surface of sphere

With those transformations of coordinates, we may calculate the distance between two points in space. We separate the sphere in grids with dimensions $[d\theta, d\varphi]$ (Figure B-19) and

we calculate the surface of this grid along with its distance from the nearest wall (Figure B-20). For the calculation of the surface we have the following double integral.

A loop is performed for the calculation of every grid and all the small surfaces are added in order to calculate the total surface of the flame. Finally, we create the distribution of the surface in function of the distance from the wall.

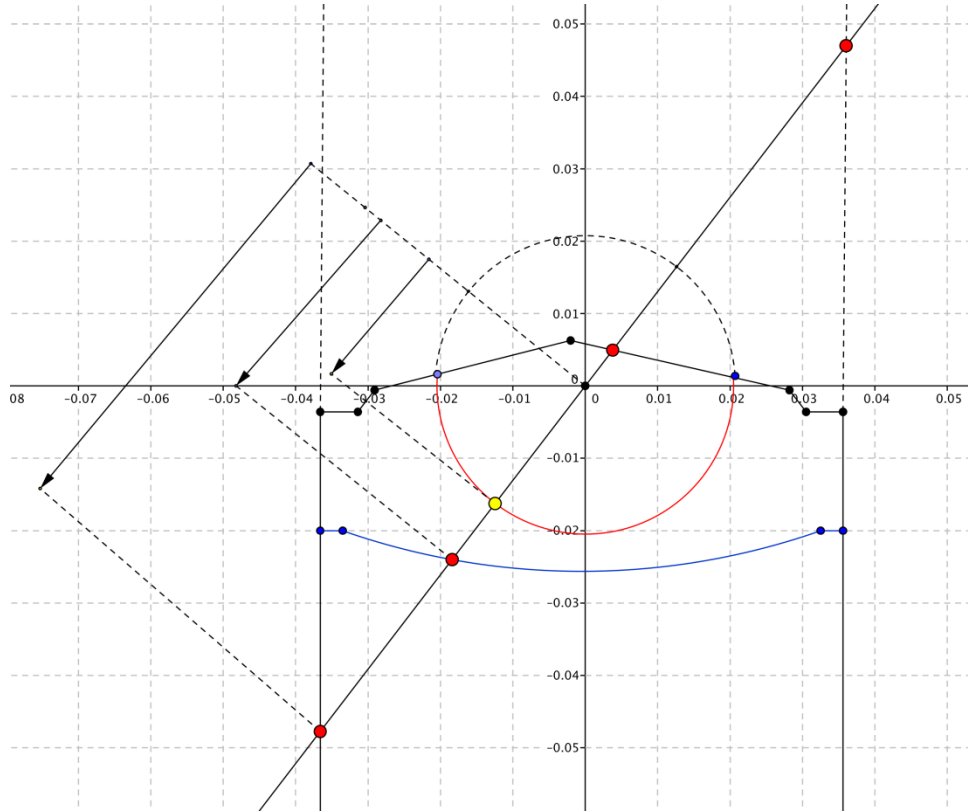


Figure B-20: Representation of all possible distances of a mesh. Yellow point is on the spherical surface and red points are the intersection in the normal direction on the mesh

Appendix C Flame Surface density equation

The objective of this appendix is to present in details the phenomenological derivation of the FSD wrinkling factor equation without entering in the details of LES terminology and equations. The rigorous theoretical derivation of this equation can be found in [52].

The burnt mass for an infinitely thin flame front, which is wrinkled by the turbulent flow is:

$$\frac{dm_b}{dt} = \rho_u s_L A_T = \rho_u s_L A_L \bar{\varepsilon} \quad (\text{C-1})$$

A general form of the burnt mass evolution is:

$$\frac{dm_b}{dt} = \frac{d\rho_b V_b}{dt} = V_b \frac{d\rho_b}{dt} + \rho_b \frac{dV_b}{dt} \quad (\text{C-2})$$

The wrinkling factor is defined as the ratio A_T between the wrinkled surface A_T and the mean surface A_L .

$$\bar{\varepsilon} = \frac{A_T}{A_L} \quad (\text{C-3})$$

The temporal derivative of the wrinkling factor can be computed in function of both surfaces:

$$\frac{d\bar{\varepsilon}}{dt} = \frac{A_L \frac{dA_T}{dt} - A_T \frac{dA_L}{dt}}{A_L^2} = \frac{1}{A_L} \left(\frac{dA_T}{dt} - \bar{\varepsilon} \frac{dA_L}{dt} \right) \quad (\text{C-4})$$

A new arrangement of equation C-4 can be:

$$\frac{1}{\bar{\varepsilon}} \frac{d\bar{\varepsilon}}{dt} = \frac{1}{A_T} \frac{dA_T}{dt} - \frac{1}{A_L} \frac{dA_L}{dt} \quad (\text{C-5})$$

The physical interpretation of the rearranged wrinkling equation explains the connection of flame wrinkling with the stretch rates $\left(\frac{1}{A} \frac{dA}{dt}\right)$ of the wrinkled flame and of the mean flame.

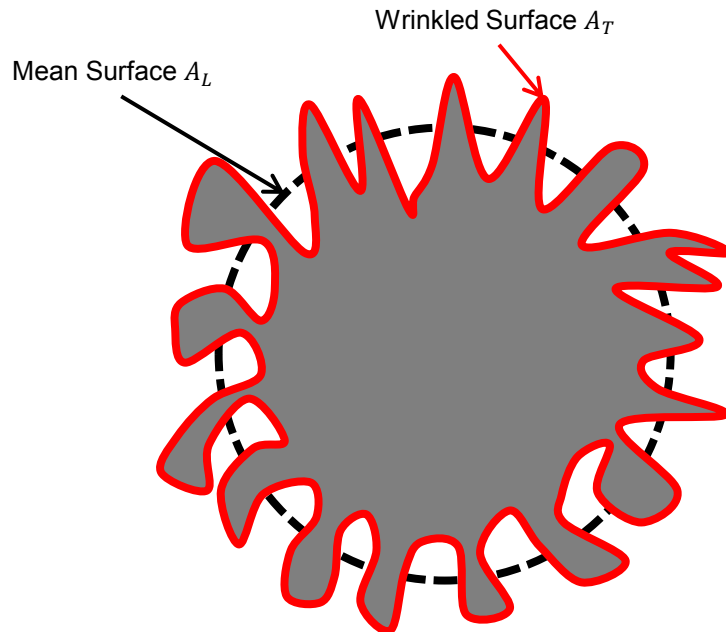


Figure C-1: Means and wrinkled flame surface

Considering a spark ignition engine configuration, as all the flame wrinkling is contained at the wrinkled flame surface A_T (Figure C-1), the mean flame front can be assumed spherical. A burned gas radius R_f can then be defined as $V_b = \frac{4}{3}\pi R_f^3$. Thus $A_L = 4\pi R_f^2$ and:

$$\frac{dA_L}{dt} = \frac{2}{R_f} \frac{dV_b}{dt} \quad (C-6)$$

Combining the all the above equations, we get:

$$\frac{1}{A_L} \frac{dA_L}{dt} = \frac{2}{R_f} \frac{\rho_u}{\rho_b} s_L \mathcal{E} - \frac{2}{3} \frac{1}{\rho_b} \frac{d\rho_b}{dt} \quad (C-7)$$

In equation (C-7) the total stretch consists of the curvature terms of spherical flames (first RHS term) and of the compressibility strain rate (second RHS term).

For a laminar flame ($\mathcal{E} = 1$), we get:

$$\frac{1}{A_{lam}} \frac{dA_{lam}}{dt} = \frac{2}{R_f} \frac{\rho_u}{\rho_b} s_L - \frac{2}{3} \frac{1}{\rho_b} \frac{d\rho_b}{dt} \quad (C-8)$$

The wrinkled flame surface evolution must take into account the presence of turbulence and its impact on the flame front. If the flow is laminar, the total flame stretch must be equal to the stretch of a laminar flame. Moreover, the turbulent strain (S_T) and curvature rate (C_T) must be modeled. These considerations are expressed in the following equations:

$$\begin{aligned} \frac{1}{A_T} \frac{dA_T}{dt} &= \frac{2}{R_f} \frac{\rho_u}{\rho_b} s_L - \frac{2}{3} \frac{1}{\rho_b} \frac{d\rho_b}{dt} + S_T + C_T \\ \lim_{\mathcal{E} \rightarrow 1} (S_T + C_T) &= 0 \end{aligned} \quad (C-9)$$

The total turbulent strain (assuming homogeneous and isotropic turbulence) can be expressed with the aid of the efficiency function (already presented in Chapter 2):

$$S_T = \Gamma \left(\frac{u'}{s_L}, \frac{L_T}{\delta_L} \right) \frac{u'}{L_T} \quad (C-10)$$

The introduction of an equilibrium wrinkling factor may offer a model for the curvature term. Curvature effects progressively balance the strain rate ones when flame wrinkling tends towards its equilibrium value. The latter can be supplied by a KPP (Kolmogorov Petrovskii Piskunov) analysis. In order to take into account the evolution of the curvature effect during the progression of the flame wrinkling towards its equilibrium value, the total turbulent stretch rate term is corrected as follows:

$$S_T + C_T = \Gamma \left(\frac{u'}{s_L}, \frac{L_T}{\delta_L} \right) \frac{u'}{L_T} \left(\frac{\mathcal{E}_{eq} - \mathcal{E}}{\mathcal{E}_{eq} - 1} \right) \quad (C-11)$$

The final form of the wrinkling factor equation is:

$$\frac{1}{A_T} \frac{dA_T}{dt} = \frac{2}{R_f} \frac{\rho_u}{\rho_b} s_L - \frac{2}{3} \frac{1}{\rho_b} \frac{d\rho_b}{dt} + \Gamma \left(\frac{u'}{s_L}, \frac{L_T}{\delta_L} \right) \frac{u'}{L_T} \left(\frac{\mathcal{E}_{eq} - \mathcal{E}}{\mathcal{E}_{eq} - 1} \right) \quad (C-12)$$

After combining equations (C-7) and (C-12), one gets the final FSD model equation:

$$\frac{1}{\mathcal{E}} \frac{d\mathcal{E}}{dt} = \Gamma \left(\frac{u'}{s_L}, \frac{L_T}{\delta_L} \right) \frac{u'}{L_T} \left(\frac{\mathcal{E}_{eq} - \mathcal{E}}{\mathcal{E}_{eq} - 1} \right) - \frac{2}{R_f} \frac{\rho_u}{\rho_b} (\mathcal{E} - 1) s_L \quad (C-13)$$

Appendix D Supplementary results of optimal advance configuration

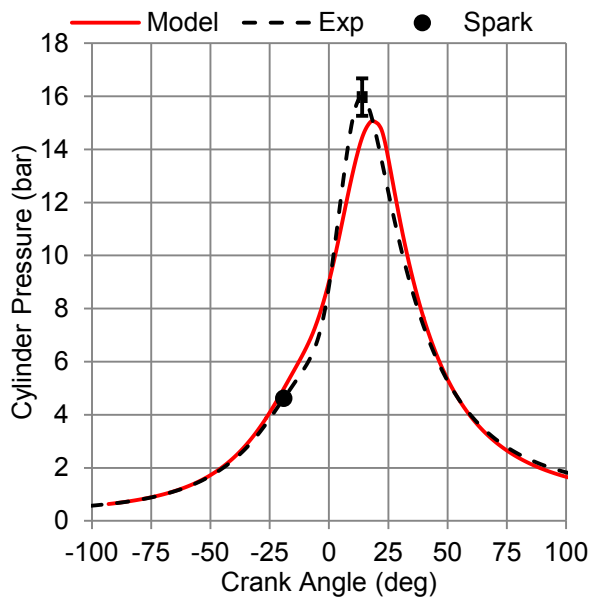


Figure D-1: Cylinder pressure for engine speed 1200 RPM and IMEP 2 bar

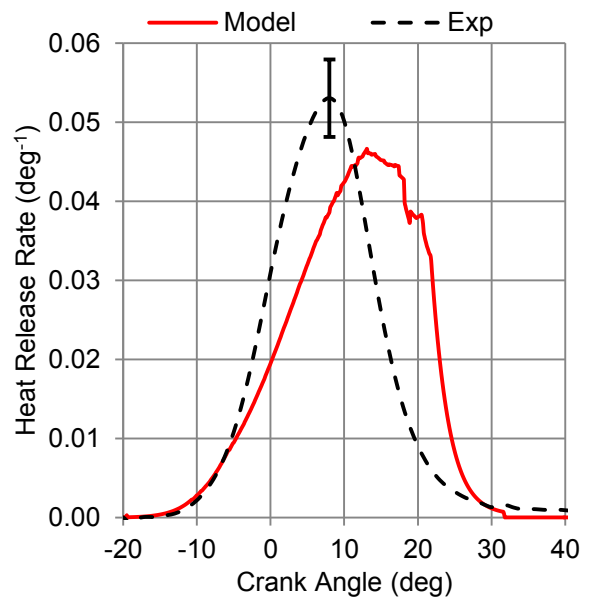


Figure D-2: Heat release rate for engine speed 1200 RPM and IMEP 2 bar

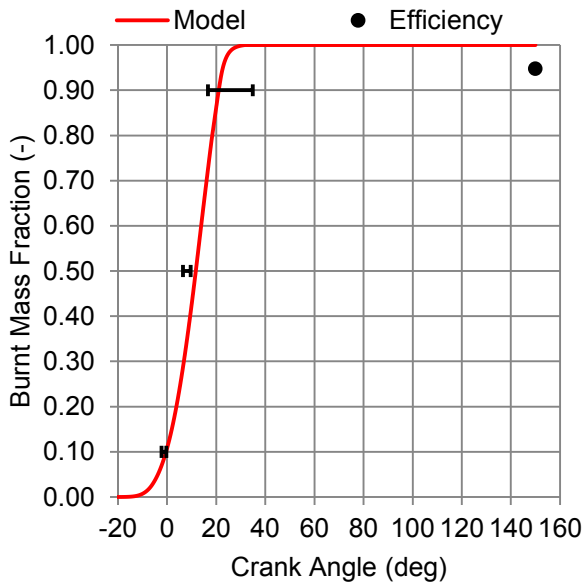


Figure D-3: Burnt mass fraction for engine speed 1200 RPM and IMEP 2 bar

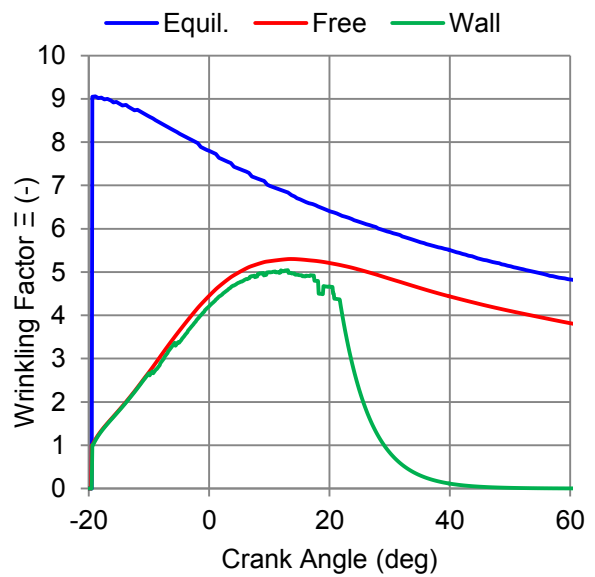


Figure D-4: Wrinkling Factor Ξ for engine speed 1200 RPM and IMEP 2 bar

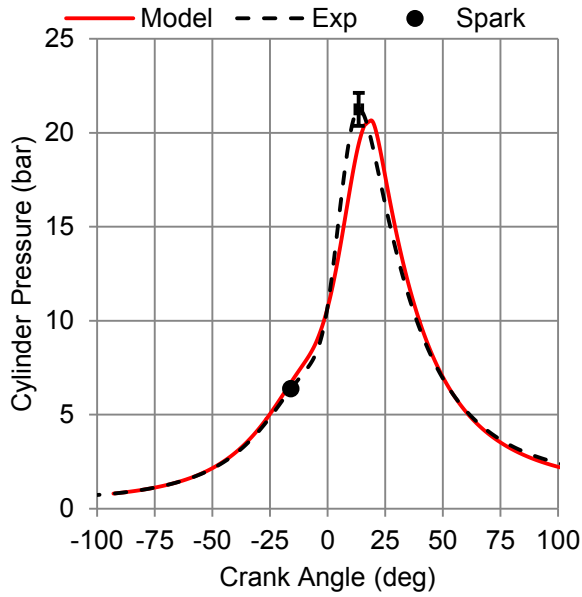


Figure D-5: Cylinder pressure for engine speed 1200 RPM and IMEP 4 bar

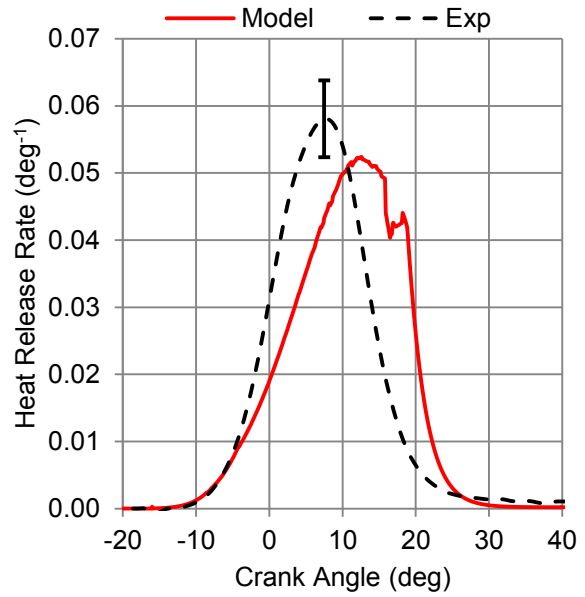


Figure D-6: Heat release rate for engine speed 1200 RPM and IMEP 4 bar

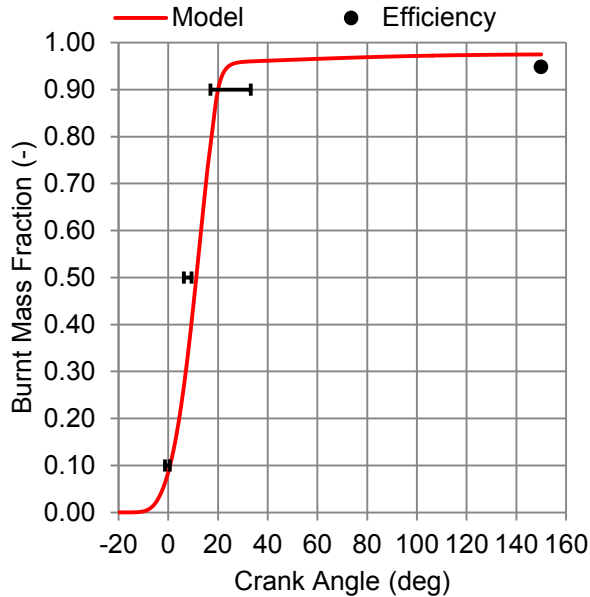


Figure D-7: Burnt mass fraction for engine speed 1200 RPM and IMEP 4 bar

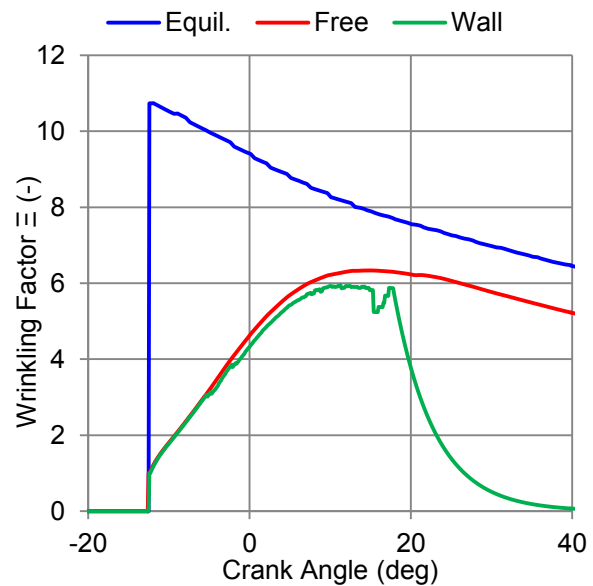


Figure D-8: Wrinkling Factor Ξ for engine speed 1200 RPM and IMEP 4 bar

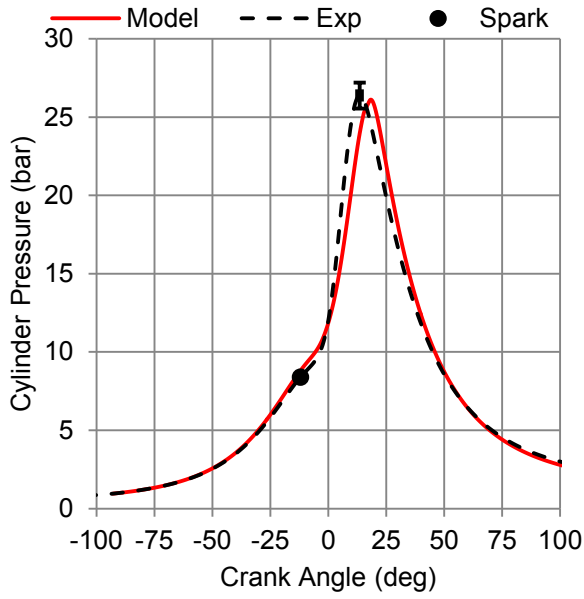


Figure D-9: Cylinder pressure for engine speed 1200 RPM and IMEP 5.5 bar

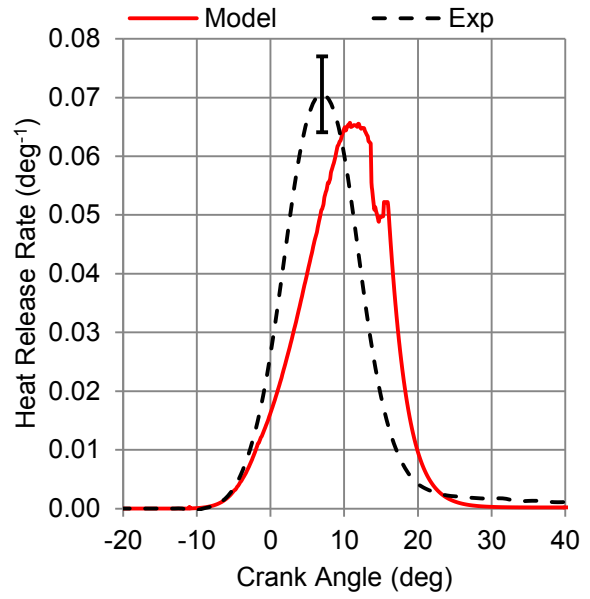


Figure D-10: Heat release rate for engine speed 1200 RPM and IMEP 5.5 bar

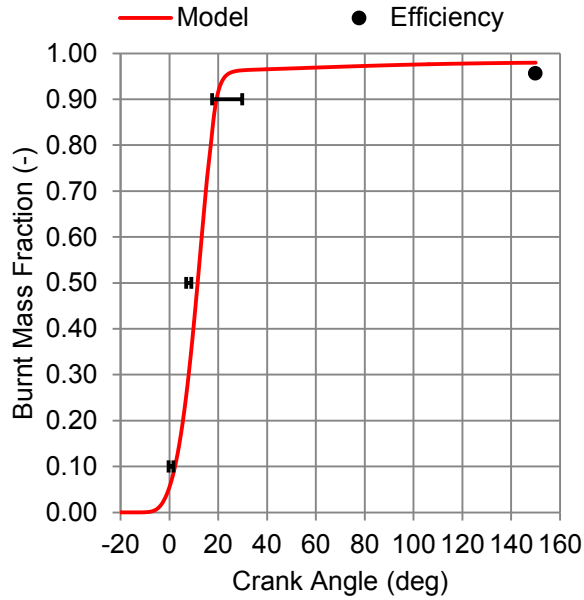


Figure D-11 : Burnt mass fraction for engine speed 1200 RPM and IMEP 5.5 bar

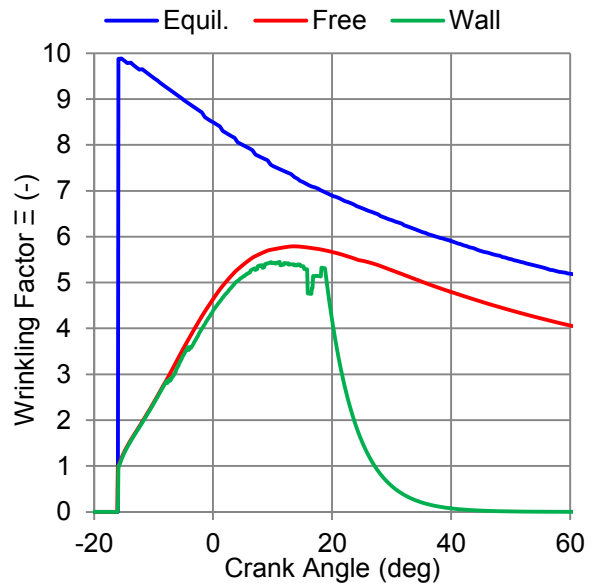


Figure D-12: Wrinkling Factor Ξ for engine speed 1200 RPM and IMEP 5.5 bar

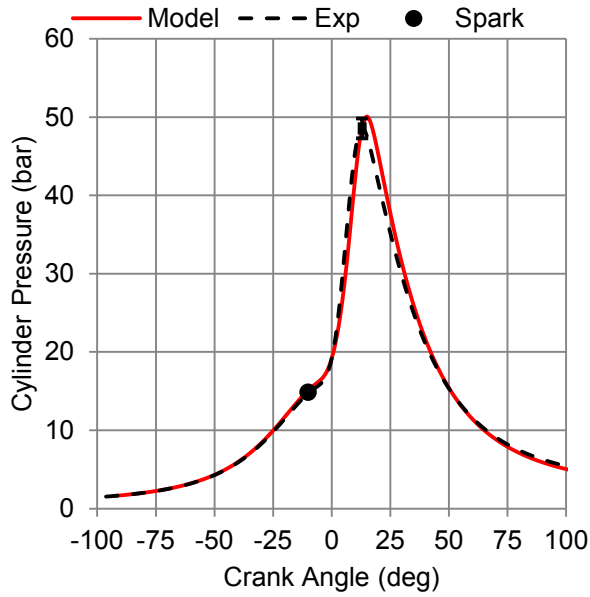


Figure D-13: Cylinder pressure for engine speed 1200 RPM and IMEP 8 bar

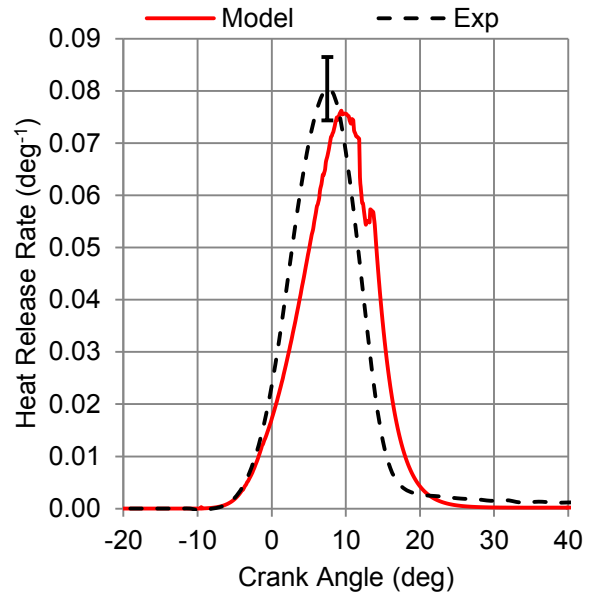


Figure D-14: Heat release rate for engine speed 1200 RPM and IMEP 8 bar

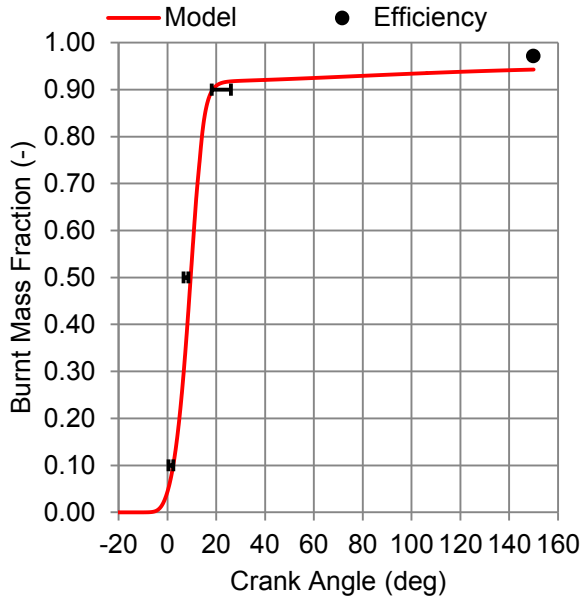


Figure D-15 : Burnt mass fraction for engine speed 1200 RPM and IMEP 8 bar

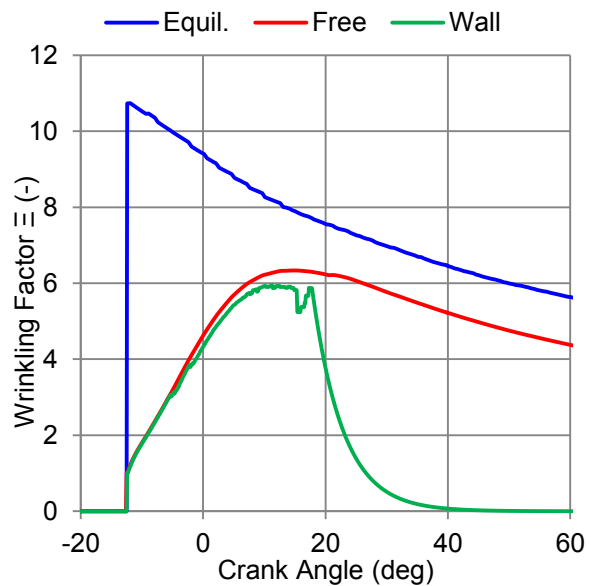


Figure D-16: Wrinkling Factor Ξ for engine speed 1200 RPM and IMEP 8 bar

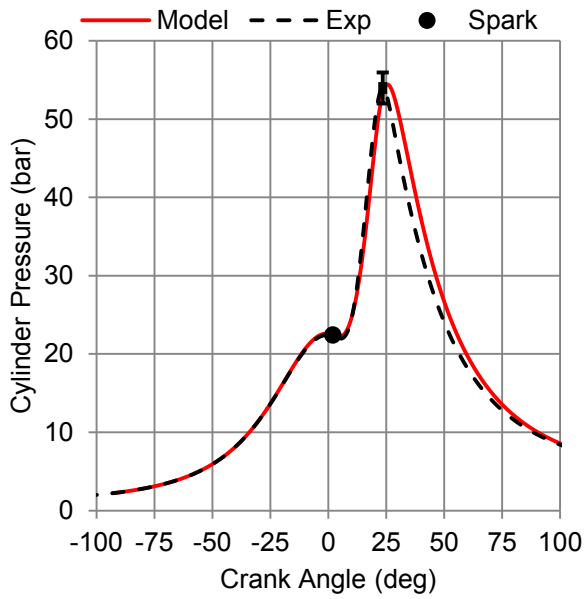


Figure D-17: Cylinder pressure for engine speed 1200 RPM and IMEP 12 bar

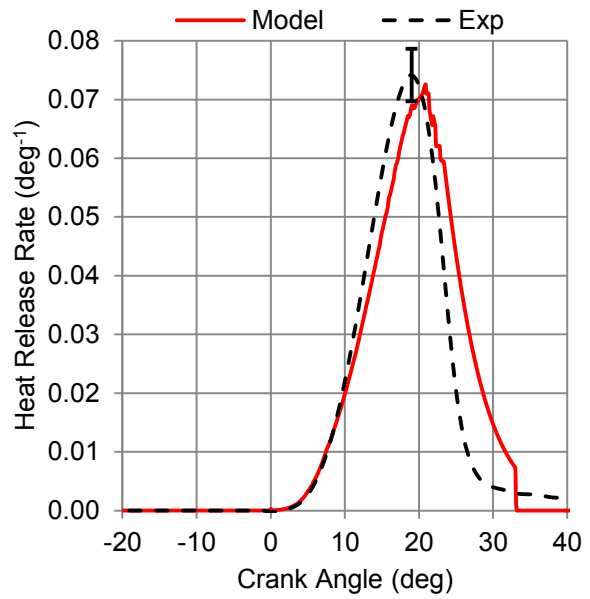


Figure D-18: Heat release rate for engine speed 1200 RPM and IMEP 12 bar

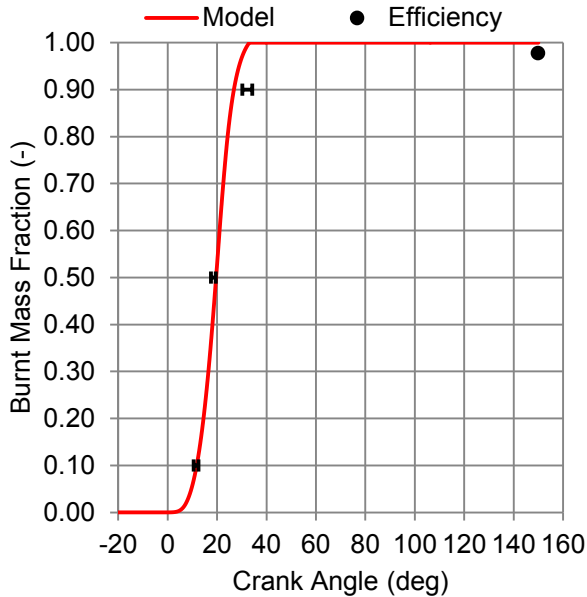


Figure D-19 : Burnt mass fraction for engine speed 1200 RPM and IMEP 12 bar

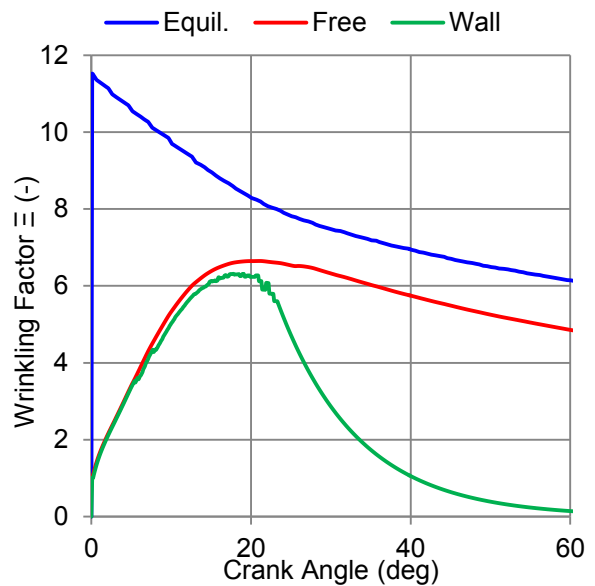


Figure D-20: Wrinkling Factor Ξ for engine speed 1200 RPM and IMEP 12 bar

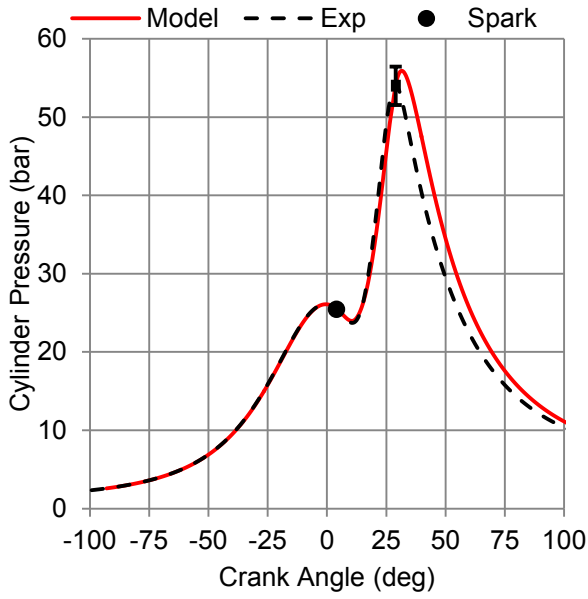


Figure D-21: Cylinder pressure for engine speed 1200 RPM and IMEP 14 bar

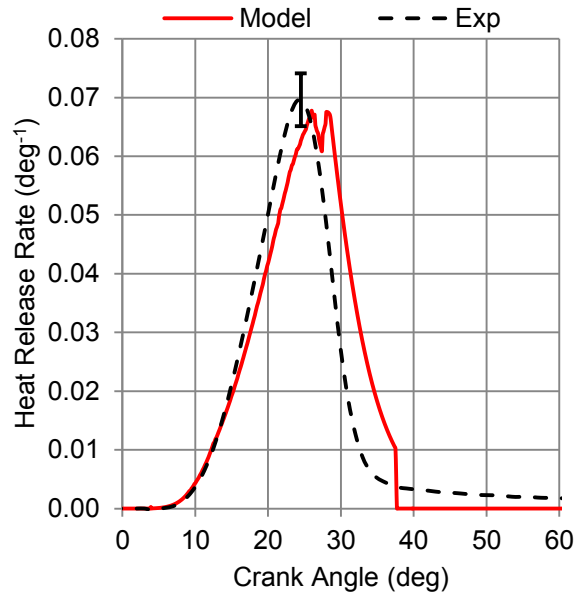


Figure D-22: Heat release rate for engine speed 1200 RPM and IMEP 14 bar

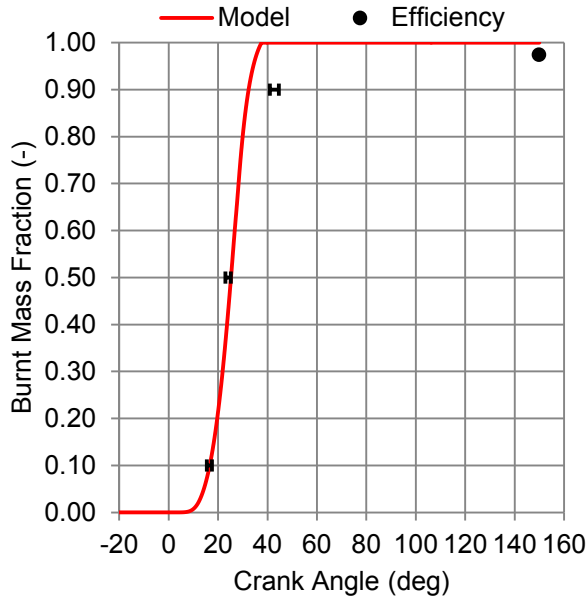


Figure D-23 : Burnt mass fraction for engine speed 1200 RPM and IMEP 14 bar

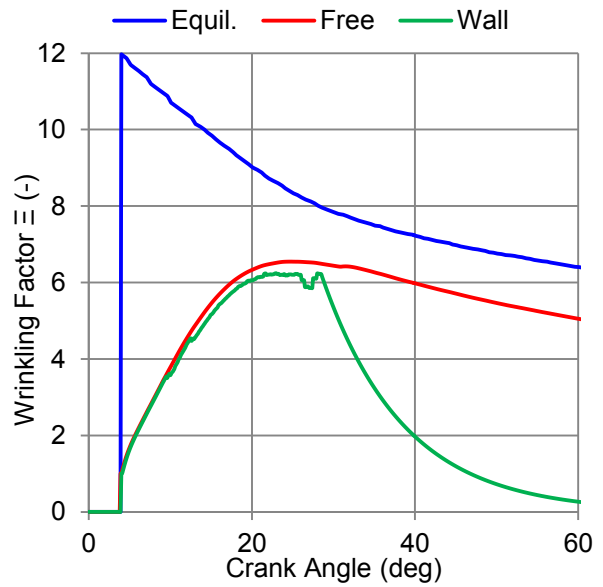


Figure D-24: Wrinkling Factor Ξ for engine speed 1200 RPM and IMEP 14 bar

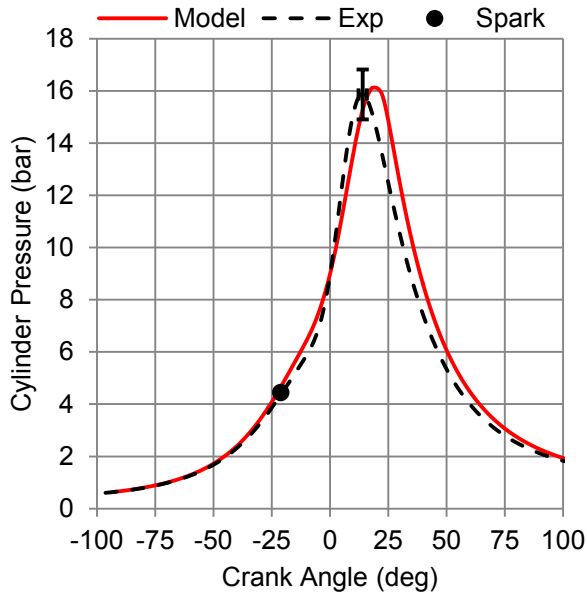


Figure D-25: Cylinder pressure for engine speed 2000 RPM and IMEP 2 bar

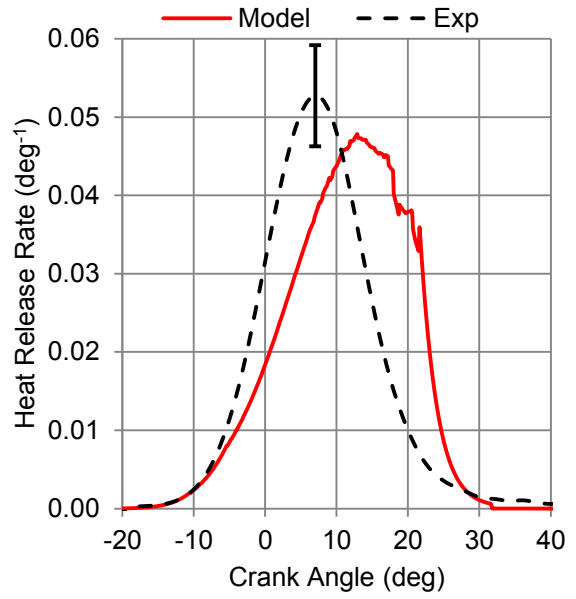


Figure D-26: Heat release rate for engine speed 2000 RPM and IMEP 2 bar

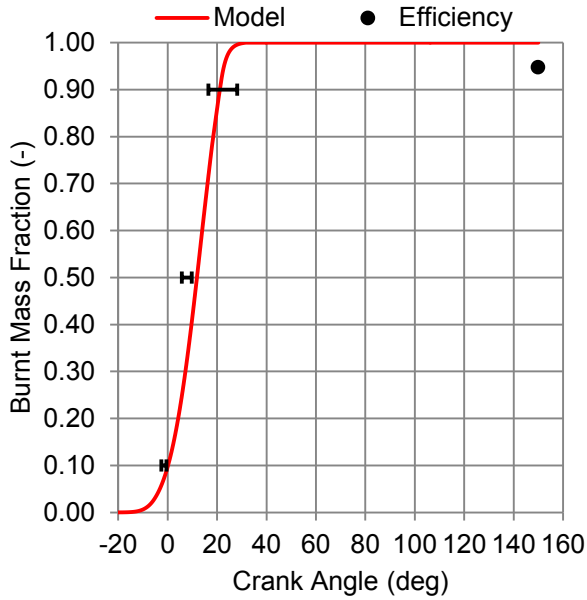


Figure D-27 : Burnt mass fraction for engine speed 2000 RPM and IMEP 2 bar

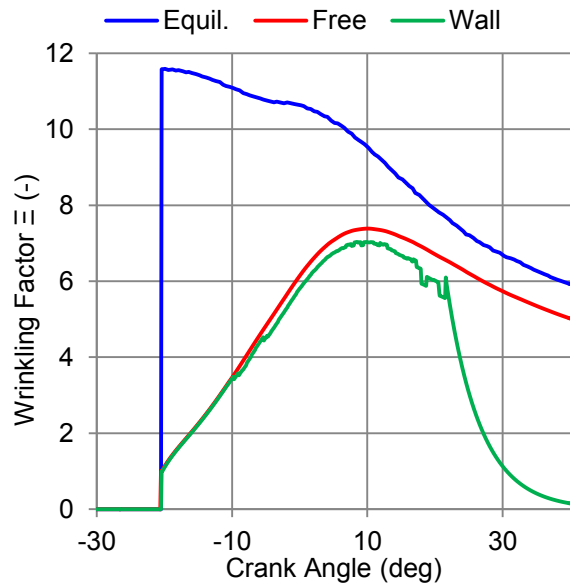


Figure D-28: Wrinkling Factor Ξ for engine speed 2000 RPM and IMEP 2 bar

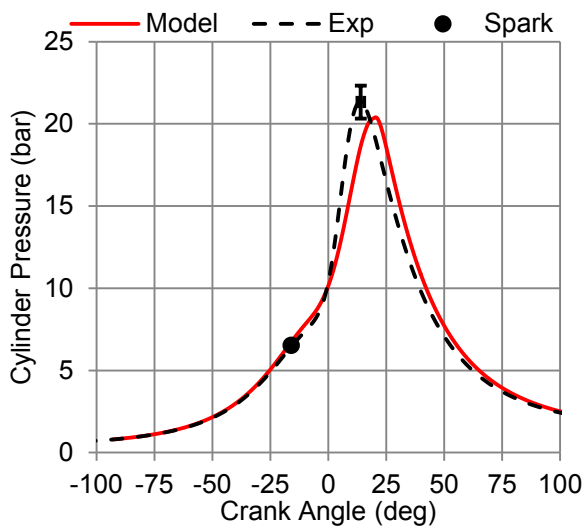


Figure D-29: Cylinder pressure for engine speed 2000 RPM and IMEP 3 bar

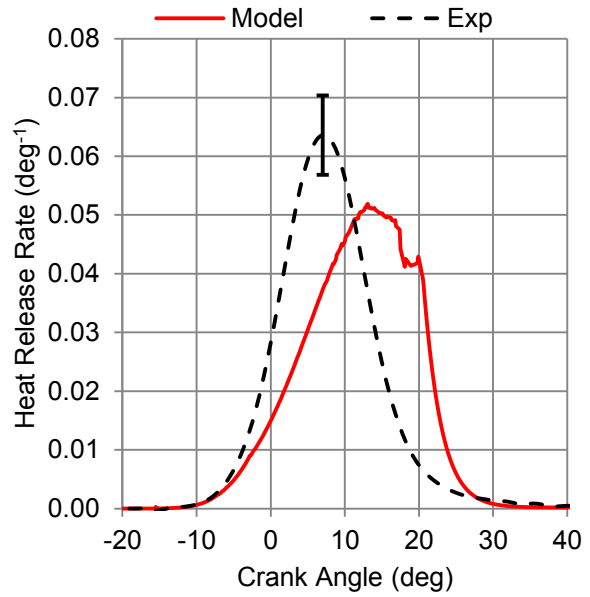


Figure D-30: Heat release rate for engine speed 2000 RPM and IMEP 2 bar

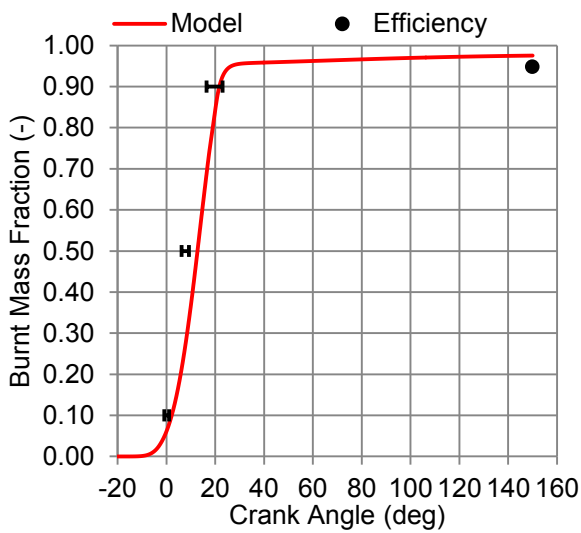


Figure D-31 : Burnt mass fraction for engine speed 2000 RPM and IMEP 3 bar

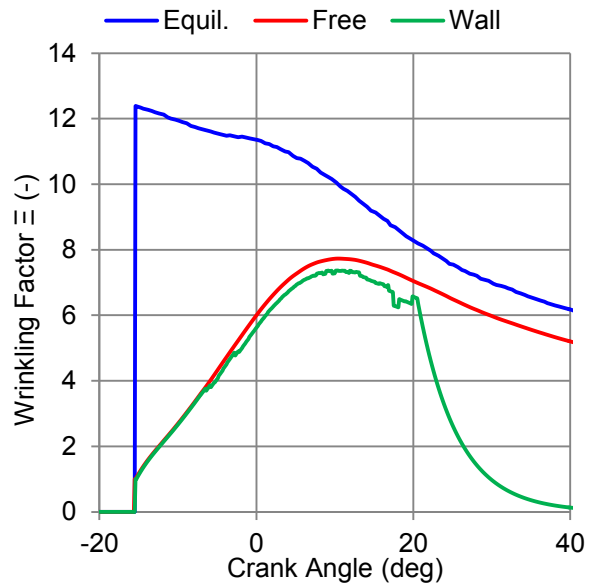


Figure D-32: Wrinkling Factor Ξ for engine speed 2000 RPM and IMEP 3 bar

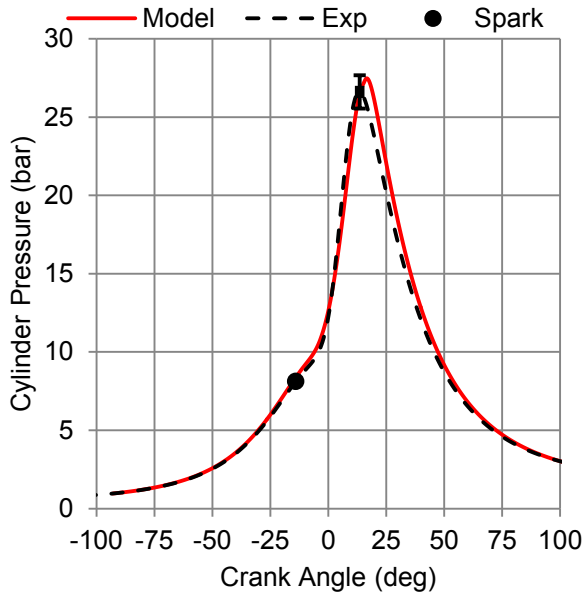


Figure D-33: Cylinder pressure for engine speed 2000 RPM and IMEP 4 bar

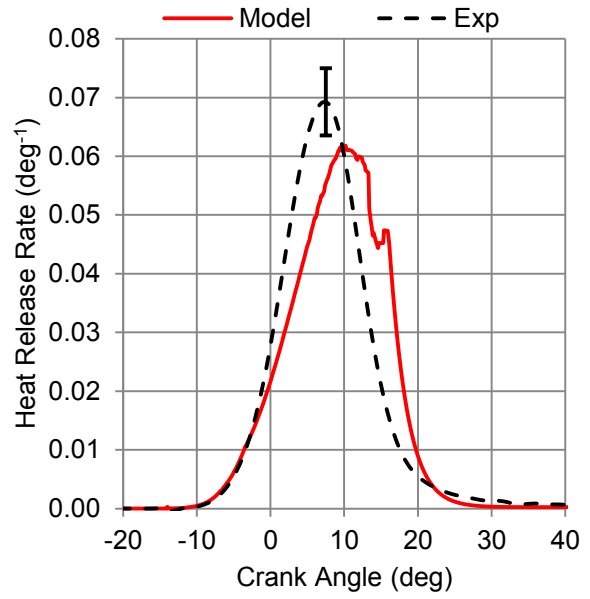


Figure D-34: Heat release rate for engine speed 2000 RPM and IMEP 4 bar

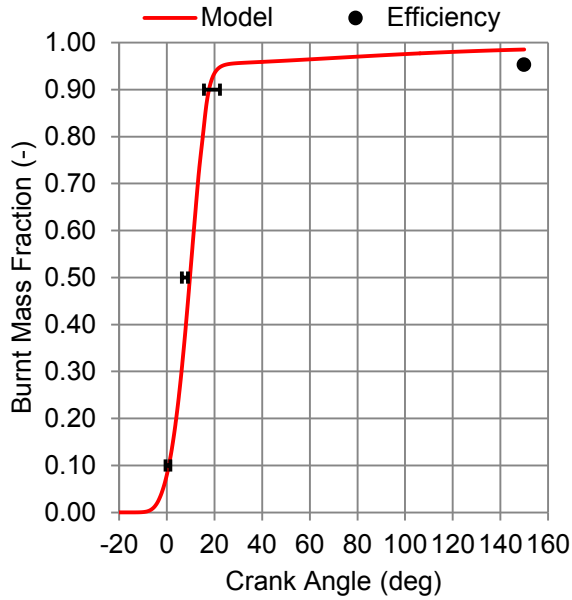


Figure D-35 : Burnt mass fraction for engine speed 2000 RPM and IMEP 4 bar

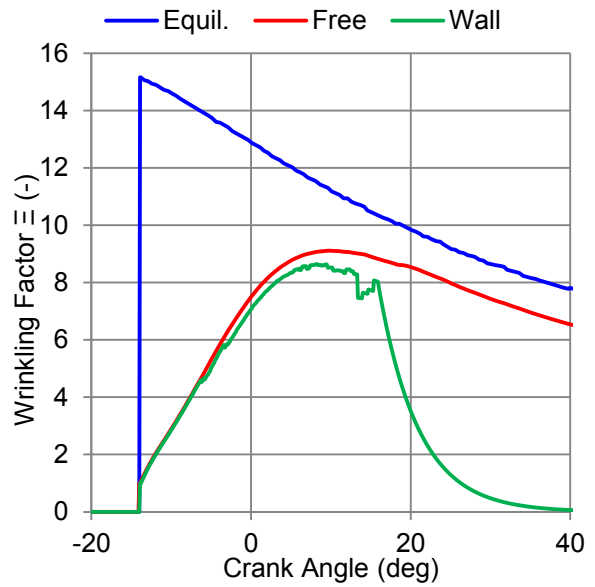


Figure D-36: Wrinkling Factor Ξ for engine speed 2000 RPM and IMEP 4 bar

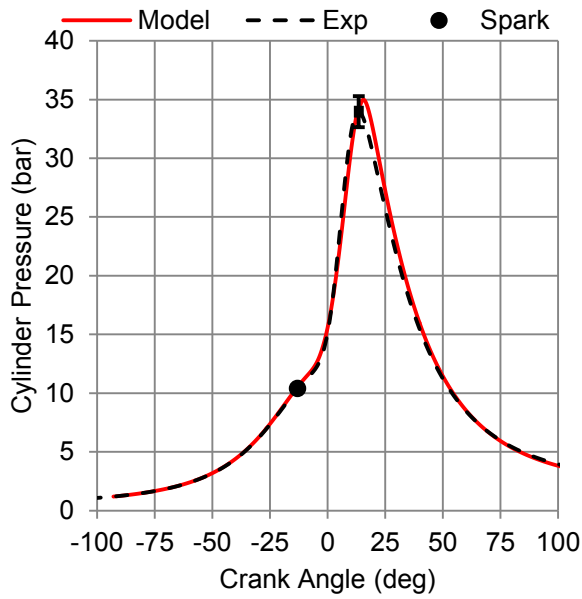


Figure D-37: Cylinder pressure for engine speed 2000 RPM and IMEP 5.5 bar

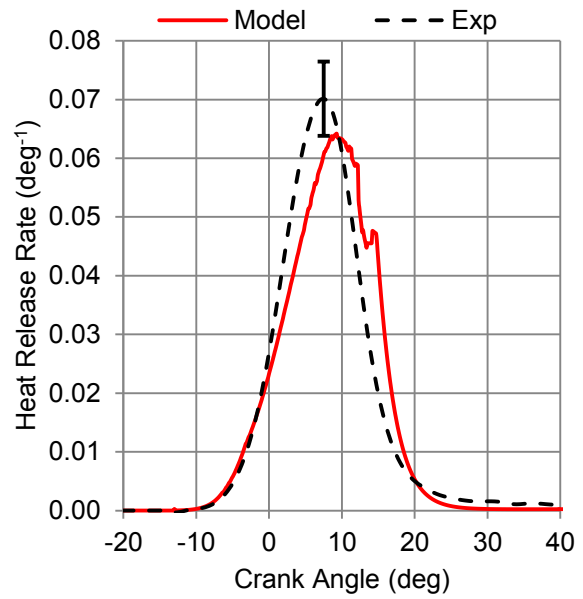


Figure D-38: Heat release rate for engine speed 2000 RPM and IMEP 5.5 bar

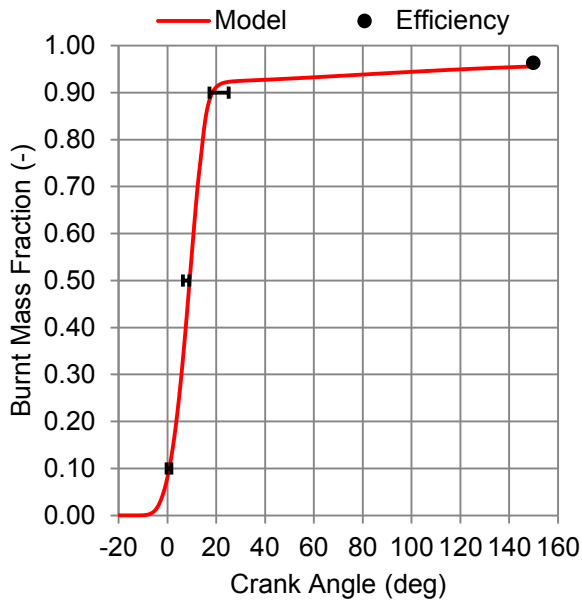


Figure D-39 : Burnt mass fraction for engine speed 2000 RPM and IMEP 5.5 bar

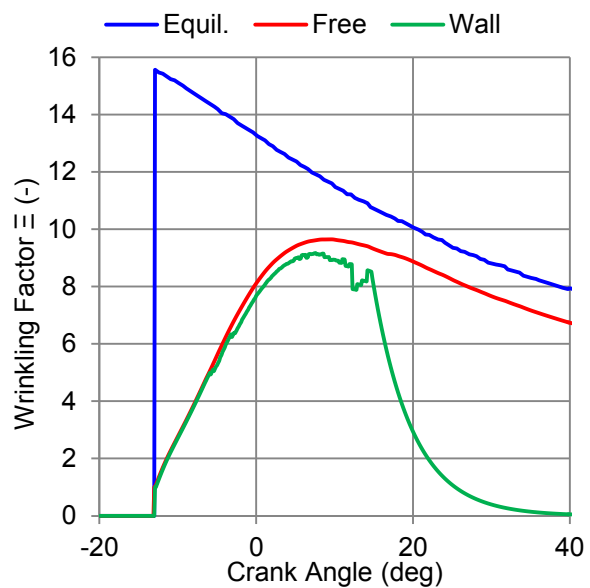


Figure D-40: Wrinkling Factor Ξ for engine speed 2000 RPM and IMEP 5.5 bar

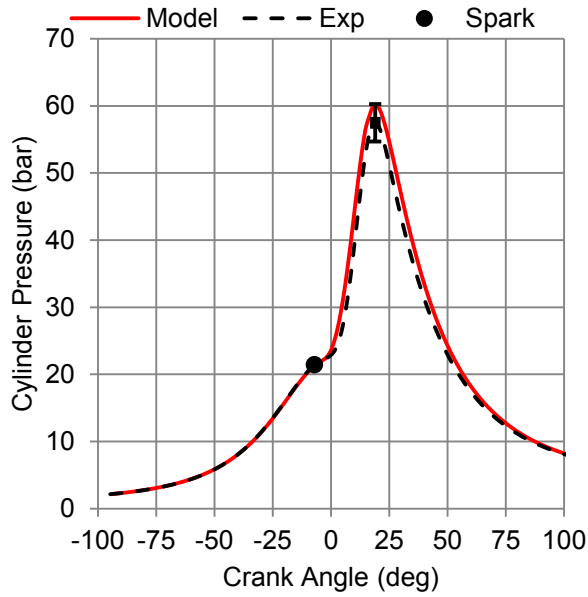


Figure D-41: Cylinder pressure for engine speed 2000 RPM and IMEP 12 bar

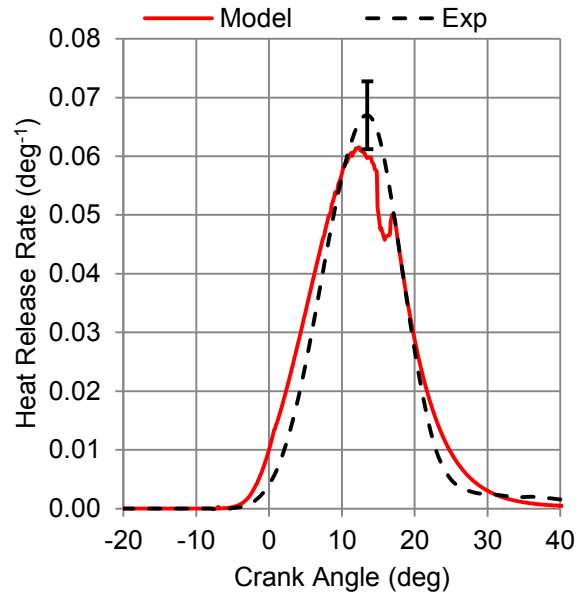


Figure D-42: Heat release rate for engine speed 2000 RPM and IMEP 12 bar

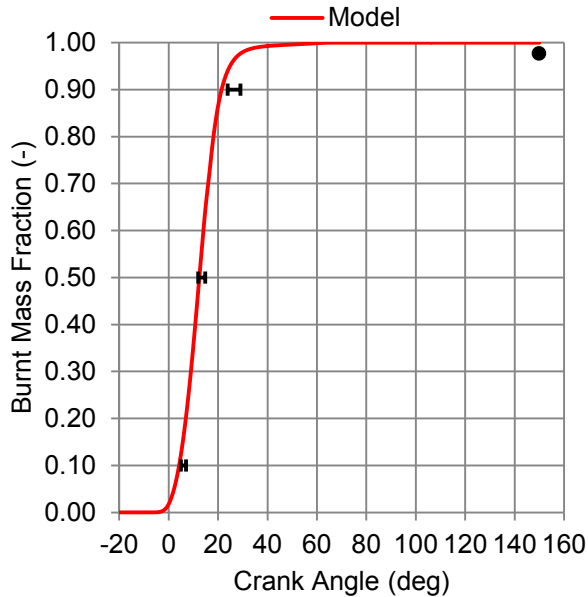


Figure D-43 : Burnt mass fraction for engine speed 2000 RPM and IMEP 12 bar

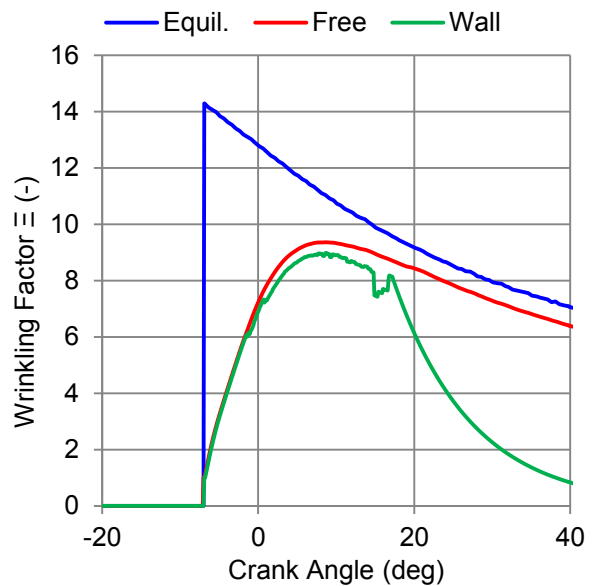


Figure D-44: Wrinkling Factor Ξ for engine speed 2000 RPM and IMEP 12 bar

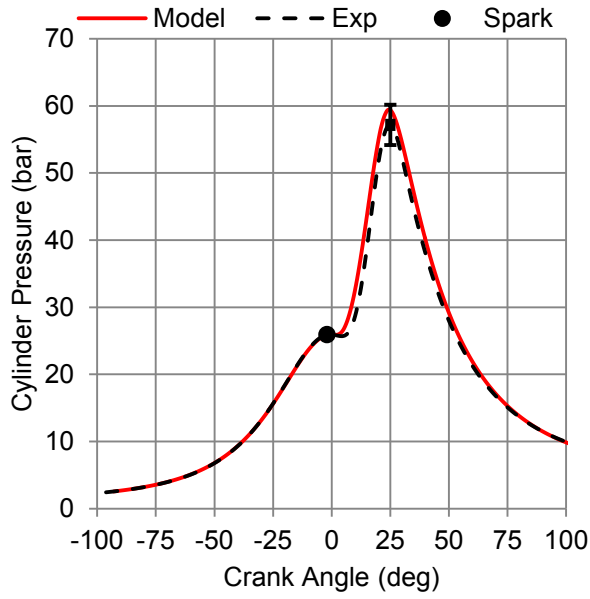


Figure D-45: Cylinder pressure for engine speed 2000 RPM and IMEP 14 bar

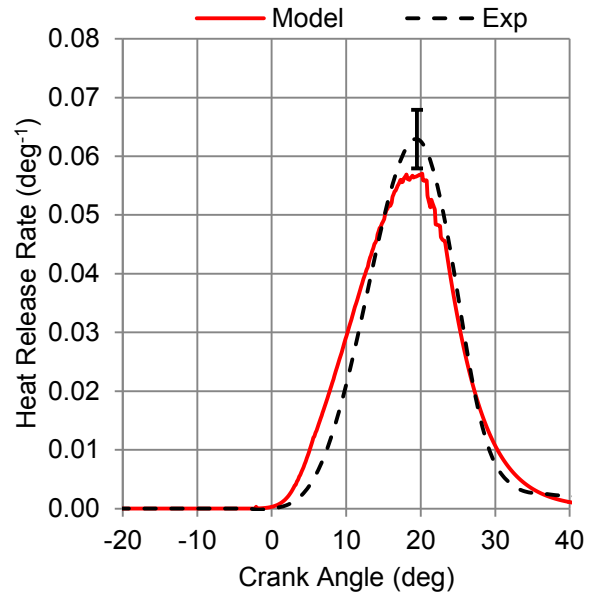


Figure D-46: Heat release rate for engine speed 2000 RPM and IMEP 14 bar

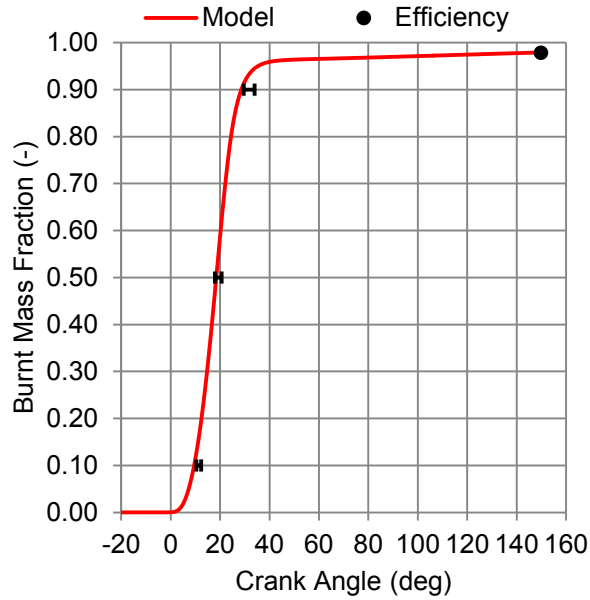


Figure D-47 : Burnt mass fraction for engine speed 2000 RPM and IMEP 14 bar

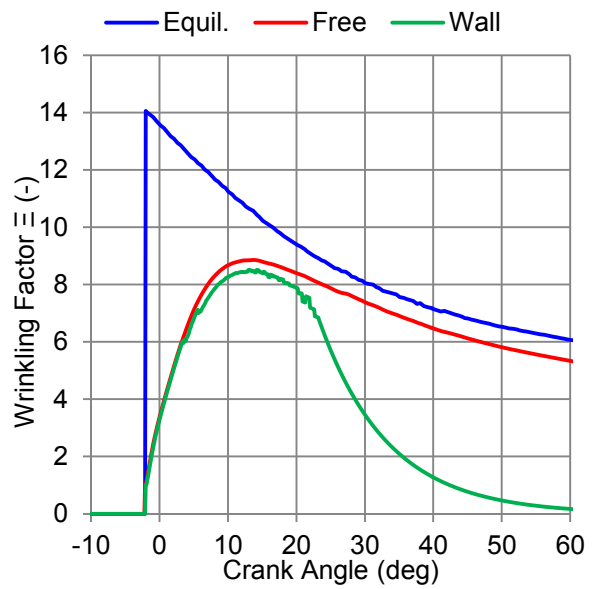


Figure D-48: Wrinkling Factor Ξ for engine speed 2000 RPM and IMEP 14 bar

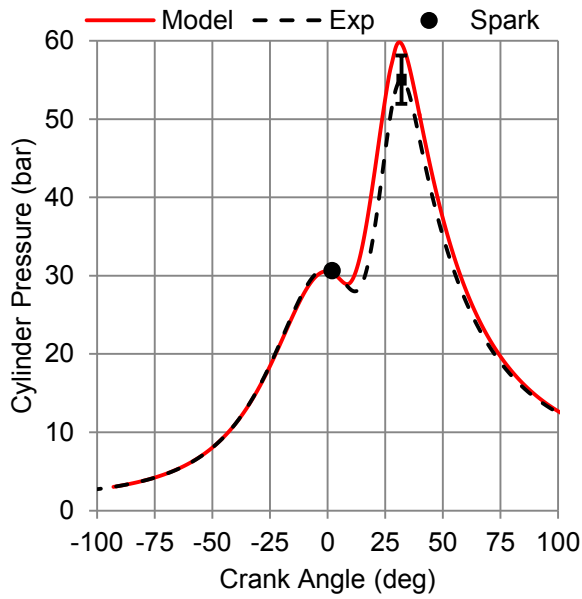


Figure D-49: Cylinder pressure for engine speed 2000 RPM and IMEP 16 bar

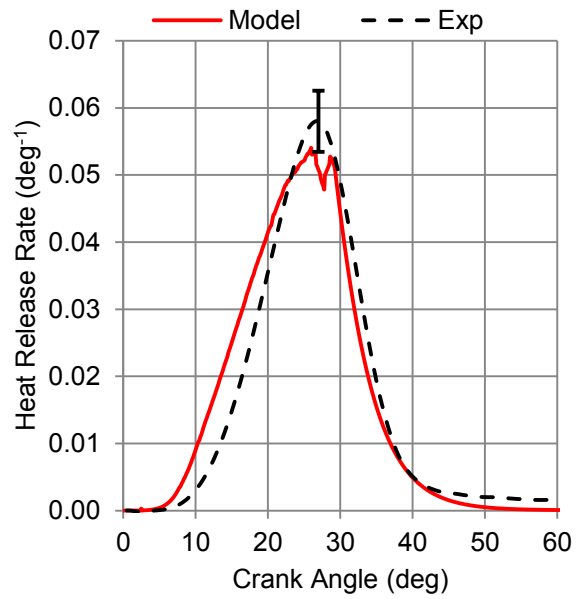


Figure D-50: Heat release rate for engine speed 2000 RPM and IMEP 16 bar

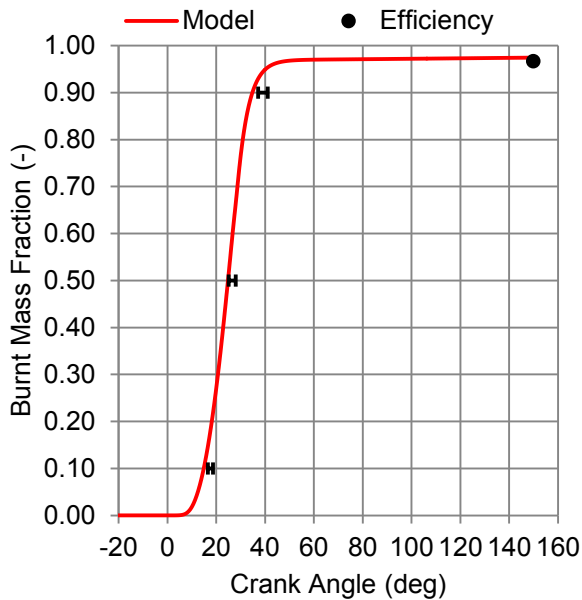


Figure D-51 : Burnt mass fraction for engine speed 2000 RPM and IMEP 16 bar

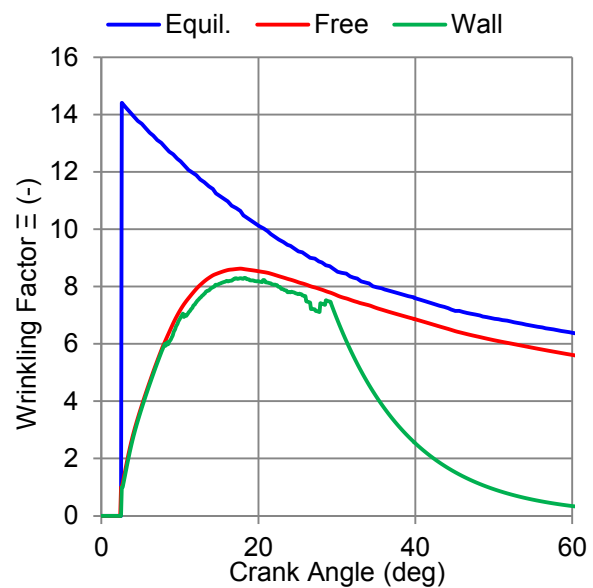


Figure D-52: Wrinkling Factor Ξ for engine speed 2000 RPM and IMEP 16 bar

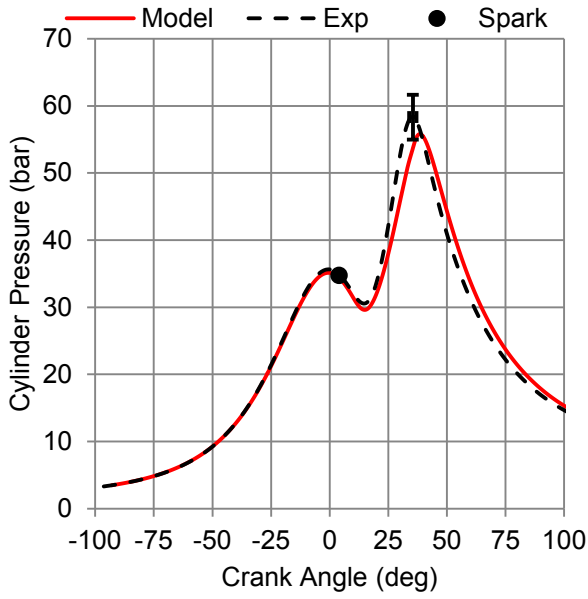


Figure D-53: Cylinder pressure for engine speed 2000 RPM and IMEP 18 bar

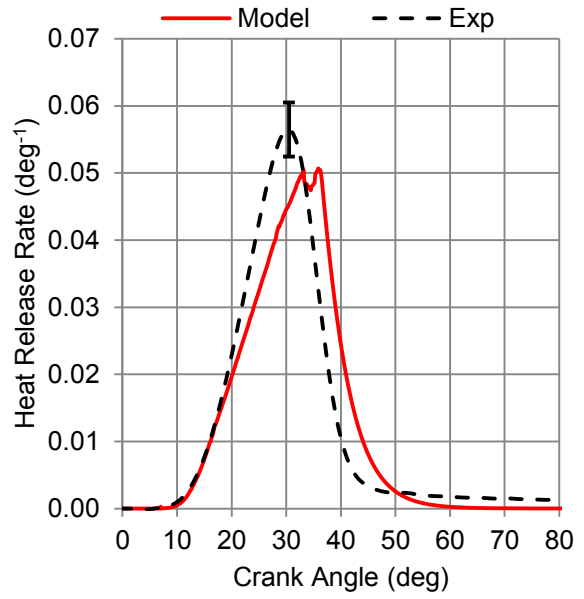


Figure D-54: Heat release rate for engine speed 2000 RPM and IMEP 18 bar

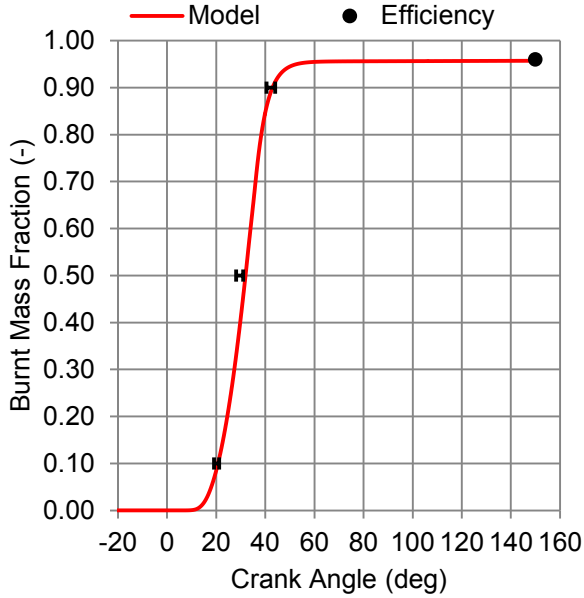


Figure D-55 : Burnt mass fraction for engine speed 2000 RPM and IMEP 18 bar

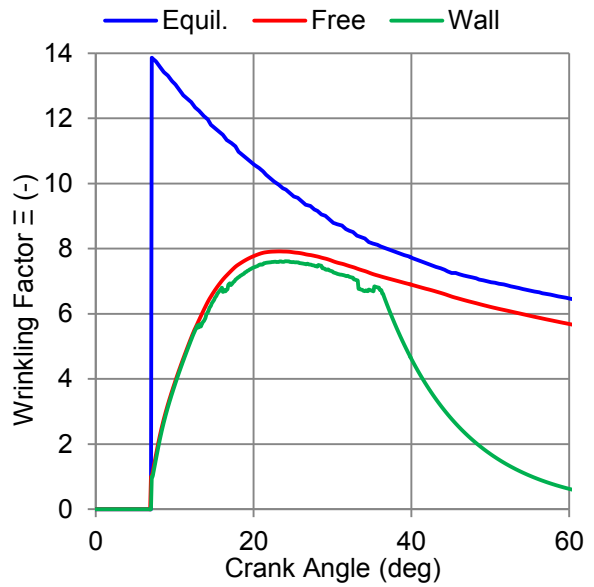


Figure D-56: Wrinkling Factor Ξ for engine speed 2000 RPM and IMEP 18 bar

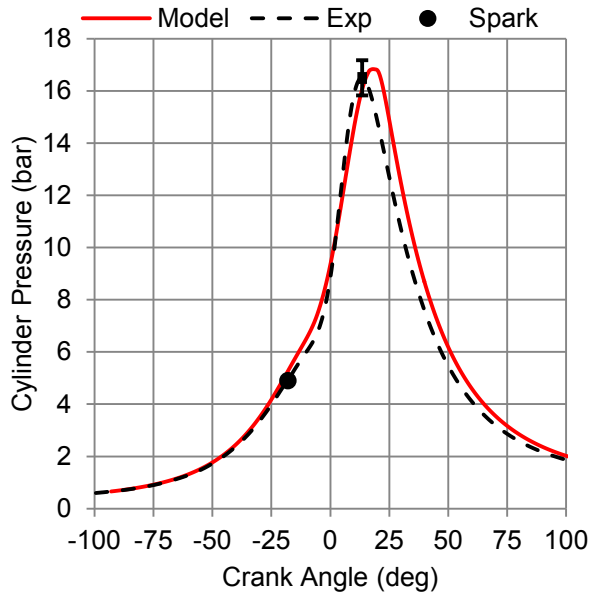


Figure D-57: Cylinder pressure for engine speed 3000 RPM and IMEP 2 bar

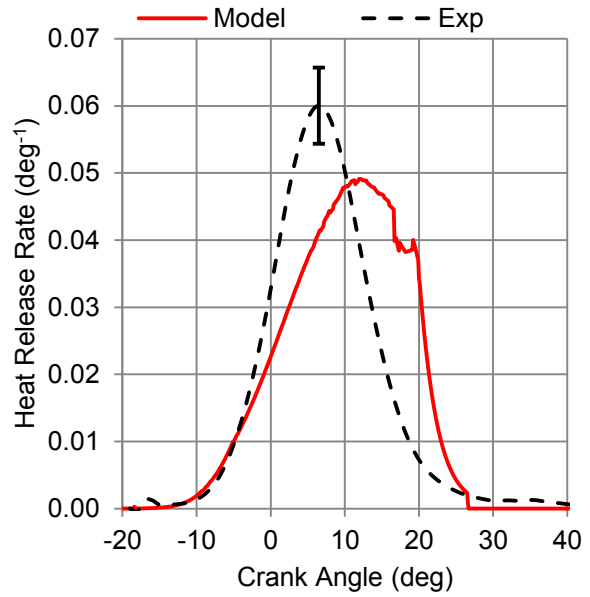


Figure D-58: Heat release rate for engine speed 3000 RPM and IMEP 2 bar

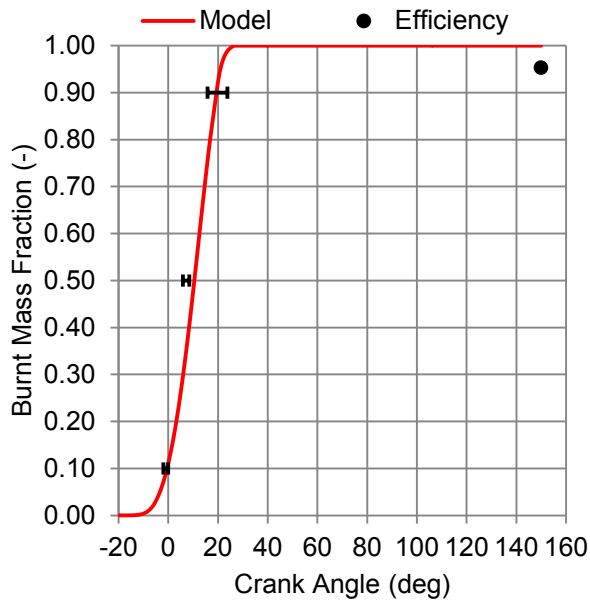


Figure D-59 : Burnt mass fraction for engine speed 3000 RPM and IMEP 2 bar

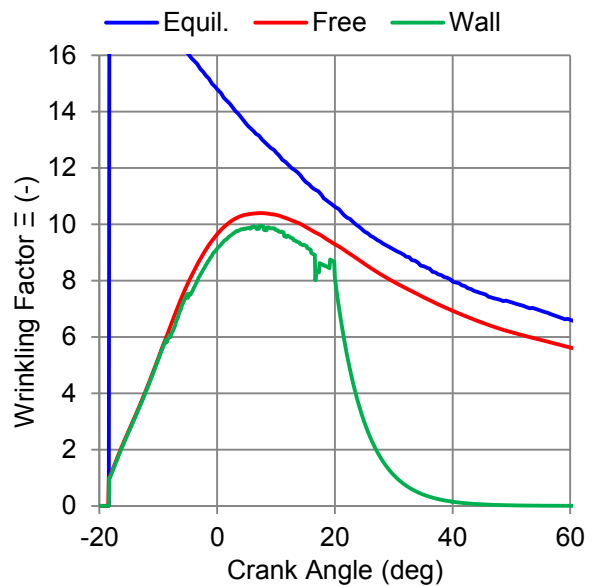


Figure D-60: Wrinkling Factor Ξ for engine speed 3000 RPM and IMEP 2 bar

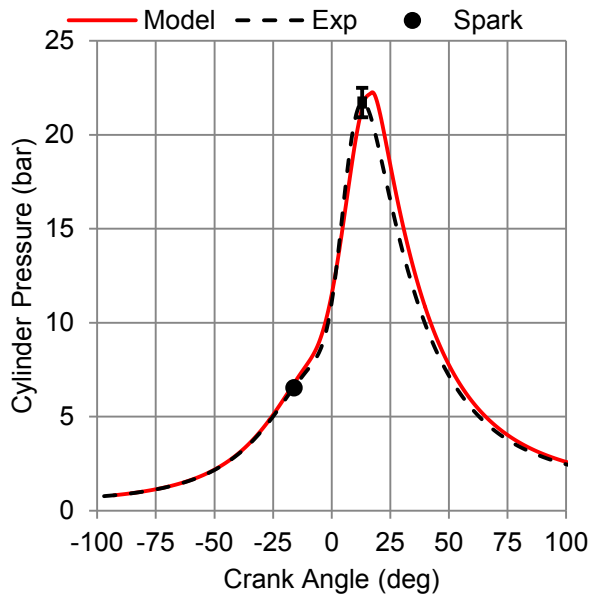


Figure D-61: Cylinder pressure for engine speed 3000 RPM and IMEP 3 bar

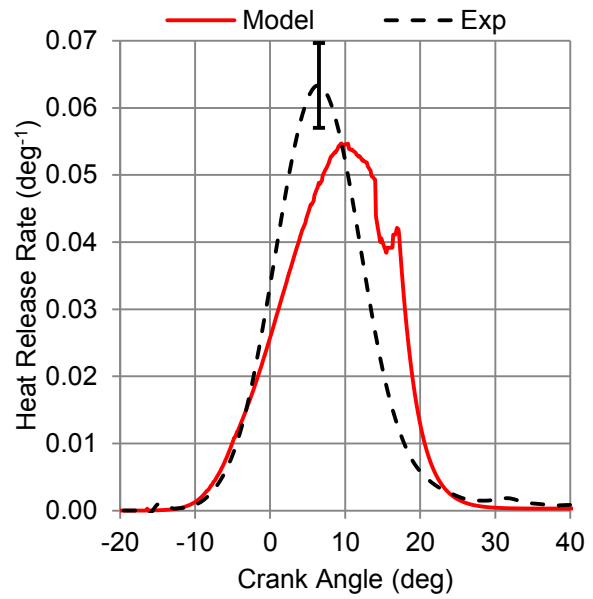


Figure D-62: Heat release rate for engine speed 3000 RPM and IMEP 2 bar

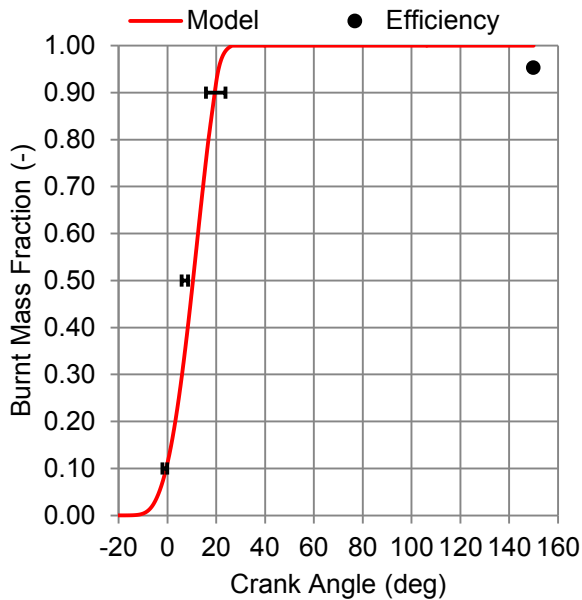


Figure D-63 : Burnt mass fraction for engine speed 3000 RPM and IMEP 3 bar

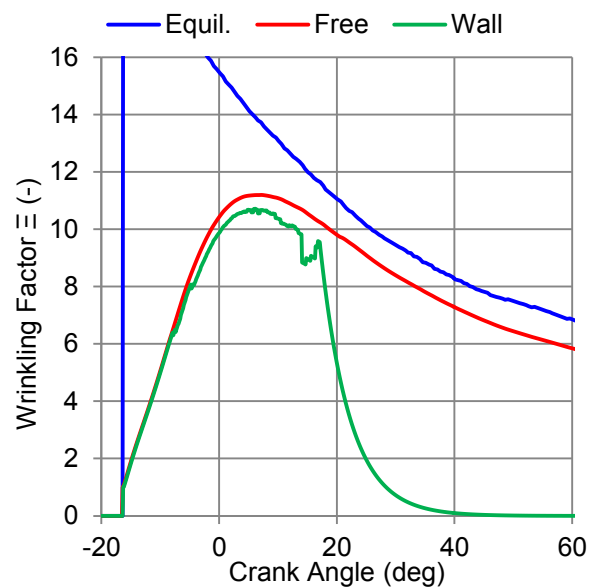


Figure D-64: Wrinkling Factor Ξ for engine speed 3000 RPM and IMEP 3 bar

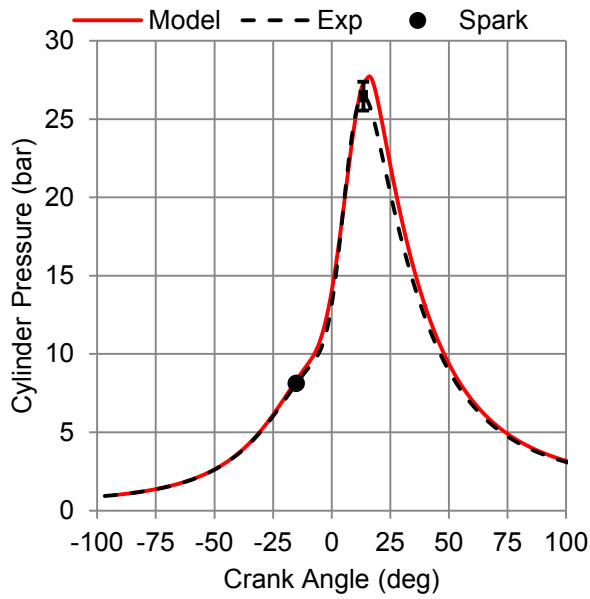


Figure D-65: Cylinder pressure for engine speed 3000 RPM and IMEP 4 bar

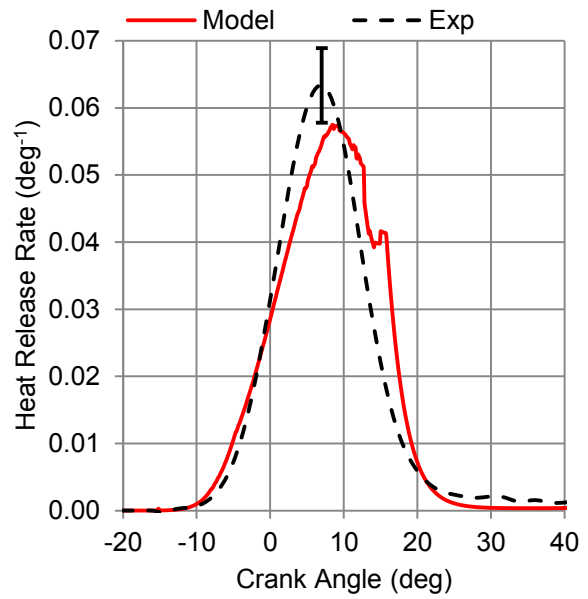


Figure D-66: Heat release rate for engine speed 3000 RPM and IMEP 4 bar

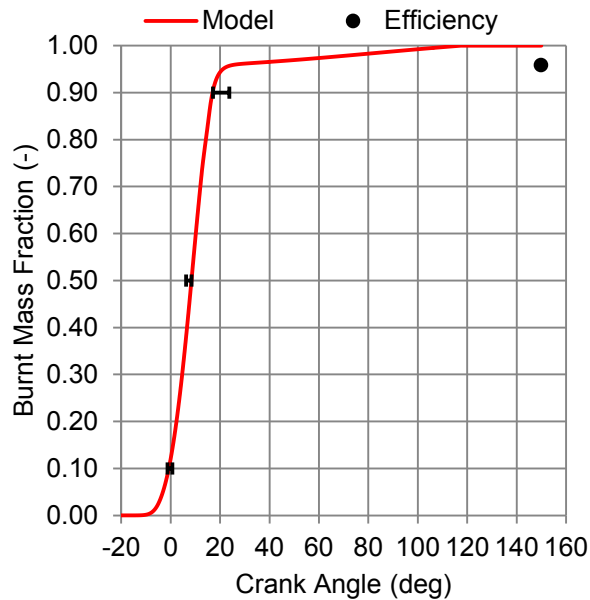


Figure D-67 : Burnt mass fraction for engine speed 3000 RPM and IMEP 4 bar

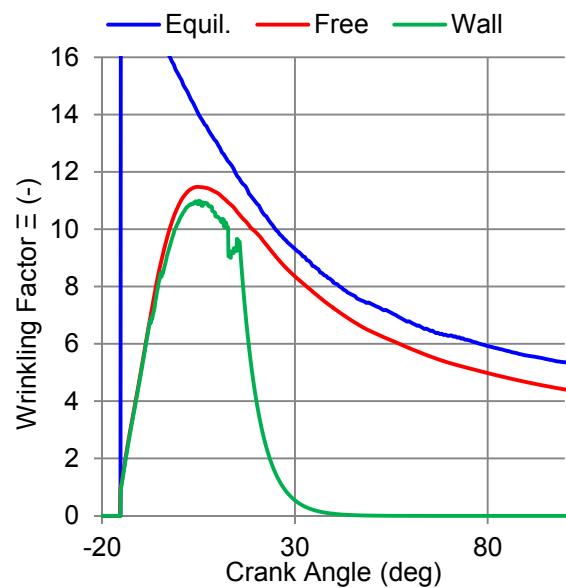


Figure D-68: Wrinkling Factor Ξ for engine speed 3000 RPM and IMEP 4 bar

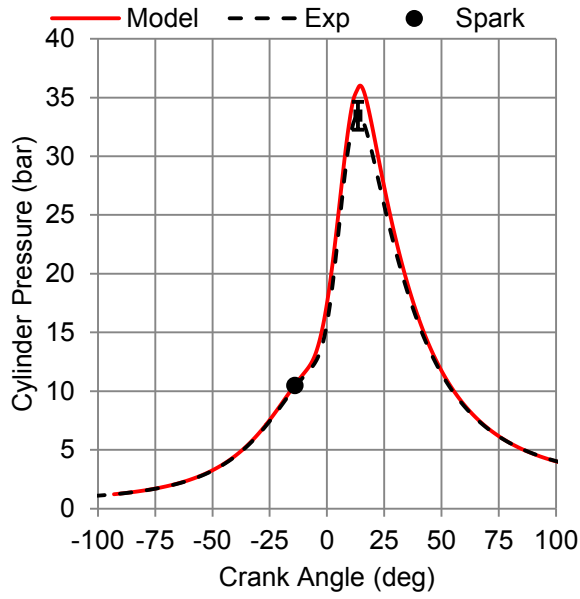


Figure D-69: Cylinder pressure for engine speed 3000 RPM and IMEP 5.5 bar

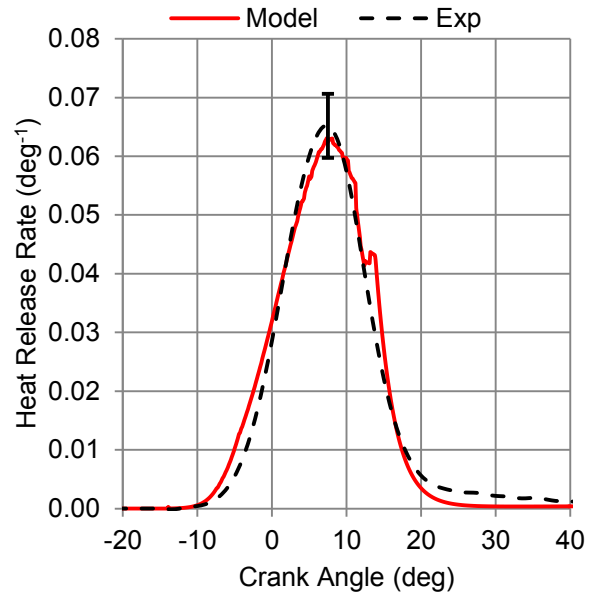


Figure D-70: Heat release rate for engine speed 3000 RPM and IMEP 5.5 bar

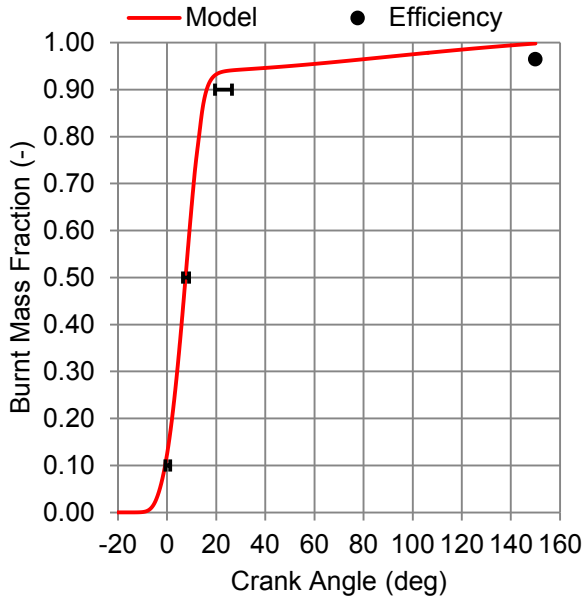


Figure D-71 : Burnt mass fraction for engine speed 3000 RPM and IMEP 5.5 bar

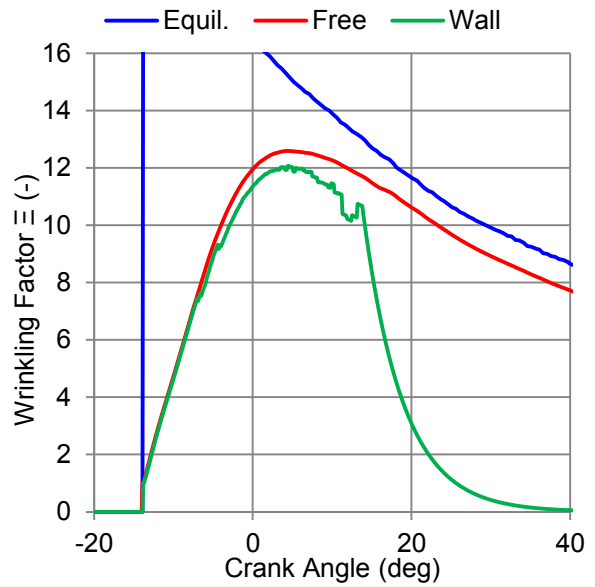


Figure D-72: Wrinkling Factor Ξ for engine speed 3000 RPM and IMEP 5.5 bar

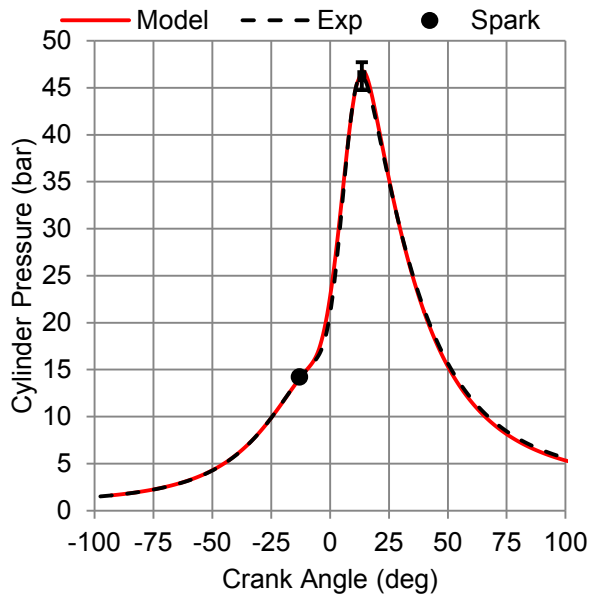


Figure D-73: Cylinder pressure for engine speed 3000 RPM and IMEP 8 bar

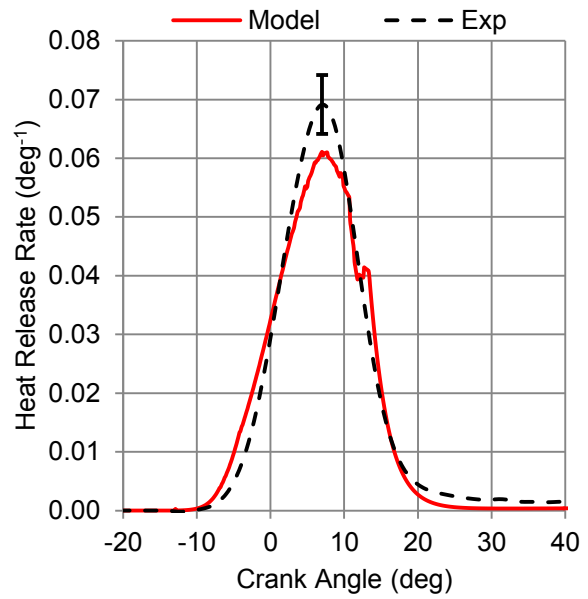


Figure D-74: Heat release rate for engine speed 3000 RPM and IMEP 8 bar

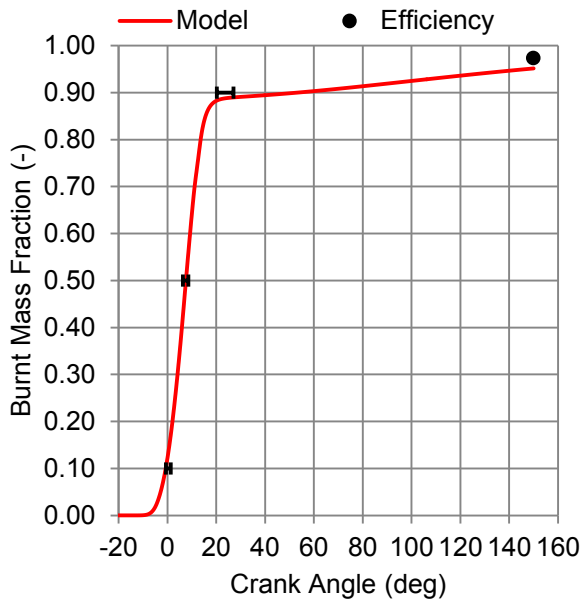


Figure D-75 : Burnt mass fraction for engine speed 3000 RPM and IMEP 8 bar

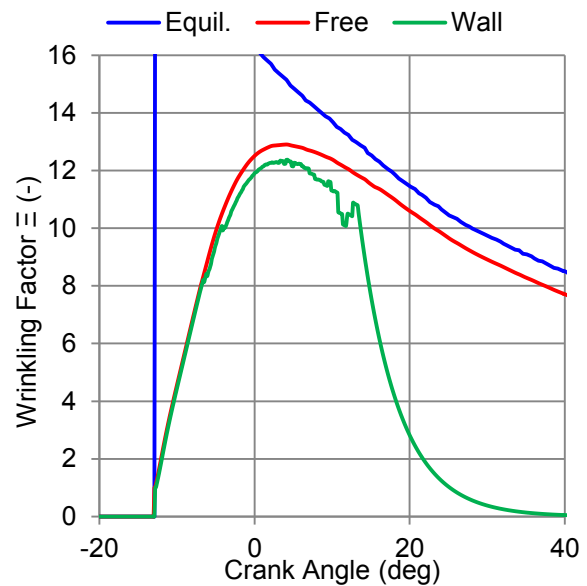


Figure D-76: Wrinkling Factor Ξ for engine speed 3000 RPM and IMEP 8 bar

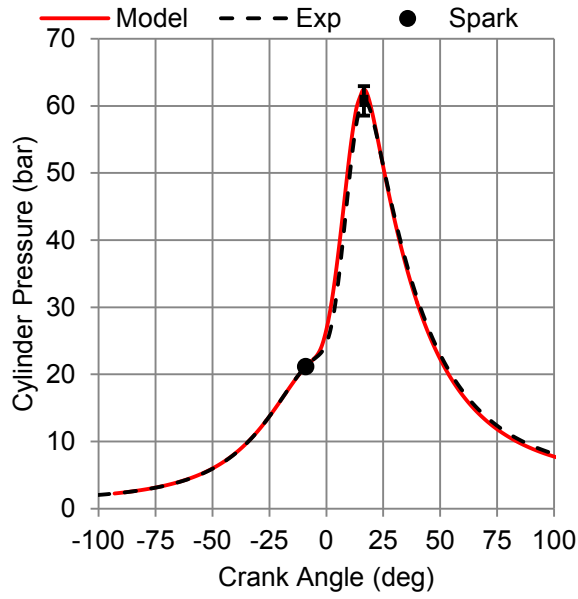


Figure D-77: Cylinder pressure for engine speed 3000 RPM and IMEP 12 bar

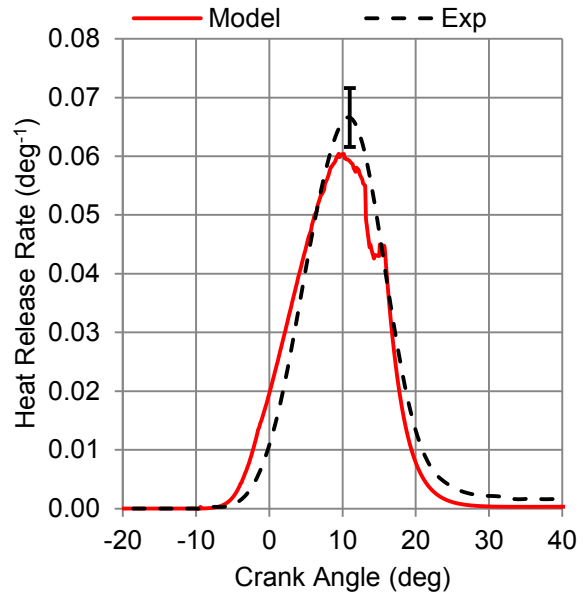


Figure D-78: Heat release rate for engine speed 3000 RPM and IMEP 12 bar

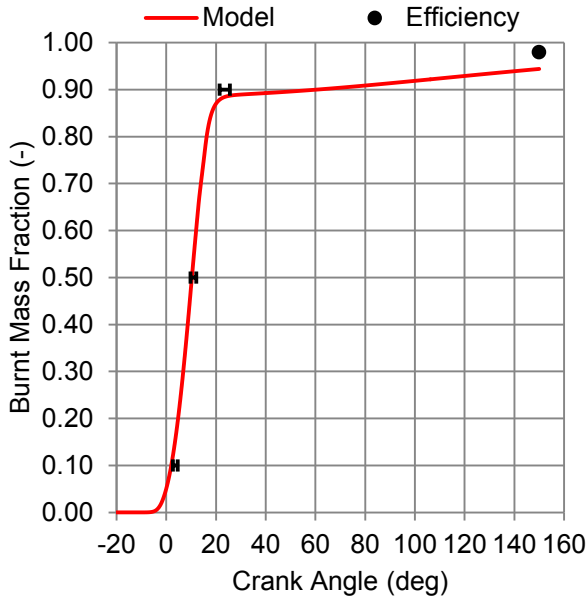


Figure D-79 : Burnt mass fraction for engine speed 3000 RPM and IMEP 12 bar

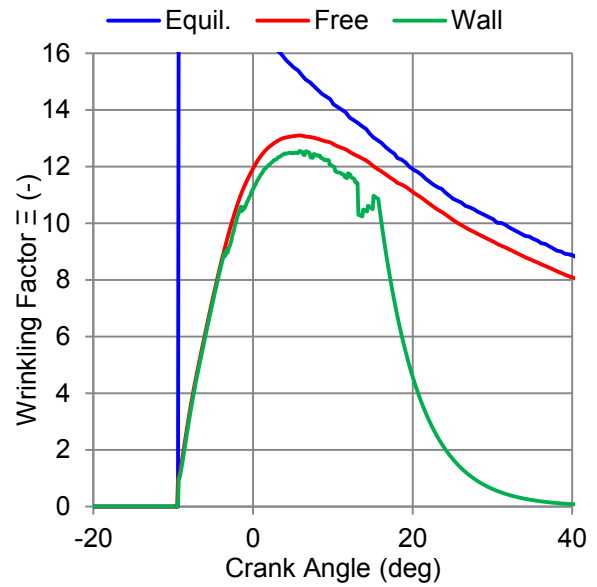


Figure D-80: Wrinkling Factor Ξ for engine speed 3000 RPM and IMEP 12 bar

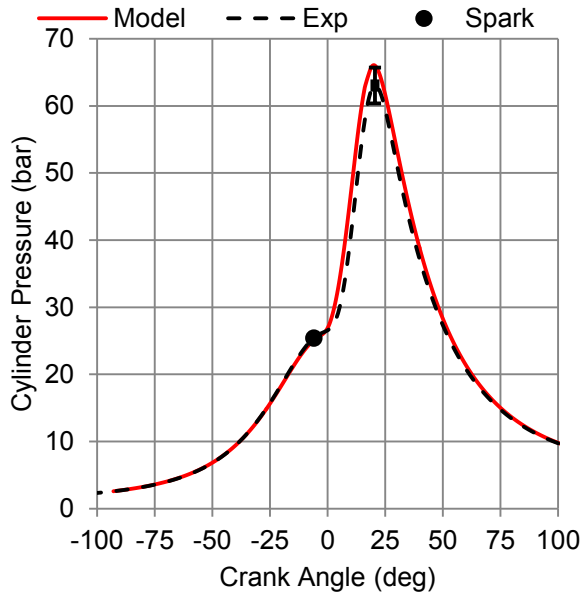


Figure D-81: Cylinder pressure for engine speed 3000 RPM and IMEP 14 bar

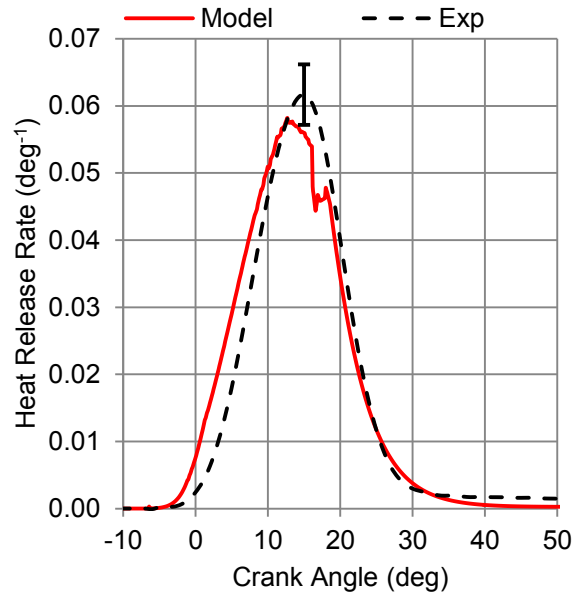


Figure D-82: Heat release rate for engine speed 3000 RPM and IMEP 14 bar

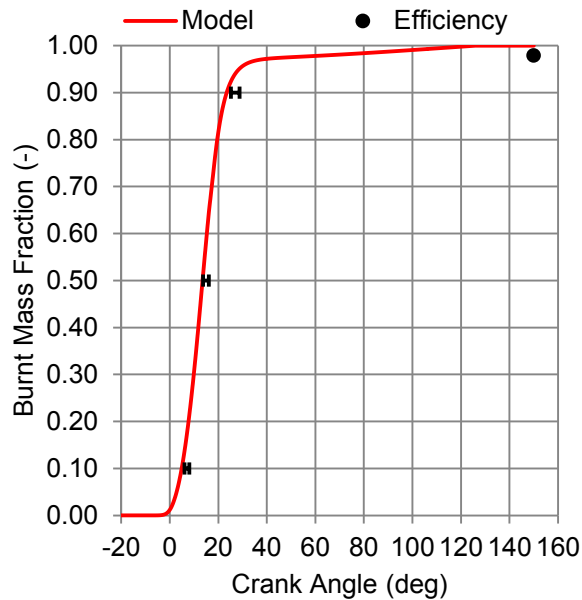


Figure D-83 : Burnt mass fraction for engine speed 3000 RPM and IMEP 14 bar

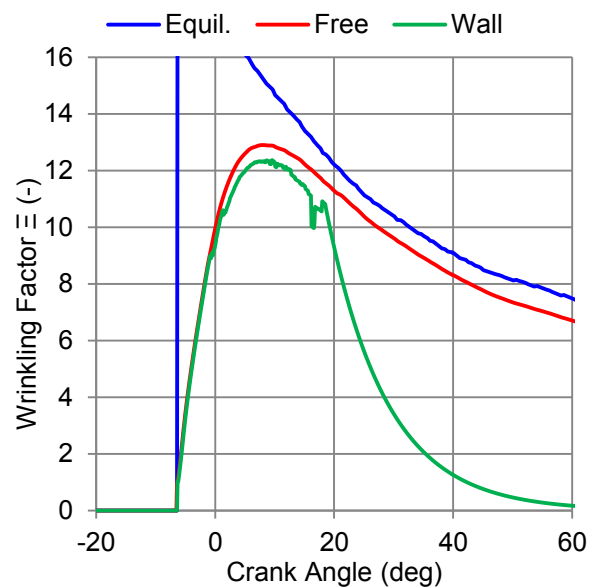


Figure D-84: Wrinkling Factor Ξ for engine speed 3000 RPM and IMEP 14 bar

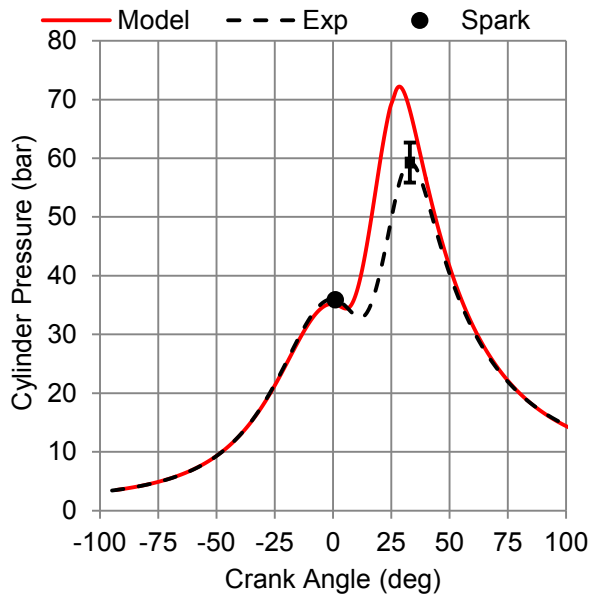


Figure D-85: Cylinder pressure for engine speed 3000 RPM and IMEP 18 bar

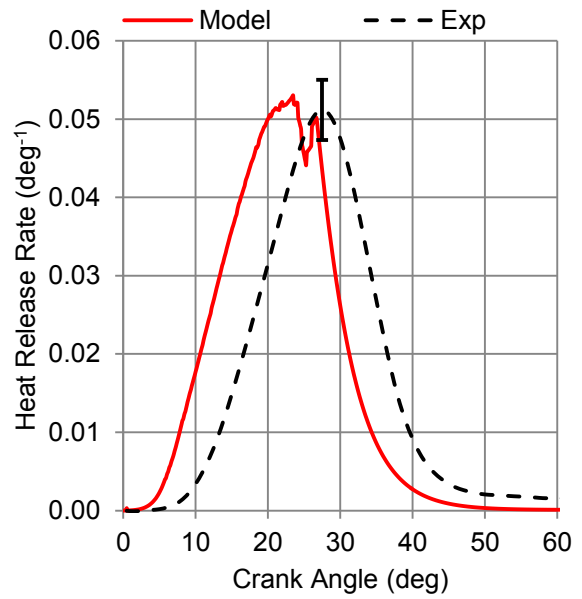


Figure D-86: Heat release rate for engine speed 3000 RPM and IMEP 18 bar

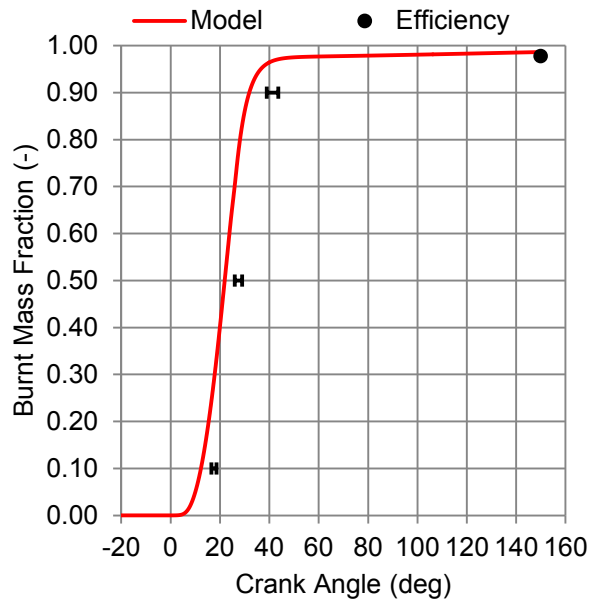


Figure D-87 : Burnt mass fraction for engine speed 3000 RPM and IMEP 18 bar

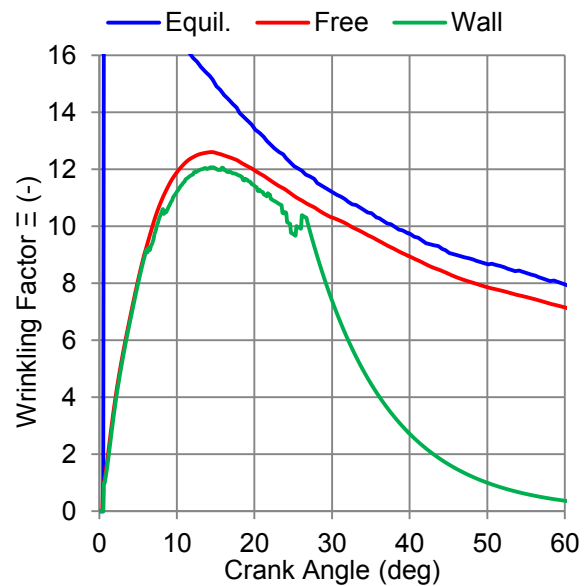


Figure D-88: Wrinkling Factor Ξ for engine speed 3000 RPM and IMEP 18 bar

Appendix E Résumé du manuscrit en français

E.1 Contexte de la conception contemporaine des moteur à allumage commandé

Introduction

Le défi actuel pour les moteurs à allumage commandé, est la réduction des émissions polluantes et de la consommation du carburant. Le besoin pour la réduction des émissions polluantes émises par les véhicules équipés d'un moteur à allumage commandé est aussi imposé par les réglementations de l'Union Européenne pour les véhicules neufs.

Le moteur à allumage commandé

Dans la plupart de moteurs à allumage commandé, l'air et le carburant sont mélangés dans le système d'admission avant qu'ils entrent la chambre de combustion. Le control de la performance est réalisé par la régulation de la masse de la charge, puisque un moteur à allumage commandé brûle toujours un mélange stœchiométrique. Dans le cas d'un moteur atmosphérique une soupape « papillon » régule la quantité d'air qui va rentrer dans la chambre de combustion. Pendant la phase d'admission le piston se déplace par le Point Mort Haut vers le Point Mort Bas. Les soupapes d'admission sont ouvertes et permettent au mélange air/carburant de rentrer dans le cylindre. Pendant la phase de compression les soupapes sont fermées et le mélange est comprimé. L'allumage se passe avant ou après (selon le point de fonctionnement du moteur) que le piston arrive au Point Mort Haut. Ensuite, les phases de combustion et d'expansion ont lieu et l'énergie chimique du carburant est transformée en énergie mécanique par la force sur le piston. Pendant la phase d'échappement, qui est la dernière phase du cycle, les soupapes d'échappement sont ouvertes et les gaz brûlés sont poussés par le piston qui monte vers le Point Mort Haut et sortent de la chambre de combustion. Les deux leviers basiques pour l'augmentation de l'efficacité sont l'augmentation du rapport volumétrique de compression et la réduction des pertes d'énergie à travers la soupape papillon (pertes de pompage).

Solutions pour la réduction des émissions et de la consommation

Les solutions technologiques pour la réduction de la consommation et des émissions pour un moteur à allumage commandé classique sont les suivantes :

- Utilisation de turbocompresseur dans des moteurs de petite cylindrée.
- Augmentation ou adaptation du rapport volumétrique de compression.
- Actuation variable des soupapes.
- Utilisation des carburants avec indice d'octane élevé.
- Dilution du mélange air/carburant.

Description de la combustion et des émissions d'un moteur à allumage commandé

Le processus de combustion commence par une décharge électrique par la bougie d'allumage. En ce moment, l'écoulement dans la chambre de combustion est fortement turbulent. Un noyau de flamme est développé entre les électrodes de la bougie. La flamme du noyau initial est laminaire et pour une période courte après l'initiation de la flamme, le noyau peut être transporté par l'écoulement turbulent loin de sa position initiale. Tandis que le noyau interagit avec la turbulence, il grandit et la flamme devient turbulente. La turbulence plisse et augmente la surface de la flamme. Lorsque la flamme arrive près de la paroi de la chambre de combustion son extinction commence.

Les émissions polluantes sont un faible pourcentage (de l'ordre de 1%) de la quantité des gaz d'échappement. Le monoxyde de carbone est prépondérant tandis que les oxydes d'azote et les hydrocarbures imbrûlés existent dans des faibles quantités.

Outils de recherche pour la combustion à allumage commandé

Les dispositifs expérimentaux et notamment les bancs moteur sont les moyens classiques pour l'évaluation de différentes définitions techniques des moteurs. L'utilisation de la simulation numérique augmente dans l'industrie automobile. Les écoulements dans les chambres de combustion des moteurs sont simulés par les outils de mécanique de fluide comme le RANS (équations Navier Stokes avec moyenne de Reynolds) et le LES (simulation des grandes échelles). La description des réactions dans la chambre de combustion est faite à l'aide des schémas de cinétique chimique complexes ou réduits ainsi qu'avec de la cinétique chimique tabulée.

La modélisation 0D est une technique bien établie dans l'industrie automobile grâce à son temps de calcul court, à sa possibilité d'analyser des différents systèmes et à sa facilité de construction d'un modèle global à partir de sous-modèles.

Objectifs et structure de ce travail

L'industrie automobile s'engage à concevoir des moteurs à combustion interne avec une efficacité augmentée et avec des émissions polluantes limitées. Les définitions techniques, qui permettent atteindre ces buts, doivent être évaluées par rapport à leur contribution à l'amélioration globale du système. Les contraintes temporelles et économiques imposées, favorisent l'utilisation de la simulation zéro dimensionnelle ou mono dimensionnelle à travers les différentes étapes d'un projet de conception, auxquels des techniques de type boucle courte doivent être appliquées.

Ce travail est dédié à la modélisation zéro-dimensionnelle de la combustion dans un moteur à allumage commandé. La modélisation physique du processus de combustion a une importance cruciale pour un modèle 0D approprié. Une analyse du processus de la combustion permet d'identifier ses phénomènes élémentaires. Ensuite, pour chaque phénomène un sous-modèle approprié peut être développé. Après cette étape, l'ensemble du modèle de combustion peut être utilisé dans un code 1D, qui résolve le processus des échanges des gaz du moteur.

La capacité de prédiction du modèle abouti doit être chiffrée à travers l'exploitation des données expérimentales des définitions techniques avec des différentes solutions technolo-

giques. Plusieurs sous-modèles doivent être calibrés avec les données expérimentales, pour qu'ils deviennent précis et rapides. Ce processus de calibration introduit des coûts élevés et des délais et elle est relativement indésirable.

Même si le modèle finale décrit la combustion de pré-mélange, il peut être aussi utilisé pour la simulation des moteurs d'injection directe après l'addition de la modélisation appropriée, qui décrira l'atomisation et l'évaporation du spray.

Le chapitre d'introduction a présenté le contexte contemporain de la conception des moteurs à allumage commandé. Une introduction courte des méthodes d'amélioration de la performance, consommation et des émissions des polluants a été donnée. Les leviers pour l'amélioration de l'efficacité ont été présentés. En plus une description de la combustion et des émissions polluantes dans un moteur à allumage commandé a été faite. Les éléments basiques des outils de recherche ont été discutés. Les avantages et les applications de la modélisation des systèmes dans le contexte industriel définissent les buts de ce travail.

Dans le deuxième chapitre, les aspects fondamentaux de la combustion turbulente sont présentés. Les différents phénomènes, qui constituent le processus de combustion, sont analysés. La théorie fondamentale pour la vitesse de flamme laminaire et l'étirement de flamme est traitée. Des détails sur la nature et les manières de calcul de la turbulence aérodynamique sont données dans ce chapitre. Les modèles de la combustion turbulente existants sont identifiés et une comparaison est faite, les résultats de laquelle permettra le choix pertinent du modèle de combustion.

Dans le troisième chapitre, le modèle global de combustion pour les moteurs à allumage commandé est présenté. Des détails sur le modèle thermodynamique et des transferts thermiques sont donnés. Le modèle de combustion proposée est analysé. Les processus proche-paroi comme l'interaction flamme-paroi, l'extinction de flamme et les réactions post flamme sont discutés et des modèles appropriés sont proposés. L'impact de l'étirement de flamme pendant la première étape de combustion est discuté. Ces résultats constituent le noyau scientifique de cette thèse et contiennent sa contribution dans la modélisation de la combustion dans les moteurs à allumage commandé.

Dans le quatrième chapitre, le modèle proposé est validé avec des résultats expérimentaux. Les configurations du banc de moteur ont été choisies attentivement. Le but est de souligner la qualité des réponses de chaque sous modèle et de montrer les limitations du modèle proposé dans le cadre de l'utilisation industrielle.

E.2 Combustion de pré-mélange turbulente: Physique et modélisation

Dans ce chapitre, les aspects fondamentaux de la combustion de pré-mélange sont exposés. La discussion est focalisée aux phénomènes qui affectent la vitesse de consommation du carburant dans le front de flamme turbulent : La vitesse de flamme laminaire et ses caractéristiques, l'étirement de flamme et l'impact de la turbulence sur la flamme. Ensuite, trois modèles de combustion turbulentes sont testés et le choix de celui qui est le plus pertinent est réalisé.

Flames laminaires de pré-mélange

Le front de flamme est une surface mince entre les gaz frais et les gaz brûlés, dans laquelle les réactions chimiques de combustion ont lieu. La flamme laminaire est caractérisée par la vitesse de consommation des gaz frais (s_L) (vitesse de flamme laminaire) et par l'épaisseur de flamme laminaire (δ_L). La vitesse de flamme laminaire est une fonction du carburant, de la richesse, de la pression, de la température du gaz frais (T_u) et de la fraction du gaz brûlé résiduel dans la chambre de combustion. La relation entre les transferts massiques (nombre de Lewis) et thermiques dans le front de flamme peut créer des instabilités qui changent la structure du front de flamme et qui altèrent la vitesse de flamme laminaire.

Étirement de flamme

L'étirement de flamme représente le taux d'augmentation de la surface de flamme en fonction du temps. Pour une flamme sphérique, comme c'est le cas dans le moteur à allumage commandé, l'étirement de flamme est inversement proportionnel au rayon de flamme (R_f) et dépend de la composition du mélange air/carburant et aussi du nombre Lewis. Il est élevé pendant le début de la combustion, lorsque les rayons de flamme sont petits. Cette discussion montre pourquoi il faut modéliser aussi l'impact de l'étirement sur la vitesse de flamme laminaire.

Turbulence dans la chambre de combustion

Dans les moteurs à allumage commandé, la turbulence peut être caractérisée comme homogène et isotrope pendant la phase de combustion. Les deux grandeurs qui décrivent la turbulence dans la chambre de combustions sont l'intensité de turbulence (u') et l'échelle intégrale (L_T). Un modèle de deux équations différentielles ordinaires (une équation pour l'énergie cinétique moyenne et une équation pour l'énergie cinétique turbulente) est utilisé pour calculer l'intensité de turbulence. L'échelle intégrale, qui est liée à la géométrie du moteur, est calculée comme une fonction du volume de la chambre de combustion.

Flames turbulentes de pré-mélange

La surface moyenne de flamme (A_L) est plissée par la turbulence. Le rapport entre la surface plissée (A_T) et la surface moyenne (A_L), qui est une fonction des caractéristiques de la flamme laminaire et de la turbulence, définit le facteur de plissement (\mathcal{E}). Le taux de masse brûlée (\dot{m}_b) est calculé par le produit de la densité du gaz frais (ρ_u), de la vitesse de flamme laminaire (s_L), de la surface moyenne de flamme (A_L) et du facteur de plissement (\mathcal{E}) ($\dot{m}_b = \rho_u s_L A_L \mathcal{E}$). Plusieurs modèles existent pour l'estimation du facteur de plissement. Trois modèles de combustion sont comparés.

Comparaison des modèles de combustion turbulente

Trois modèles de combustion 0D ("Eddy Burn Up", "Fractal", Densité de Surface de Flamme) ont été codés dans le logiciel de simulation 1D "GT-POWER" et des simulations d'un moteur monocylindre ont été faites. La comparaison des résultats de simulation avec des données expérimentales focalise sur l'impact de la turbulence au front de flamme et montre la capacité de prédictions de chaque approche.

Le modèle Eddy Burn Up a donné une simulation satisfaisante du début de combustion mais il ne décrit pas correctement la fin de la combustion puisque le terme exponentiel, qui est utilisée pour la description de la fin de combustion, n'est pas une solution pertinente. Eddy Burn Up model contient trois coefficients pour la description du front de flamme turbulente ($C_{tb}, A_{ST}, C_{\tau t}$). C_{tb} varie avec le régime du moteur et reste constant avec la charge, tandis que les deux autres coefficients restent constants. Le modèle fractal a un coefficient (C_R), qui varie avec le régime du moteur et avec la charge. Les coefficients, qui définissent la dimension fractale sont constantes. Le modèle de Densité de Surface de Flamme a un seul coefficient qui varie avec le régime et la charge. Contrairement à l'intensité de turbulence, qui a été prise par des résultats de calculs 3D, l'échelle intégrale a été modélisée comme une fonction avec du volume de la chambre.

Les résultats de la pression ont été très satisfaisants, même si le dégagement d'énergie n'était pas correctement prédit. La calibration pour les points de faible charge a été difficile pour tous les modèles. Les modèle fractal aussi que le modèle de densité de surface de flamme montrent des tendances plus claires si ces point sont exclus. Le début de combustion est décrit moyennement bien par ces deux modèles, à cause de la tabulation du rayon de flamme. Le modèle Eddy Burn Up semble être plus approprié pour le début de la combustion. Le modèle Fractal et le modèle de Densité de Surface de Flamme montrent de similarités au dégagement d'énergie, qui sont dues à l'approche fractale commune pour la modélisation de l'interaction turbulence-flamme de ces modèles. Seulement le modèle de Densité de Surface de flamme donne une description physique du début de combustion et décrit une flamme avec une augmentation graduelle du plissement à l'aide de la fonction d'efficacité. L'interaction flamme-paroi diminue le plissement du front de flamme et le dégagement d'énergie. Aucune diminution du plissement n'a été observée pendant que la flamme approche la paroi. Cette déficience montre qu'une modélisation de l'interaction flamme-paroi doit être modélisée.

E.3 Développent et validation d'un modèle de combustion à allumage commandé

Le modèle FSD (Densité de Surface de Flamme), qui a été retenu, est complété par des sous modèles pour (i) l'interaction flamme-paroi, (ii) la contribution des réactions post-flamme au dégagement de l'énergie et (iii) l'impact de l'étirement de flamme a la vitesse de flamme laminaire. Les conclusions scientifiques, qui sont tirées par la validation de ces sous-modèles, sont décrites dans les sections suivantes.

Interaction flamme-paroi

Le modèle de Densité Surface de Flamme est amélioré avec un modèle d'interaction flamme-paroi. Les configurations basiques d'extinction de flamme laminaire sont aussi applicables dans des flammes turbulentes, qui sont les cas dans les moteurs à allumage commandé. Un modèle de géométrie simplifiée a été développé pour le calcul de la surface de la flamme moyenne, du volume et de la distribution de la surface de flamme en fonction de la distance à la paroi. Afin de valider la capacité de prédiction du modèle par rapport à la géométrie de la chambre de combustion, le modèle d'interaction-flamme paroi prend en compte la géométrie de la chambre de combustion, la turbulence aérodynamique et les conditions de pression et de température dans le cylindre, par une fonction phénoménologique d'atté-

uation. Cette fonction calcule un plissement global modifié en fonction de la distribution de la surface moyenne à la paroi. L'impact de l'interaction-flamme paroi a été simulé pour des cas de variation de position de la bougie d'allumage et de variation de sa longueur (quatre configurations ont été utilisées). La position de la bougie a plus d'influence que sa longueur. Le dégagement d'énergie est radicalement altéré dans le cas de la position latéral de la bougie, quand le modèle d'interaction de flamme à la paroi est implémenté. Dans le cas de la bougie projetée, l'impact de la paroi sur le noyau de flamme initial est retardé, puisque la flamme se trouve loin de la culasse. La pression maximale est réduite quand le modèle d'interaction flamme paroi est utilisé pour toutes les quatre configurations. L'atténuation du facteur de plissement et de la surface moyenne pendant la fin de combustion est capté par le modèle. Sa limitation repose sur le fait que l'existence d'une surface de flamme moyenne sphérique n'est pas certaine pendant la dernière étape de la combustion. Des résultats pertinents ont été récupérés en comparaison avec les données expérimentales pour les quatre configurations en termes de pression et de dégagement d'énergie.

Réactions post-flamme

Un nouveau sous-modèle pour les réactions post-flamme (CO et HC) et le dégagement d'énergie, basé sur la chimie à l'équilibre, la cinétique chimique réduite et des phénomènes de diffusion, est ajouté au modèle de combustion. Le dégagement de chaleur du front de flamme est modélisé avec le modèle "interactions-flamme paroi". Le modèle de combustion est introduit dans un modèle thermodynamique de deux zones, qui calcule la pression cylindre et les températures des gaz frais et des gaz brûlés, la composition et les transferts thermiques. Le sous-modèle du CO utilise des équations de chimie réduite, afin de calculer l'évolution cinétique du CO pendant la phase d'expansion. Le modèle prédit un temps caractéristique pour le CO qui est comparable avec des résultats de la chimie complexe, tandis qu'il a les avantages de rapidité et de simplicité. Pour les hautes températures (2200 K) le CO cinétique et le CO d'équilibre sont égaux. La température, au-dessous de laquelle la concentration du CO fige (1800 K), est captée, même si la chimie adoptée est réduite. Malgré que les valeurs prédites du CO à l'échappement soient constamment sous-estimées pour les cas étudiés, le modèle a montré sa capacité de reproduire les tendances de la cinétique du CO. Il a été aussi montré, qu'une prédiction du CO améliorée demande un calcul plus précis des valeurs à l'équilibre. Le sous-modèle de post-oxydation des HC est contrôlé par un phénomène de réaction et diffusion. L'approche développée consiste à décomposer ces deux processus et à introduire un temps de relaxation, qui représente le temps nécessaire pour que le mélange atteigne les conditions d'auto-inflammation. Les réactions HC sont dominantes pendant la dernière étape de la combustion après que 90% de la charge a brûlé. Des résultats pertinents sont trouvés pour une gamme des points de fonctionnement du moteur. Cette approche de modélisation permet une description plus physique des réactions post-flammes et de leur contribution au dégagement d'énergie total, tout en conservant la rapidité en termes de temps de calcul et la simplicité en termes de théorie de modélisation.

Étirement

Le modèle de combustion est amélioré avec un sous-modèle pour l'impact de l'étirement de flamme. Les résultats de la simulation sont comparés avec des résultats expérimentaux

déjà publiés des différents mélanges pauvres (isooctane, propane et méthane), qui présentent presque la même vitesse de consommation non-étirée pendant le début de la combustion, pendant lequel le plissement de la flamme est petit. Les simulations du rayon du front de flamme et de la vitesse de propagation de flamme montrent les mêmes tendances que les résultats expérimentaux. Le mélange du méthane se propage plus rapidement que celui du propane, tandis qu'ils ont la même vitesse de propagation d'après les expériences. Les différences entre expériences et simulations pour le rayon de flamme sont dues à la manière de calculations différente par les images tomographiques dans les expériences et par les surfaces sphériques dans les simulations. La tendance du plissement du front de flamme est aussi captée par le modèle: Les mélanges de propane et de méthane ont le même plissement, tandis que le mélange d'isooctane a des valeurs moins élevées. Les valeurs absolues des expériences sont plus élevées que celles des simulations, parce que les valeurs des rayons sont plus élevées dans les expériences. L'étirement de flamme est presque pareil pour les trois mélanges dans les expériences et dans les simulations. Finalement, l'impact de la vitesse de flamme étirée n'est visible pour méthane, puisque les deux vitesses sont presque égales. L'impact de l'étirement devient visible pour le propane et il est prépondérant pour l'isooctane.

E.4 Validation du modèle pour des différentes configurations de moteur

Comparaison des résultats de simulation avec des points de fonctionnement à l'avance optimale

La variation en fonction du régime et de la charge du moteur des grandeurs qui interviennent dans la combustion dans un moteur à allumage commandé est tracée, en simulant plusieurs points de fonctionnements du moteur. Le comportement qualitatif de cette variation est montré au tableau suivant (▲ : augmentation, ▼ : diminution, — : pas de variance) :

	Intensité de turbulence (u')	Échelle intégrale (L_T)	Température gaz frais (T_u)	Densité des gaz frais (ρ_u)	Vitesse de flamme laminaire (s_L)
Régime	▲	—	—	▼	▲
Charge	—	—	▲	▲	—
	Épaisseur de flamme laminaire (δ_L)	Fonction d'efficacité (Γ)	Plissement de flamme (ε)	Rayon de flamme (R_f)	Surface moyenne de flamme laminaire (A_L)
Régime	—	▲	▲	—	—
Charge	▼	▲	—	—	—

Essais pour la validation des sous-modèles

La comparaison des résultats de simulation avec une série des résultats expérimentaux des plusieurs points de fonctionnement a montré les conclusions suivantes:

- Le coefficient de la calibration du modèle de Densité de Surface de Flamme est très sensible au rapport de l'intensité de turbulence à la vitesse de flamme laminaire (u'/s_L).
- Les tendances de CA10 et CA50 sont captées par le modèle, même si une modification de l'angle d'avance à l'allumage est exigée, puisque la première étape de la combustion n'est pas physiquement modélisée.

- Pendant la dernière étape de la combustion, le modèle ne peut pas calculer de rayon de front de flamme. Ce n'est pas sûr si la forme de la surface du front de flamme peut être modélisée par un front de flamme sphérique. Cette incertitude explique pourquoi les tendances de CA90 sont partiellement captées.
- Une conclusion pour la variation de la richesse est que la corrélation de la vitesse de flamme laminaire prend bien en compte cette variation et que le même coefficient pour la combustion turbulente est valable dans des cas similaires.
- Une conclusion pour les cas avec les carburant essence/éthanol est que le modèle de combustion, comme il a été amélioré avec une corrélation de flamme laminaire pour l'éthanol, prend en compte la variation de la flamme laminaire et que le même coefficient de turbulence peut être utilisé dans des cas similaires.

Une conclusion pour la relation de Metgalchi et Keck est que les points avec 0% à 15% sont correctement modélisés avec le même coefficient que le cas d'avance à l'allumage optimale. Finalement, pour la corrélation SAE 2010-01-0620 on observe que même si sa correction en fonction des résiduels est moins lourde que celle de Metgalchi et Keck, elle ne peut pas être utilisée avec les mêmes coefficients d'avance à l'allumage optimale. Ce résultat est lié aux valeurs plus basses de vitesse laminaire, qui sont calculées par cette corrélation pour les mêmes conditions de pression et de température.

E.5 Conclusions et perspectives

Le développement des moteurs à allumage commandé avec une basse consommation de carburant, émissions régulées et performance suffisante, est atteint par la combinaison des différentes solutions technologiques. Il y a une nécessité de diminuer le coût de l'évaluation de ces technologies. La simulation numérique est une méthode prometteuse et peu chère en comparaison avec le banc moteur traditionnel.

La modélisation monodimensionnelle est une technique bien établie dans l'industrie. Elle offre un calcul du processus des échanges des gaz, qui est suffisamment précis et rapide. Cette technique de simulation est complétée par des modèles de combustion phénoménologiques zéro-dimensionnels, qui prennent en compte les différents aspects de la combustion à allumage commande, comme les caractéristiques de la flamme laminaire, la turbulence aérodynamique et son impact à la turbulence.

Dans ce travail, pour la création d'un modèle de combustion zéro-dimensionnel, qui soit capable de décrire correctement la physique de la combustion, les pas suivants ont été suivis:

- Les aspects cruciaux de la flamme laminaire et turbulente ont été identifiés.
- Trois versions de modèles de combustion typiques ont été comparées par rapport à la description physique du processus de la combustion. Le résultat de cette comparaison a indiqué le modèle, qui est le plus pertinent. (Le modèle de Densité de Surface de Flamme).
- Le modèle de Densité de Surface de Flamme, qui a été retenu, a été amélioré avec la modélisation physique des différents phénomènes, qui ont un effet sur le dégagement d'énergie et qui ne font pas partie de modèle initial. Ces phénomènes sont :
 - L'interaction flamme-paroi.
 - Les réactions post-flamme.

- L'étirement de flamme.
- Finalement, le modèle proposé est validé pour plusieurs définitions techniques des moteurs. Chaque définition a un impact sur un paramètre spécifique du moteur. L'analyse montre quels sont les intervalles de confiance et les limitations du modèle proposé.

Les conclusions spécifiques des travaux, qui ont été décrits dans les paragraphes antérieurs, sont élaborées dans les sections suivantes. Les opportunités pour la continuation des travaux sont présentées dans la dernière section de ce chapitre.

Comparaison des modèles de combustion de pré-mélange turbulente

Trois modèles de combustion à allumage commandé (Eddy Burn Up, Fractal, FSD) ont été codés comme modèles d'utilisateur dans le logiciel de simulation 1D GT-POWER™ et des simulations ont été faites pour un moteur monocylindre.

- Les résultats de pressions cylindre sont très satisfaisants pour tous les modèles.
- La calibration pour des points de faible charge était difficile pour tous les modèles.
- Le modèle de Densité de Surface de Flamme (FSD) est retenu car:
 - Il simule un facteur de plissement égal à un au début de la combustion, lorsque la flamme est quasi-laminaire.
 - It describes physically the turbulence-flame interaction through its efficiency function.

Le modèle retenu doit être complétée par rapport aux phénomènes d'interaction flamme-paroi et des réactions post-flamme.

Interaction flamme-paroi

Un sous-modèle phénoménologique est développé pour la simulation de l'interaction flamme-paroi est de la diminution du plissement de flamme.

Il intègre l'impact de (i) la diminution de la température du front de flamme, (ii) sa restriction par la géométrie de la chambre et (iii) l'impact de la couche limite. Un facteur de plissement modifié est calculé en fonction de la distribution à la paroi de la surface moyenne.

- Quatre configurations géométriques différentes (avec la variation de la longueur et de la position de la bougie d'allumage) sont testées.
- La diminution du plissement de flamme et de la surface moyenne est captée par le modèle.
- La position de la bougie a une influence plus importante que sa longueur par rapport à l'interaction flamme paroi.
- L'impact de l'interaction flamme paroi est plus évident pour la position latérale que la position centrale de la bougie.
- Les résultats des simulations pour la pression du cylindre et le dégagement de chaleur sont satisfaisants pour toutes les configurations.

Réactions post-flamme

Le sous-modèle des réactions post-flamme (CO et HC), qui est basé sur une chimie à l'équilibre, sur une cinétique chimique réduite est sur des phénomènes de diffusion/réaction, est utilisé pour l'amélioration la simulation du dégagement d'énergie.

- Le temps caractéristique de la cinétique du CO est comparable avec des résultats de chimie complexe, tandis que son calcul reste rapide et simple.
- L'effet de "figeage" (la fraction du CO reste quasi constant) est capté par le modèle.
- Une variation de la richesse est faite et le modèle capte les tendances des valeurs du CO mesurées à l'échappement.
- L'étape finale de la combustion est dominée par le processus lent de la diffusion et de l'oxydation des HC.
- Un temps de relaxation est utilisé pour la décomposition du processus de diffusion et de post-oxydation des HC.
- La quantité des HC consommée pendant cette étape est cohérente en comparant avec la quantité mesurée des HC à l'échappement, pour plusieurs points de fonctionnement.
- Le modèle de post-oxydation des HC offre une description réaliste de la dernière étape de la combustion, tout en restant rapide et relativement simple.

Étirement

L'évaluation du sous-modèle de l'étirement de flamme, qui prend en compte les caractéristiques thermo-diffusifs du mélange, est réalisée à l'aide des résultats expérimentaux déjà publiés. L'impact de l'étirement de flamme est pris en compte au calcul de la vitesse de flamme laminaire étirée. La comparaison des expériences avec les simulations a montré que:

- Les tendances du rayon de flamme et de la vitesse de propagation de flamme sont similaires dans les expériences et les simulations. Les variations entre les rayons de flamme et les vitesses de propagation simulés et expérimentaux sont dues aux considérations géométriques différentes de l'expérience et de la simulation.
- Le plissement de flamme suit les mêmes tendances que les expériences: Il diminue pour un nombre de Lewis croissant.
- L'étirement de flamme est plutôt similaire pour tous les mélanges testés dans les simulations et les expériences.
- L'impact de l'étirement de flamme est plus visible sur la fraction massique brûlée pour un nombre de Lewis croissant.

Validation du modèle pour des différentes configurations du moteur

La comparaison des résultats de la simulation du modèle par une série des expériences de plusieurs points de fonctionnement avec une avance à l'allumage optimale et avec d'autres configurations spécifiques a montré que:

- Le coefficient de calibration du modèle FSD est très sensible au rapport de l'intensité de turbulence de la vitesse de flamme laminaire (u'/s_L).
- Les tendances de CA10 et CA50 sont récupérées par le modèle, même si une modification de l'avance à l'allumage est nécessaire, puisque la première étape de combustion n'est pas modélisée physiquement.
- Lors de la toute dernière étape de la combustion, le modèle ne peut pas calculer un rayon du front de flamme. La forme du front de flamme est susceptible de ne pas être décrite avec précision par un front de flamme sphérique. Cette incertitude explique pourquoi les tendances de CA90 et l'efficacité de combustion sont partiellement récupérés.

- Les coefficients du facteur de plissement des points de fonctionnement à l'avance optimale peuvent être utilisés dans le cas de variation de richesse.
- De même, les coefficients du facteur de plissement des points de fonctionnement à l'avance optimale peuvent être utilisés dans le cas d'un carburant essence/éthanol avec une corrélation de vitesse de flamme laminaire différente de celle qui a été utilisée pour les carburants typiques avec essence.
- Dans les cas de fraction des résiduels élevée, réalisés avec le VVT des soupapes d'admission, les coefficients du facteur de plissement des points de fonctionnement à l'avance optimale peuvent être utilisées jusqu'à 15% des résiduels.

Perspectives

Des chemins intéressants de travaux dans le futur se sont ouverts pendant l'amélioration du modèle zéro-dimensionnel de combustion :

Le modèle d'interaction flamme-paroi simule la diminution du plissement de flamme en se basant sur des résultats numériques et expérimentaux. Cependant, la contribution de l'écoulement laminaire dans la couche limite et la contribution des transferts thermiques par la flamme chaude vers la paroi froide ne sont pas discernées. Une amélioration possible pourrait être l'implémentation d'un modèle des transferts thermiques plus détaillé, qui simulerait le flux intense de chaleur depuis le front de flamme vers la paroi. Une stratification possible, à travers une fonction de densité de probabilité par exemple, de la température de gaz frais (T_u) serait aussi applicable. La température réduite aux environs de la paroi aurait un impact sur les caractéristiques de la flamme laminaire (épaisseur δ_L et vitesse de réaction s_L). En plus, la région de la couche limite pourrait être aussi modélisée, même pour une géométrie 0D, avec une "loi de la paroi pour la vitesse de l'écoulement" appropriée (u^+ , y^+ formulation comme elle est proposée par von Karman). Cette approche aurait un impact sur les caractéristiques de la flamme turbulente (intensité de turbulence u' et échelle de longueur L_T).

Les réactions post-flamme du CO et des HC imbrûlés sont prises en compte par les modèles proposés. Les grandeurs fondamentales, qui ont un effet sur les deux réactions post-flamme sont les températures des gaz frais et brûlés (T_u et T_b), la masse des HC imbrûlés (m_u) et les fractions massiques à l'équilibre (Y_i). L'estimation de la température des gaz frais peut être améliorée comme il a été discuté dans le paragraphe dernier. La température des gaz brûlés peut être modélisée à travers un modèle thermodynamique multizone. La stratification de température qui apparaîtrait dans les gaz brûlés, permettra de calculer la concentration du CO plus précisément. Une manière plus détaillée pour le calcul de la concentration à l'équilibre (notamment du CO) pourrait améliorer l'estimation de la concentration du CO à l'échappement. En plus, un modèle pour les volumes morts peut être introduit dans le modèle de combustion. Le mélange d'air/carburant qui entre dans les volumes morts et qui rentre dans la chambre de combustion baisserait la quantité du carburant consommé dans le front de flamme et augmenterait les HC consommés en mode post-flamme. Finalement, une chimie plus détaillée (avec plusieurs espèces) augmenterait aussi les fractions massiques du CO.

L'impact de l'étirement de flamme est très important spécialement pendant la première étape de la combustion. Dans ce travail, l'impact de l'étirement est modélisé que par un de ses composants. Autrement dit, c'est que la courbure de la flamme qui est prise en compte

par le modèle d'étirement de la flamme. L'omission du composant de cisaillement est basée sur les conclusions d'autres chercheurs. Une perspective intéressante serait d'explorer sous quelles conditions le cisaillement de flamme (flame strain) peut avoir un impact important. Son importance se montrerait par des expériences spéciales ou par des simulations numériques directes (DNS) avec des flammes de nombre de Lewis qui varie et avec des échelles de longueur suffisamment petites comme c'est le cas dans un moteur à allumage commandé. Une modélisation physique du processus d'allumage pourrait aussi offrir une prédiction plus précise de la surface de flamme initiale qui améliorerait les données d'entrée du modèle d'étirement.

References

- [1] H. Eichlseder and A. Wimmer, "Future perspectives of the IC engine," *14th Int. Conf. "Transport air ..."*, 2005.
- [2] S. Davis, S. Diegel, and R. Boundy, "Transportation energy data book: Edition 33," 2014.
- [3] T. J. Bell MC, Tomlin AS, Seakins PW, Kale GM, Watson A, Andrews GE, Routledge MN, *LANTERN - Leeds health Air pollution, Noise, Traffic and Emissions Research Network*. Leeds: Institute for Environment and Health, 2004.
- [4] L. S. Pilotto, R. M. Douglas, R. G. Attewell, and S. R. Wilson, "Respiratory effects associated with indoor nitrogen dioxide exposure in children.," *Int. J. Epidemiol.*, vol. 26, no. 4, pp. 788–796, Aug. 1997, doi: 10.1093/ije/26.4.788.
- [5] *Regulation (EC) No 715/2007 of the European Parliament and of the Council of 20 June 2007 on type approval of motor vehicles with respect to emissions from light passenger and commercial vehicles (Euro 5 and Euro 6) and on access to vehicle repair and mai. .*
- [6] "Monitoring of ACEA's commitment on CO2 emission reduction from passenger cars (2001)." 2003.
- [7] "EU CO2 standards for passenger cars and light-commercial vehicles | International Council on Clean Transportation." [Online]. Available: <http://www.theicct.org/eu-co2-standards-passenger-cars-and-lcvs>. [Accessed: 03-Feb-2015].
- [8] J. B. Heywood, *Internal Combustion Engine Fundamentals*. McGraw-Hill Science/Engineering/Math, 1988.
- [9] R. Bosch GmbH, *Gasoline-Engine Management*. 2004.
- [10] W. F. Ball, N. S. Jackson, A. D. Pilley, and B. C. Porter, "The Friction of a 1.6 Litre Automotive Engine-Gasoline and Diesel," *SAE Tech. Pap. 860418*, Feb. 1986, doi: 10.4271/860418.
- [11] J. B. Heywood, "Combustion and its Modeling in Spark-Ignition Engines," in *COMODIA*, 1994, vol. 94, pp. 1–15.
- [12] R. Stone, *Introduction to Internal Combustion Engines*, 4th ed. London: Palgrave Macmillan.
- [13] G. P. Merker, C. Schwarz, G. Stiesch, and F. Otto, *Verbrennungsmotoren.: Simulation der Verbrennung und Schadstoffbildung*. 2004.

- [14] C. T. Bowman, "Kinetics of pollutant formation and destruction in combustion," *Progress in Energy and Combustion Science*, vol. 1, no. 1. pp. 33–45, Jan-1975. doi: 10.1016/0360-1285(75)90005-2.
- [15] J. B. Heywood and E. Sher, *Two-Stroke Cycle Engine: It's Development, Operation and Design*. Taylor & Francis, 1999.
- [16] C. Meneveau and T. Poinso, "Stretching and quenching of flamelets in premixed turbulent combustion," *Combust. Flame*, vol. 86, no. 4, pp. 311–332, 1991, doi: 10.1016/0010-2180(91)90126-V.
- [17] T. Poinso and D. Veynante, *Theoretical and Numerical Combustion 3rd Edition*. 2012.
- [18] O. Laget, B. Reveille, L. Martinez, K. Truffin, C. Habchi, and C. Angelberger, "LES Calculations of a Four Cylinder Engine," *SAE Tech. Pap.*, no. 2011–01–0832, Apr. 2011, doi: 10.4271/2011-01-0832.
- [19] C. Pera, S. Richard, and C. Angelberger, "Exploitation of Multi-Cycle Engine LES to Introduce Physical Perturbations in 1D Engine Models for Reproducing CCV," *SAE Tech. Pap.*, no. 2012–01–0127, Apr. 2012, doi: 10.4271/2012-01-0127.
- [20] A. Schmid, M. Grill, H.-J. Berner, M. Bargende, S. Rossa, and M. Bottcher, "Development of a quasi-dimensional combustion model for stratified SI-engines," *SAE Tech. Pap.*, no. 2009–01–2659, Nov. 2010, doi: 10.4271/2009-01-2659.
- [21] R. J. Blint, "The Relationship of the Laminar Flame Width to Flame Speed," *Combustion Science and Technology*, vol. 49, no. 1–2. Taylor & Francis Group, pp. 79–92, 30-Sep-1986. doi: 10.1080/00102208608923903.
- [22] R. G. Abdel-Gayed, D. Bradley, M. N. Hamid, and M. Lawes, "Lewis number effects on turbulent burning velocity," *Symp. Combust.*, vol. 20, no. 1, pp. 505–512, Jan. 1985, doi: 10.1016/S0082-0784(85)80539-7.
- [23] B. Renou, A. Boukhalfa, D. Puechberty, and M. Trinité, "Effects of stretch on the local structure of preely propagating premixed low-turbulent flames with various lewis numbers," *Symp. Combust.*, vol. 27, no. 1, pp. 841–847, Jan. 1998, doi: 10.1016/S0082-0784(98)80480-3.
- [24] B. Renou, A. Boukhalfa, D. Puechberty, and M. Trinité, "Local scalar flame properties of freely propagating premixed turbulent flames at various Lewis numbers," *Combust. Flame*, vol. 123, no. 4, pp. 507–521, Dec. 2000, doi: 10.1016/S0010-2180(00)00180-2.

- [25] B. Renou and A. Boukhalfa, "An Experimental Study of Freely Propagating Premixed Flames at Various Lewis Numbers," *Combust. Sci. Technol.*, vol. 162, no. 1, pp. 347–370, Jan. 2001, doi: 10.1080/00102200108952148.
- [26] F. Williams, "A review of some theoretical considerations of turbulent flame structure," *AGARD Conf. Proceeding, 1975*, 1975.
- [27] M. Matalon and B. J. Matkowsky, "Flames as gasdynamic discontinuities," *J. Fluid Mech.*, vol. 124, pp. 239–259, 1982, doi: 10.1017/S0022112082002481.
- [28] F. Halter, T. Tahtouh, and C. Mounaïm-Rousselle, "Nonlinear effects of stretch on the flame front propagation," *Combust. Flame*, vol. 157, no. 10, pp. 1825–1832, Oct. 2010, doi: 10.1016/j.combustflame.2010.05.013.
- [29] P. Sagaut and C. Cambon, *Homogeneous Turbulence Dynamics*. Cambridge University Press, 2008.
- [30] P. Sagaut, *Turbulence: Une Introduction*. Notes de cours, 2012.
- [31] C. R. Ferguson and A. T. Kirkpatrick, *Internal Combustion Engines: Applied Thermosciences*. 2000.
- [32] F. Bozza, A. Gimelli, N. Federico, S. S. Merola, and B. M. Vaglieco, "Validation of a Fractal Combustion Model through Flame Imaging," *SAE Tech. Pap.*, no. 2005-01-1120, Apr. 2005, doi: 10.4271/2005-01-1120.
- [33] F. Bozza, G. Fontana, E. Galloni, and E. Torella, "3D-1D Analyses of the Turbulent Flow Field, Burning Speed and Knock Occurrence in a Turbocharged SI Engine," in *8th International Conference on Engines for Automobiles*, 2007, no. 2007-24-0029, 10.4271/2007-24-0029.
- [34] F. Bozza, A. Gimelli, L. Strazzullo, E. Torella, and C. Cascone, "Steady-State and Transient Operation Simulation of a 'Downsized' Turbocharged SI Engine," in *SAE Technical Paper*, 2007, no. 2007-01-0381, 10.4271/2007-01-0381.
- [35] R. Borghi, "On the structure and morphology of turbulent premixed flames," *Recent Adv. Aerosp. Sci.*, 1985.
- [36] N. Peters, "The turbulent burning velocity for large-scale and small-scale turbulence," *Journal of Fluid Mechanics*, vol. 384, pp. 107–132, 1999, doi: 10.1017/S0022112098004212.
- [37] H. Shen, P. C. Hinze, and J. B. Heywood, "A Study of Cycle-to-Cycle Variations in SI Engines Using a Modified Quasi-Dimensional Model," *SAE Tech. Pap.*, no. 961187, 1996, doi: 10.4271/961187.

- [38] J. C. Keck, "Turbulent flame structure and speed in spark-ignition engines," *Symp. Combust.*, vol. 19, no. 1, pp. 1451–1466, Jan. 1982, doi: 10.1016/S0082-0784(82)80322-6.
- [39] G. P. Beretta, M. Rashidi, and J. C. Keck, "Turbulent flame propagation and combustion in spark ignition engines," *Combustion and Flame*, vol. 52, pp. 217–245, Jan-1983. doi: 10.1016/0010-2180(83)90135-9.
- [40] S. Verhelst and C. G. W. Sheppard, "Multi-zone thermodynamic modelling of spark-ignition engine combustion - An overview," *Energy Convers. Manag.*, vol. 50, no. 5, pp. 1326–1335, May 2009, doi: 10.1016/j.enconman.2009.01.002.
- [41] C. D. Rakopoulos, C. N. Michos, and E. G. Giakoumis, "Thermodynamic Analysis of SI Engine Operation on Variable Composition Biogas-Hydrogen Blends Using a Quasi-Dimensional , Multi-Zone Combustion Model," *SAE Tech. Pap. 2009-01-0931*, vol. 2, no. 1, pp. 880–910, Apr. 2009, doi: 10.4271/2009-01-0931.
- [42] M. Metghalchi and J. C. Keck, "Laminar burning velocity of propane-air mixtures at high temperature and pressure," *Combustion and Flame*, vol. 38, no. null, pp. 143–154, Jan-1980. doi: 10.1016/0010-2180(80)90046-2.
- [43] M. Metghalchi and J. C. Keck, "Burning velocities of mixtures of air with methanol, isooctane, and indolene at high pressure and temperature," *Combust. Flame*, vol. 48, pp. 191–210, Jan. 1982, doi: 10.1016/0010-2180(82)90127-4.
- [44] M. Grill, T. Billinger, and M. Bargende, "Quasi-Dimensional Modeling of Spark Ignition Engine Combustion with Variable Valve Train," *SAE Tech. Pap.*, no. 2006–01–1107, Apr. 2006, doi: 10.4271/2006-01-1107.
- [45] A. Boiarciuc and A. Floch, "Evaluation of a 0D Phenomenological SI Combustion Model," *SAE Tech. Pap.*, no. 2011–01–1894, Aug. 2011, doi: 10.4271/2011-01-1894.
- [46] M. Rivas, P. Higelin, C. Caillol, O. Sename, E. Witrant, and V. Talon, "Validation and Application of a New 0D Flame/Wall Interaction Sub Model for SI Engines," *SAE Int. J. Engines*, vol. 5, no. 3, pp. 718–733, Aug. 2011, doi: 10.4271/2011-01-1893.
- [47] T. Hattrell, C. G. W. Sheppard, A. A. Burluka, J. Neumeister, and A. Cairns, "Burn Rate Implications of Alternative Knock Reduction Strategies for Turbocharged SI Engines," *SAE Tech. Pap.*, no. 2006–01–1110, Apr. 2006, doi: 2006-01-1110.
- [48] V. L. Zimont, "Theory of turbulent combustion of a homogeneous fuel mixture at high reynolds numbers," *Combust. Explos. Shock Waves*, vol. 15, no. 3, pp. 305–311, 1979, doi: 10.1007/BF00785062.
- [49] A. M. Steinberg and J. F. Driscoll, "Straining and wrinkling processes during turbulence–premixed flame interaction measured using temporally-resolved

- diagnostics,” *Combust. Flame*, vol. 156, no. 12, pp. 2285–2306, Dec. 2009, doi: 10.1016/j.combustflame.2009.06.024.
- [50] S. Richard, S. Bougrine, G. Font, F. A. Lafossas, and F. le Berr, “On the Reduction of a 3D CFD Combustion Model to Build a Physical 0D Model for Simulating Heat Release, Knock and Pollutants in SI Engines,” *Oil Gas Sci. Technol.*, vol. 64, no. 3, pp. 223–242, Jun. 2009, doi: 10.2516/ogst/2008055.
- [51] H. G. Weller, G. Tabor, A. D. Gosman, and C. Fureby, “Application of a flame-wrinkling les combustion model to a turbulent mixing layer,” *Symposium (International) on Combustion*, vol. 27, no. 1, pp. 899–907, Jan-1998, doi: 10.1016/S0082-0784(98)80487-6.
- [52] S. Richard and D. Veynante, “A 0-D flame wrinkling equation to describe the turbulent flame surface evolution in SI engines,” *Comptes Rendus Mécanique*, vol. 343, no. 3, pp. 219–231, Mar. 2015, doi: 10.1016/j.crme.2014.09.003.
- [53] S. Bougrine, “0-Dimensional Modeling of the Combustion of Alternative Fuels in Spark Ignition Engines,” Ecole Centrale Paris, 2012.
- [54] F. Charlette, C. Meneveau, and D. Veynante, “A power-law flame wrinkling model for LES of premixed turbulent combustion Part II: Dynamic formulation,” *Combust. Flame*, vol. 131, no. 1–2, pp. 181–197, Oct. 2002, doi: 10.1016/S0010-2180(02)00401-7.
- [55] F. Charlette, C. Meneveau, and D. Veynante, “A power-law flame wrinkling model for LES of premixed turbulent combustion Part I: non-dynamic formulation and initial tests,” *Combust. Flame*, vol. 131, no. 1–2, pp. 159–180, Oct. 2002, doi: 10.1016/S0010-2180(02)00400-5.
- [56] J. Duclos, D. Veynante, and T. Poinsot, “A comparison of flamelet models for premixed turbulent combustion,” *Combustion and Flame*, vol. 95, no. 1–2, pp. 101–117, Oct-1993, doi: 10.1016/0010-2180(93)90055-8.
- [57] R. Herweg and R. R. Maly, “A Fundamental Model for Flame Kernel Formation in S. I. Engines,” *SAE Tech. Pap.*, no. 922243, Oct. 1992, doi: 10.4271/922243.
- [58] R. J. Blint, “Flammability limits for exhaust gas diluted flames,” *Symp. Combust.*, vol. 22, no. 1, pp. 1547–1554, Jan. 1989, doi: 10.1016/S0082-0784(89)80165-1.
- [59] D. Bradley, M. Lawes, and M. S. Mansour, “Flame surface densities during spherical turbulent flame explosions,” *Proc. Combust. Inst.*, vol. 32, no. 1, pp. 1587–1593, Jan. 2009, doi: 10.1016/j.proci.2008.06.020.
- [60] S. Chaudhuri, F. Wu, D. Zhu, and C. K. Law, “Flame speed and self-similar propagation of expanding turbulent premixed flames,” *Phys. Rev. Lett.*, vol. 108, no. 4, 2012, doi: 10.1103/PhysRevLett.108.044503.

- [61] P. H. Pierce, J. B. Ghandhi, and J. K. Martin, "Near-Wall Velocity Characteristics in Valved and Ported Motored Engines," *SAE Technical Paper*, no. 920152. 01-Feb-199210.4271/920152.
- [62] S. Demesoukas, C. Caillol, P. Higelin, and A. Boiarciuc, "Zero-Dimensional Spark Ignition Combustion Modeling - A Comparison of Different Approaches," in *SAE Technical Paper*, 2013, no. 2013-24-0022, 10.4271/2013-24-0022.
- [63] H. K. Newhall, "Kinetics of engine-generated nitrogen oxides and carbon monoxide," *Symp. Combust.*, vol. 12, no. 1, pp. 603-613, Jan. 1969, doi: 10.1016/S0082-0784(69)80441-8.
- [64] J. Vancoillie, J. Demuyne, L. Sileghem, M. Van De Ginste, S. Verhelst, L. Brabant, and L. Van Hoorebeke, "The potential of methanol as a fuel for flex-fuel and dedicated spark-ignition engines," *Appl. Energy*, vol. 102, pp. 140-149, Feb. 2013, doi: 10.1016/j.apenergy.2012.05.065.
- [65] X. Wu, Q. Li, J. Fu, C. Tang, Z. Huang, R. Daniel, G. Tian, and H. Xu, "Laminar burning characteristics of 2,5-dimethylfuran and iso-octane blend at elevated temperatures and pressures," *Fuel*, vol. 95, pp. 234-240, May 2012, doi: 10.1016/j.fuel.2011.11.057.
- [66] X. Wu, Z. Huang, X. Wang, C. Jin, C. Tang, L. Wei, and C. K. Law, "Laminar burning velocities and flame instabilities of 2,5-dimethylfuran-air mixtures at elevated pressures," *Combust. Flame*, vol. 158, no. 3, pp. 539-546, Mar. 2011, doi: 10.1016/j.combustflame.2010.10.006.
- [67] P. Brequigny, G. Dayma, F. Halter, C. Mounaïm-Rousselle, T. Dubois, and P. Dagaut, "Laminar burning velocities of premixed nitromethane/air flames: An experimental and kinetic modeling study," *Proc. Combust. Inst.*, vol. 35, no. 1, pp. 703-710, 2015, doi: 10.1016/j.proci.2014.06.126.
- [68] N. C. Blizard and J. C. Keck, "Experimental and Theoretical Investigation of Turbulent Burning Model for Internal Combustion Engines," *SAE Tech. Pap.*, no. 740191, Feb. 1974, doi: 10.4271/740191.
- [69] S. M. Candel and T. J. Poinso, "Flame Stretch and the Balance Equation for the Flame Area," *Combustion Science and Technology*, vol. 70, no. 1-3. Taylor & Francis Group, pp. 1-15, 06-Mar-199010.1080/00102209008951608.
- [70] Z. Chen, "On the extraction of laminar flame speed and Markstein length from outwardly propagating spherical flames," *Combust. Flame*, vol. 158, no. 2, pp. 291-300, Feb. 2011, doi: 10.1016/j.combustflame.2010.09.001.
- [71] D. Bradley, R. A. Hicks, M. Lawes, C. G. W. Sheppard, and R. Woolley, "The Measurement of Laminar Burning Velocities and Markstein Numbers for Iso-octane-

- Air and Iso-octane–n-Heptane–Air Mixtures at Elevated Temperatures and Pressures in an Explosion Bomb,” *Combust. Flame*, vol. 115, no. 1–2, pp. 126–144, Oct. 1998, doi: 10.1016/S0010-2180(97)00349-0.
- [72] D. Bradley, M. Lawes, and M. S. Mansour, “Explosion bomb measurements of ethanol–air laminar gaseous flame characteristics at pressures up to 1.4MPa,” *Combust. Flame*, vol. 156, no. 7, pp. 1462–1470, Jul. 2009, doi: 10.1016/j.combustflame.2009.02.007.
- [73] A. P. Kelley, A. J. Smallbone, D. L. Zhu, and C. K. Law, “Laminar flame speeds of C5 to C8 n-alkanes at elevated pressures: Experimental determination, fuel similarity, and stretch sensitivity,” *Proc. Combust. Inst.*, vol. 33, no. 1, pp. 963–970, 2011, doi: 10.1016/j.proci.2010.06.074.
- [74] P. Brequigny, C. Mounaïm-Rousselle, F. Halter, B. Moreau, and T. Dubois, “Impact of Fuel Properties and Flame Stretch on the Turbulent Flame Speed in Spark-Ignition Engines,” *SAE Tech. Pap.*, no. 2013–24–0054, Sep. 2013, doi: 10.4271/2013-24-0054.
- [75] P. G. Aleiferis, J. Serras-Pereira, and D. Richardson, “Characterisation of flame development with ethanol, butanol, iso-octane, gasoline and methane in a direct-injection spark-ignition engine,” *Fuel*, vol. 109, pp. 256–278, Jul. 2013, doi: 10.1016/j.fuel.2012.12.088.
- [76] P. Brequigny, F. Halter, C. Mounaïm-Rousselle, B. Moreau, and T. Dubois, “Thermodiffusive Effect on the Flame Development in Lean Burn Spark Ignition Engine,” *SAE Tech. Pap.*, no. 2014–01–2630, Oct. 2014, doi: 10.4271/2014-01-2630.
- [77] R. N. Dahms, M. C. Drake, T. D. Fansler, T. W. Kuo, and N. Peters, “Understanding ignition processes in spray-guided gasoline engines using high-speed imaging and the extended spark-ignition model SparkCIMM. Part B: Importance of molecular fuel properties in early flame front propagation.,” *Combust. Flame*, vol. 158, no. 11, pp. 2245–2260, Nov. 2011, doi: 10.1016/j.combustflame.2011.04.003.
- [78] S. Bougrine, S. Richard, O. Colin, and D. Veynante, “Fuel Composition Effects on Flame Stretch in Turbulent Premixed Combustion: Numerical Analysis of Flame-Vortex Interaction and Formulation of a New Efficiency Function,” *Flow, Turbul. Combust.*, vol. 93, no. 2, pp. 259–281, Jun. 2014, doi: 10.1007/s10494-014-9546-4.
- [79] J. R. Dormand and P. J. Prince, “A family of embedded Runge-Kutta formulae,” *Journal of Computational and Applied Mathematics*, vol. 6, no. 1, pp. 19–26, Mar-1980. doi: 10.1016/0771-050X(80)90013-3.
- [80] D. Stull and H. Prophet, “JANAF thermochemical tables,” 1971.

- [81] J. W. Fox, W. K. Cheng, and J. B. Heywood, "A Model for Predicting Residual Gas Fraction in Spark-Ignition Engines," *SAE Tech. Pap.*, no. 931025, Mar. 1993, doi: 10.4271/931025.
- [82] B. McBride, M. Zehe, and S. Gordon, "NASA Glenn coefficients for calculating thermodynamic properties of individual species," 2002.
- [83] C. Olikara and G. Borman, "A computer program for calculating properties of equilibrium combustion products with some applications to IC engines," *SAE Tech. Pap.*, no. 750468, 1975.
- [84] G. Woschni, "A Universally Applicable Equation for the Instantaneous Heat Transfer Coefficient in the Internal Combustion Engine," *SAE Tech. Pap.*, no. 670931, Feb. 1967, doi: 10.4271/670931.
- [85] O. Pajot, C. Mounaïm-Rousselle, and D. Queiros-Conde, "New Data on Flame Behaviour in Lean Burn S.I. Engine," *SAE Tech. Pap.*, no. 2001-01-1956, May 2001, doi: 10.4271/2001-01-1956.
- [86] F. N. Egolfopoulos, H. Zhang, and Z. Zhang, "Wall effects on the propagation and extinction of steady, strained, laminar premixed flames," *Combust. Flame*, vol. 109, no. 1-2, pp. 237-252, Apr. 1997, doi: 10.1016/S0010-2180(96)00152-6.
- [87] C. K. Westbrook, A. A. Adamczyk, and G. A. Lavoie, "A numerical study of laminar flame wall quenching," *Combustion and Flame*, vol. 40, pp. 81-99, Jan-1981. doi: 10.1016/0010-2180(81)90112-7.
- [88] B. Boust, J. Sotton, S. A. Labuda, and M. Bellenoue, "A thermal formulation for single-wall quenching of transient laminar flames," *Combust. Flame*, vol. 149, no. 3, pp. 286-294, May 2007, doi: 10.1016/j.combustflame.2006.12.019.
- [89] F. Foucher, S. Burnel, C. Mounaim-Rousselle, M. Boukhalfa, B. Renou, and M. Trinité, "Flame wall interaction: Effect of stretch," *Exp. Therm. Fluid Sci.*, vol. 27, no. 4, pp. 431-437, Apr. 2003, doi: 10.1016/S0894-1777(02)00255-8.
- [90] F. Foucher, S. Burnel, and C. Mounaïm-Rousselle, "Evaluation of burning rates in the vicinity of the piston in a spark-ignition engine," *Proc. Combust. Inst.*, vol. 29, no. 1, pp. 751-757, Jan. 2002, doi: 10.1016/S1540-7489(02)80096-7.
- [91] T. Poinso, D. Haworth, and G. Bruneaux, "Direct simulation and modeling of flame-wall interaction for premixed turbulent combustion," *Combustion and Flame*, vol. 95, no. 1-2, pp. 118-132, Oct-1993. doi: 10.1016/0010-2180(93)90056-9.
- [92] G. Bruneaux, "Flame-wall interaction simulation in a turbulent channel flow," *Combustion and Flame*, vol. 107, no. 1-2, pp. 27-36, Oct-1996. doi: 10.1016/0010-2180(95)00263-4.

- [93] F. Foucher and C. Mounaïm-Rousselle, "Fractal approach to the evaluation of burning rates in the vicinity of the piston in a spark-ignition engine," *Combust. Flame*, vol. 143, no. 3, pp. 323–332, Nov. 2005, doi: 10.1016/j.combustflame.2005.06.007.
- [94] K. N. C. Bray, "Studies of the Turbulent Burning Velocity," *Proc. R. Soc. A Math. Phys. Eng. Sci.*, vol. 431, no. 1882, pp. 315–335, Nov. 1990, doi: 10.1098/rspa.1990.0133.
- [95] S. Labuda, M. Karrer, J. Sotton, and M. Bellenoue, "Experimental Study of Single-Wall Flame Quenching at High Pressures," *Combust. Sci. Technol.*, vol. 183, no. 5, pp. 409–426, 2011, doi: 10.1080/00102202.2010.528815.
- [96] A. Ratzke, G. Butzbach, and F. Dinkelacker, "Simulating the Near-Wall Flame Extinction for Gas Engine Application," *Proc. Eur. Combust. Meet. 2013*, pp. 1–6, 2013.
- [97] J. A. Gatowski, J. B. Heywood, and C. Deleplace, "Flame photographs in a spark-ignition engine," *Combustion and Flame*, vol. 56, no. 1. pp. 71–81, Apr-1984 10.1016/0010-2180(84)90006-3.
- [98] J. Valério, M., Raggi, K., and Sodré, "Model for Kinetic Formation of CO Emissions in Internal Combustion Engines," *SAE Tech. Pap.*, no. 2003–01–3138, Oct. 2003, doi: 10.4271/2003-01-3138.
- [99] S. Bougrine, S. Richard, J.-B. Michel, and D. Veynante, "Simulation of CO and NO emissions in a SI engine using a 0D coherent flame model coupled with a tabulated chemistry approach," *Appl. Energy*, vol. 113, pp. 1199–1215, Jan. 2014, doi: 10.1016/j.apenergy.2013.08.038.
- [100] K.-C. Wu and S. Hochgreb, "The Roles of Chemistry and Diffusion on Hydrocarbon Post-Flame Oxidation," *Combustion Science and Technology*, vol. 130, no. 1–6. pp. 365–398, Dec-1997 10.1080/00102209708935749.
- [101] K.-C. Wu and S. Hochgreb, "Numerical simulation of post-flame oxidation of hydrocarbons in spark ignition engines," *SAE Tech. Pap.*, no. 970886, Feb. 1997, doi: 10.4271/970886.
- [102] C. Hasse, M. Bollig, N. Peters, and H. A. Dwyer, "Quenching of laminar iso-octane flames at cold walls," *Combust. Flame*, vol. 122, no. 1–2, pp. 117–129, Jul. 2000, doi: 10.1016/S0010-2180(00)00107-3.
- [103] G. A. Lavoie, "Correlations of Combustion Data for SI Engine Calculations- Laminar Flame Speed, Quench Distance and Global Reaction Rates," *SAE Tech. Pap.*, no. 780229, Feb. 1978, doi: 10.4271/780229.

- [104] R. Bird, W. Stewart, and E. Lightfoot, *Transport phenomena*. John Wiley & Sons, 2007.
- [105] J. A. M. Robert J Kee, Graham Dixon-Lewis, Jürgen Warnatz, Michael E Coltrin, “A Fortran computer code package for the evaluation of gas-phase, multicomponent transport properties,” *Sandia Natl. Lab.*, 1988.
- [106] N. S. Savva and D. T. Hountalas, “Evolution and application of a pseudo-multi-zone model for the prediction of NO_x emissions from large-scale diesel engines at various operating conditions,” *Energy Convers. Manag.*, vol. 85, pp. 373–388, Sep. 2014, doi: 10.1016/j.enconman.2014.05.103.
- [107] C. D. Rakopoulos and C. N. Michos, “Development and validation of a multi-zone combustion model for performance and nitric oxide formation in syngas fueled spark ignition engine,” *Energy Convers. Manag.*, vol. 49, no. 10, pp. 2924–2938, Oct. 2008, doi: 10.1016/j.enconman.2008.02.011.
- [108] C. Caillol, T. Delorme, and B. Porterie, “Modeling of nitric oxide formation in lean burn natural gas engines using a presumed probability density function method,” in *Clean Air 2005, Lisbon*, 2005.
- [109] J. K. Bechtold and M. Matalon, “The dependence of the Markstein length on stoichiometry,” *Combust. Flame*, vol. 127, no. 1–2, pp. 1906–1913, Oct. 2001, doi: 10.1016/S0010-2180(01)00297-8.
- [110] U. C. Müller, M. Bollig, and N. Peters, “Approximations for burning velocities and Markstein numbers for lean hydrocarbon and methanol flames,” *Combust. Flame*, vol. 108, no. 3, pp. 349–356, Feb. 1997, doi: 10.1016/S0010-2180(96)00110-1.
- [111] R. N. Dahms, M. C. Drake, T. D. Fansler, T. W. Kuo, and N. Peters, “Understanding ignition processes in spray-guided gasoline engines using high-speed imaging and the extended spark-ignition model SparkCIMM. Part A: Spark channel processes and the turbulent flame front propagation,” *Combust. Flame*, vol. 158, no. 11, pp. 2229–2244, Nov. 2011, doi: 10.1016/j.combustflame.2011.03.012.
- [112] P. Giansetti and P. Higelin, “Residual Gas Fraction Measurement and Estimation in Spark Ignition Engine,” *SAE Tech. Pap.*, no. 2007–01–1900, Jul. 2007, doi: 10.4271/2007-01-1900.
- [113] and B. F. V. Liou, T. M., Hall, D. A., “Laser Droplet Velocimetry Measurements in Valved and Ported Engines,” *SAE Tech. Pap.*, no. 840375, Feb. 1984, doi: 10.4271/840375.
- [114] C. and W. J. H. Bopp, S. Vafidis, “The Effect of Engine Speed on the TDC Flowfield in a Motored Reciprocating Engine,” *SAE Tech. Pap.*, no. 860023, Feb. 1986, doi: 10.4271/860023.

- [115] J. N. Mattavi and G. M. C. R. Laboratories, *Combustion modeling in reciprocating engines*. Plenum Press, 1980.
- [116] P. E. Kapus, A. Fuerhapter, H. Fuchs, and G. K. Fraidl, "Ethanol Direct Injection on Turbocharged SI Engines - Potential and Challenges," *SAE Tech. Pap.*, no. 2007-01-1408, Apr. 2007, doi: 10.4271/2007-01-1408.
- [117] C. Marriott, M. Wiles, J. Gwidt, and S. Parrish, "Development of a naturally aspirated spark ignition direct-injection flex-fuel engine," *SAE Int. J. Engines*, vol. 1, no. 1, pp. 267-295, Apr. 2009, doi: 10.4271/2008-01-0319.
- [118] K. Nakama, J. Kusaka, and Y. Daisho, "Effect of Ethanol on Knock in Spark Ignition Gasoline Engines," in *Small Engine Technology Conference*, 2008, vol. 1, no. 2008-32-0020, pp. 1366-1380, 10.4271/2008-32-0020.
- [119] I. Z. Syed, Y. Yeliana, A. Mukherjee, J. D. Naber, and D. Michalek, "Numerical Investigation of Laminar Flame Speed of Gasoline - Ethanol/Air Mixtures with Varying Pressure, Temperature and Dilution," *SAE Tech. Pap.*, no. 2010-01-0620, Apr. 2010, doi: 10.4271/2010-01-0620.
- [120] S. Bougrine, S. Richard, and D. Veynante, "Modelling and Simulation of the Combustion of Ethanol blended Fuels in a SI Engine using a 0D Coherent Flame Model," in *9th International Conference on Engines and Vehicles*, 2009, no. 2009-24-0016, 10.4271/2009-24-0016.

Sokratis DEMESOUKAS

Modélisation 0D/1D de la combustion pour l'optimisation des systèmes de combustion des moteurs à allumage commandé

Résumé :

De nos jours, la conception de moteurs à combustion interne à allumage commandé exige une consommation de carburant réduite et des émissions polluantes faibles, tout en conservant une performance adéquate. Le coût élevé des essais expérimentaux vient en faveur de l'utilisation de la simulation numérique pour l'évaluation de nouvelles définitions techniques. La modélisation phénoménologique zéro-dimensionnelle de combustion permet d'évaluer les différentes définitions techniques en tenant compte de différents aspects de de la combustion à allumage commandé comme la géométrie, la flamme laminaire et l'impact de la turbulence. Ces modèles calculent également la concentration des espèces de gaz d'échappement. Afin de créer un modèle de combustion, qui pourra décrire la physique de la combustion, les aspects principaux de la combustion prémélangée laminaire et turbulent sont identifiés. Trois versions de modèles de combustion typiques sont comparées en termes de description physique du processus de combustion. Le résultat de cette comparaison a indiqué le modèle le plus pertinent (le modèle de densité de surface de flamme). Ce modèle est retenu et il est complété avec la modélisation physique des plusieurs phénomènes qui affectent le taux de dégagement de chaleur. Ces phénomènes sont l'interaction flamme-paroi, les réactions post flamme et l'étirement de flamme. Enfin, le modèle proposé est validé pour plusieurs configurations techniques. Chaque configuration a un impact sur un paramètre spécifique de moteur. Cette analyse montre quels sont les intervalles de confiance et les limitations du modèle proposé.

Mots clés : modélisation, combustion, allumage commandé, interaction flamme-paroi, réactions poste-flamme, étirement

0D/1D combustion modeling for the combustion systems optimization of spark ignition engines

Summary:

Nowadays, the design of Spark Ignition internal combustion engines is focused on the reduction of fuel consumption and low pollutant emissions, while conserving an adequate output power. The high cost of experimental testing comes in favor of the use of numerical simulations for the assessment of engine technologies. Phenomenological Zero-Dimensional combustion models allow evaluating various technical concepts since they take into account various aspects of spark ignition combustion such as chamber geometry, laminar flame characteristics (thickness and speed) and the impact of turbulence. Such models also calculate species concentration of the exhaust gases. In order to create a zero-dimensional combustion model, which can be able to describe correctly the physics of combustion, the key aspects of laminar and turbulent premixed combustion are identified. Three versions of typical combustion models are compared in terms of physical description of the combustion process. The result of this comparison indicated the most physically pertinent model (the Flame Surface Density model). This model is retained and is enhanced with physical modeling of the several phenomena, which affect the heat release rate. Those phenomena are the wall-flame interaction, post-flame reactions and flame stretch. Finally, the proposed model is validated for several engine configurations. Each configuration has an impact on a specific engine parameter. This analysis shows which are the confidence intervals and the limitations of the proposed model.

Keywords : spark ignition combustion, wall-flame interaction, post-flame reactions, stretch



Laboratoire PRISME – Université d'Orléans
8, rue Leonard de Vinci
45072 Orléans Cedex 2
FRANCE

